THE NEW GENERATION MICROWAVE PLASMA ASSISTED CVD REACTOR FOR DIAMOND SYNTHESIS

By

Yajun Gu

A DISSERTATION

Submitted to
Michigan State University
in partial fulfillment of the requirements
for the degree of

DOCTOR OF PHILOSOPHY

Electrical Engineering

2011

ABSTRACT

THE NEW GENERATION MICROWAVE PLASMA ASSISTED CVD REACTOR FOR DIAMOND SYNTHESIS

By

Yajun Gu

In view of the important, recent, opportunity to commercially synthesize high quality single crystal diamond (SCD) and polycrystalline diamond (PCD), there is a need to continue to improve existing microwave plasma assisted reactor designs that enable high quality and high deposition rate SCD synthesis. It is now widely recognized that both the quality and growth rates of microwave plasma assisted CVD (MPACVD) synthesized diamond are improved by using high power density microwave discharges operating at pressures above 160 Torr. Thus the object of this research is to design, develop, optimize and experimentally evaluate a new generation 2.45 GHz microwave plasma assisted chemical vapor deposition (MPACVD) reactor and associated processes methods that are both robust and are optimized for high pressure and high power density operation, and thereby take advantage of the improved deposition chemistry and physics that exist at high pressures. This MPACVD reactor operates with high power densities and at pressures up to 320 Torr. Differences from earlier MPACVD reactor designs include an increase in applicator and

dome radii and the excitation of the applicator with a new hybrid electromagnetic mode. The reactor is experimentally evaluated by synthesizing single crystal diamond (SCD) at pressures from 180-320 Torr with absorbed power densities between 300 to 1000 W/cm^3. Without N_2 addition SCD growth rates as high as 80 microns/hour were observed. A SCD growth window between 950 ℃ to 1300 ℃ was identified and within this growth window growt h rates were 1.2-2.5 times greater than the corresponding growth rates for earlier reactor designs. SCD characterization by micro-Raman spectroscopy, SIMS, and by IR-UV transmission spectroscopy indicated that the synthesized SCD quality is that of type IIa diamond.

To my wife Huiyuan Tang

and my parents Zhongping Gu and Haopei Chen

ACKNOWLEDGEMENTS

First I would like to express sincere gratitude to my major advisor Dr. Jes Asmussen for his guidance, encouragement, mentorship and support throughout the development of this research and the writing of this dissertation. Thanks are also due to the other members of my advisory committee: Dr. Timothy Grotjohn, Dr. Donnie Reinhard and Dr. Greg Swain. Sincere appreciation is to Dr. Thomas Schuelke, Michael Becker, M. Kagan Yaran and all Fraunhofer USA CCL personnel for laboratory assistant. Additional thanks are given to all fellow graduate students for their help and friendship.

This research was supported by Center for Coatings and Laser Applications Fraunhofer USA and the Richard M. Hong Chaired Professorship.

TABLE OF CONTENTS

LIST OF TABLES

LIST OF FIGURES

CHAPTER 1

INTRODUCTION

1.1 Introduction

In view of the important, recent, opportunity to commercially synthesize a variety of high quality diamond materials, i.e. polycrystalline diamond (PCD) and single crystal diamond (SCD), there is a need to further improve existing microwave plasma assisted reactor designs and to develop entirely new designs that are able to achieve diamond synthesis at high rates. For example, certain applications require (30-150 μm/hr) high deposition rates and often some reactor users desire both high rates and very high quality [1-3] diamond. Also since it is important to increase deposition rates it is desirable to develop and optimize new reactors designs and processes in the 100-300 Torr (The unit Torr is a non-SI unit of pressure with the ratio of 760 Torr to 1 standard atmosphere) pressure regime.

This Ph.D. thesis investigates the design and development of a new microwave plasma-assisted CVD reactor. The investigation begins by employing a generic but versatile microwave reactor design which has a variety of dimensions that can be modified, “reshaped” and adjusted to allow process optimization for different diamond synthesis applications. In particular the generic reactor geometry can be varied by changing characteristic reactor dimensions, such as varying both height and radius of the cavity, adjusting the shape, position and the size of the substrate holder, etc.

Reactor designs variations are first investigated by starting with an existing benchmark reactor design and then modifying it, i.e. by varying the dimensions, via numerical modeling to produce a new reactor design. Building upon intuition gleaned from past reactor designs and experimental CVD diamond synthesis experience this thesis research modifies existing reactor designs by varying the size and shape of the applicator and plasma reactor volume and then experimentally evaluates these design modifications in CVD diamond synthesis applications. Numerical electromagnetic reactor models are also employed to calculate and provide an understanding of the electromagnetic field patterns within the new reactor design. In particular the experimental experiences of the most promising reactor design, identified in this thesis as Reactor C, is experimentally explored using 2.45 GHz excitation over 180-300 Torr operating pressure regime. First and briefly, PCD is synthesized and then SCD is experimentally examined.

1.2 Research objectives

The objective of this thesis research is to design, develop, optimize and experimentally evaluate a new generation 2.45 GHz microwave plasma assisted chemical vapor deposition (MPACVD) reactor and associated diamond synthesis processes that enable the synthesis of polycrystalline diamond (PCD) or single crystalline diamond (SCD) at high deposition rates. The proposed thesis research will extend the currently existing MSU reactor technologies to operate at high pressures, and high power densities.

This thesis research involves two specific activities: (1) an engineering related, technology development activity and (2) an activity that verifies a specific scientific hypothesis. The technology development involves the invention, the building and the experimental evaluation of new MPACVD machines/instruments that synthesize diamond at high pressures (180- 320 Torr) and high absorbed microwave power densities (300-1000 W/cm^3). The scientific hypothesis that is experimentally evaluated is that as the MPACVD diamond synthesis process is moved to higher pressures (> 180 Torr) that: (1) growth rate increases and (2) high quality diamond can be synthesized over an expanded range of methane concentrations.

These objectives will be accomplished by performing the following tasks:

(1) A literature review and comparative analysis of existing MPACVD reactor technologies--- i.e. performing a state-of-the-art assessment of current commercially available MPACVD reactors;

(2) Identify and develop a promising design and then build it and experimentally evaluated it in specific diamond synthesis applications.

(3) Perform a numerical electromagnetic field (EMF) simulation analysis of the current MSU generic reactors. Identify the important dimensions of the generic MSU reactor (R_1, R_2, R_3, R_4 etc. and L_1, L_2 etc. See Figure 1.1) and vary these dimensions to develop an improved understanding of reactor EMF behavior.

(4) Evaluate the new reactor design in MPACVD synthesis of PCD at high pressures (180-300 Torr) and high power densities (300-1000 W/cm^3) over a one inch diameter substrate area; and

(5) Perform a specific detailed experimental evaluation of the new reactor design by synthesizing high quality SCD in the high pressure and high power density operating regime.

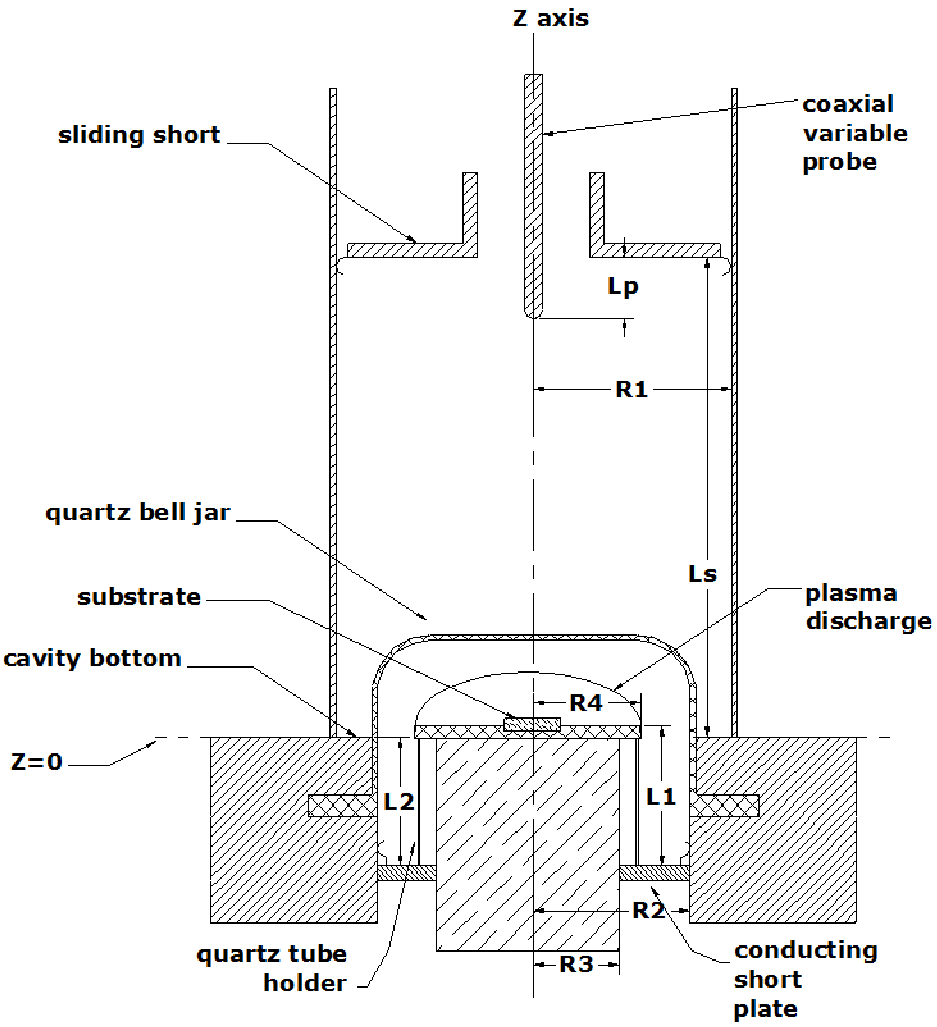

Figure 1.1 Generic microwave plasma reactor cross section

The specific detailed work in task (4) includes (a) the exploratory synthesis of PCD over one inch diameter and over the indicated high pressure and high power density regime. Synthesized material is up to 1-2mm thick. Outputs will include reactor roadmaps of the operating regime and absorbed microwave power density versus pressure measurements.

The specific detailed work in task (5) will include (a) the synthesis of high

quality (optical) individual SCD crystals on 3.5x3.5mm HTHP diamond seeds, (b) then the scaling up of the process to synthesize 4 SCD crystals at a time, and finally (c) the process will be scaled up to investigate the synthesis of SCD over 7x7mm SCD seed crystals to produce large area, high quality (optical, type IIa) SCD crystals. Other outputs are the experimental identification of deposition rates versus the various experimental conditions and the diamond quality versus experimental conditions. SIMS, transmission measurements, Raman, etc. will be used to measure diamond quality.

1.3 Thesis Outline

Certain preliminary aspects of the thesis research are described in Chapters 2-7 below. In Chapter 2, a brief literature review of commercially available reactor technologies is presented and deposition chemistry is reviewed along with additional background information. The background information includes the theory of diamond synthesis as is currently presented in the literature. The literature review of commercially available reactor technologies includes descriptions of the: (1) MSU microwave plasma assisted CVD reactor, (2) ASTeX (SEKI) microwave plasma reactor, (3) Aixtron Ellipsoidal Reactor, (4) CYRANNUS iplas Plasma System, and (5) LIMHP bell jar reactor.

Chapter 3 analyzes and compares the commercially available MPACVD diamond synthesis reactors. The similarities and differences between the reactor designs are noted and then if possible the output performance of the different reactor designs is compared. Reactor designs and the associated reactor

performance is a multi-dimensional variable optimization problem. Thus this chapter first identifies and classifies the many experimental and reactor design variables and then establishes several performance criteria, i.e. performance “figures of merit”, from which the reactor performance can be calculated and compared.

Chapter 4 begins with the description of the generalized microwave reactor concept, and then describes the early MSU microwave reactor designs. In the past these reactor designs sometimes have been referred to as microwave cavity plasma reactors (MCPR). Then it describes the design process of the new reactor which is identified here as Reactor C (the fourth generation MSU CVD reactor). The “new” numerical reactor models will calculate the electromagnetic field patterns versus reactor shape and size within the reactor. Then building upon intuition from past reactor designs the proposed new generation reactor, Reactor C, is identified.

Chapter 5 starts with the experimental subsystems overview of Reactor C. Then the concept of the multivarible parameter space for microwave plasma assisted diamond deposition is described. The experimentally measured road map and absorbed microwave discharge power density versus pressure is then presented for Reactor C and the experimental results of polycrystalline diamond synthesis are presented. The experimental results include determining the relationships between the output variables such as growth rate versus pressure and methane concentration, CVD diamond surface morphology and Raman spectra study.

Chapter 6 describes the CVD single crystal diamond synthesis results over the 240-320 Torr pressure regime. Eight sets of the experimental results include total gas flow rate vs. output variables, substrate holder location vs. output variables, deposition pressure vs. output variables, substrate vs. output variables, methane concentration vs. output variables, nitrogen concentration vs. output variables, deposition time vs. output variables, and substrate size vs. output variables. Micro-Raman spectroscopy, SIMS, and IR-UV transmission spectroscopy measurements on the synthesized diamond showed that the SCD synthesized with Reactor C was of similar quality to type IIa diamond.

Chapter 7 summarizes the research that is investigated in this thesis and proposes suggestions for future work.

CHAPTER 2

LITERATURE REVIEW AND ANALYSIS FOR MICROWAVE PLASMA ASSISTED CVD DIAMOND SYNTHESIS

2.1 Introduction

Over the past two decades, progress in the field of microwave plasma assisted chemical vapor deposition (MPACVD) has led to the synthesis of high quality polycrystalline diamond (PCD) and single crystal diamond (SCD) [4-6]. Thus a general understanding has emerged of how diamond is synthesized in a plasma assisted environment and additionally a number of MPACVD machines are now available commercially. This chapter in Section 2.2 will briefly review the current understanding of CVD diamond synthesis, and then in Section 2.3 will

describe the different commercial MPACVD machines that are now available for purchase. Currently the MPACVD reactor technology has developed a number of commercially available designs. These microwave assisted plasma reactors include (1) the MSU microwave plasma assisted CVD reactor (MPCR), (2) the ASTeX microwave plasma sources, (3) the Aixtron Ellipsoidal Reactor, (4) the CYRANNUS iplas Plasma System, and (5) the LIMHP bell jar reactor. Here in this chapter as part of the proposed thesis research, the most common commercially available reactors are reviewed. In the next chapter the performance of each of these reactors is compared by calculating and comparing a number of reactor performance measurements. The performance measurements will be calculated from experimental data that is available in the published and reviewed literature. These reactor performance measurements are (a) discharge absorbed power density (b) CVD diamond growth rate i.e. linear growth rate or weight gain, (c) diamond film uniformity, (d) diamond quality, and (e) energy efficiency (which is referred to in later chapters as specific yield).

2.2 CVD Diamond Synthesis

2.2.1 Diamond Properties

Diamond is a transparent crystal of tetrahedral bonded carbon atoms (sp^3) that crystallizes into the diamond lattice. This lattice is a variation of the face centered cubic (FCC) structure [7] and can be viewed as the superposition of two FCC lattices one displaced relative to the other along the body diagonal by one quarter of lattice parameter from the origin. At room temperature, the unit cell is

cubic with a side length approximately equal to 0.357 nm. Four valence electrons in each carbon atom form strong covalent bonds by sp^3 hybridization with nearest neighbor distance of 0.15 nm (see Figure 2.1).

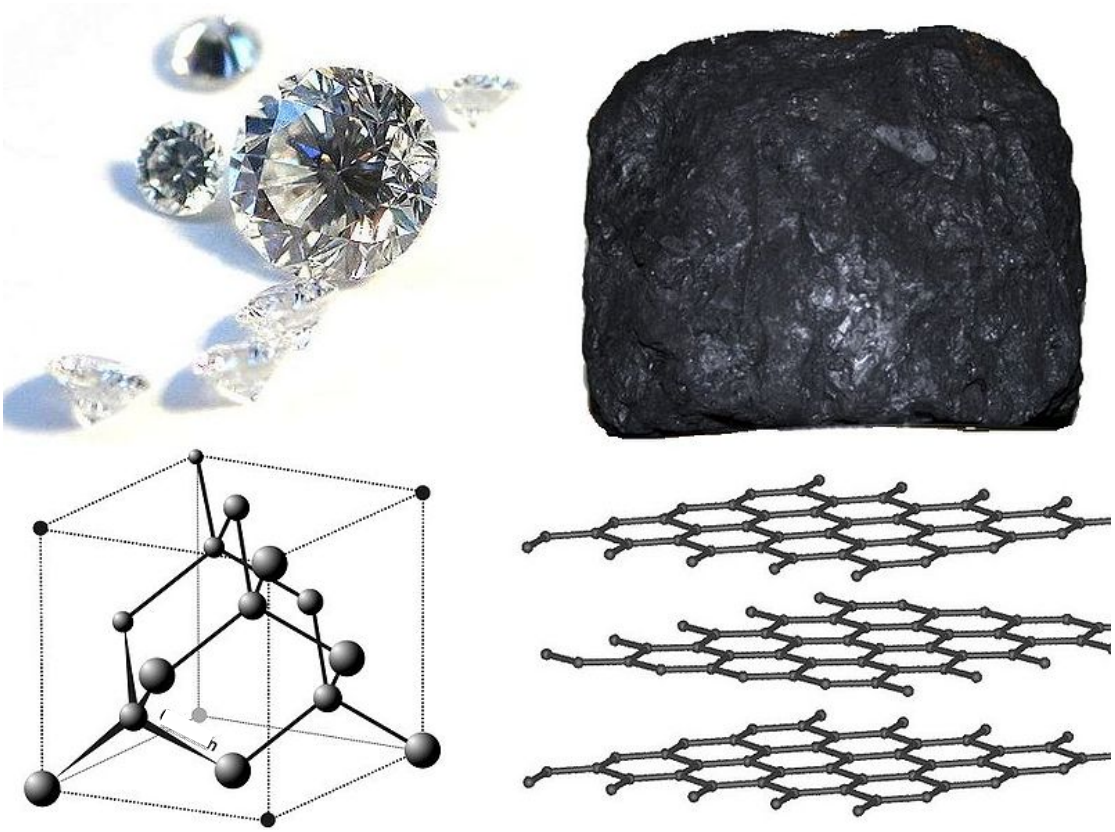

Figure 2.1 Comparison of diamond and graphite, which are two allotropes of carbon [7] “For interpretation of the references to color in this and all other figures, the reader is referred to the electronic version of this dissertation.”

Diamonds have been adapted for many uses because of the material’s exceptional physical characteristics.

- Hardness = 10,000 kg/mm^2

Diamond is the hardest known naturally occurring material, scoring 10 on the Mohs scale of mineral hardness. Diamond is extremely strong due to the structure of its carbon atoms, where each carbon atom has four neighbors joined to it with covalent bonds. [8]

- Toughness = 2.0 MPa $m^{1/2}$

  Unlike hardness, which only denotes resistance to scratching, diamond's toughness of tenacity is only fair to good. Toughness relates to the ability to resist breakage from falls or impacts. Due to diamond's perfect and easy cleavage, it's vulnerable to breakage. The toughness of natural diamond is good when compared to other gemstones, but poor compared to most other engineering materials. [9, 10]

- Optical properties

  Due to impurities and structural defects, in nature diamonds occur in various colors – black, brown, yellow, gray, white, blue, orange, purple to pink and red. Pure diamonds would be transparent and colorless.

  Diamonds are classified into two main types, according to the nature of defects present and how they affect light absorption: [11]

  Type I diamond has nitrogen atoms as the main impurity, at a concentration of up to 1%. If the N atoms are in pairs or larger aggregates, they give the diamond pale yellow color. Type Ia can have nitrogen concentrations as high as 2500 ppm atomic. If the N atoms are dispersed throughout the crystal in isolated sites, they give the diamond an intense yellow or occasionally brown tint; these are classified as Type

Ib.

Type II diamond differs from type I diamond because type II has very few nitrogen impurities. Type IIb, which account for ~0.1% of gem diamonds, is also nitrogen free but contains boron. So they are usually blue or gray due to boron atoms scattered within the crystal matrix. Type IIa diamonds also have a broad optical transparency from the deep ultraviolet to the far infrared. However, high purity diamond does have absorption in the wavelength range of 2 to 7 microns (wavelength) due to the excitation of vibration modes of C-C bonds. [12]

- Electrical properties

  Most diamond is a good electrical insulator. Natural blue diamonds (type IIb) are semiconductors due to substitutional boron impurities replacing carbon atoms. Both p-type (boron-doped) and n-type (phosphorus-doped) diamond film can be synthesized during chemical vapor deposition. [13]

- Thermal conductivity = 900-2,320 W/mK

  One of the most notable properties of diamond is high thermal conductivity, because of the strong covalent bonding within the crystal. It is already used in semiconductor applications as a heat sink or heat spreading material in order to prevent silicon and other semiconducting materials from overheating. [14]

- Thermal stability

  Diamond oxidizes in air (converts to graphite) if heated over 700 °C. At atmosphere pressure, diamond is not as stable as graphite. Diamond is

definitely not “forever”. However, due to its large kinetic energy barrier, diamond is metastable. It will not convert to graphite under standard conditions of temperature and pressure. [15, 16]

These exceptional properties make diamond a very promising material for variety of applications ranging from space, semiconductor industrial, biochemistry, etc. applications.

2.2.2 The CVD Diamond Growth Process

CVD diamond growth is a very complex process. A full description of the CVD diamond growth requires knowing all the chemical reactions at the gas phase and the substrate surface, and being able to describe the details of surface kinetics such as absorption-desorption, abstraction and migration phenomena. Although currently there is no model to describe all aspects of CVD diamond growth, some simplified ones are still available to help us understand what happens. A typical example of growth process is displayed in Figure 2.2. [17]

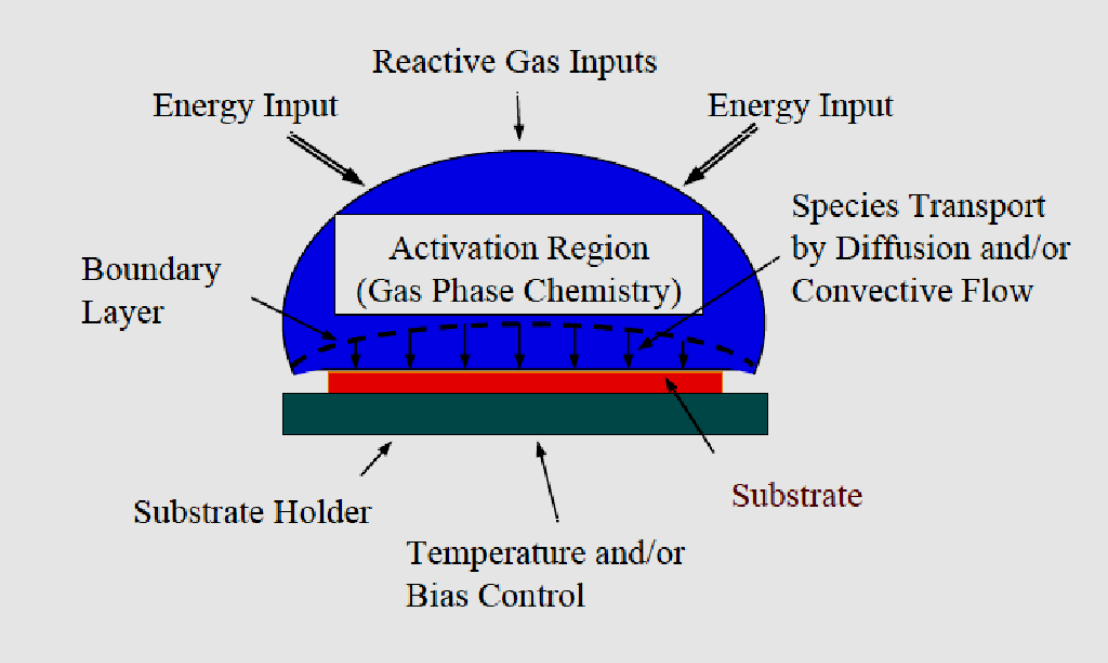

Figure 2.2 General CVD diamond growth process

The input process gases, i.e. CH_4, H_2, etc., are first mixed in the reactor and then pass through the plasma. When the reactive gas inputs pass through the plasma discharge activation region, they are ionized and dissociated. The microwave plasma activation creates ions and electrons and also results in breaking down the molecules into reactive radicals and atoms. Also the microwave energy heats the gas in the discharge to high temperatures of the order of 2000 – 4000 Kelvin. As these reactive radicals hit the substrate surface, they continue to mix and interact with the hydrogen terminated diamond substrate surface and continue to undergo a set of complex surface reactions.

The role of the microwave plasma assisted CVD diamond system is to create the chemical and thermal environment needed for diamond deposition. This environment for the standard hydrogen-methane deposition process has the

following attributes.

The first and a very important parameter is the substrate temperature during the deposition. The temperature is in the range of 400 °C to 1400 °C according to the previous research [18]. If the substrate temperature is too high, it converts the diamond to graphite.

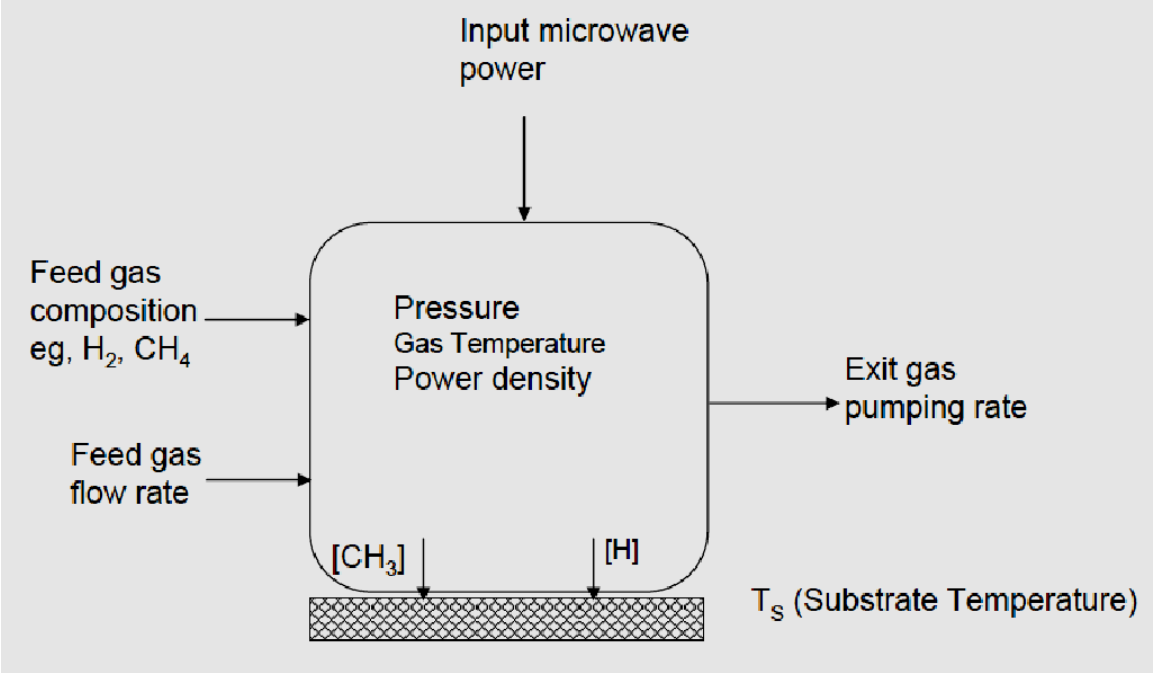

Figure 2.3 Reduced variable model of the MPACVD process [12]

Two types of essential radicals need to be supplied to the growth surface. They are atomic hydrogen [H] and an appropriate carbon-containing growth species such as $[CH_3]$ (See Figure 2.3). The vital roles of H atoms are to activate and cycle hydrocarbon species on the surface to permit growth in the diamond phase of carbon and not the graphite phase [12].

At the gas phase when the input process gases H_2 and CH_4 are first mixed in the reactor, there is direct electron-impact dissociation at low pressure: [19]

$$e^- + H_2 \rightarrow e^- + 2H \quad (1)$$

and thermal dissociation at high pressure:

$$H_2 + H \rightarrow 3H \quad (2)$$

As far as CH_3 production is concerned, at low pressure (M is a third body):

$$CH_4 + M \rightarrow CH_3 + H + M \quad (3)$$

and at high pressure, CH_3 production is due to CH_4 dissociation through collisions with H atoms at high pressure:

$$CH_4 + H \rightarrow CH_3 + H_2 \quad (4)$$

This reaction (4) usually happens very close to the surface and it can also happen in the reverse. The production rate of CH_3 depends on the gas temperature. From the model that F Silva et al [19] used, the optimal CH_3 production occurs within the gas temperature range 1200 – 2200 K.

The substrate surface reactions were described by the Harris and Goodwin model [20]. See Figure 2.4. The first important reaction is the hydrogen abstraction surface reaction and the associated rate, $R_{abs\text{-}H}$. This reaction is given by equation (5) below, where C_d^* is an open carbon site.

$$C_dH + H \rightarrow C_d^* + H_2, \quad (5)$$

$$R_{abs\text{-}H} = k_1[H]$$

In equation (5) k_1 is the reaction rate constant and [H] is the atomic hydrogen concentration at the surface. The abstraction results in an open carbon site on the diamond surface, which can be filled by either the adsorption of another atomic hydrogen or a carbon radical species (e.g. CH_3). The reaction and associated rate, R_{adH}, of hydrogen adsorption onto an open site, C_d^*, is given by

$$C_d^* + H \rightarrow C_dH \qquad (6)$$

$$R_{adH} = k_2[H]$$

The growth species CH_3 can also be adsorbed on to the surface with the reaction and associated rate for an open surface site given by

$$C_d^* + CH_3 \rightarrow C_dCH_3 \qquad (7)$$

$$R_{adC} = k_3[CH_X]$$

Once the growth species is on the surface, it can then proceed along one of two primary paths. The first path is thermal desorption from the surface leading to an open site on the surface again. The reaction and associated rate for a given adsorbed site is

$$C_dCH_3 \rightarrow C_d^* + CH_3 \qquad (8)$$

$$R_{des} = k_4$$

The other pathway is the incorporation of the adsorbed carbon species into the diamond structure. The general event that begins this mechanism in growth

models is an abstraction of hydrogen from the adsorbed carbon species.

$$C_dCH_3 + H \rightarrow C_dCH_2 + H_2 \qquad (9)$$

$$R_{abs\text{-}CHx} = k_5[H]$$

Under steady state conditions, this set of reactions can be combined to give a growth rate G given by [21,22]

$$\qquad (10)$$

where n_s is the surface site density which is 2.61 X 10^{-9} mol/cm^2 on (100) surfaces, and n_d is the molar density of diamond, which is 0.2939 mol/cm^3.

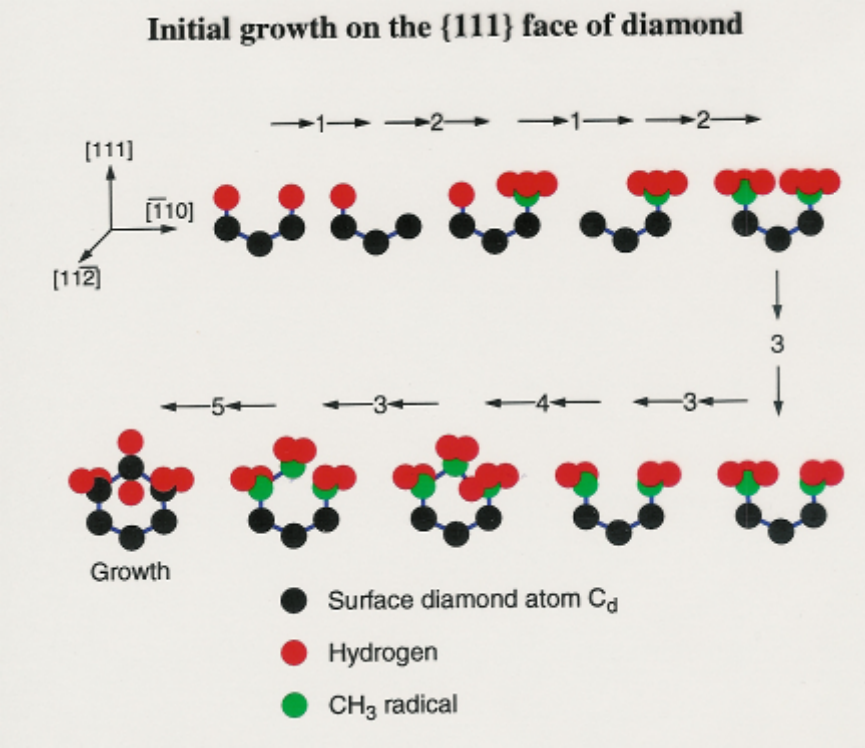

Figure 2.4 Growth model for diamond synthesis [20]

To conclude, a general view of the deposition process on the surface is one where at first atomic hydrogen is bonded to almost the entire diamond surface. The primary mechanism that opens sites on the surface is by abstraction of surface-terminating hydrogen by atomic hydrogen.

Low hydrogen surface coverage can result in sp^2-like terminations on the diamond surface, which can lead to growth defects and If the hydrogen coverage is low enough, graphitic/amorphous film deposition. An empirical model (see Figure 2.5) for the defects, X_{def}, incorporated during diamond growth is

$$X_{def} \propto \frac{G}{[H]^k} \qquad (11)$$

where k is an empirical fit that is often selected as k = 2. The growth rate given by equation (10) can be reduced to

$$G \propto \frac{[CH3]\{H\}}{3x10^{15}cm^{-3} + [H]} \qquad (12)$$

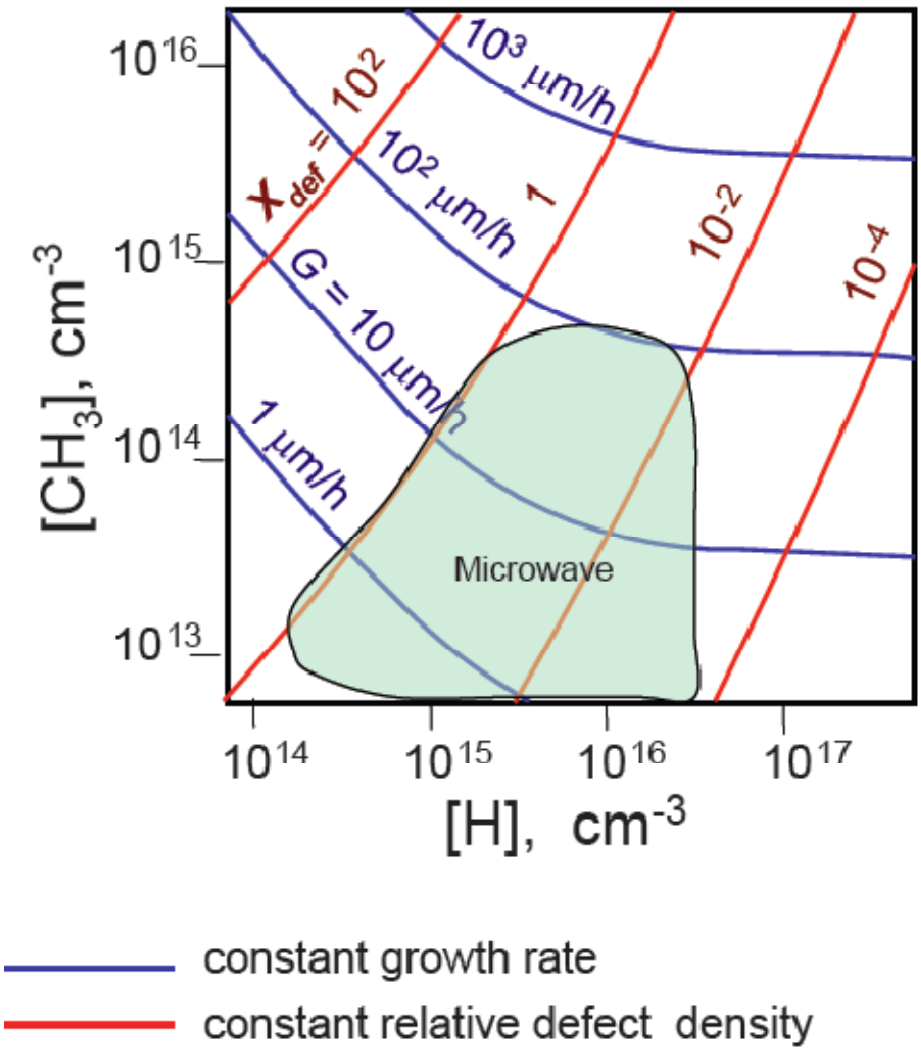

Figure 2.5 Growth rate and relative defect density [20]

Hence, the higher quality diamond can be synthesized when the carbon species concentration in the input gas flow is low and atomic hydrogen concentration is high. At high pressures, microwave discharges in hydrogen and methane gas mixtures separate from the reactor walls. They become freely floating and assume shapes that are related to the shape of the impressed electromagnetic (EM) fields. At pressures of 100 Torr or more, thermal

dissociation will produce more atomic hydrogen than direct electron-impact dissociation at lower pressure (see Figure 2.6). These discharges have high densities of radical species, i.e. H and CH_3 radicals. The atomic hydrogen concentration increases 800 times and CH_3 species concentration increases 8 times when the pressure increases from 37.5 to 225 Torr. Also for the same methane concentration, the growth rate increases more than 200 times and the defect X_{def} drops more than 100 times when the pressure increases from 37.5 to 225 Torr. So we can say that higher quality diamond can be synthesized with higher growth rates at higher pressures. Also the previous experimental work [23, 24] (see Figures 2.7, 2.8) indicates that the growth rate increases as the pressure and the microwave discharge absorbed power density increase.

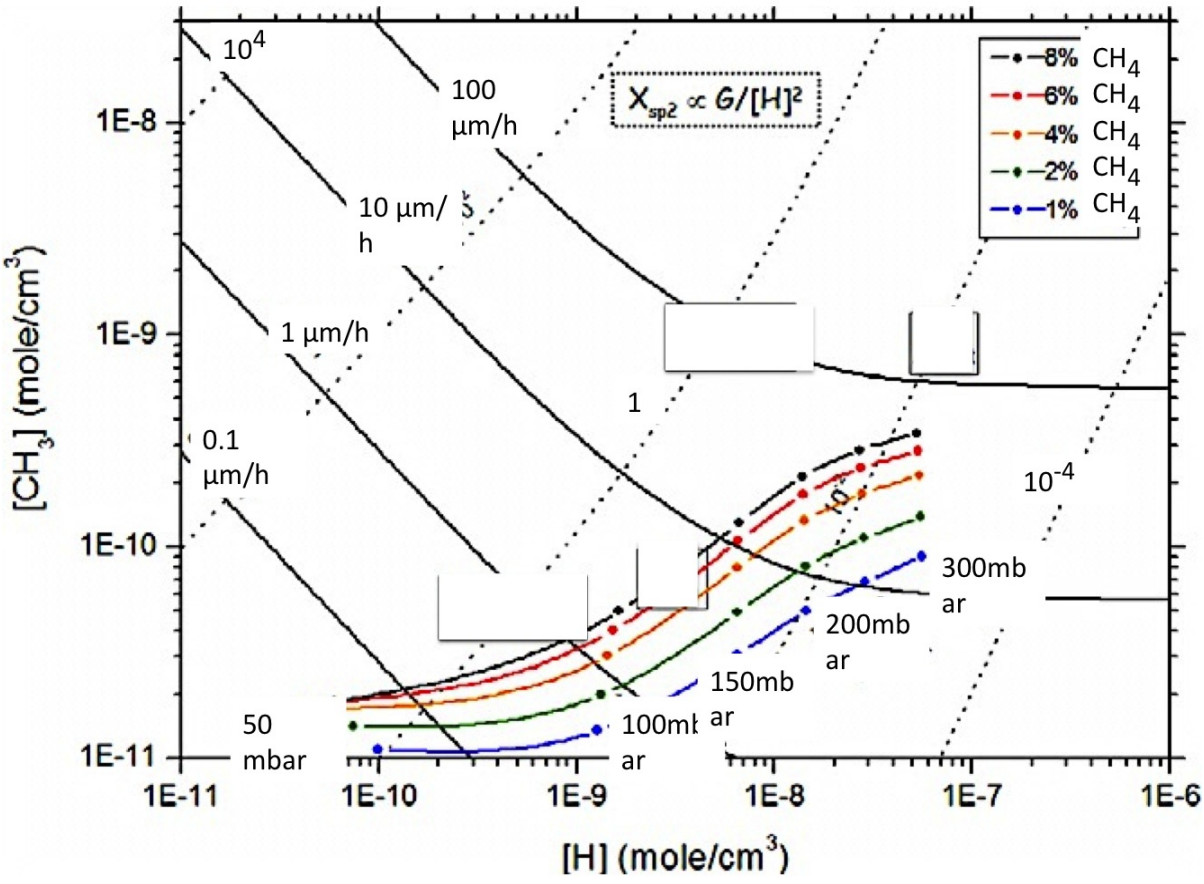

Figure 2.6 The operating ranges of CVD diamond deposition process for different pressure and different methane concentration

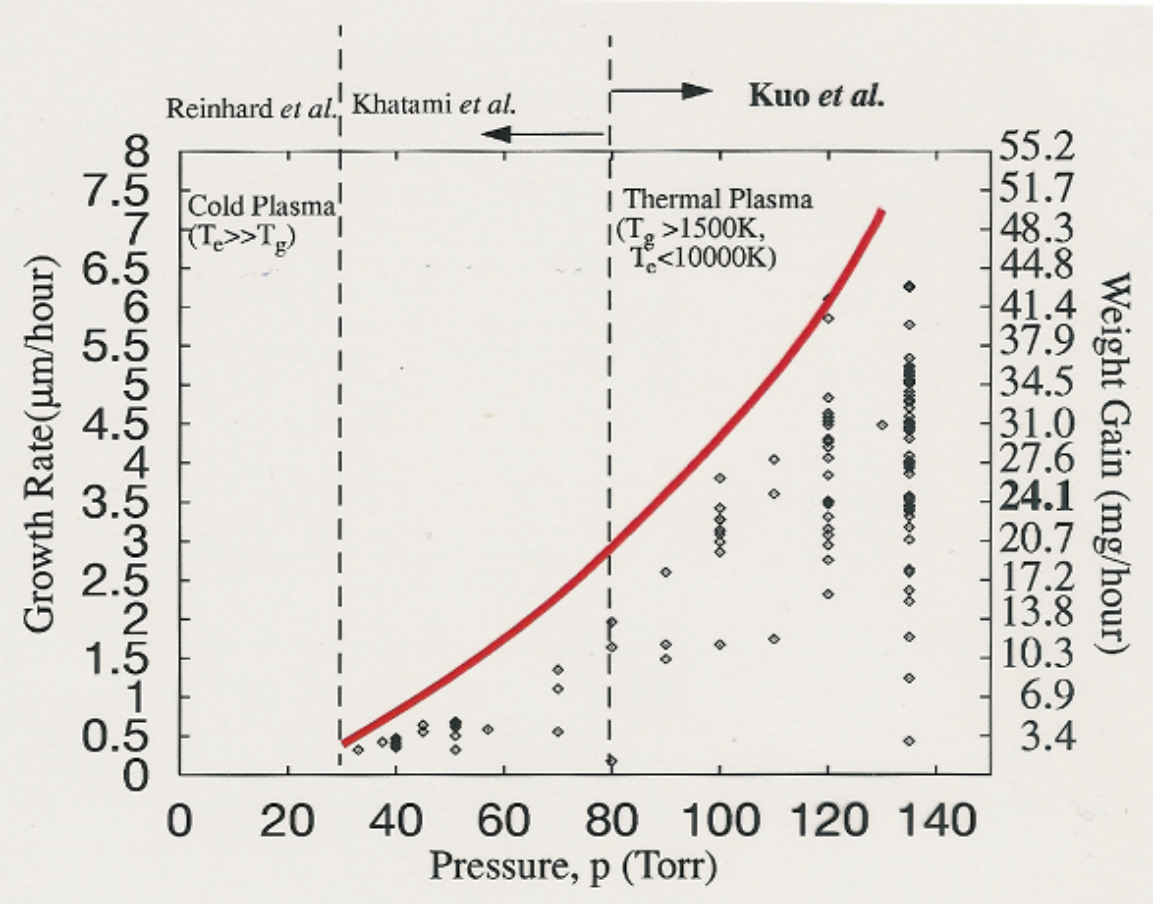

Figure 2.7 Growth rate versus pressure and CH_4 concentration [24]

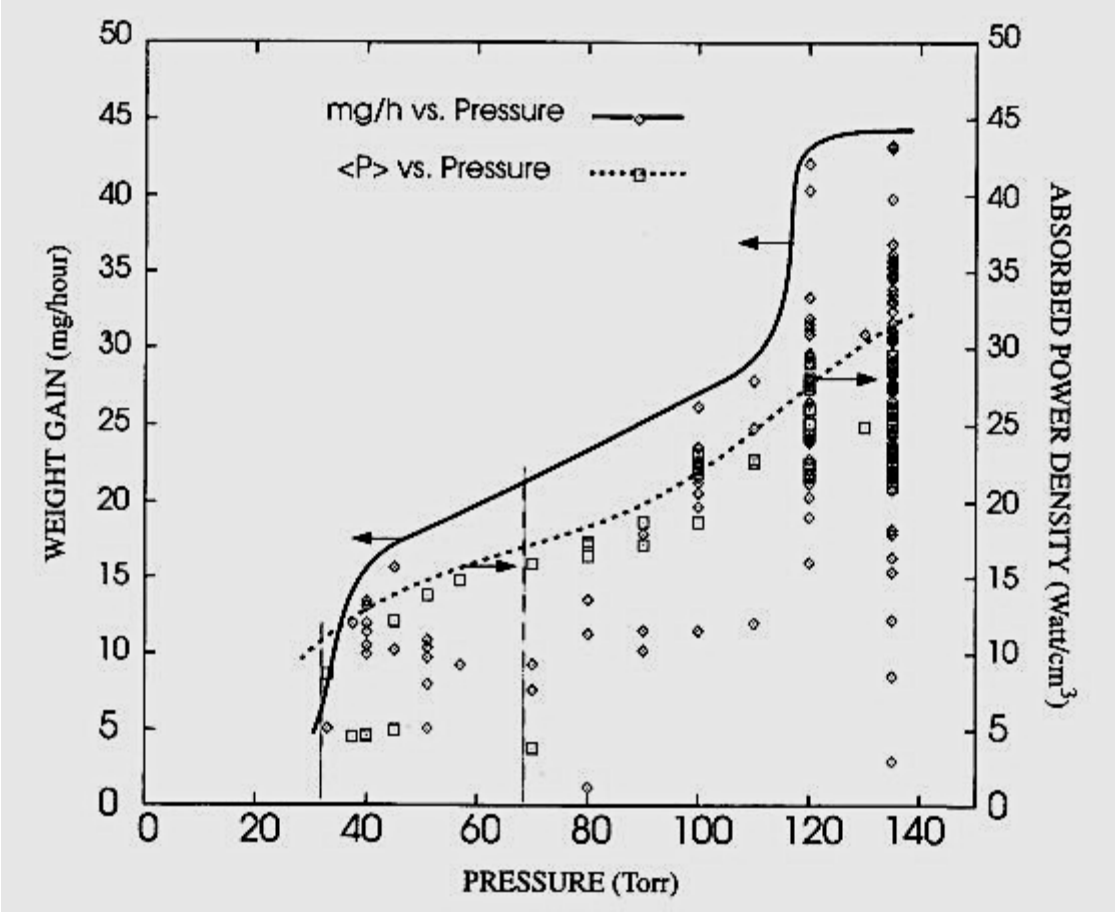

Figure 2.8 Growth rate and power density versus pressure [24]

2.3 A Review Of Commercially Available Reactors

2.3.1 The MSU Microwave Plasma Reactors

The MSU microwave plasma assisted CVD reactor (See Figure 1.1) was amongst the first microwave plasma assisted reactor concepts developed for diamond film growth. The first generation of MSU's MPACVD reactor was developed and built in the Fall of 1986 by J. Asmussen and placed into operation in the Fall of 1987 at Norton Company in Salt Lake City, Utah. The reactor design was based on a microwave plasma reactor concept invented by J. Asmussen

while at Michigan State University and patented by MSU (See Asmussen et al [25-33]). The technology was licensed to Wavemat Inc. by MSU, and Norton Company obtained an exclusive sub-license during 1987-1999 period from Wavemat for the application of this technology to diamond film deposition. The second generation MSU microwave plasma assisted CVD reactor was developed by Asmussen and his graduate students J. Zhang and K.P. Kuo during 1988–1992 period [34]. The improvement over earlier designs was that this reactor had the coaxial coupling probe located at the top end of the cavity, instead of on the side of the cavity. Here this reactor is referred to as Reactor A. Also in the 1989-1990 time period the reactor concept was physically scaled up by the factor 2.7 [35,36], and was then excited at 915 MHz. Based on this scale up, a MPACVD diamond synthesis reactor was designed, built and installed by Wavemat Inc. at Norton Co. in 1992. Thus the deposition area was increased by over seven times [37]. The reactor system has a power supply of 30 kW (although it was never operated at that input level), and also had an input coaxial coupling probe at the top of the cavity and a movable substrate stage. At the time of installation at Norton Co., it was the first scaled up, 915 MHz MPACVD diamond synthesis machine in the world.

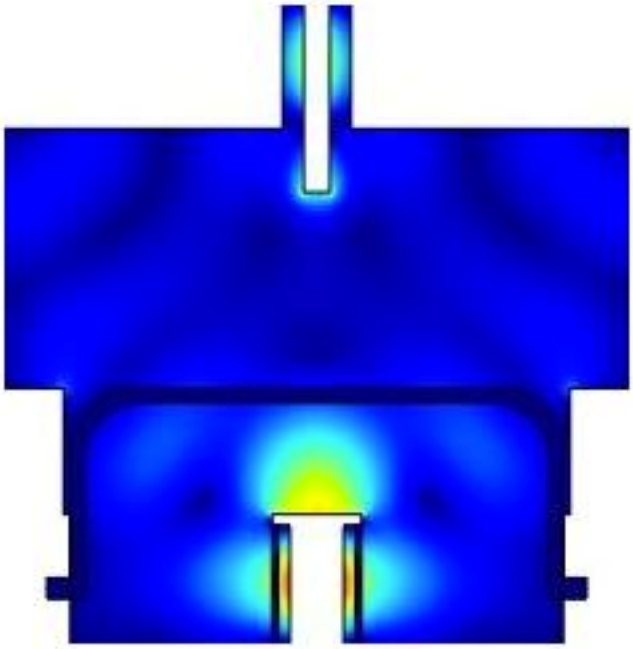

Figure 2.9 Numerical simulation of the fourth generation MSU microwave plasma assisted CVD reactor

Recently the MSU reactor design was extended to higher pressures (180 – 240 Torr) and higher power density operation. [38] This third generation MSU reactor, identified as Reactor B in this thesis, is able to provide a higher discharge plasma power densities by shrinking the size of the substrate holder and water cooling stage and by operating at high pressures of 160 – 240 Torr. The reactor developed in this PhD thesis research is the fourth generation MSU microwave plasma assisted CVD (MPACVD) reactor and is identified here as Reactor C. The major modifications of Reactor C are the redesign of the applicator itself, which includes larger applicator and quartz dome dimensions, and a scaled-up base plate. An example of numerical simulation of the electromagnetic field of the reactor is shown in Figure 2.9. Specific details of the

redesign will be further discussed in Chapter 4.

Reactors A, Reactor B and Reactor C have been exclusively licensed to Lambda Technologies Company by Michigan State University in 2002, 2009 and 2011 respectively. The power supply subsystem, the gas flow control, pressure control, and exhaust subsystem have been implemented by Lambda Technologies and they are now commercially available. An example of these MPACVD machines is shown in Figures 2.10 – 2.11 (Figures from www.microcure.com). The reactor design incorporates the internal cavity tuning. The inherent performance provides the ultimate operating flexibility and control of gas plasma density and uniformity over a wide range of operating conditions and gasses. DiamoTek 700 is a small area (1-4 inch diameter deposition area) diamond MPACVD system (Figure 2.10). It provides precise plasma control, efficient energy coupling and full auto computer controlled cycle profiling process. The power range of this system is from 1.2 kW to 10 kW at 2.45 GHz and the operating pressure regime is from 20 to 160 Torr. The DiamoTek 1800 is a large area (6-8 diameter deposition area) MPACVD reactor using 915 MHz microwave excitation (Figure 2.11). It employs 5 kW – 30 kW microwave power and can be operated from 20 – 180 Torr with 1 – 10 microns/hr deposition rate (PCD).

Figure 2.10 DiamoTek 700

Figure 2.11 DiamoTek 1800

2.3.2 ASTeX (SEKI) High-Pressure Microwave Plasma Source

The microwave plasma reactor introduced in this section is commercially available from a company called Seki Technotron, formerly known before 1998 as AsTex Research. Their commercially available products include a first generation AX5200 1.5kW, AX5250 5kW Microwave Plasma CVD system, and a second generation AX6550/6560 2.45GHz 8kW Microwave Plasma CVD system, and an AX6600 915MHz 100kW microwave plasma CVD reactor. Their reactors can be grouped into: (1) a cylindrical reactor and (2) a clamshell (non-cylindrical) reactor.

Numerical Simulation of SEKI system (ASTEX)

The first generation of the SEKI reactor, i.e. the cylindrical reactor as shown in Figure 2.12, excites the plasma with the TM_{013} mode (see Figure 2.12(a)) by employing a coaxial antenna coupling system (see Figure 2.12(b)). The numerically calculated electromagnetic field patterns and the plasma gas temperature distribution results which are shown in Figure 2.12(b) and 2.12(c) were performed by Silva et al [19]. The excitation mode and the coupling method are similar to those employed by Reactor A. A major difference between two reactors is the way SEKI system shapes and locates the dielectric window. The microwave energy is introduced into the cylindrical applicator by a coaxial antenna and the dielectric window is a quartz plate located approximately at the cavity mid-plane of Figure 2.12(b). Modeling of the H_2 plasma gas temperature distribution is presented in Figure 2.12(c).

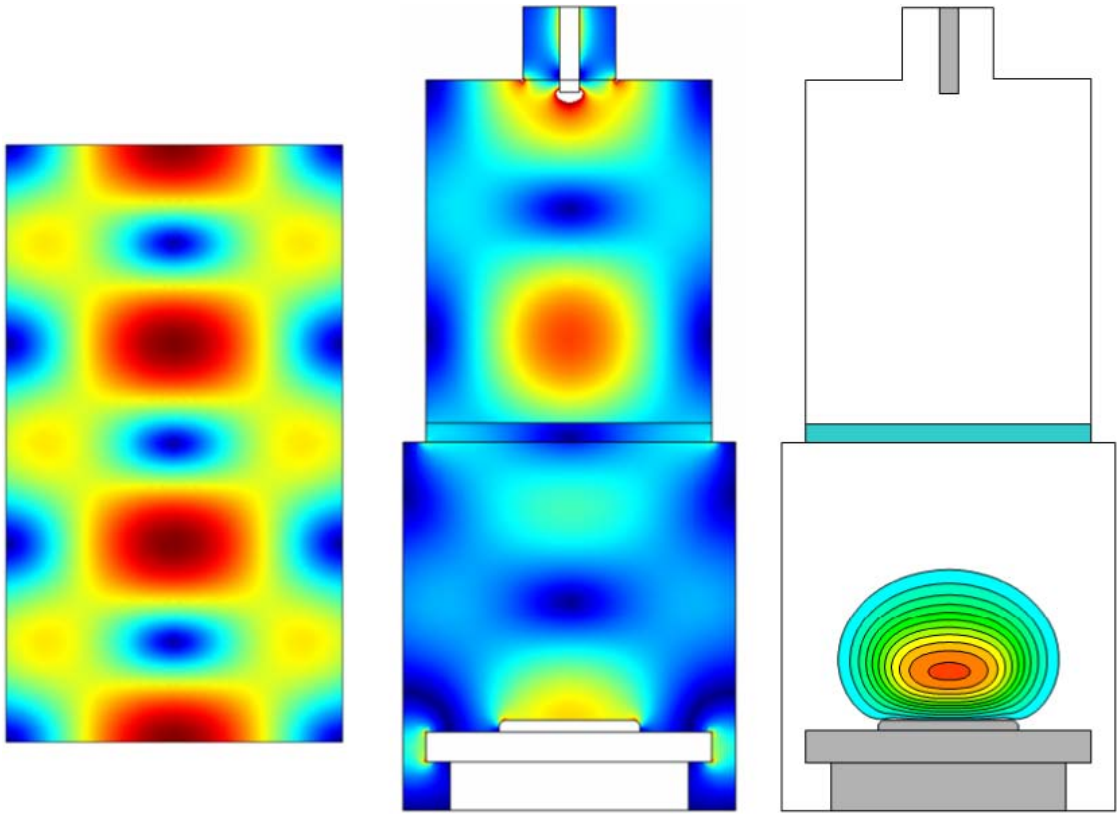

(a) (b) (c)

Figure 2.12 Cross-sectional views of the SEKI reactor design. The applicator is excited in the approximate TM_{013} mode [19]

The second generation of SEKI reactor design and its associated electromagnetic field simulation are shown in Figure 2.13. It uses a non-cylindrical cavity (i.e. the clam shell reactor) and is phi symmetric. Several peculiarities have been presented for this reactor. First, SEKI claims that it uses the TM_{011} mode as the main excitation mode. However, secondary radial lobes, which are related to the TM_{021} mode, are shown above the substrate holder in the simulation in Figure 2.13 (a). Other EM field patterns exist below the

substrate holder and at the top clamshell region (TM_{011}). The reactor is also a hybrid mode cavity. Second, the microwave energy is introduced by a coaxial feed located at the bottom of the cavity. Third, there is no quartz dome exposed directly to the plasma when it is operated properly and this allows the reactor to have a good power handling capability. Hemawan et al who is using the second generation 915 MHz SEKI reactor also performed numerical simulation. They showed three different modes with electromagnetic field patterns in Figure 2.14 - 2.16. [39] It is not clear how the reactor is adjusted (i.e. how the reactor shape or top position is adjusted) to obtain these modes. They might use shim sets or a mechanically moving parts to adjust the distance between the substrate holder and the top of the cavity. At a given excitation frequency of the reactor, only one mode can exist at a time, but apparently there are several modes that exist near each other. Hemawan et. at. is investigating which is the best mode for the SCD synthesis (i.e. see Figures 2.14-2.16).

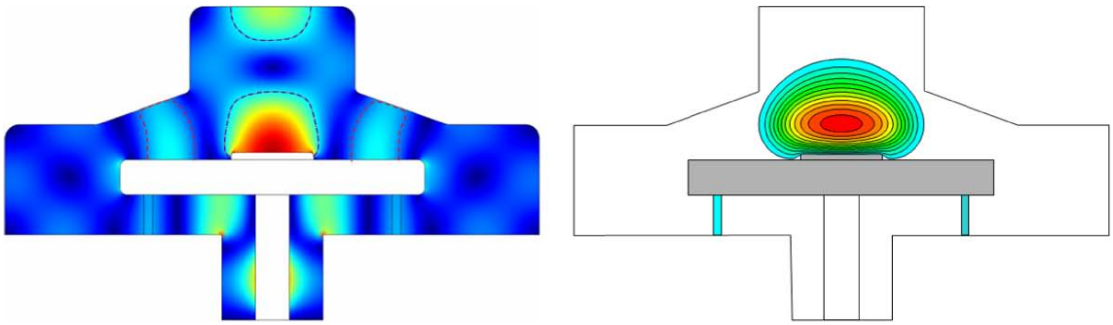

(a) (b)

Figure 2.13 Illustration of the second generation SEKI reactor; Quartz window is located underneath the cooling stage [19]

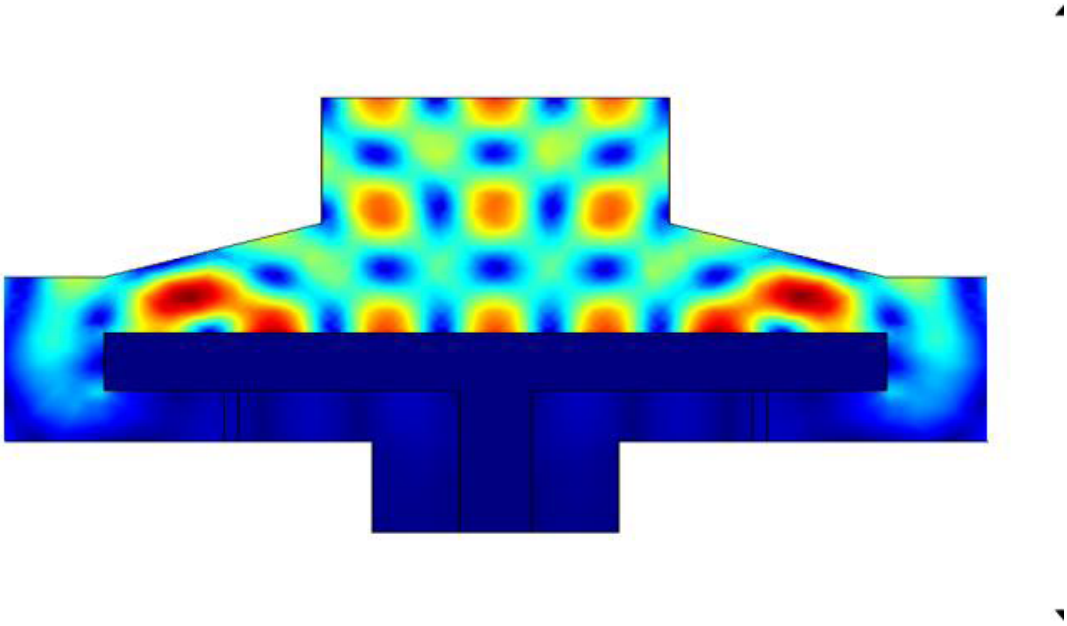

Figure 2.14 Electric field pattern of the second generation 915 MHz SEKI reactor; Mode 1 [39]

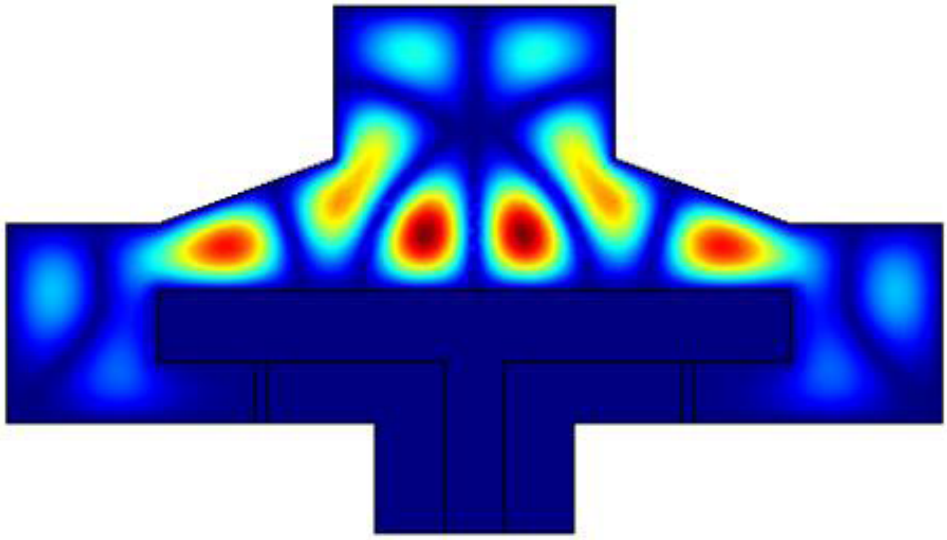

Figure 2.15 Electric field pattern of the second generation 915 MHz SEKI reactor; Mode 2 [39]

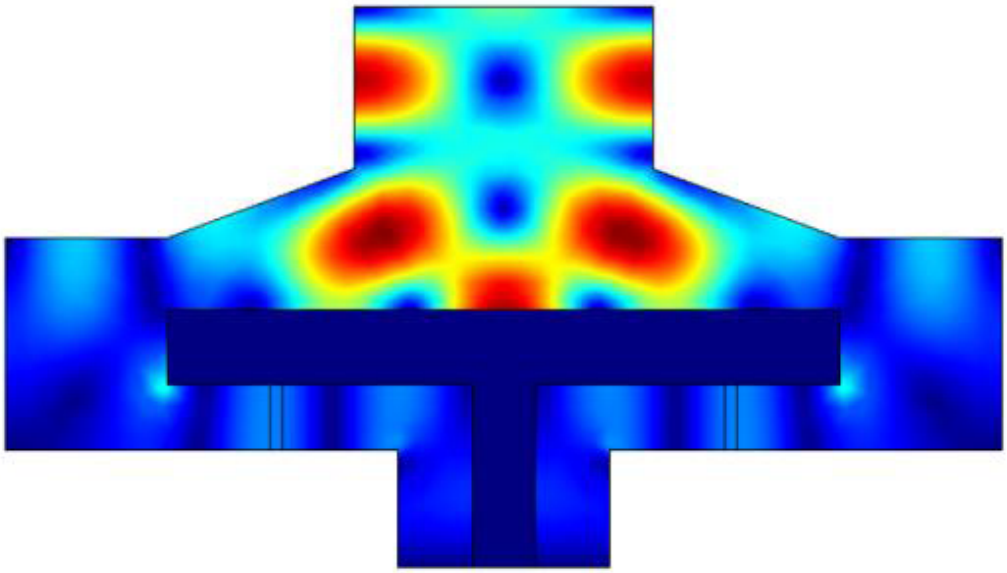

Figure 2.16 Electric field pattern of the second generation 915 MHz SEKI reactor; Mode 3 [39]

The commercial system and cross-sectional schematic diagram of the SEKI second generation high pressure microwave plasma reactor are shown in Figure 2.17 [40] and 2.18 [41]. The microwave plasma 2.45 GHz CVD system shown in Figure 2.17 is equipped with a 8 kW power supply and occupies a laboratory foot print of 2m × 5m [42, 43]. The system also includes a chamber, for introducing the process gas that is used for the specific diamond synthesis process. Generally, a CVD process is accomplished on a single flat electrode on which the microwave energy is applied through the coaxial input feed located on the

underside of the electrode. Microwave energy radially propagates along the bottom surface of the electrode and the plasma is formed on the top of the electrode.

Figure 2.17 ASTeX 8 kW semi-production microwave plasma CVD system

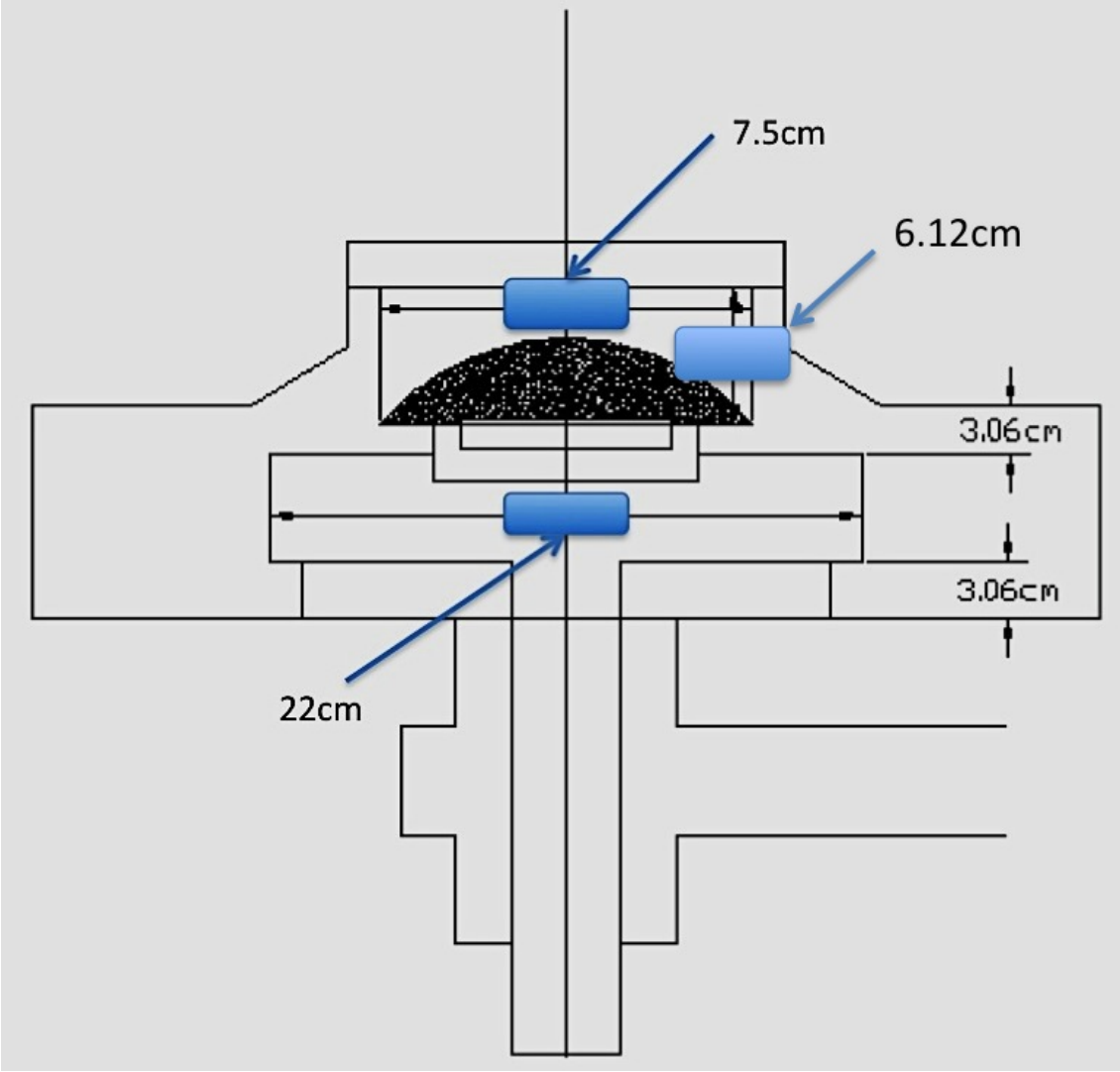

Figure 2.18 Schematic of the 5-kW 2.45GHz microwave CVD reactor [41]

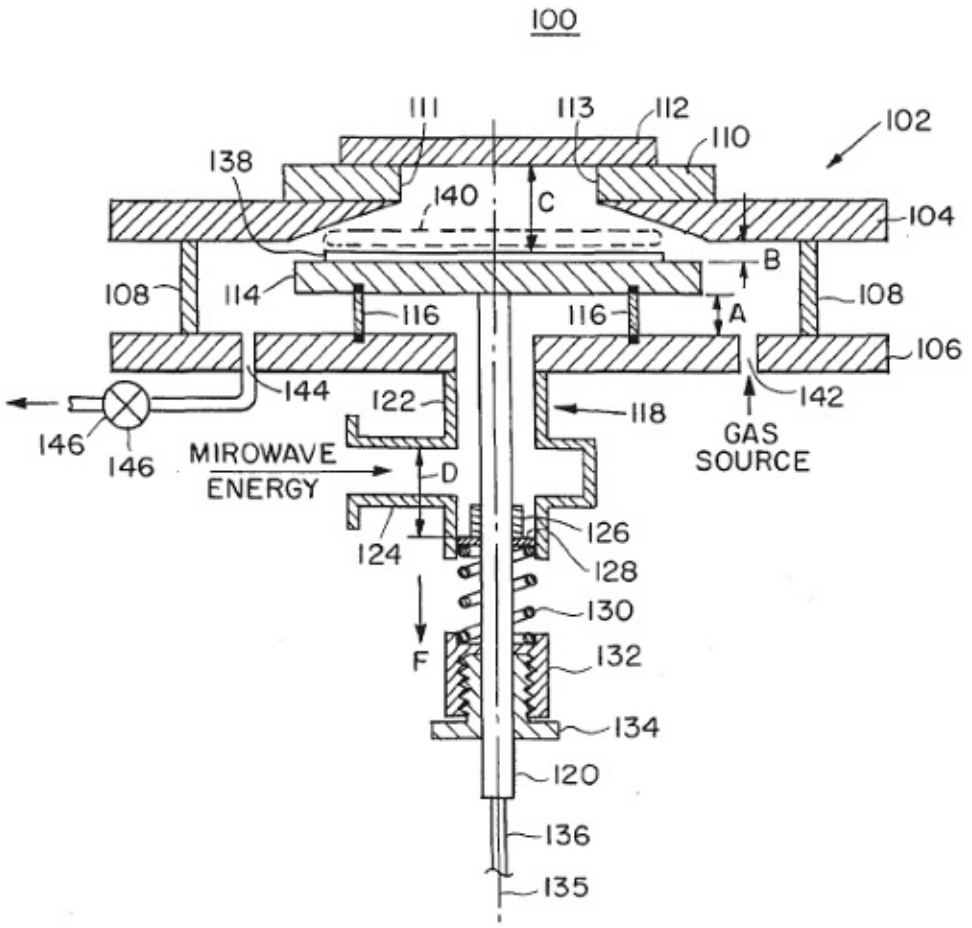

Figure 2.19 Schemetic of ASTeX microwave plasma CVD system; [41]

More detailed cross sectional views of the reactor are displayed in Figs. 2.18 and 2.19. In particular reactor 100 (Figure 2.19) includes reactor chamber 102 for containing the gas to be energized into plasma with microwave energy. Gas is provided from 142 and exhausted through 144 by vacuum pump 146. Microwave power is provided to the underside of electrode 114 by a fundamental mode coaxial transmission line 118 with center conductor 120 connected to 114. The quartz ring window 116 is an annular ring placed toward the outer edge of 114.

The quartz ring is placed in a low electric field region to act as a vacuum seal for the reactor to prevent heating, coating, etching and plasma breakdown at window 116. This arrangement is to assist in the forming of the plasma on the upper side of the electrode. Window 116 is sealed against both 106 and 114 by fixing spring 130 to apply downward force on 114.

The clamshell reactor was scaled up in size by exciting it with 915 MHz microwave energy and increasing the reactors dimensions by a factor of 2.7. See Fig. 2.20. This reactor was used to explore process conditions for diamond growth [44, 45]. The aluminum wall reactor is approximately 0.3 m in diameter and the copper cooling stage at the center of the reactor is 111 mm in diameter. The Si substrates 138 of up to 76mm in diameter (25- and 51-mm substrates were single-crystalline Si, 76-mm substrates were polycrystalline Si) and up to 9.5 mm thick, which were abraded with diamond powder of 15-30 μm and were placed on a molybdenum holder on top of the cooling stage.

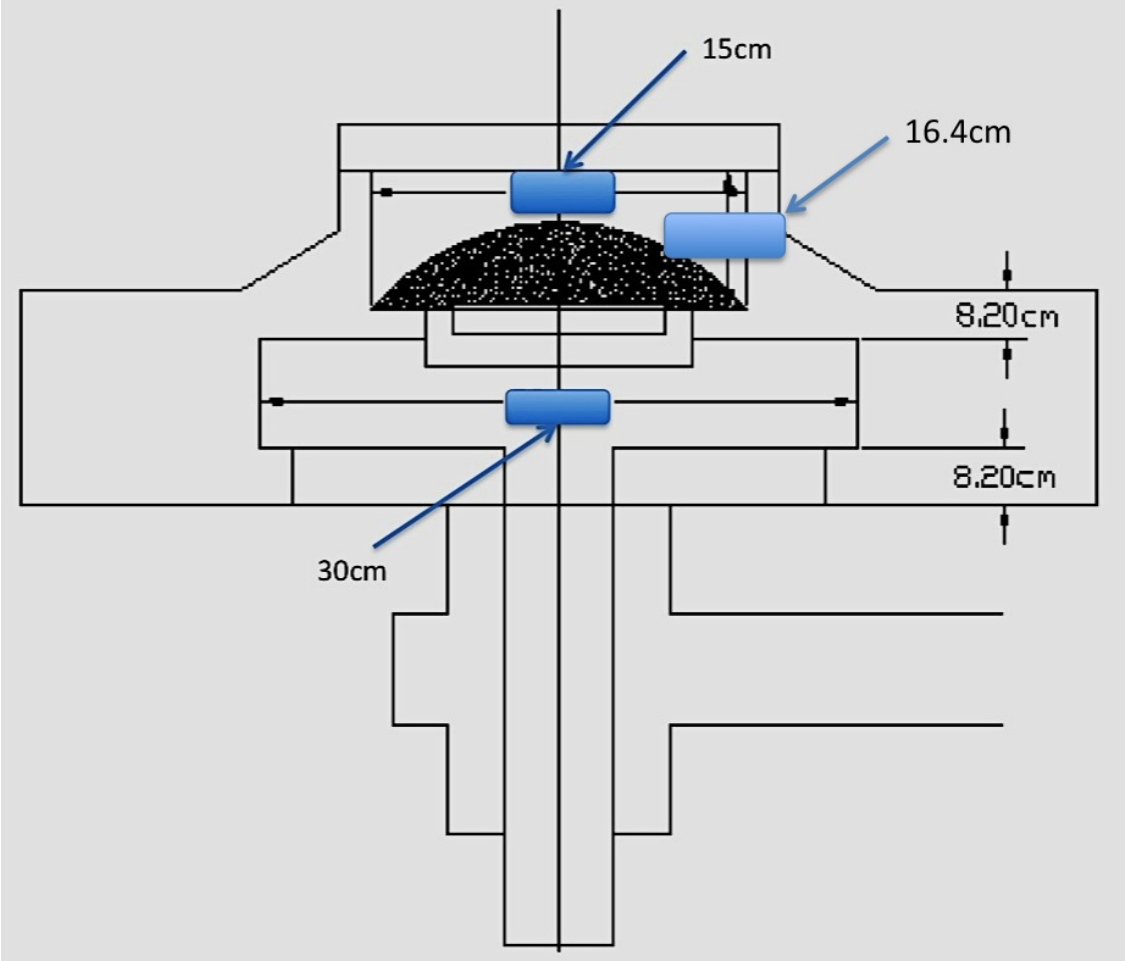

Figure 2.20 Schematic of the 60-kW 915MHz microwave CVD reactor [41]

Substrate Cooling System:

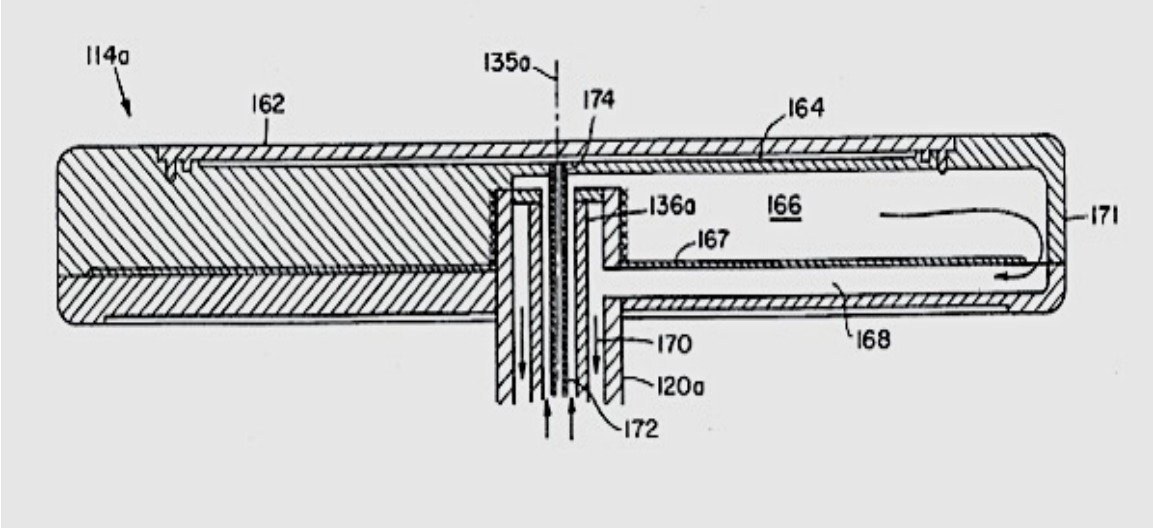

Figure 2.21 Substrate holder cooling system schemetic [41]

The cooling system for the clamshell reactors includes both water cooling and air cooling. Figure 2.21 displays a cross sectional view of the substrate cooling system. 172 is cooling water in and 170 is cooling water out. Air cooling is also used to control the temperature during process. 174 is hollow to provide a passageway to cylindrical chamber 164 machined just below 162. The rate of heat transfer from the substrate in 162 into 114 may be controlled by providing a gas through 174 to fill 164. Substrate electrode cooling can be accomplished by providing a means to flow a cooling fluid through the electrode.

Plasma Shape:

In Figure 2.19 surface 111 and 113 approximate a curve varying inversely with electrode radius to create an axisymmetric, uniform, relatively thin elongated disc-shaped plasma 140. The size of the plasma is approximately equal to the size of substrate 138 located in the substrate holder 114. It is noted here that as described in the US patent [41] that the thickness and radius of 110 can be

varied to tune the reactor and to adjust the plasma. It could be that this reactor with its variable height clamshell dome allows the different excitations of EM modes that have been described by Hemawan et. al. [39]

2.3.3 Ellipsoidal Reactor (Aixtron) 1998

AIXTRON's ellipsoid diamond reactors are based on microwave reactor developments at Fraunhofer Institute for Applied Solid State Physics, located in Freiburg, Germany. Due to its special ellipsoidal geometry, it has been shown experimentally that this reactor offers a good performance for producing thick polycrystalline diamond coatings on large substrates.

Numerical Simulation of Aixtron system

The AIXTRON reactor system is a non-cylindrical cavity which uses an ellipsoidal cavity. Despite its large dimensions, this innovative cavity shape has the advantage of having only two main field maxima, located at the foci of the ellipsoid. (See Figure 2.22) Due to its special geometry, this reactor offers a uniform coating of large substrates.

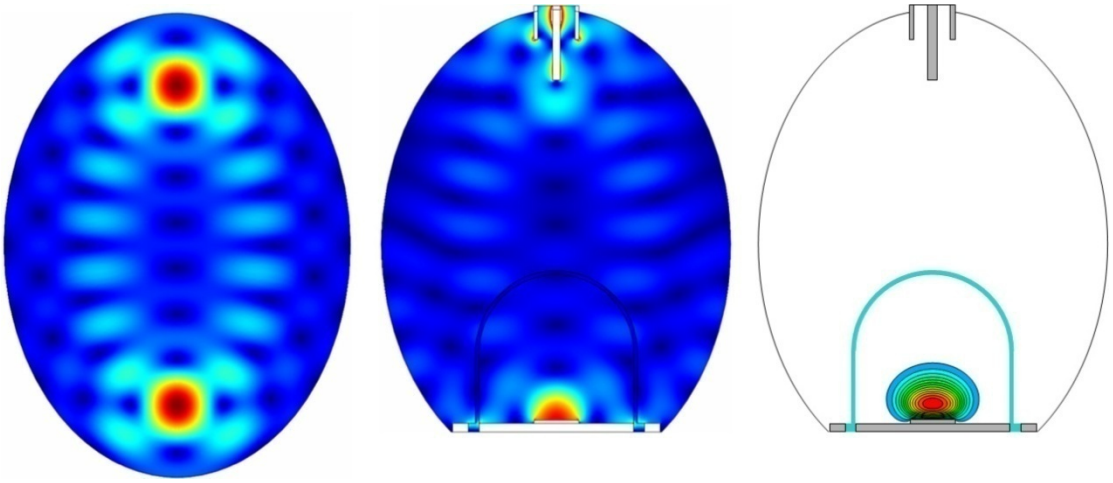

Figure 2.22 Illustration of the AIXTRON reactor cross section exploiting an ellipsoidal resonant cavity (Left). An antenna provides the coupling and the quartz dome is shown (Center). Modeling of 150 Torr H_2 plasma is presented (Right) [19]

Figure 2.23(a) shows how the TM_{012} field distribution from a cylindrical cavity evolves when the cavity transitions from a cylindrical to an ellipsoidal geometry. The sequence of three field maxima along the cylindrical cavity axis is transformed into two main maxima located at the foci separated by a smaller secondary maximum for the ellipsoidal cavity. If a larger reactor is employed as shown in Figure 2.23 (a), a TM_{036} mode can be excited in the cylindrical cavity. When the ellipsoidal shape is employed the seven field maxima of the cylindrical cavity are transformed into two main maxima as is shown in Figure 2.23.

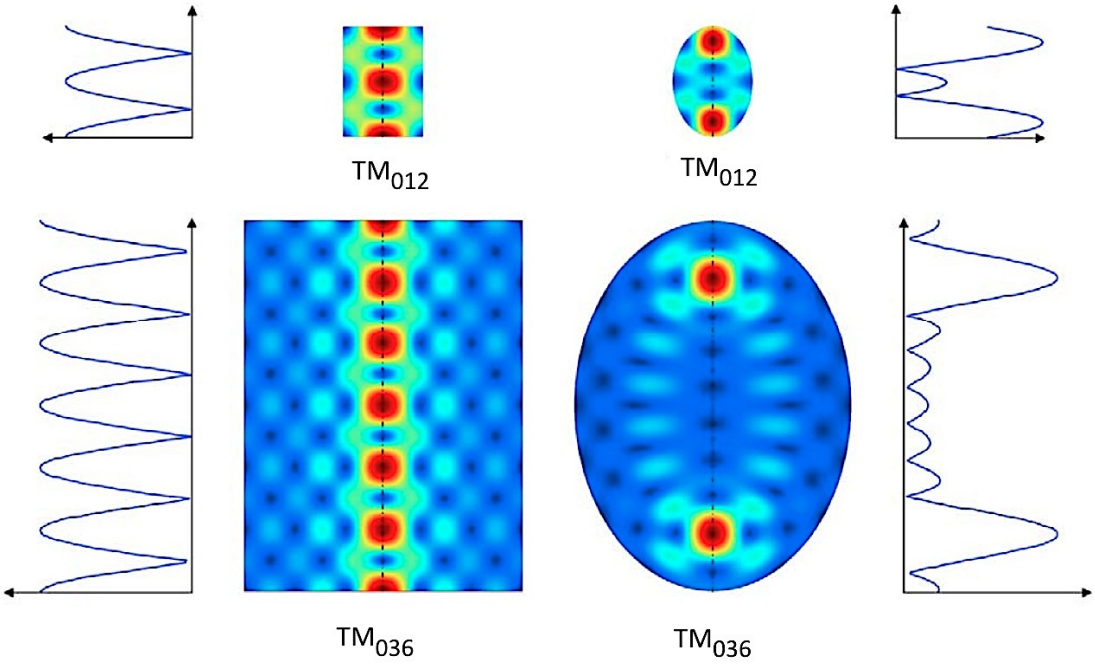

(a) (b)

Figure 2.23 Evolution of the electric field pattern for TM_{012} mode and TM_{036} mode from cylindrical to ellipsoidal cavity. The side graphs indicate the axial profiles of electric field strength [19]

System diagram photos of the ellipsoid microwave plasma reactor are shown in Fig. 2.24 and 2.25. Microwave energy is coupled from a waveguide system into an ellipsoid cavity via an axial antenna. A hemispherical plasma discharge is created and is placed in direct contact of the substrate inside a quartz bell jar. Here the plasma is ignited and the deposition takes place. The silicon substrates are placed on a water-cooled substrate holder. Two types of the commercial

systems, named P6 and P60, are available and operated at 2.45GHz and 915MHz respectively.

Figure 2.24 AIXTRON P6 ellipsoid microwave plasma system

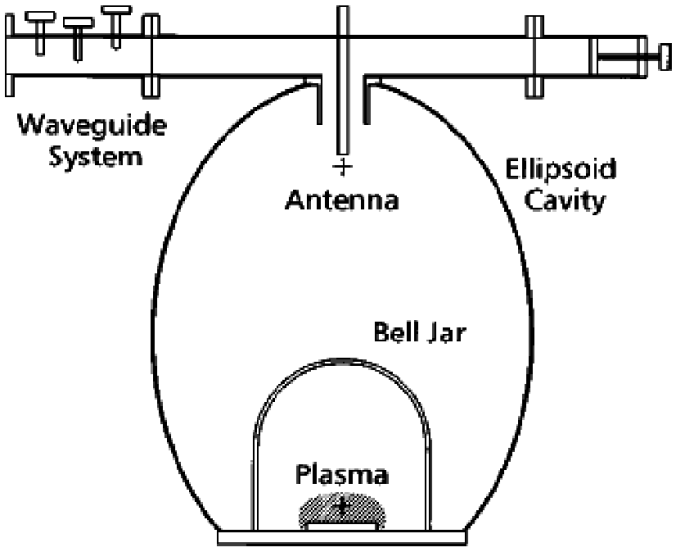

Figure 2.25 Ellipsoid microwave plasma reactor [46]

Another group W.Z. Tang et. al. [47] from University of Science and Technology Beijing, China recently introduced a new compact cavity type ellipsoidal microwave plasma reactor. After performing systematic numerical simulations on ellipsoidal cavities, they selected an ellipsoidal cavity with radius, R, and height, Z, values of 165 mm and 435 mm respectively. From Figure 2.26, we can see the compact ellipsoidal cavity has the maximum electric field intensity above the center of the substrate holder (bottom of the cavity). The resonant modes for the compact ellipsoidal cavity and the AIXTRON reactor are TM_{033} and TM_{036}, respectively. A plasma ball has been ignited in this compact ellipsoidal cavity and hemisphere plasma is created above the center of the substrate holder. To date no further research and experimental evaluation of using this reactor for diamond deposition has been published. But this compact ellipsoidal reactor is expected to be an improved more compact reactor design for MPACVD

diamond deposition.

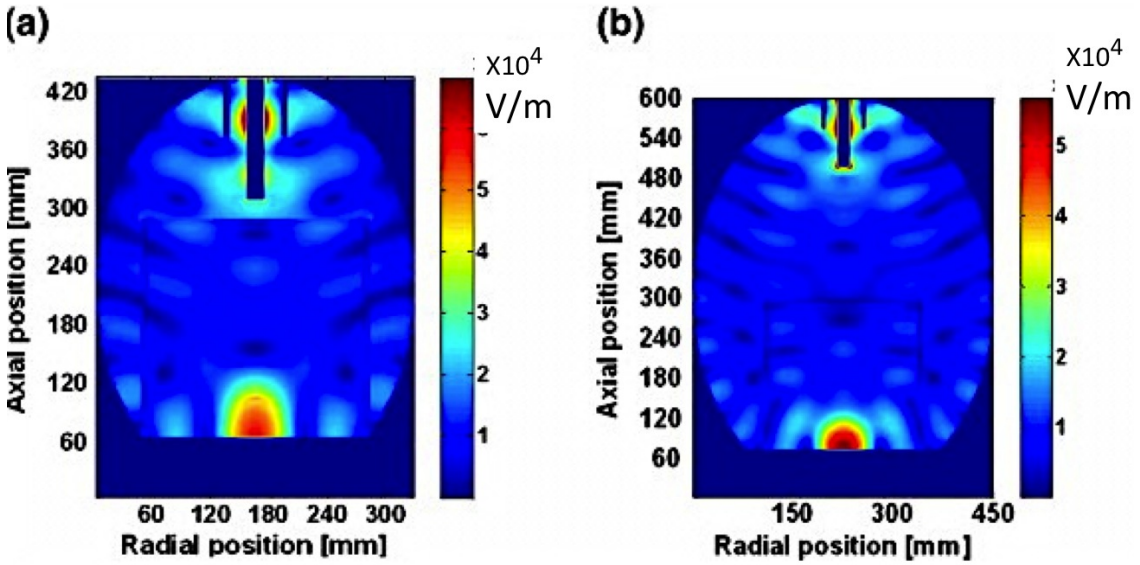

Figure 2.26 (a) Electric field distribution in the selected compact ellipsoidal cavity and (b) Electric field distribution in the original AIXTRON ellipsoidal reactor [47]

2.3.4 CYRANNUS Plasma System (iplas) 1996

The iplas plasma systems from CYRANNUS have some great features. For example their plasma systems can run continuously at any pressure and the applicator system is fed with microwave power from the side and is equally distributed to the whole cavity.

Numerical Simulation of IPLAS system

Similar to the MSU and SEKI reactors, the iplas system (Figure 2.27 and 2.28) excites the TM_{01n} resonant modes. The major difference is the method of microwave coupling into the applicator. For the iplas cavity microwave coupling is achieved with a series of gaps in a toroidal waveguide wrapped around the cylindrical cavity instead of a coupling probe. The length of each gap is an

integer number of guided wavelengths (four in this case). As is shown in Figure 2.27, the coupling waveguide is wrapped around the cylindrical cavity and the slots are positioned every other half-wavelength. The waveguide has been arranged along the cavity vertical wall. The mode excited within the cylindrical cavity is TM_{012}. The quartz window in this reactor consists of a tube located inside the cavity to prevent plasma ignition at the slot's location. In the absence of quartz windows, the slot would experience the same pressure, as the processing environment and the plasma would be ignited in the slot in the high electric field region. So the use of the cylindrical quartz window allows one to properly select the cavity excitation region and excite the cavity with a single region of maximum plasma power density (Figure 2.28). This region as shown in Figure 2.27 is close to the substrate surface. It is not clear where the substrate is located, i.e. in the middle or the bottom of the cavity, during the deposition. It probably depends on the specific application.

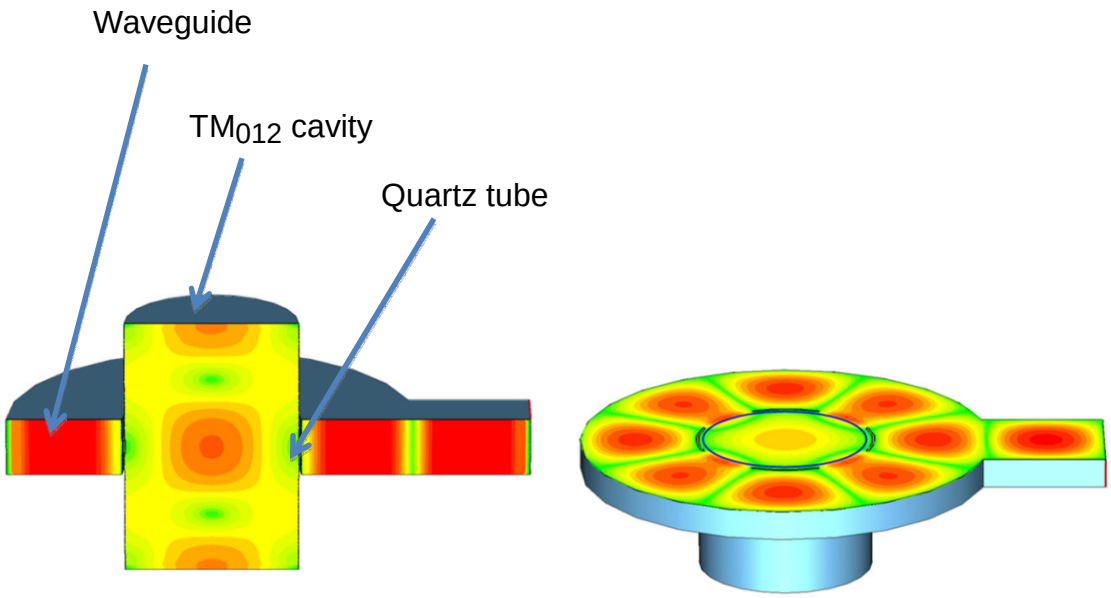

Figure 2.27 Illustration of the IPLAS reactor [19]

The magnetic field distribution (shown in Figure 2.29) in the waveguide switches from clockwise to counterclockwise rotation every half-wavelength. So the cavity openings have to be chosen to only select the waveguide sections where the magnetic field is rotating in the same direction as the magnetic field in cavity, thereby exciting the resonance TM_{012} mode.

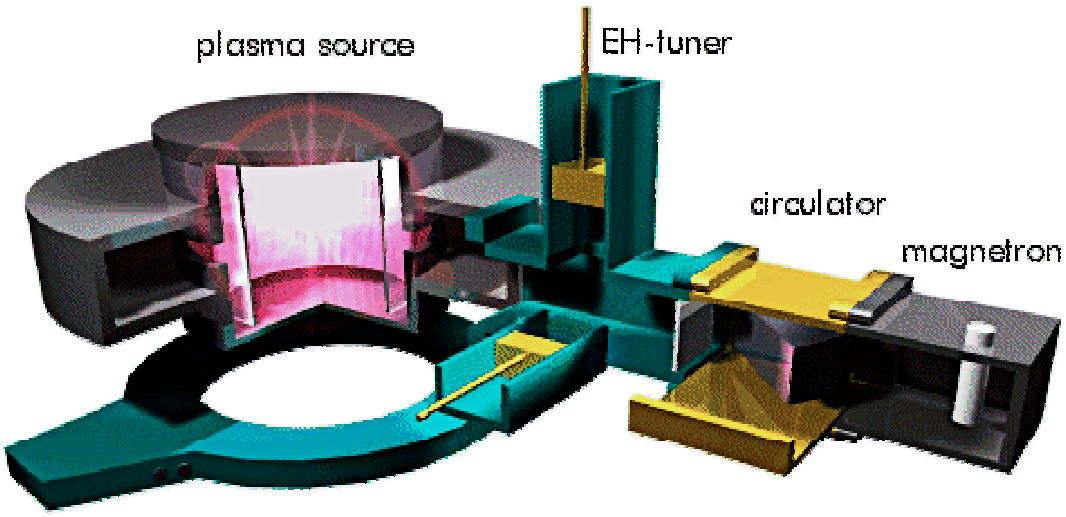

Figure 2.28 Schematic diagram of CYRANNUS plasma system [47]

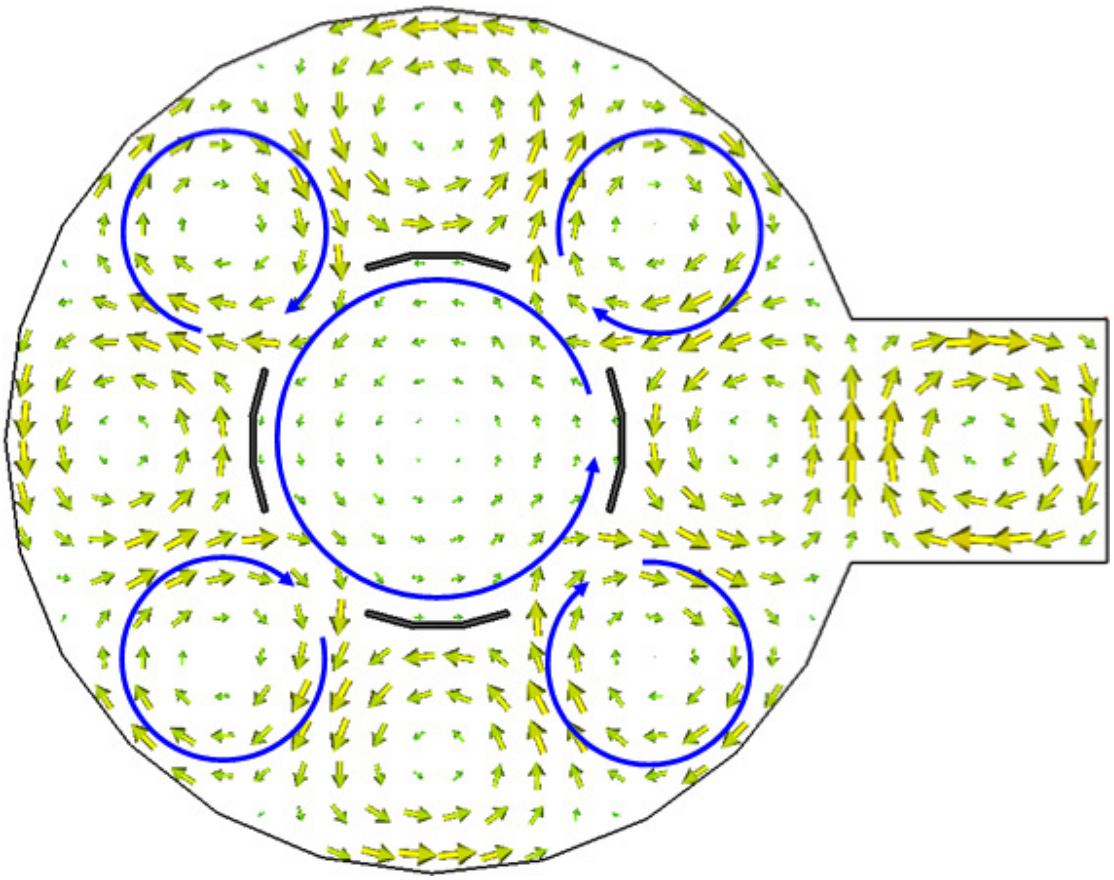

Figure 2.29 Magnetic field distributions in a transverse cut plane for the waveguide and reactor [19]

A photograph of a commercially available CYRANNUS iplas plasma system is shown in Figure 2.30. Plasma generation is possible with many different process gases, such as air, O_2, H_2, N_2, C_xH_y or Ar [47]

Figure 2.30 Manual CYRANNUS plasma system [47]

As shown in Figure 2.28 the plasma source is fed with microwave power from the right. The waveguide system is excited with microwave power from the magnetron. The microwave energy passes through the circulator and the EH-tuner, before it is coupled into the plasma source. Any reflected power is reflected back to the circulator and then is absorbed in a water load.

2.3.5 LIMHP bell jar reactor

This bell jar reactor is the result of the collaboration between Plassys and the CNRS laboratory LIMHP in Villetaneuse, France.

Numerical Simulation of LIMHP system

LIMHP system is very similar to the MSU system. The first generation of LIMHP reactor is a bell jar type reactor with a TM_{023} mode as shown in Figure 2.31. The cylindrical cavity has a diameter of 250 mm, as compared to 178 mm to MSU Reactor A, with a metal meshed outer cylindrical structure. Although this provides a large access window to inspect the plasma, at high input powers it causes a heating problem when pressures are above 110 Torr.

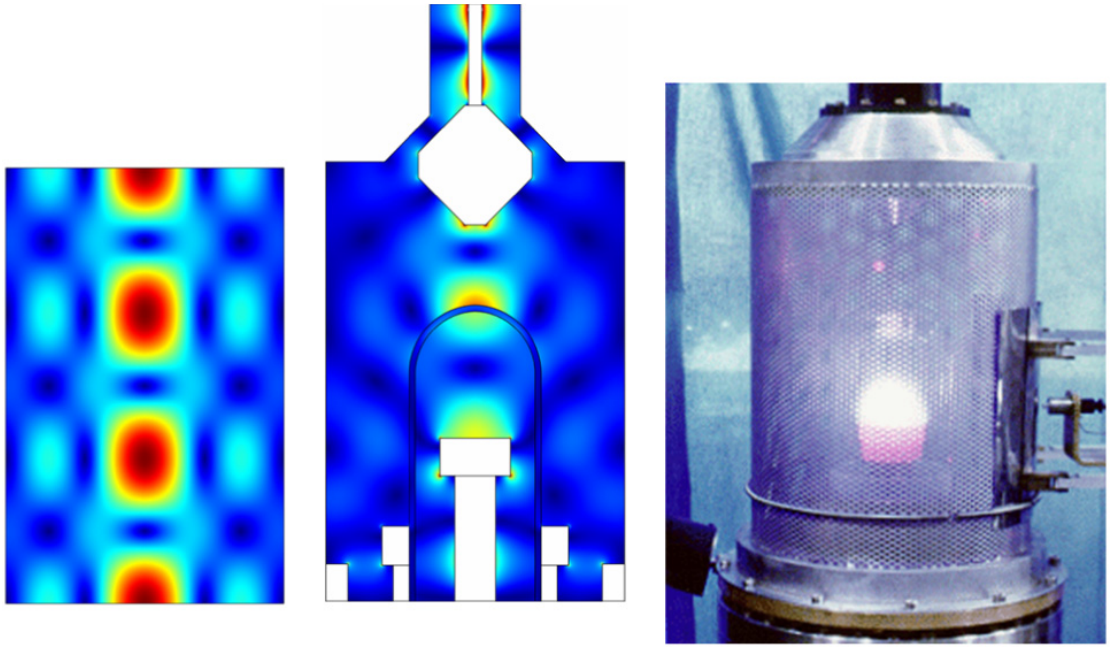

Figure 2.31 LIMHP first generation bell jar reactor designed in 1990: TM_{023} Electric field pattern (left); LIMHP coupled cavity with substrate holder and quartz bell jar (center); photograph of an H_2 plasma at 18 Torr and 600 W power [19]

In order to circumvent the heating problems a second generation of the LIMHP reactor was designed. The quartz bell jar of the first generation reactor

was difficult to cool and then was replaced with a window located at the top of a TM_{022} mode cavity. See Figure 2.32. The microwave coupling into the cavity was achieved via an excitation probe just like MSU system. The lower part of the cavity was able to move which enables modifying the geometrical size of the cavity and matching. Thus it appears that they are using the same variable coupling probe and sliding short matching that was patented many years ago. (Ref US patents by Asmussen et. al 4,507,588, 4,130,566, 4,691,662, and 4,943,345 [25-33])

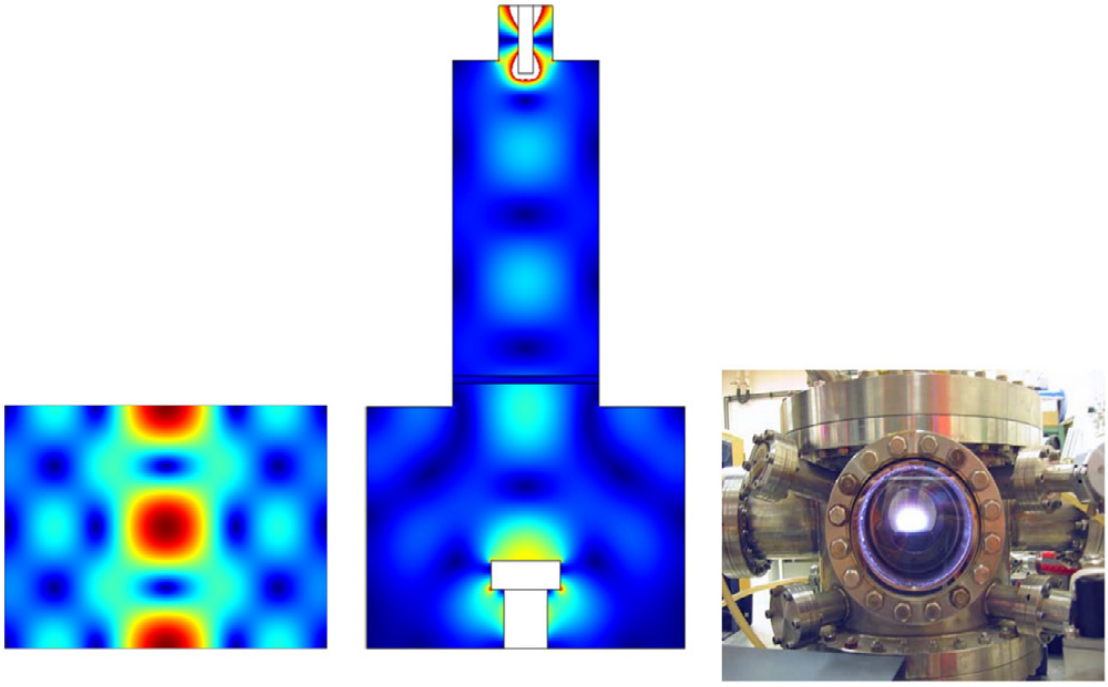

Figure 2.32 Second generation LIMHP stainless steel reactor designed in 1994. TM_{022} Electric field pattern (left); LIMHP coupled cavity with substrate holder and quartz window (center); photograph of H_2 plasma at 100 mbar [19]

Figure 2.33 shows the cross section view of the third generation LIMHP

reactor. It's an optimization of their first generation bell jar reactor. To achieve higher power operation, the diameter of the quartz bell jar is increased to move the quartz walls away from the plasma. The cavity geometry is also modified to obtain higher power density plasma with better radial homogeneity. The third generation LIMHP shows excellent performance for working pressures from 150 Torr to 225 Torr and good handling of heat fluxes to the walls.

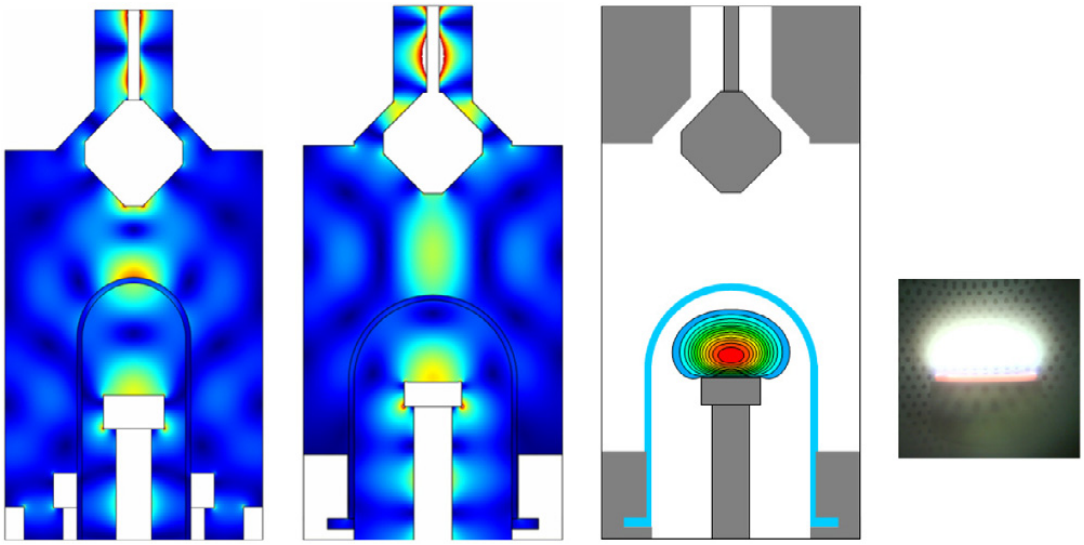

Figure 2.33 Third generation LIMHP reactor (optimization of the first generation) [19]

Two kinds of commercially available reactor designs are reported by LIMHP for diamond synthesis. Figure 2.34 shows stainless steel reactor for high-purity single crystalline diamond synthesis and Figure 2.35 shows "Bell-jar" reactor for polycrystalline diamond deposition and plasma diagnostics. These reactors are also known as BJS150 MPACVD Bell Jar diamond deposition reactor, manufactured by PLASSYS Company.

Figure 2.34 LIMHP stainless steel reactor [48]

Figure 2.35 LIMHP bell jar reactor [48]

2.4 Development of inch-size single crystal diamond wafer production (SEKI reactor system)

Seen as the future of wide band gap semiconductor materials, single-crystal diamonds need to be fabricated in at least inch-size wafers if they are to be of use in industry. This section presents a recent development of inch-size SCD wafer production. H. Yamada et al. [49] has applied the first generation SEKI 2.45 GHz microwave plasma CVD system for high rate homoepitaxial growth of single crystal diamond with the thickness as large as 10 mm. Figure 2.36 shows two different types of substrate holder design. One is called “open” type, which supports the diamond seed on the Molybdenum rod and another is called “enclosed” type, which supports the seed inside the drilled hole. The hole size can be varied according to the original diamond seed size. This design is very similar to MSU CVD system holder design except for the so-called “enclosed” type. The MSU design sits the diamond seed on the bottom of the Molybdenum to improve the cooling condition.

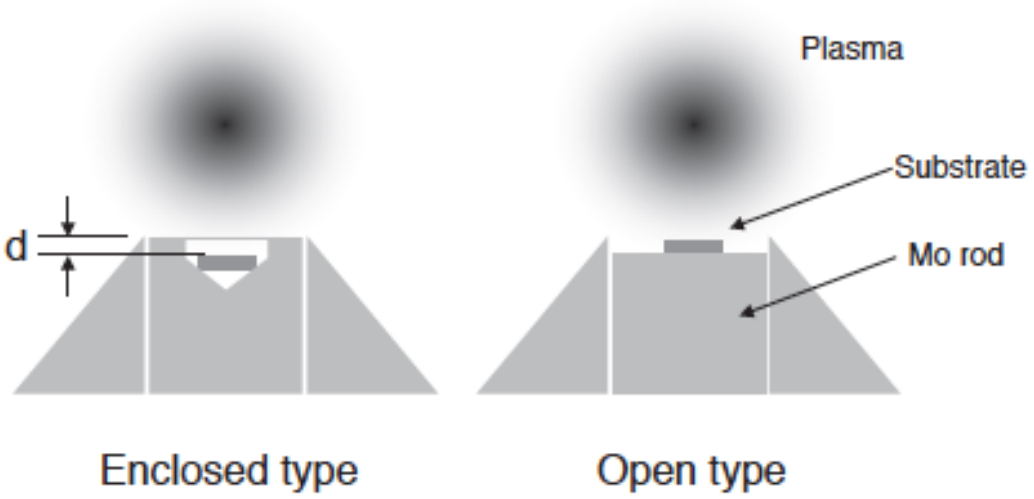

Figure 2.36 Schematic illustration of “open” and “enclosed” type holders [49]

The research shows the diamond films grown by the open type indicates the promotion of edge growth which is mostly proved to be polycrystalline diamond. In contrast, the films grown by the enclosed type indicates very little growth of polycrystalline diamond. This is a big advantage of enclosed type over open type, because we always want to eliminate the poly rims in order to grow high quality single crystal diamond. The poly rims are also responsible for the shrinkage of the growth area (see Chapter 4 in this thesis). In Figure 2.36, there is an important parameter d which is the distance between the holder top surface and diamond top surface. As d becomes smaller, the grown surface becomes smoother. It shows macroscopically flat surface morphology at d = 0.6 mm. Diamond doesn’t grow at the four corners, due to the lower temperature surrounding the holder. However, as shown in Figure 2.37, the growth rate for enclosed type holder increases as d value is decreased and approaches growth rate of open type holder at 100-160 microns per hour. It was not clearly described

how the growth rate was measured. That is it was not stated whether growth rate was determined by weight gain or linear encoder.

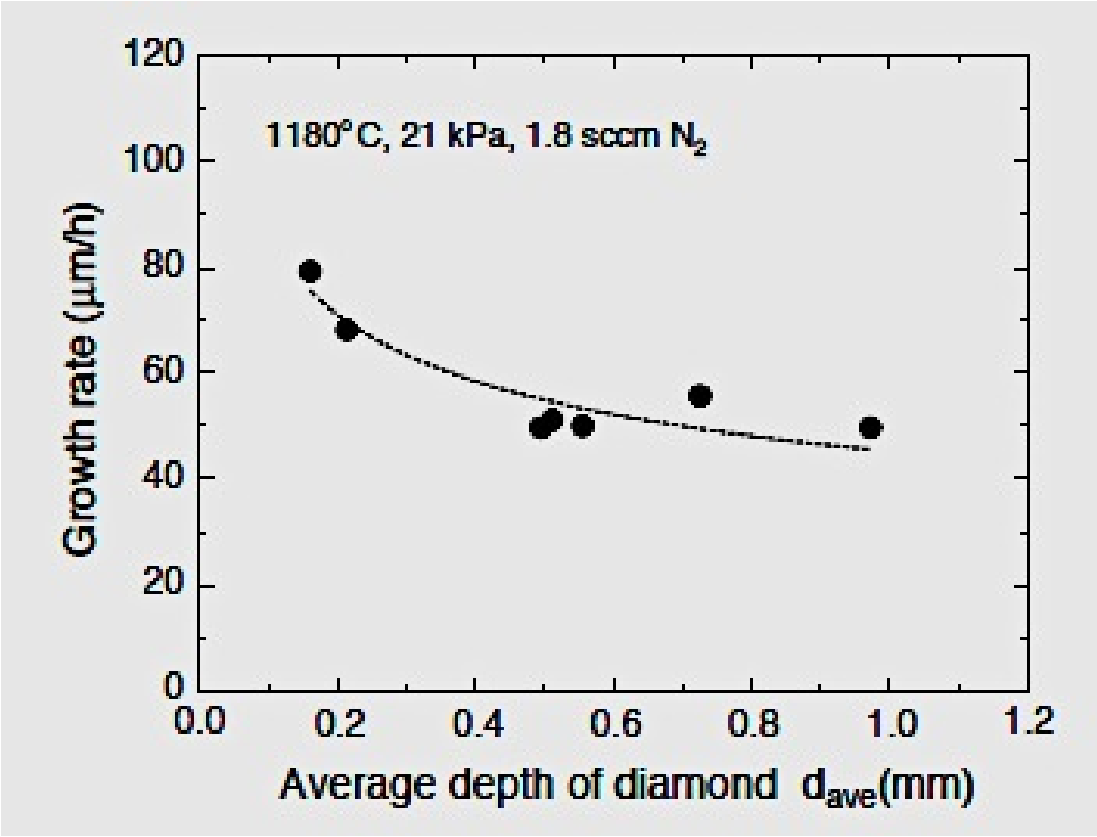

Figure 2.37 Growth rate of diamond films for enclosed type holder as a function of the depth d [49]

Optimum growth strategy for CVD diamond has also investigated by this research group. These process steps are displayed pictorially in Figure 2.38. Lift-off process using ion implantation was successfully applied to produce a thick and large single crystal CVD diamond plate. The first step was to grow a 40 μm thick film on the ion implanted HPHT single crystal CVD diamond substrate. Then the diamond film was separated from the substrate after wet etching of the ion implanted layer. Then a much thicker layer of 470 μm was grown on the

separated plate with the average growth rate of 7.8 μm/h. The fourth step is to apply a high rate growth on the side {100} surface of a thick diamond for the purpose of three dimensional enlargements in crystal size. Although the side surface of diamond is covered by polycrystalline diamond after step 3, it can be laser-cut and the inside single crystal diamond still has some degree of optical transparency. Once again a lift-off process is applied to achieve a large area CVD diamond plate. By this method, a 12.6 x 13.3 mm^2 single crystal diamond plate was produced with thickness of 0.2 mm by high-rate growth (32 μm/h) (Figure 2.39).

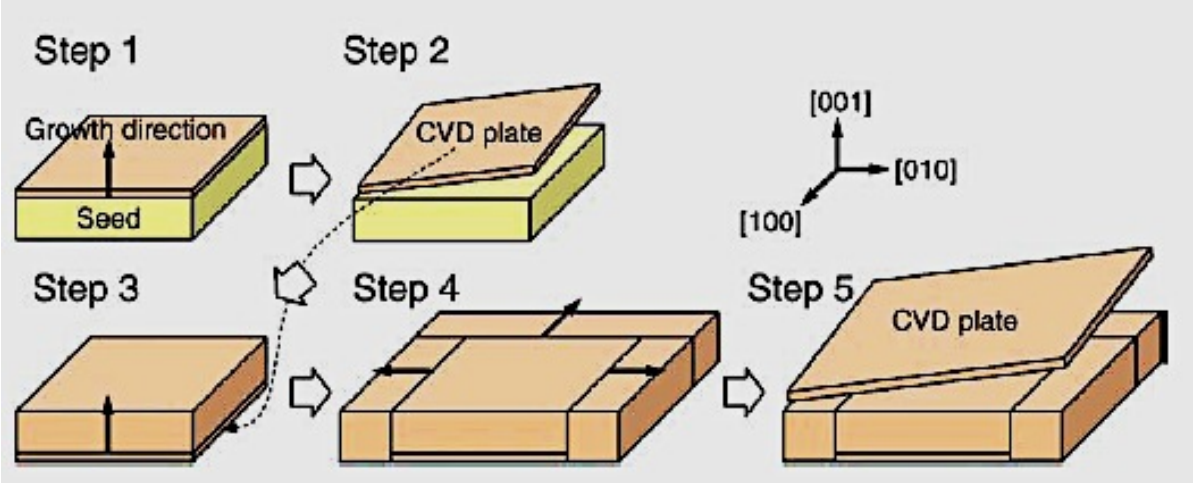

Figure 2.38 Steps to enlarge a CVD diamond plate by combination of lift-off process and side surface growth [50]

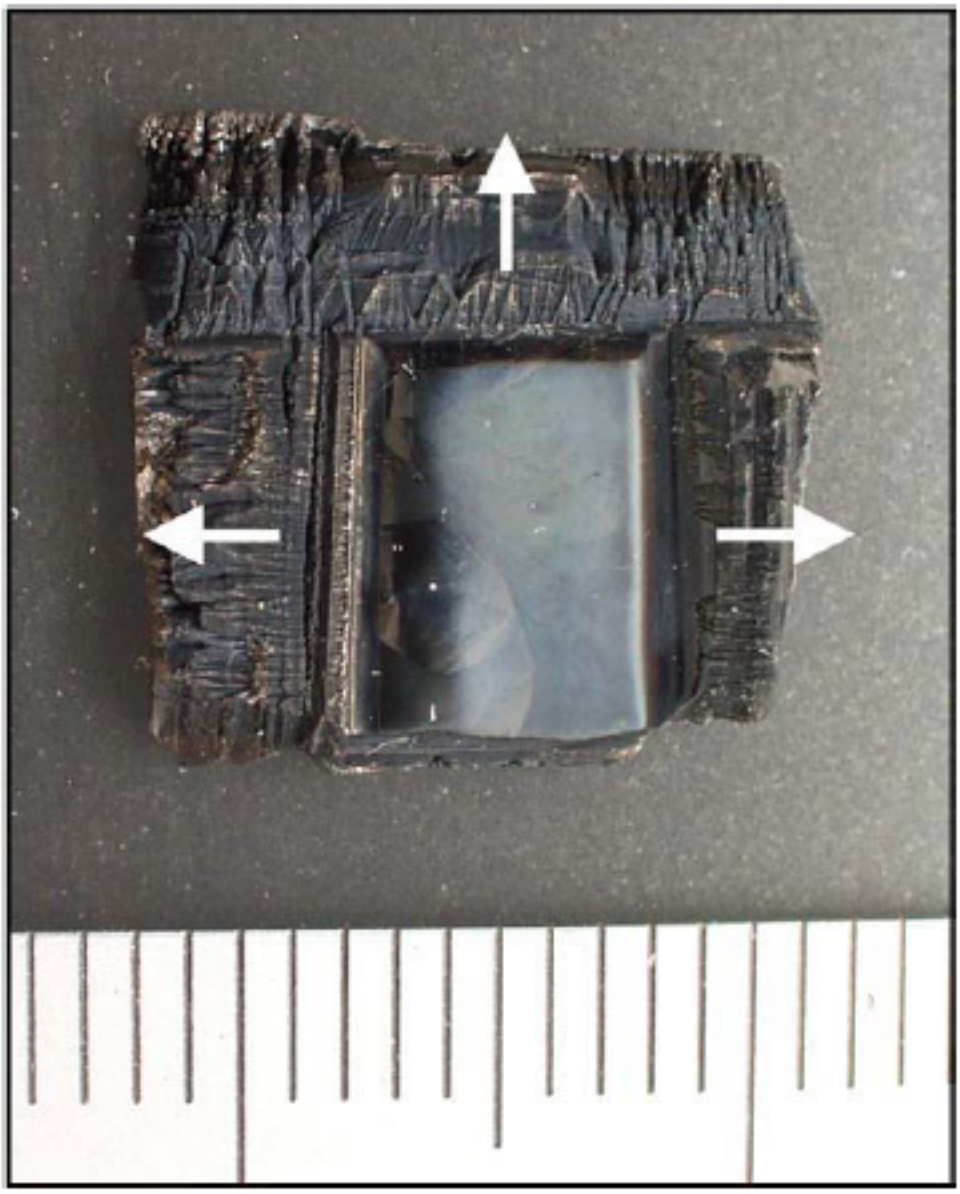

Figure 2.39 A half-inch (12.6x13.3x3.7 mm^3) single crystal diamond fabricated via enlarging process [50]

In order to obtain a single crystal wafer more than 1 inch in diameter, a so-called “mosaic wafer” technique was developed [51]. SCD layers can grow on

several small plates, which have been arranged appropriately so that the upper layer has a smooth larger surface. The maximum size of mosaic wafer obtained by this group is 16 x 16 mm^2, which consisted of 16 SCD plates, each 4 x 4 mm^2. It can be easily realized that the importance of obtaining the identical small SCD plates for the mosaic wafer process. Once again the lift-off process using ion implantation can be utilized to clone the seed crystal (See Figure 2.40 and 2.41). The Raman spectra of the mosaic wafer along a line crossing the junction between the seed crystals shows that FWHM is approximately 1.5 times large on the junction than the other region in a distances of 0.3 – 1.0 mm. The FWHM of all the Raman spectra are less than 5 cm^{-1} which is close to that of HPHT Ib substrate. For the IR transmission measurement, they also claim the mosaic wafer shows characteristics close to type IIa SCD.

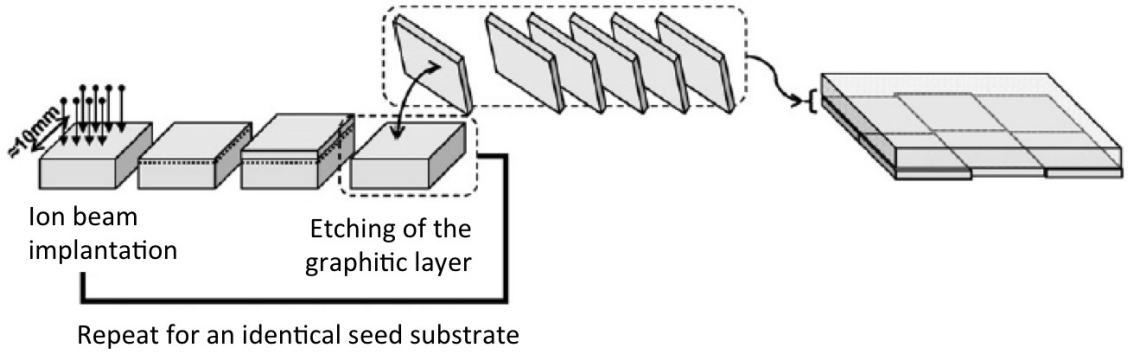

Figure 2.40 “Mosaic wafer” process: Several clones are jointed into one large diamond plate [51]

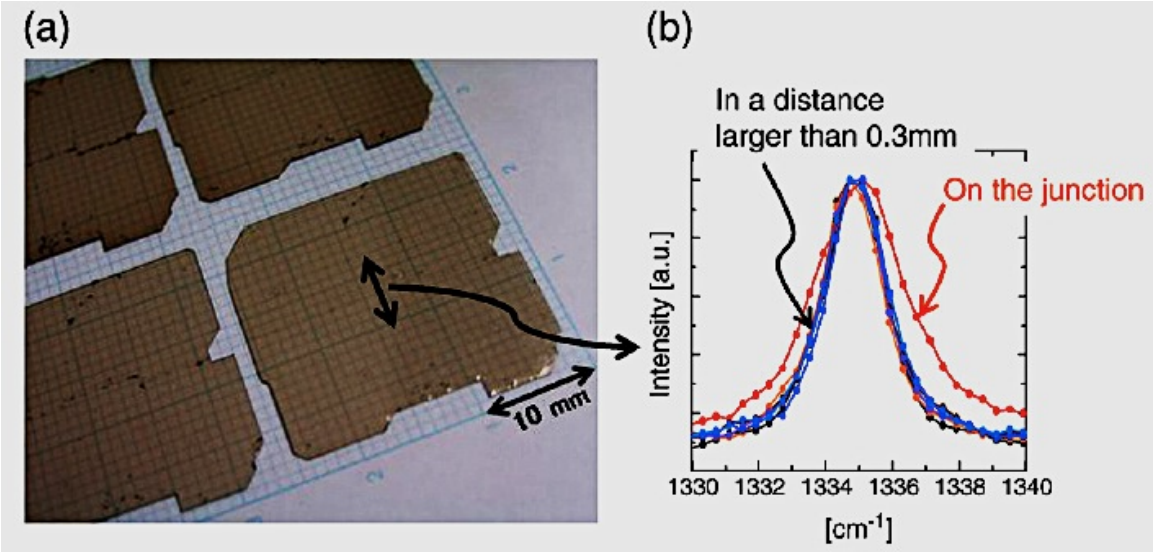

Figure 2.41 (a) Mosaic wafer made of SCD clone plates and (b) Raman spectra measured at the junction [51]

CHAPTER 3

ANALYSIS OF MICROWAVE PLASMA ASSISTED CVD REACTORS

3.1 Introduction

This Chapter analyzes and compares the commercially available MPACVD diamond synthesis reactors. The similarities and differences between the reactor designs are noted and then if possible the output performance of the different reactor designs is compared. Reactor designs and the associated reactor performance is a multi-dimensional variable optimization problem. Thus this chapter first identifies and classifies the many experimental and reactor design variables and then establishes several performance criteria from which the reactor performance can be calculated and compared. Section 3.2 describes the multi-dimensional variable space and the differences in the commercially

available reactor designs are discussed in Section 3.3. A number of performance measures or “figures of merit” are defined in Sections 3.4 and Section 3.5. These performance measures are calculated for each reactor and then are employed to compare the performance of the different reactor designs. In Section 3.6 the differences between the reactors are summarized.

3.2 Microwave Plasma Reactor Design Variables, Experimental Process Variables And Performance Variables

In order to systematically compare the performance of the different commercially available microwave plasma assisted CVD reactors, it is essential to identify the many input variables that influence the behavior of the reactor. Most of these variables have been identified in earlier MSU theses and publications [24,52,53], and thus they are only briefly summarized here. The nonlinear relationships between the three main groups of variables are presented. The three basic groups are (1) input variables, U; (2) internal variables, X; and (3) output variables, Y.

The input variables are defined as the variables that are independently controlled by an experimental operator or reactor designer. The input variables can be further subdivided into

(1) Experimental controllable input variables, U_1

U_1 includes deposition pressure, incident microwave power, feed gas

composition, and total flow rate

(2) Reactor geometry design variables, U_2

U_2 includes applicator size and configuration, substrate holder location and size, electromagnetic mode and cavity tuning, and quartz dome geometry

(3) Deposition process variables, U_3

U_3 includes substrate material and size, substrate seeding and nucleation procedure and deposition time

The internal variables are defined as the internal plasma reactor states. Internal variables X include absorbed microwave power, plasma volume, substrate temperature, and absorbed power density.

The output variables, Y, can be divided into two groups.

(1) Reactor performance, Y_1

Y_1 includes linear growth rate, total growth rate and carbon conversion efficiency

(2) Film characteristics, Y_2

Y_2 includes film uniformity, film structural quality, film morphology and film texture.

The sub-sections and chapters that follow in this section quantify the relationships between the input variables, U, and internal variables, X = f(U), the input variables and output variables, Y = g(U), and the internal variables and

output variables, Y= h(X).

Given a set of independently fixed input variables U_1, e.g. deposition pressure, incident microwave power, and feed gas composition, changing the reactor design can have a big influence on the output performance of the CVD diamond process. Different electromagnetic modes are excited due to different applicator geometries i.e. reactor shape, reactor size, configuration. We can also benefit from the larger size of the reactor or quartz dome to deposit diamond at higher operating pressure. The cooling stage and substrate holder design will also influence the cooling condition during the CVD process.

3.3 A Comparison of Commercially Available Reactor Designs

Each of the reactor designs described in Chapter 2 has evolved over the past 15 – 30 years, and at a “first glance” they appear to be quite different from one another. In this section these commercially available MPACVD reactor designs are compared. Here each reactor concept is reviewed by comparing the specific reactor designs with the MSU developed MPACVD reactor design principles that have evolved at MSU over the past 30 years. These MSU design principles are as follows: what is (1) the applicator size and shape, (2) the method of electromagnetic field excitation, (3) the method of cavity applicator coupling and matching, (4) the ability and the ease of the design to scale up the

reactor size by lowering the excitation frequency (5) the location of the substrate within the applicator and (6) the ability of the reactor design to optimize the CVD process by applicator size and substrate position adjustment.

All the reactor applicators have a shape that is phi-symmetric. Some applicators are just simple cylindrical cavities. Examples of these are the SEKI 1^{st} generation reactor, the LIMHP 1^{st} and 3^{rd} generation reactors, the iplas reactor and the MSU Reactor A. While the AIXTRON reactor is phi symmetric the cavity applicator shape is ellipsoidal. As the shape of the AIXTRON applicator varies versus the axial position, the electromagnetic field intensity also varies versus axial position. Starting from the coupling probe at the top of the reactor, the electromagnetic field is first unfocused and then as the Z=0 position is approached the electromagnetic field is refocused onto the substrate. Thus the EM energy flux density varies over the applicator cross section as it passes from the input coupling port through the applicator to the discharge load. The more advanced reactor designs have more complex, phi-symmetric, shapes. Examples of these are the SEKI 2^{nd} generation reactor, the LIMHP 2^{nd} generation reactor and the MSU Reactor B. In each of these designs the applicator radius varies versus the axial position.

All the reactor designs employ a single, phi-symmetric, TM_0 mode excitation. Thus this appears to be the common method of producing the microwave discharge within all the applicators. Examples of excitation modes are the TM_{013} for the SEKI 1^{st} generation reactor, the TM_{013} mode for the MSU

Reactor A, the TM_{012} for the iplas reactor and the TM_{023} mode for the LIMHP 1st generation reactor. The AIXTRON reactor is excited in the ellipsoidal TM_{036} mode, as is shown in Figure 2.22[19]. However its size can be reduced and then the ellipsoidal TM_{033} mode can be excited [54]. This mode excitation leads to a more physically compact reactor. The reactors with more complex shapes have the following mode excitations: (1) the hybrid TM_{013} + TEM_{001} mode for the MSU Reactor B, and (2) the TM_{022} mode for LIMHP 2nd generation reactor. However it is not clear what single mode is excited in the SEKI 2nd generation reactor. An electromagnetic analysis of the reactor has been performed by F. Silva et. al. [19]. The result indicates that more than one mode may be excited. That is, as shown in Figure 12 of the reference [19], the EM field patterns consist of a main field cavity TM_{011} mode as well as secondary radial field maxima typical of TM_{021} mode. A recent investigation by Hemawan et. al. [39] also indicates more than one mode can be excited.

Most of these reactors including MSU Reactors A and B, the SEKI first generation and AIXTRON use excitation probes for microwave coupling into the reactor. The LIMHP reactor uses a coaxial octahedron excitation probe. Apparently the LIMHP designs use this variable radii probe to enhance the impedance matching into the discharge-loaded applicator.

These reactors also have different impedance matching methods. Both the MSU Reactors A and B and the LIMHP use internal impedance matching.

The MSU reactors use a sliding short and an adjustable excitation probe for internal impedance matching. Similar to the sliding short in the MSU reactors, the lower part of the LIMHP reactor is made of a movable metallic plate which enables modifying the geometrical size of the cavity, i.e. the cavity length, and hence enables reactor matching similar to the MSU reactor design. External matching is employed by the SEKI, the AIXTRON and the iplas reactors. The SEKI 2nd generation reactor uses triple screws and AIXTRON uses triple stubs for external impedance matching, while the iplas uses an E-H tuner for external impedance matching. The advantage of external matching is there are no or very few moving parts in the reactor to prevent possible leaking or fine adjustment. However the triple stubs or triple screw tuners introduce impedance matching challenges of their own. Their triple tuners do not have the flexibility as internal impedance matching and under specific experimental conditions can introduce significant waveguide wall losses.

Usually these commercially available reactor designs locate the substrate in a high electric field region for better deposition results. MSU Reactors A and B and the LIMHP have a similar design which allows the substrate holders to be moved up and down for different plasma discharge locations and for different process conditions. The SEKI 2nd generation has a fixed substrate position which is not easily optimized for different CVD process conditions. It is not clear in a diamond synthesis application exactly where in the iplas reactor the substrate is located, but it is believed it is placed in the high electric field region which is somewhere in the center of the cavity.

All of these reactors have a similar ability to electromagnetically scale up the reactor to larger reactor sizes when they are excited with 915 MHz microwave energy. When reducing the excitation frequency to 915 MHz, the reactor size increases by the factor of 2.7. However the input power doesn't scale linearly with discharge volume nor with substrate area. Rather the required input power scales as (substrate area)$^{0.75}$ [55]. The ratio of plasma diameters excited at 915 MHz is also not proportional to the ratio of excitation wavelength. For example it is 2.13 instead of 2.7 [19].

3.4 Measurement of Output Variables

3.4.1 Measurement of Film Growth Rate

Film growth rate (GR) can be calculated in two different ways. The linear growth rate (LGR) is pretty straightforward. We can measure the total substrate thickness before (A_1) and after (A_2) the CVD diamond synthesis and divide by deposition time (t_d). Usually we use the unit as microns per hour.

$$\text{LGR} = \frac{A1 - A2}{t_d} \ \mu\text{m/h} \qquad (1)$$

The other growth rate that is employed in this thesis is called total growth rate (TGR). It is determined by measuring the total weight gain ($W_1 - W_2$) of the substrate and dividing by the deposition time (t_d), where W_1 is silicon substrate weight before deposition and W_2 is silicon substrate weight plus CVD diamond film weight after deposition. The unit is mg per hour. It can also be converted to

microns per hour. Here A is the deposition area (for example 0.35x0.35 cm^2 for HPHT seeds), and D is the diamond density of 3.51 g/cm^3, then

$$\text{TGR} = \frac{w_1 - w_2}{t_d}\ \text{mg/h} = \frac{w_1 - w_2}{A * D * t_d}\ \mu\text{m/h} \qquad (2)$$

3.4.2 Measurement of Carbon Conversion Efficiency

Carbon Conversion Efficiency (CCE) is the percentage of carbon atoms in the input gases, which are converted into CVD diamond [23]. Let's use the previous definition of Total Growth Rate (TGR) over 1" diameter silicon substrate, then the carbon conversion efficiency is

$$\text{CCE} = \frac{TGR\ \frac{mg}{h}\ X\ \frac{1}{1000}\frac{g}{mg}\ X\ \frac{1}{60}\frac{hr}{min}\ X\ \frac{1}{12}\frac{mole}{g}\ X\ \frac{6.02E23}{1}\frac{atom}{mole}}{CH4\ \frac{cc}{min}\ X\ \frac{1}{1000}\frac{liter}{cc}\ X\ \frac{1}{22.4}\frac{mole}{liter}\ X\ 6.02E23\ \frac{atom}{mole}}\ X\ 100\% \qquad (3)$$

3.4.3 Measurement of Specific Yield

Specific yield (SY) is defined as the absorbed power input (p_a) per diamond film total growth rate in the units of kW-h/g. It is a measure of the electric deposition efficiency. Since people usually published their total growth rate TGR, in mg per hour, then the SY is given by

$$\text{SY (kW-h/g)} = p_a / \text{TGR} \qquad (4)$$

3.4.4 Measurement of Absorbed Microwave Power Density

The absorbed microwave power density $<P_{abs}>$ is defined as the input absorbed power divided by the plasma volume V_p. At each experimental operating condition, i.e. pressure, gas mixture, etc., the plasma volume can be approximated by taking size calibrated photographs of the discharge.

$$<P_{abs}> = P_{abs} / V_p \quad (5)$$

3.4.5 Measurement of Diamond Quality

The surface morphology of the grown diamond can be evaluated by visual inspection with the human eye. Since the impurities and defects in the CVD diamond can cause discoloration, the optical transparency (how well the film lets through the visible light) can also be determined qualitatively by the human eye visual inspection. The optical microscope can be also used as a first simple evaluation of the diamond quality. Thus the microscope is usually integrated with 2-D and 3-D image processing computer program to allow optical observation and analysis of the samples.

Raman spectroscopy is one of the most common methods to investigate the diamond quality. Using Raman spectra we can easily detect graphite, amorphous diamond like carbon, carbonaceous compounds and many other kinds of impurities in the CVD diamond film. Very good quality diamond displays a single ultra-sharp, narrow and high intensity peak at 1332 cm^{-1} in the Raman scan with a very small value of Full Width Half Maximum (FWHM). For high

quality diamond no peaks are detected for the graphite carbon peak at 1597 cm^{-1} and sp^2 silicon carbon at 520 cm^{-1}. This indicates that the CVD polycrystalline diamond grown contains none or very little graphitic content in the film. So the diamond quality can be quantized by scanning the Raman spectra, the noting the positions of the high intensity peaks and measuring the FWHM of the high intensity diamond peak.

3.5 Calculation of Reactor Performance

3.5.1 ASTEX (SEKI) MPACVD reactor system

3.5.1.1 Introduction

In the following section, the performance of all commercially available reactors are compared by employing a number of reactor performance measurements. The performance measurements are calculated from experimental data that is available in the published literature. Since there is a lack of comparable experimental data in the literature, the comparison that is presented here may not be complete. For example some of the input experimental conditions/parameters are missing for many of the data/results that are presented in the published literature [42,44,46,48]. The SEKI reactor, which is the most commonly used reactor, has the most experimental data available in the literature. Hence the SEKI reactors are analyzed in the following performance measures: (a) CVD diamond growth rate (linear or by weight gain), (b) discharge absorbed power density, (c) energy efficiency i.e. SY, and (d) diamond quality.

3.5.1.2 Results for 2.45 GHz SEKI reactor system

SEKI reactor performance data was presented for the SEKI AX5250, 2.45 GHz, 5 kW, which is the first generation SEKI design by Y. Ando et al. [42]. Diamond films were grown on 1-inch silicon wafers of 0.5 mm thickness by a 5 kW 2.45 GHz microwave plasma CVD system using CH_4-H_2 and CH_4-H_2-O_2 reaction gas mixtures.

Growth parameters: Operating pressure at 100-120 Torr, total gas flow rate at 400 sccm, microwave power at 2.0-4.5 kW, CH_4 concentration at 0.25 - 8% and O_2 concentration at 0 - 3%.

1) The growth rate: It was found that the growth rate increased with CH_4 concentration, the input microwave power and the gas pressure. (See Figure 3.1 [42]) The maximum value of the growth rate is 9.3 μm/hr when the CH_4 concentration is 2 or 4%, a microwave power of 4.5 kW and gas pressure of 120 Torr. The substrate temperature was 905 - 955 °C.

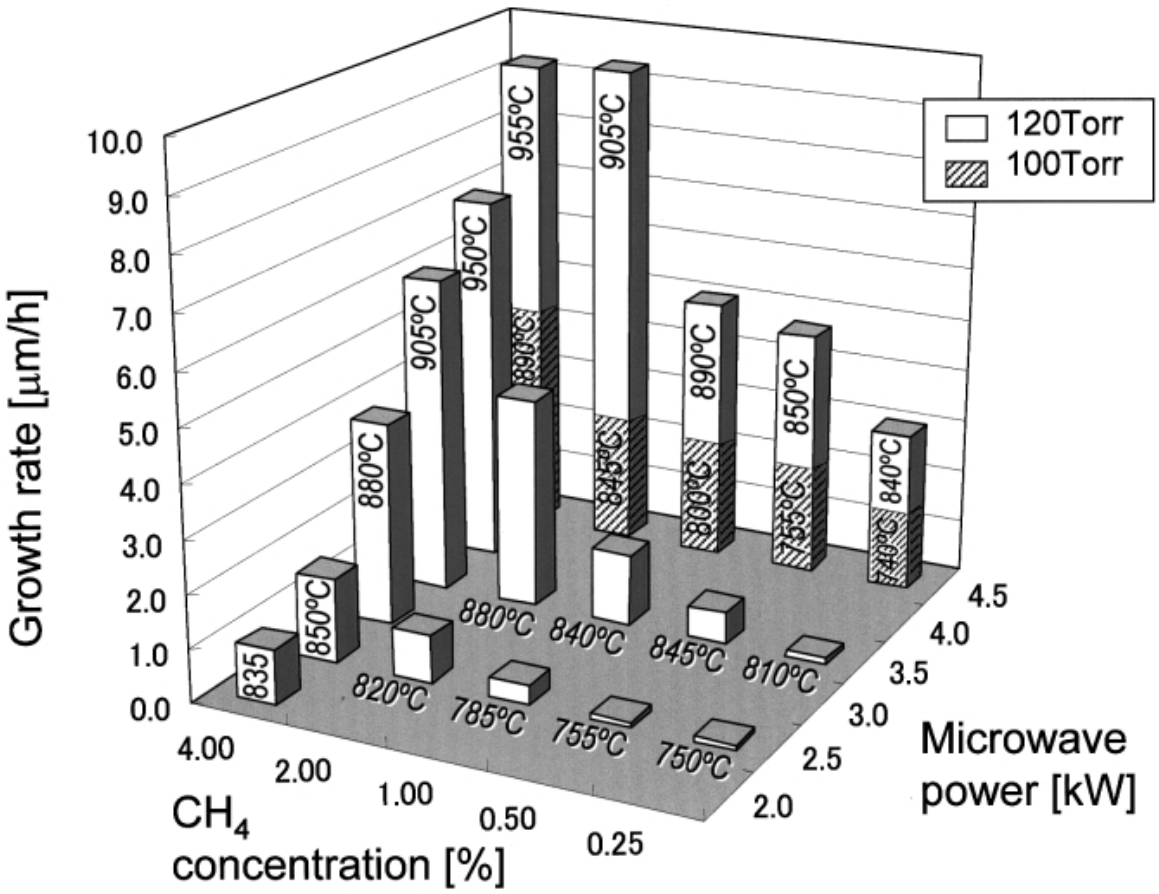

Figure 3.1 Growth rate as a function of CH_4 concentration, microwave power and gas pressure for SEKI AX5250 [42]

2) The quality of diamond films: the quality of diamond films is related to the methane concentration. The Raman spectra obtained from the diamond film with 2% CH_4 concentration and hence growth rate of 9.3 μm/hr indicate the existence of non-diamond contents in the film. On the other hand at 1% CH_4 concentration, the growth rate was 2.4 μm/hr and the diamond didn't have any non-diamond contents. This

diamond quality variation versus methane concentration is typically true for all MPACVD reactors.

3) The specific yield: Specific yield is a measure of the energy efficiency of the deposition process. So the higher the specific yield the more electrical energy kW-h is required to deposit a certain weight of diamond. In this case, the SEKI system uses 4.5 kW microwave power to deposit diamond at 9.3 μm/hr on a 1-inch wafer at 4% methane/hydrogen concentration. So at 120 Torr, 4% CH_4/H_2 concentration, 4.5 kW microwave power, and 955 ℃ subst rate temperature, the specific yield SY(kW-h/g) = P_a / (TGR*A*D) (See Section 3.4.2) for SEKI equals to 4.5kW / (9.3μm/h * 3.51g/cm^3 * π * (2.54/2 cm)^2 / 10^4) = 272.2 kW-h/g.

4) The microwave plasma power density measurement: The plasma can be approximated as disc-shaped, thus a cylinder is used to calculate the discharge plasma volume. For this SEKI 2.45 GHz diamond system, we have approximate plasma radius r=4 cm and h<B=one half wavelength=6.12 cm (Figure 2.19), then $V=\pi r^2 h= 307\ cm^3$. (r is the approximate plasma discharge radius and h is the approximate plasma discharge height) This yields power densities of 4.5 kW / 307 ≈ 14.7 W/cm^3.

3.5.1.3 Results for 915 MHz SEKI reactor system

For the deposition process of 915MHz system [44], first, the reactor was pumped down to less than 0.1 Torr. Subsequently, the process gas composed of methane and hydrogen of 0.5 - 5% was introduced. Carbon dioxide was also added in certain processes. The source gas was 1200 - 5000 sccm of H_2, 4 - 200 sccm of CH_4, and 0 - 100 sccm of CO_2. The pressure was adjusted to a range of 85 - 125 Torr by a pumping throttle valve. The plasma is ignited at 10 kW and incident power could be increased to 60 kW. Heating of the substrate holder was not necessary. The substrate temperature was controlled by balancing input heat originating from the input microwave power/discharge and the removable of heat by cooling stage. The cooling stage was cooled with a 90 kW chiller. The ASTeX 60 kW 915 MHz CVD system has been used under the following experimental conditions: (1) gas pressure: 60-200 Torr, (2) H_2: 2000 sccm, (3) CH_4: 20-100 sccm, and (4) growth rate: 2-10 μm/h [44].

1) The substrate temperature: the substrate temperature is the most important factor to control the characteristics of deposited diamond. Many factors such as microwave power, gas composition, gas pressure, substrate materials and substrate holder design will affect the substrate temperature. For this system, with microwave power and gas pressure of 45 kW and 80 Torr, the substrate temperature reaches 700°C or higher, which is the typical diamond deposition temperature.

The temperature variation from center to edge of a 150mm wafer is less than 35°C.

2) The surface morphology: the surface morphology is affected by the process conditions. The average crystal size is 20-30 μm for the sample grown with 0.8% CH_4 at 60 kW on a Si substrate. The macro-Raman spectra show a well-defined diamond peak at 1333 cm^{-1}. The α parameter [45] was calculated by comparing the facet shapes of an isolated diamond particle before and after the growth. At the region of lower T_S and higher CH_4 concentration C_m, the value of α is larger than 3. A decrease in C_m or increase in T_S leads to decrease of α. α~1 is obtained under the condition of (CH_4+CO_2) / (H_2+CH_4+CO_2) = 1 %, CO_2/CH_4 = 0.17 and T_S~1270 K. The α parameter was reduced by adding CO_2.

3) The film texture: Another two samples which were obtained with CH_4 concentration of ~0.5%, substrate temperature 1000 – 1040 °C and chamber pressure of 125 Torr, were grown on 25 mm diameter Si substrates. They are approximately 20 μm in thickness. The average crystal size is 0.5 - 1 μm. Difference of growth temperature was reflected to film crystal size.

4) The gas flow rate: the gas flow rates of hydrogen and methane were fixed at 2000 sccm and 100 sccm, respectively.

5) The specific yield: The 915 MHz SEKI system uses 60 kW microwave power to deposit diamond at 7 μm/hr on a 6-inch wafer (Substrate temperature is around 1050 °C) at 5% methane/hydrogen concentration 110 Torr (Table 3.1). So the specific yield for SEKI equals to 40kW / (3μm/h * 3.51g/cm^3 * π * (2.54*6/2 cm)^2 / 10^4) = 208.3 kW-h/g.

Gas pressure Torr	Microwave power kW	Substrate temperature °C	Growth rate μm/h	Raman width cm^{-1}
85	20	720	0.2	6.5
100-115	40	850-880	3	
125	60	1050	7	11

* The conversion efficiency from CH_4 to diamond exceeds 10% in the third case

Table 3.1 Growth rate for SEKI 915MHz reactor [56]

3.5.1.4 Estimation Of Absorbed Plasma Power Density

For SEKI 915MHz diamond system, we have an approximate plasma radius R=9cm and plasma height h<B=one half wavelength = 16.4 cm, then V = πr^{2}h = 4171 cm^3. The power densities vary from 45kW/4171 = 10.79 W/cm^3 to

60kW/4171 = 14.4 W/cm^3

3.5.2 MSU MPACVD reactor system

3.5.2.1 Results for 2.45 GHz MSU reactor system

The MSU 2.45GHz reactor [24], Reactor A, has the following ranges of reactor input variables.

1) Deposition pressure p=80-140 Torr,
2) Absorbed Microwave Power P_t=3-5kW
3) Methane Concentration c=1-8%
4) Substrate Temperature T_S=800-1250C
5) Total Flow Rate f_t=100-1400 sccm
6) Deposition Time t=4-200 Hours

The MSU reactor [24] has the following ranges of reactor output variables.

1) Linear Growth Rate 4-7 μm/h,
2) Total Growth Rate 27-50 mg/h,
3) Specific Yield: 69-300 kW-h/g
4) Carbon Conversion Efficiency 1-12%
5) Absorbed Microwave Power Density: 32-43 W/cm^3

3.5.2.2 Results for 915 MHz MSU reactor system

The MSU 915MHz reactor [37] has the following ranges of reactor input

variables.

1) Deposition pressure p=40-160 Torr,
2) Absorbed Microwave Power P_t=3-12kW
3) Methane Concentration c=1.7-7%
4) Total Flow Rate f_t=2000 sccm
5) Substrate Temperature T_s=700-1300C
6) Wafer Size 150mm

The MSU reactor [37] has the following ranges of reactor output variables.

1) Linear Growth Rate 320-390 nm/h
2) Thickness variation 4-15% (Percentage of the standard deviation from the average thickness across the wafers)
3) Absorbed Microwave Power Density: For MSU 915 MHz 10 kW diamond system, the plasma is hemisphere shape. We have approximate plasma radius R=7.5 cm, so the plasma volume V_p= (2/3)* πr^3 = 883 cm^3. The power density is 10kW/883 = 11.3 W/cm^3.
4) Specific Yield SY (kW-h/g) = P_a / TGR (See Section 3.4.2). For the MSU 915MHz reactor, the absorbed power is 6.7 kW. The growth rate is 460 nm/h. The wafer is 6-inch in diameter. So the SY is 6.7kW / (0.46µm/h * 3.51g/cm^3 * π * (2.54*6/2 cm)^2 / 10^4) = 227.6 kW-h/g [37].

It has also been reported the MSU 915MHz reactor worked at 125 Torr [57]. The absorbed power is 11.5 kW. The growth rate is 10-18 μm/hr. The approximate cylindrical-shape plasma in this case is diameter of 14 cm and 10 cm high. So the plasma volume $V = \pi r^2 h \approx 1500\ cm^3$. The absorbed power density is 7.7 W/cm^3 at 125 Torr. The specific yield with higher pressure operation in this case is 10-18 kW-h/g.

3.5.3 AIXTRON ellipsoidal reactor system

The AIXTRON ellipsoidal reactor was found to exhibit a variety of beneficial performance properties that are summarized below.

a) The plasma is very intense, spatially extended and in good contact with the substrate

b) The plasma position is very stable. It remains above the substrate irrespective of the gas pressure and the microwave power

c) The microwave-plasma coupling is excellent. No tuning is necessary to minimize the reflected power (however there are three tuning stubs in the external waveguide system for power matching)

d) The system allows the homogeneous deposition of diamond wafers with 2-3 inches in diameter (at 2.45GHz)

Typical process parameters are given in Table 3.2.

Parameter	Value	
Microwave frequency	2.45GHz	915MHz
Microwave power	3-6kW	20-60kW
Substrate size	1-3 inches	2-6 inches
Pressure range	50-200 mbar	
Methane concentration	0.5-5.0 vol. %	
Gas flow	100-500 sccm	1-5 slm
Growth rate	1-15 µm/h (depending on the process conditions with which the film quality was aimed)	
Thermal conductivity	>20 W/cm K at room temperature	

Table 3.2 Process parameters for Aixtron reactor

This ellipsoid CVD diamond deposition system is successfully used to manufacture thick CVD-diamond optical grade lenses [46]. A microwave power of 6 kW at a frequency of 2.45GHz works at temperatures between 700 and 900°C and pressures ranging from 75 to 150 Torr. The feed-gas is 1-2% methane in hydrogen. Reference samples of the lens material reached a thermal conductivity of 20.8 W/cm K, which is almost as high as the best values reported for natural type IIa diamond (20-25 W/cm K). Also the samples which have 0.06 cm^{-1} at 10.6 µm for an IR absorption coefficient are nearly as low as that of type IIa

diamond (0.03-0.05 cm^{-1})

Although much technical progress has been obtained with ellipsoidal plasma reactors, the ellipsoidal reactor geometry also has some drawbacks: the whole system is rather spacious and is expensive to build.

3.5.4 CYRANNUS (iplas) reactor system

It is not very clear how iplas reactor performs due to lack of the available diamond synthesis publications that use the iplas reactor system. Below is the Technical specifications [47]:

frequency: 2.45 GHz, 915MHz

power required: 1 - 30 KW

plasma shape: ellipsoid, sphere, disc-like

plasma diameter: approx. 70-400 mm

pressure range: 0 - 1000 mbar

3.5.5 LIMHP reactor system

The LIMHP commercially available reactor system BJS150 has a 6 kW microwave generator (switch mode power supply), a bell jar type reactor, and a 2-inch substrate holder. It shows the ability to produce discharges with high microwave power densities and to grow high quality CVD diamond at high growth rates. For polycrystalline diamond growth, the growth rate is up to 20 microns per hour and the uniformity is ±5% on 2-inch wafer. These results are similar to those

reported by Zuo et. al [58] who used a MSU reactor A. For single crystalline diamond growth, the FWHM of the diamond Raman line at 1332cm^{-1} is 1.6cm^{-1}, and there was no infrared absorption from 4000 – 10000cm^{-1} [48].

3.6 Summary

In this chapter, the commercially available MPACVD diamond synthesis reactors designs were compared. The detailed description of the comparison was presented in Section 3.3 and also is summarized in Tables 3.3-3.5.

	Manufacturer	Reactor Shape	Excitation Mode
MSU A,B	Lambda	7-inch cylinder	TM_{013}+TEM_{001}
SEKI 1st gen	AsTeX	7-inch cylinder	TM_{013}
SEKI 2nd gen	AsTeX	Clamshell	TM_{02n}
AIXTRON	AIXTRON	Ellipsoidal	TM_{036}
iplas	CYRANNUS	5-inch Cylinder	TM_{012}
LIMHP 1st /3rd	PLASSYS	9-inch cylinder	TM_{023}
LIMHP 2nd gen	PLASSYS	Cylinder with variable radii	TM_{022}

Table 3.3 Design Specifications Among Commercially Available Reactors 1

	Impedance matching	Substrate position	Scalability
MSU A,B	2-way Internal	adjustable	Yes, 915MHz
SEKI 1st gen	Not clear	Not clear	Not clear
SEKI 2nd gen	Triple screws	Fixed	Yes, 915MHz
AIXTRON	Triple stubs	Not clear	Yes, 915MHz
iplas	E-H tuner	Not clear	Yes, 915MHz
LIMHP 1st /3rd	Internal	adjustable	Yes, 915MHz
LIMHP 2nd gen	Internal	adjustable	Yes, 915MHz

Table 3.4 Design Specifications Among Commercially Available Reactors 2

	Plasma space	Power input	Microwave coupling
MSU A,B	Quartz dome	Top-load	Excitation probe
SEKI 1st gen	Quartz plate	Top-load	Excitation probe
SEKI 2nd gen	open	Bottom-load	Not clear
AIXTRON	Quartz dome	Top-load	Excitation probe
iplas	Quartz tube	Toroidal	Gap
LIMHP 1st /3rd	Quartz dome	Top-load	Octahedron probe
LIMHP 2nd gen	Quartz plate	Top-load	Octahedron probe

Table 3.5 Design Specifications Among Commercially Available Reactors 3

Moreover the output performance of these reactor designs has been compared in Table 3.6-3.7.

	CH_4 /H_2	Total flow rate sccm	Pressure range Torr	Incident power kW	Substrate Temperature C	Growth rate μm/h	Specific Yield kW-h/g	Power Density W/cm^3
SEKI 2.45 GHz	0.25-8%	400	100-120	2.0-4.5	830-955	2.4-9.3	<272	<14.7
MSU 2.45 GHz	1-8%	100-1400	80-140	3-5	800-1130	4-7	69-300	32-43
AIXTRON 2.45 GHz	0.5-5%	100-500	40-150	3-6		1-15		

Table 3.6 Comparison among 2.45GHz diamond deposition systems

	CH_4/H_2	Total flow rate sccm	Pressure range Torr	Incident power kW	Substrate Temperature C	Growth rate μm/h	Specific Yield kW-h/g	Power Density W/cm^3
SEKI 915MHz	0.5-5%	1200-5000	85-125	60	720-1050	0.2-7	<208	10.8-14.4
MSU 915MHz	1.7-7%	<2000	40-70	3-8	700-940	0.32-0.39	<228	<11.3
MSU 915MHz(2)	7%	<2000	125	11.5	800-1300	10-18	10-18	7.7
AIXTRON 915MHz	0.5-5%	1000-5000	40-150	20-60		1-15		
iplas 915MHz			1-atm	1-30				

Table 3.7 Comparison among 915MHz diamond deposition systems

Due to the lack of experimental data in the published literatures, the

comparison of the output performance of the different reactor designs cannot be easily made. The SEKI reactor, however, has the most experimental data available in the literatures and we at MSU also have considerable performance data on the MSU 2.45 GHz and 915 MHz reactor designs. Thus a comparison is made between the SEKI Reactor and the MSU Reactor and also the performance is made between the 2.45 GHz reactors and the 915 MHz reactors.

First a comparison between the SEKI 2.45 GHz and the 915 MHz reactors is presented. Their performance was already calculated under similar conditions (at about 120 Torr) in Section 3.5.1. Using the data already calculated in Section 3.5.1.2-3.5.1.3 the comparison under similar operating conditions is presented below.

1) The growth rate for the SEKI 2.45 GHz reactor is 9.3 μm/h. The growth rate for the SEKI 915 MHz reactor is 7 μm/h.
2) The power density for the SEKI 2.45 GHz reactor is 14.7 W/cm^3.

   The power density for the SEKI 915 MHz reactor is 10.8-14.4 W/cm^3.
3) The specific yield for the SEKI 2.45 GHz reactor is 272 kW-h/g.

   The specific yield for the SEKI 915 MHz reactor is 208 kW-h/g.

Thus one can say that when the SEKI reactor technology is scaled with 915 MHz excitation up to larger areas the growth rate decreases slightly, the power density also decreases slightly and the specific yield decreases (i.e. the electrical energy efficiency improves) about 10%.

Under similar 110-140 Torr condition the MSU reactor has the following figures of merit:

1) The growth rate for the MSU 2.45 GHz reactor is 5-7 μm/h [24]. The growth rate for the MSU 915 MHz reactor is about 10 μm/h [57].
2) The power density for the MSU 2.45 GHz reactor is 32-43 W/cm^3. The power density for the MSU 915 MHz reactor is 7.7 W/cm^3.
3) The specific yield for the MSU 2.45 GHz reactor is 70 kW-h/g. The specific yield for the MSU 915 MHz reactor is 20 kW-h/g.

The growth rate improves slightly as the MSU reactor is scaled up. In scaling up the MSU reactor design, the absorbed power density decreases by four while the growth rate only increases slightly. The specific yield is reduced significantly from 70 kW-h/g to 18 kW-h/g. This reduction in specific yield is due to the increased deposition area and low absorbed power densities of the 915 MHz MSU reactor design.

One can compare the SEKI reactor with the MSU reactor. The growth rates for the MSU and Seki reactors are similar for both 2.45 GHz and 915 MHz systems. The absorbed power density for SEKI reactor is smaller at 2.45 GHz but greater at 915 MHz than MSU reactor. This difference may be caused by the discharge size estimate that we made for the SEKI design, i.e. we may have over or under estimated the plasma size thereby reducing or increasing the absorbed power densities for the SEKI reactors. It is important to note here that while we

can calculate the plasma volume in the MSU reactor directly from our MSU laboratory experiments, in this study we must estimate the plasma volume in the SEKI MPACVD machines by using the sparse experimental data available in the literature.

The specific yield for the MSU reactors are considerably lower than the specific yield for SEKI reactors. This is true for both the 2.45 GHz and the 915 MHz MSU reactors designs. For example, for 2.45 GHz, specific yield for the MSU design is 70 kW-h/g and specific yield for the SEKI design is 272 kW-h/g. Thus the MSU reactor is about 4 times more electrically efficient. For 915 MHz, specific yield for the MSU design is about 20 kW-h/g and specific yield for the SEKI design is 208 kW-h/g. Thus the MSU 915 MHz reactor is about 10 times more electrically efficient than the 915 MHz design.

Why is this true? We do not know for sure but two possible reasons are as follows:

1) The MSU reactor has a more efficient impedance matching system (internal for MSU designs versus external matching for SEKI designs)
2) The MSU MPACVD reactors utilize diamond synthesis processes that create a discharge that is focused on the substrate and also the system is operated in such a way that the discharge is created away from and is not in contact with the reactor walls. All synthesis data that is reported in the literature for the MSU reactors uses synthesis processes that operate within a process road map (see

[12] Page 218). When operating within this road map reactor wall heating is low and controlled. This would be true for reactor designs that employ quartz walls or metal walls. Establishing an appropriate road map is useful for all reactors because once the plasma discharge touches the reactor walls wall losses then increase. If additional power is added to the process when the discharge is touching the walls then the plasma density at the wall surfaces increases and the walls losses further increase, and then the discharge position is no longer optimized for efficient operation. It appears that the SEKI reactor is operated in this manner. For example the SEKI reactor is reported to use of 45 – 60 kW for their 915 MHz design under similar experimental conditions the MSU reactor only requires 10 – 15 kW. It appears that the SEKI reactor is operated outside a safe and efficient process road map. Therefore it is not surprising that the reactor wall losses (both thermal losses and radical losses) are smaller in the MSU reactor design than for the SEKI design.

CHAPTER 4

THE NEW GENERATION MSU MICROWAVE PLASMA ASSISTED CVD REACTOR DESIGN

4.1 Introduction

In this chapter the design and development of a new generation MSU microwave plasma-assisted CVD reactor is presented. This investigation begins with a review of early reactor designs. Then a generic but versatile microwave reactor design concept (See Figure 1.1) is outlined. It has a variety of dimensions that can be modified, “reshaped” and adjusted to allow process optimization for different diamond synthesis applications. Here as part of this thesis research different reactor design variations are investigated first by starting with the generic, benchmark reactor design and then modifying it, i.e. by varying the dimensions, via intuition from past reactor design experiences and via numerical

electromagnetic cavity applicator modeling to produce a new reactor design. These “new” numerical reactor models will calculate the electromagnetic field patterns versus reactor shape and size within the reactor. Then building upon the performance of earlier MSU reactor designs. The proposed new generation reactor design is realized by modifying existing reactors; i.e. by varying the size and shape of the applicator and plasma reactor volume within existing MSU reactors. An important consideration during the new reactor design process was to position the intense microwave discharge that is observed at high pressures away from the reactor walls. Thus MSU reactor designs with larger applicator diameters and with larger quartz dome diameters were considered design possibilities. Finally a “good” next generation reactor design was selected and then it was constructed and experimentally evaluated.

4.2 Microwave Cavity Plasma Reactor Design

Before we describe the design process for the new MSU fourth generation reactor (Reactor C), a number of design principles are introduced in this section. These design principles have evolved at MSU over the past 30 years as the know-how and knowledge of how to efficiently produce and control microwave discharges were discovered. The history of how this knowledge and know-how were developed has been described in over 30 PhD theses that have been awarded at MSU. These design principles are listed below.

1) **Single mode excitation**: Single mode excitation is employed so that the microwave energy can be controlled and focused. Thus the microwave discharge

can be created and maintained above and in good contact with the substrate. For the MPACVD diamond synthesis application, the mode is expected to be a phi-symmetric TM_0 mode in order to produce a phi symmetric microwave discharge.

2) **Internal cavity impedance matching**: This feature includes a moveable (variable) sliding short and an adjustable coupling probe. This allows efficient microwave power coupling into the variable microwave discharge load. That is as the input variables such as pressure, power, gas mixture, and gas flow rate are varied, the reactor is detuned and thus the impedance match into the reactor is lost. Thus as the experimental variables change the variable sliding short and adjustable probe allow the reactor to be readily retuned to a good impedance match while still maintaining the same single mode excitation. This method of impedance matching is always superior to external impedance matching since it avoids the high standing wave fields that exist in the waveguides that are external to the reactor. If internal matching is employed then the applicator and the overall microwave delivery system avoids the EM losses in the external waveguides. Under some circumstances these losses can be a significant fraction of the incident power.

3) **Variable substrate position**: The substrate holder is located on a movable stage that is an integral part of the microwave applicator. The ability to adjust the position of the stage allows additional adjustment and local fine tuning/focusing of the electromagnetic fields around and directly above the substrate. This is especially important at the higher pressures as the discharge

absorbed power density increases and when the discharge constricts and becomes buoyant.

4) **Four tuning variables L_p, L_s, L_1, and L_2**: These variables enable the nonlinear optimization of discharge positioning, discharge size adjustment, growth rate enhancement, impedance matching, i.e. process optimization --- thereby allowing for robust and efficient processes development and an adaptable and versatile over all system operation.

5) **Scalability of the reactor design**: Although the new Reactor C will be excited at 2.45 GHz microwave energy, the scalability of the reactor must be considered during the design process. That is the reactor design should be scalable by a factor of 2.7 as the excitation frequency is varied from 2.45 GHz to 915 MHz. All practical reactor designs should be electromagnetically scalable. Thus as for all our final designs if the excitation frequency is reduced from 2.45 GHz to 915 MHz, the reactor geometry should be able to be increased by the factor of 2.7. The scalability of the plasma discharge itself has been described in section 2.3.6.1. [55]

4.3 The Generalized Microwave Reactor Design Concept

A generalized MSU reactor design is introduced in this section. This design concept has been already described in a US patent application by J. Asmussen and Y. Gu [59]. All the previous generations of MSU microwave

plasma reactor designs can be thought of as special cases of this generalized design. The concept was first envisioned over fifteen years ago and, over many years, specific cases have been developed and thus enable specific reactor designs to be applied to many different microwave excited applications.

In its most generalized form the microwave reactor is formed by many separate cylindrical coaxial and cylindrical waveguide sections each of which has a different radii and variable lengths. An example of the generalized reactor design is shown below in Figure 4.1. It consists of an input section and sections 1-5. The purpose of each section 1-5 is (a) to guide and transmit microwave energy to the discharge load, (b) to impedance match the microwave power into the discharge, and (c) to appropriately spatially focus or refocus the microwave energy as it is transmitted through each individual waveguide section. By adjusting the position of the substrate, $Z_S = L_1 - L_2$, in sections 4 and 5 above and below the Z=0 plane, the electromagnetic (EM) field in the vicinity of the substrate can be varied (although in the vicinity of the substrate the electric field is primarily in the axial direction, both the E_Z and the E_r electric field components around the substrate vary as Z_S is varied) to achieve the desired CVD process growth rate and growth uniformity, The choice of the specific configuration, i.e. the number of and the specific lengths of each of the cylindrical waveguide sections that one employs in a particular design, depends upon on the requirements of the particular application. As is indicated in Figure 4.1, the waveguide section 3 can be further divided into multiple sections, 3(a), 3(b), etc.,

each with a different length L3a, L3b, etc. and radius, R3a, R3b, etc.

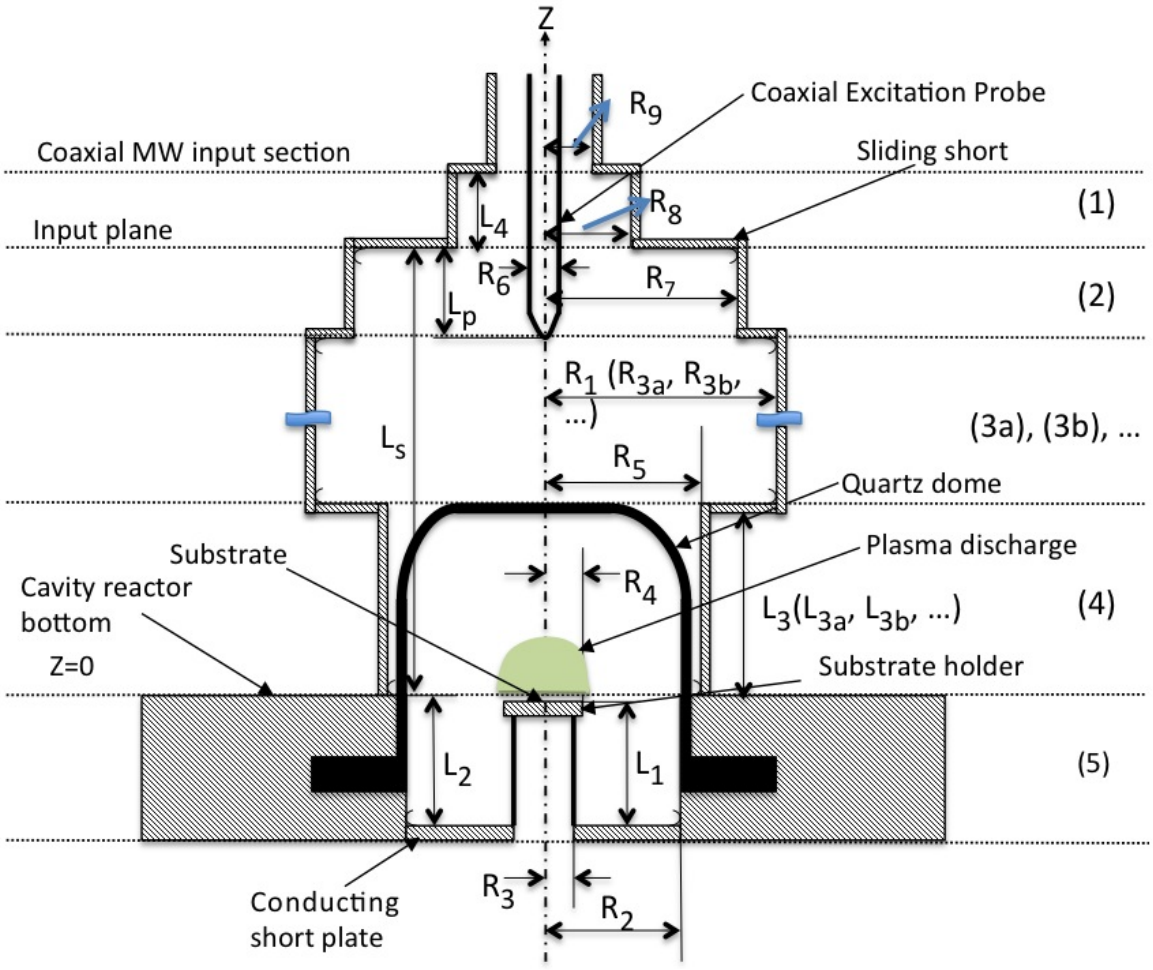

Figure 4.1 The cross section of the generalized reactor design

A cross section of a specific, simpler embodiment of the more generalized reactor design is shown in Figure 4.2. This reactor design is very close to the final design described later in this chapter. Thus it is used here to further describe a specific example reactor design and to explain a specific reactor operation in greater detail.

As indicated in earlier MCPR descriptions the cavity is phi-symmetric about a center Z-axis, and the Z=0 plane is identified as the bottom of the reactor

and the top of the substrate holder is located in the vicinity of the Z=0 plane. The substrate position is given by $Z_S = L_1 - L_2$. The reactor shown in Figure 4.2, is divided into five interconnected but distinct cylindrical waveguide sections.

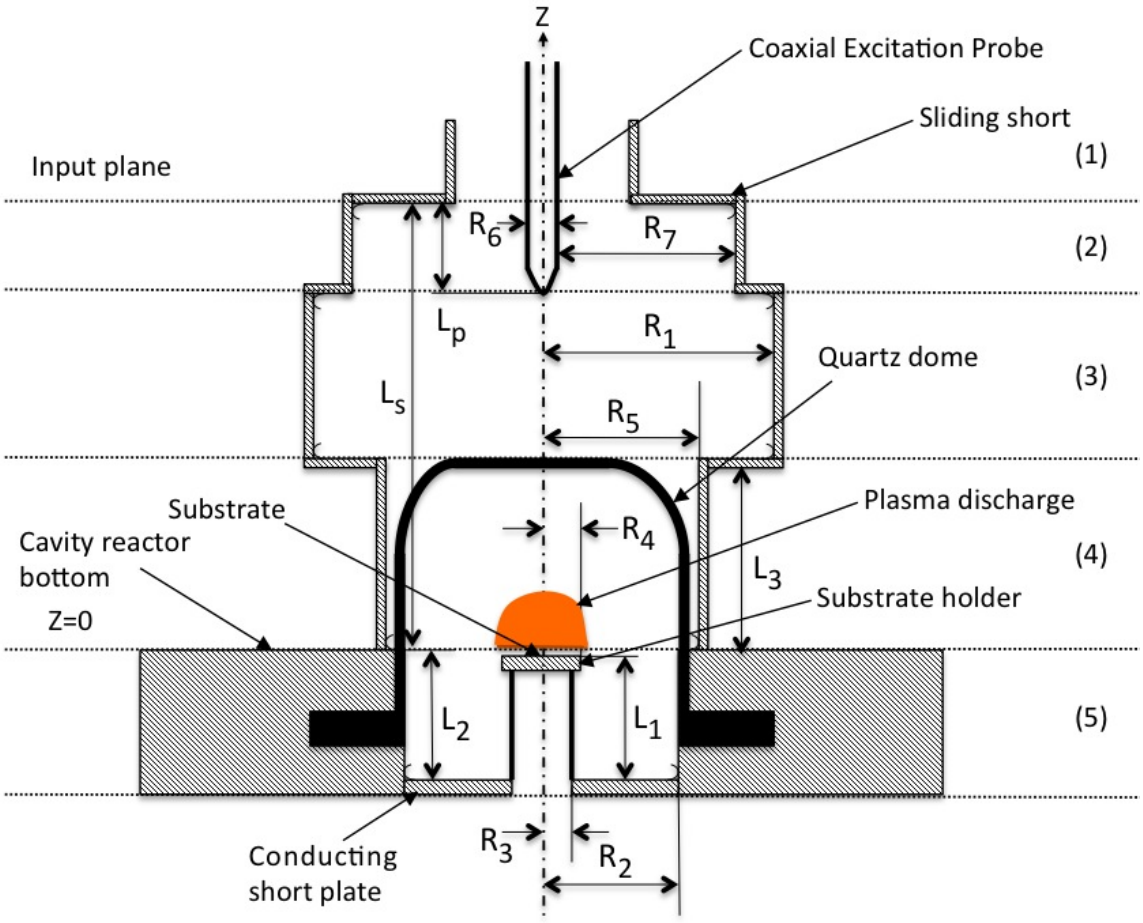

Figure 4.2 The cross section of a specific embodiment of the MSU reactor design

From the top to the bottom we identify these sections as:

section 1: which is the coaxial input microwave feed;

section 2: which is a length adjustable coaxial waveguide impedance

matching section of length L_p and radii R_6 and R_7

section 3: which is a cylindrical waveguide section of length L_S-L_3-L_p and of radius R_1;

section 4: which is an additional cylindrical waveguide section of radius R_5, and length L_3;

section 5: which is a variable length, coaxial cavity section with radii R_2 and R_3 and variable length L_2. The length L_1 of the cylindrical center conductor of section 5 can be also independently variable. The substrate is placed on the top of the center conductor of section 5 near the Z=0 plane. Thus the position of the substrate is independently variable and is defined by $Z_S = L_1 – L_2$. The center conductor of section 5 also serves as the substrate holder and can be independently externally heated or cooled.

As shown in Figure 4.2, section 1 is the coaxial waveguide input power port. Section 2, the second cylindrical coaxial waveguide section, behaves as an internal cavity impedance matching section where in practice L_p is often adjusted to be close to a quarter TEM wavelength. In practice the radial dimensions of this section, i.e. R_6 and R_7, can be chosen to allow the propagation of a single TEM mode or the propagation of both the coaxial TEM and TM_{01} modes. Section 3 also acts like an internal cavity impedance matching section and for the case shown by Figure 4.2, the radius, R_1 is larger than the radii of sections 1 and 2.

This causes an EM field intensity redistribution over the waveguide cross section of section 3 and for a given high input power operation produces a lower standing wave electromagnetic (EM) field intensity and allows a lower EM power flux density (W/cm^2) to be transmitted through the cross section area of the empty waveguide region of section 3 than the power flux density being transmitted through the cross section areas of sections 1 and 2; i.e. section 3 unfocuses the microwave power as it is transmitted through the reactor preventing at high input powers discharge formation in section 3.

Section 4 also acts like an additional internal cavity impedance matching section similar to section 3. However the EM field is refocused (onto the center and along axis of the applicator) due to the reduced radial dimension of the cavity. Since it is desired to create an intense EM field region above the substrate around the Z=0 plane and then maintain a microwave discharge in this region at the center axis of the reactor, the EM fields in section 4 are refocused onto the substrate holder location around the Z=0 plane. This is accomplished by reducing the radius from R_1 in section 3 to R_5 in section 4 and then the appropriate, additional coaxial waveguide, section 5, is added to the bottom of the applicator. This creates a strong electric field along the Z-axis at the surface of the substrate.

Section 5, $-L_2<Z<0$, behaves as a coaxial waveguide section with TEM mode excitation. When excited with 2.45 GHz microwave energy only the TEM waveguide mode is excited in this section. By adjusting the coaxial cavity lengths L_1 and L_2 to about a half TEM wavelength, i.e. 6.12 cm using 2.45 GHz

excitation, a standing wave TEM_{001} mode EM field is excited in this section and a perpendicular electric field is produced on the surface of the substrate. The substrate position is further adjusted by slightly varying the substrate position Z_s above and below the Z=0 plane.

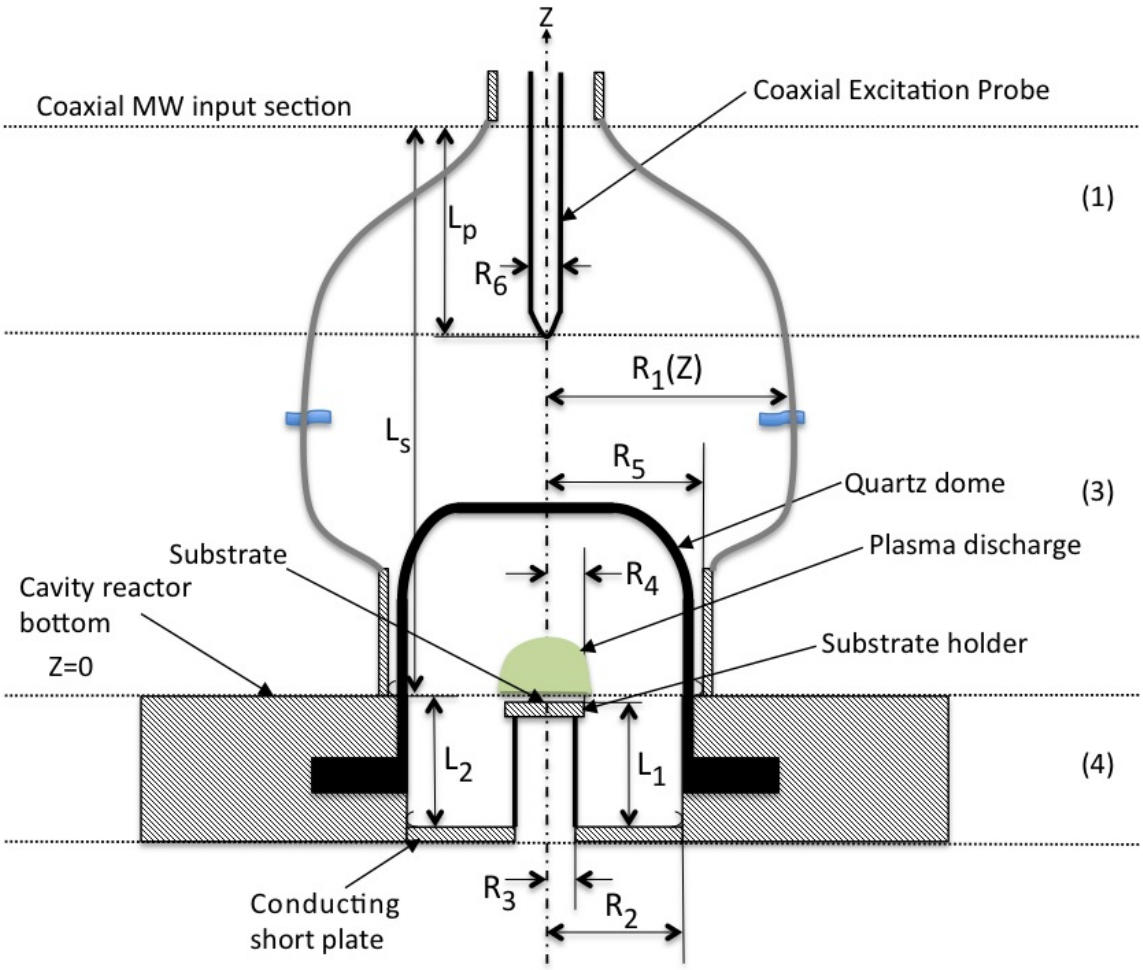

Figure 4.3 Cross section of a continuously variable generalized reactor

Another example of the generalized reactor is shown in Figure 4.3. Here the individual sections that are shown in Figure 4.1 with a different radii and length are replaced by a continuously varying applicator radius R(z). As one

moves from the top of the applicator down toward the Z=0 plane, R(z) first increases and then as the substrate location is approached the radius decreases. Thus the discrete cylindrical sections shown in Figure 4.1 are replaced with a gradual and continuous variation of R(z). The exact variation of R(z) versus z depends on the desired EM unfocusing and refocusing that is required by specific plasma processing applications. If the radial variation is ellipsoidal, then this generalized reactor R(z) becomes similar to the AIXTRON ellipsoidal reactor. However it differs by the additional TEM excited section 4.

4.4 Early MSU MPACVD Reactor Designs

The first MSU MPACVD reactor was designed in the 1986 – 1987 by Jes Asmussen. It was one of the first reactor concepts in the world that moved the reactor technology beyond the simple tubular microwave plasma-assisted CVD reactor technology that was initially used by Kamo et. al. [60] to demonstrate MPACVD diamond growth. The cross section of the reactor is shown in Figure 4.4. It can be viewed as a simple, special case of the generalized reactor described in Section 4.3, but has the variable coaxial coupling probe input at the side of the applicator. The reactor has cylindrical brass walls (1) that form the outer conducting shell of the cavity applicator. The diameter of the first reactor was 7 inches (17.8 cm). The sliding short (2) is electrically connected to the cavity walls (1) via finger stock (3). The sliding short (2) is water-cooled (41) and forms the top end of the cavity. It can be moved up and down along the longitudinal axis of the cylindrical cavity walls (1) to change the electrical and

physical height of the cavity applicator. The bottom end of the cavity (4) is formed by the water-cooled (10) base plate (40) and substrate holder (13). Microwave power is coupled into the cavity through an adjustable coaxial power input port which is comprised of the variable length power coupling probe (17) and the outer conductor (18). Either the TM_{011} or the TM_{012} mode could be excited.

Input gases flow into the discharge area (6) via the gas input channel (7) inside the base plate. The quartz dome (5) confines the working gas to the lower section of the cavity where the microwave fields produce a plasma discharge adjacent to the substrate (14). A metal screen (9) is used to prevent the microwave energy from radiating out of the bottom of the applicator, but still allows the input gases to flow downstream into the vacuum pump system. A quartz tube (12) is placed under the substrate holder. It sits on a graphite base (11), which in turn sits on the metal screen (9). Once the plasma (6) is ignited, it can be viewed through the top screened window (15).

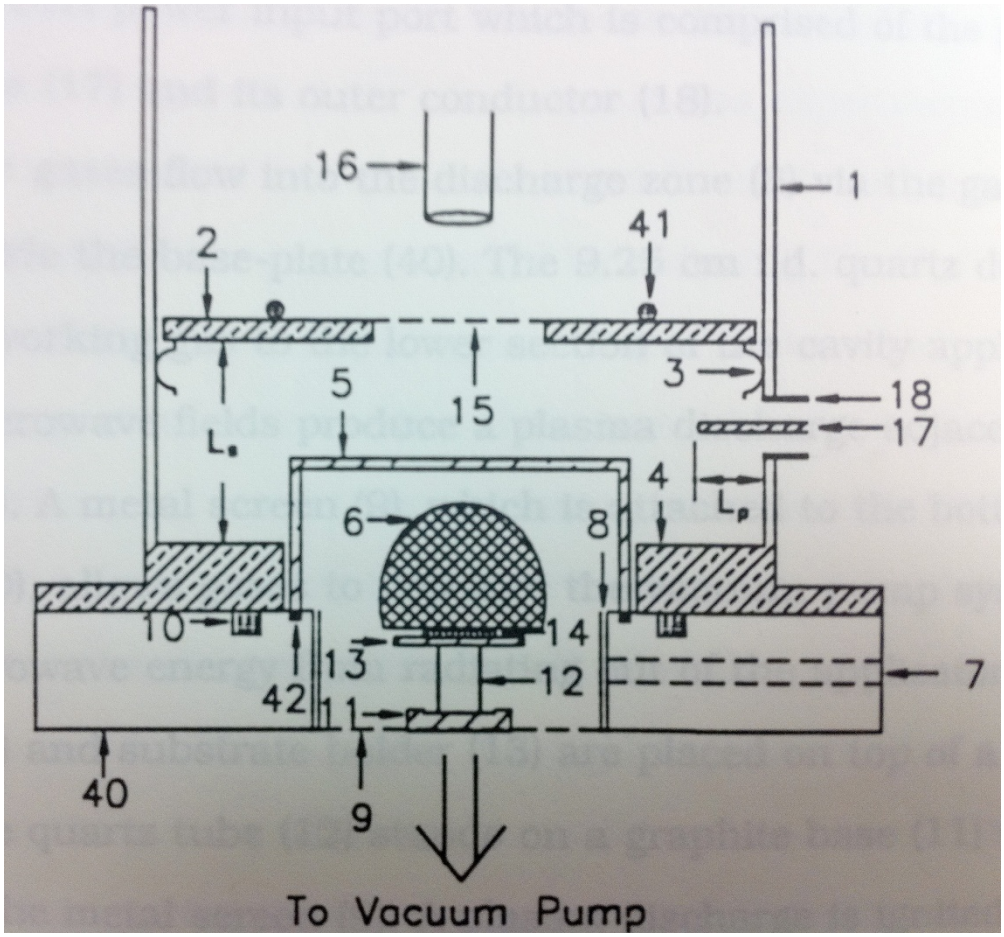

Figure 4.4 Schematic Drawing of the first generation MSU reactor [52]

The second generation MSU MPACVD reactor, described in this thesis as Reactor A, is shown in Figure 4.5. One of the important differences between the second generation and first generation reactor is that the input power coupling probe is located at the top end of the cavity, instead of on the side of the cavity. This is a very important change because now the system is entirely phi-symmetric and the microwave power can be more uniformly distributed into the plasma. Similar to the first design the sliding short and coupling probe adjustments, L_s and L_p, provide the internal cavity impedance tuning mechanism to minimize the reflected power. The other difference is that the Reactor A cavity

applicator was designed to be longer (i.e. L_S can be larger) than the first generation applicator design so that either TM_{012} or TM_{013} mode can be excited. One additional cooling air inlet was added (not shown in Figure 4.5) for external air input to cool the cavity and quartz dome. The original viewing window existing in the first generation reactor served both as the exhaust port for the cooling air and as a viewing port which allowed measurement of the substrate temperature by an optical pyrometer.

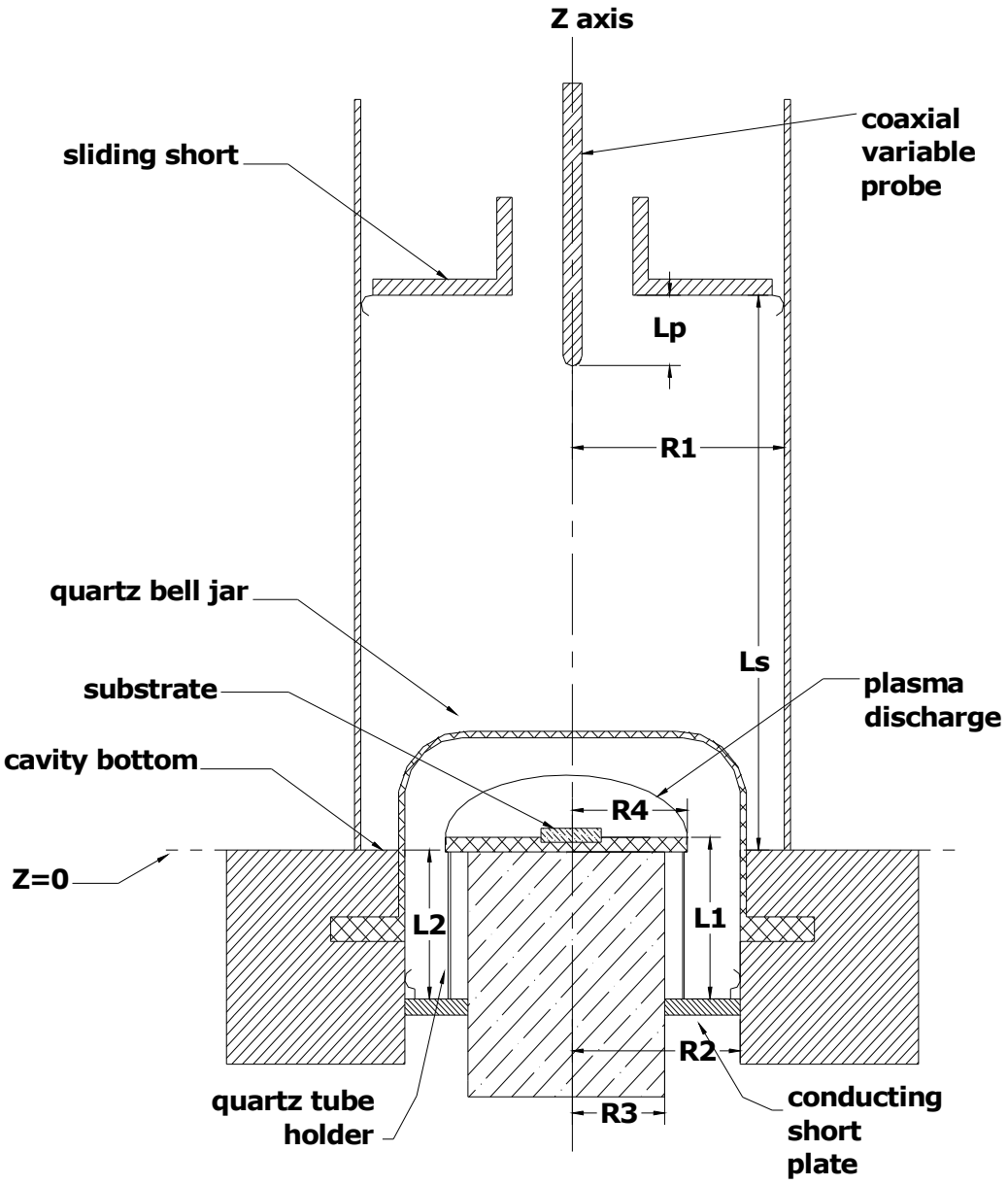

Figure 4.5 Cross sectional schematic drawing of the Reactor A [24]

The cross section of the third generation reactor [53] Reactor B is displayed in Figure 4.6. The purpose of this modification is to allow microwave plasma assisted CVD operation at higher discharge power densities (>400 W/cm^3) and higher pressures (150 – 260 Torr). This was done by reducing the

substrate holder radius R_4 from 5.08 cm to 3.24 cm and the coaxial cavity inner conductor (cooling stage) radius R_3 from 4.13 cm to 1.91 cm. The microwave cavity applicator is still a single mode applicator but excites a single hybrid mode. The hybrid excitation mode is a combination of TM_{013} in the cylindrical region Z > 0 and the TEM_{001} for the coaxial region Z < 0. After adjusting L_s and L_1 to excite the TEM_{001} modes, a high electric field is excited in the vicinity of the z=0 plane at the transition region between the cylindrical and coaxial section. When L_1 and L_2 are adjusted to be around 6.12 cm, the electric field is normal to the top of the "substrate" surface, which is positioned on the center conductor electrode. For a given applicator input power as the electrode diameter is reduced, the intensity of the normal electric field on the substrate surface increases. In the presence of a microwave discharge, this results in a high absorbed power density discharge above and in good contact with the substrate. The performance of this reactor is described in Kadek Hemawan's PhD thesis [53] and in a recent paper [38]. Both Reactors A and B are now commercially available by Lambda Technologies (See Figure 2.10).

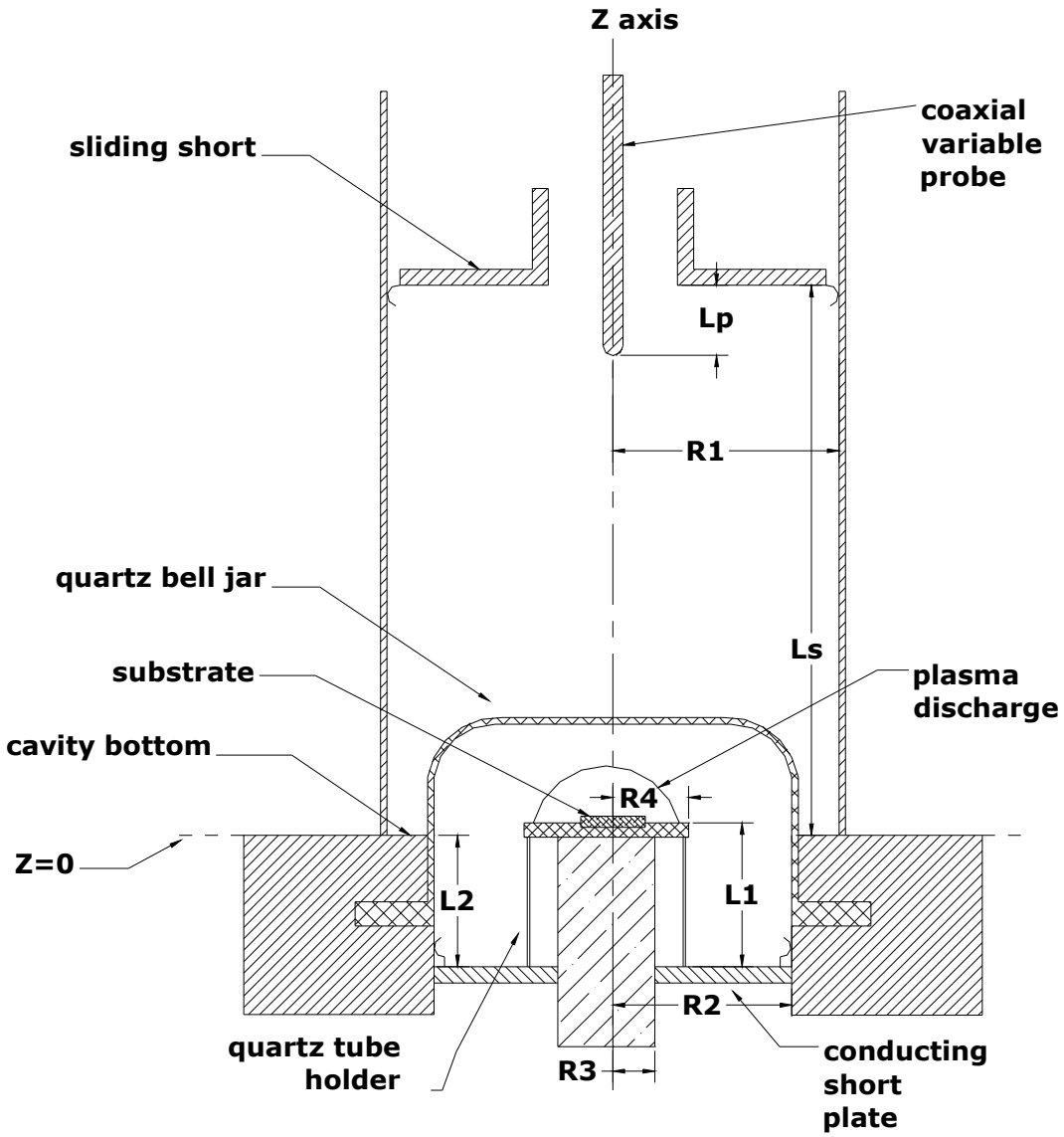

Figure 4.6 Cross Sectional schematic drawing of the Reactor B [53]

4.5 Reactor C: Initial Design Objectives

As described in reference [38] and [53], the Reactor B design performed well. The only difference between Reactor A and Reactor B was the reduction in

center conductor area of Reactor B by a factor of 4 over Reactor A, i.e. the radii R_3 ad R_4 of Reactor A were reduced from 4.13 cm and 5.08 cm respectively to 1.91 cm and 3.24 cm in Reactor B. This allowed an increase in the operating pressure to 240 Torr and at a constant pressure it increases the absorbed microwave power density by a factor of 4-5 over Reactor A (see the microwave power density measurements presented in Section 5.5). In order to further extend the MSU reactors' ability to operate at higher pressure and have a robust and efficient reactor operation over a 240 – 320 Torr pressure regime, the Reactor C design was carried out.

As shown in Figure 4.7, when the pressure increases the discharge shrinks and constricts and becomes more intense. At pressures of 100 Torr or more, microwave discharges in hydrogen and methane gas mixtures separate from the reactor walls. They become freely floating and assume shapes that are related to the shape of the impressed electromagnetic (EM) fields. At very high pressures microwave discharges become very non-uniform, intense and "arc like". They may even move about the discharge chamber as they react both to buoyant forces and to convective forces caused by the gas flows around and within the discharge. These discharges have high densities of radical species, i.e. H and CH_3 radicals, which enable increased diamond growth rates at high pressures [19].

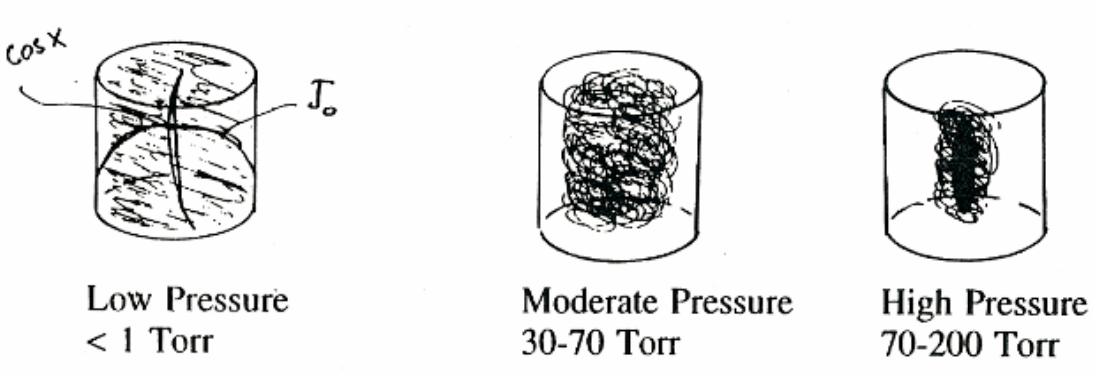

Figure 4.7 Microwave Discharge Behavior vs. Pressure

There are a number of important issues associated with utilizing high pressure MPACVD discharges for diamond synthesis. First, because of the discharge's high gas temperatures, the substrate must be appropriately cooled to the desired deposition temperature. The reactor walls, in contrast to the substrate, must be protected from the intense high temperatures of the discharge and from the active discharge species. As a result it is desirable that the hot discharge be separated from and placed out of direct contact from the reactor walls.

Thus the final Reactor C design incorporated a number of changes/improvements over the earlier MCPR designs that allow robust and efficient operation at higher pressures, at high power densities and over longer diamond synthesis process times. The experimental evaluation of Reactor B that was reported in reference [38] revealed that when the operating pressure was increased from 160 Torr to 240 Torr, the microwave discharge power density greatly increased to 300-450 W/cm^3. As pressure was increased from 160 Torr to over 200 Torr, the gas temperature increased and the quartz walls and the cavity

walls were heated. Thus it was desirable to locate the quartz walls and the cavity walls further away from the intense microwave discharge zone.

Thus in the Reactor C design the reactor diameter is increased from 7 inches (17.78cm) of Reactor A and B to 12 inches (30.48cm). The quartz dome diameter was increased from 5.125 inches (13.02cm) of Reactor A and B to 8.5 inches (21.59cm). Thus in our new Reactor C design both the metal and dome walls are pulled away from the discharge zone, which thereby reduces plasma and radical species wall interactions as well as reduced the conductive and convective discharge heat flux losses (per area) to the walls.

4.6 Reactor C: Design Realization Process

This section describes the design realization process that was employed for the new and specific Microwave Plasma Assisted (MPACVD) Reactor C design.

4.6.1 Initial Design Calculations

As the first step in the reactor design process we employ simple, straight forward, classical, cylindrical cavity electromagnetic theory to calculate the cavity size, i.e. the radii and lengths for 2.45 GHz excitation. This design approach was used in earlier reactor designs and as a first approximation assumes that the cavity reactor is an empty cylindrical structure with perfectly conducting walls. Even though the empty cylinder is a major over simplification of the actual cavity reactor, i.e. neglecting the coaxial wave guide and input coupling probe, the

substrate holder and even the plasma itself, it has in the past yielded excellent overall, final dimensions for the reactor.

The electromagnetic field theory of this microwave plasma reactor begins with Maxwell's equations, from which we can develop second-order differential equations with wave solutions [61]. Solutions of the wave equations can be found in the form of vector potentials. Assumptions have been made to calculate the eigenfrequencies (or natural frequencies). The resonant reactor is assumed to have perfectly conducting walls filled with a homogeneous, lossless, source-free medium (air). Free space material constants μ_0, ε_0 are used in this case. For such a reactor, it can be shown that the electric and magnetic field components and the resonant frequency for the TM_{npq} and TE_{npq} resonant mode are given by

$$E_r = j\frac{B_{npq}}{\omega\mu\varepsilon}\frac{\chi_{np}}{R_1}\frac{\pi}{L_s}J_0'(\chi_{np}r/R_1)\sin(\pi z/L_s) \quad (1)$$

$$E_\phi = 0 \quad (2)$$

$$E_z = j\frac{B_{npq}}{\omega\mu\varepsilon}\left(\frac{\chi_{np}}{R_1}\right)^2 J_0(\chi_{np}r/R_1)\cos(\pi z/L_s) \quad (3)$$

$$H_r = 0 \quad (4)$$

$$H_\phi = -\frac{B_{npq}}{\mu}\frac{\chi_{np}}{R_1}J_0'(\chi_{np}r/R_1)\cos(\pi z/L_s) \quad (5)$$

$$H_z = 0 \quad (6)$$

$$(f_{res})_{npq}^{TM} = \frac{1}{2\pi R_1\sqrt{\mu_0\varepsilon_0}}\sqrt{X_{np}^2 + \left(\frac{q\pi R_1}{L_s}\right)^2} \quad (7)$$

$$(f_{res})_{npq}^{TE} = \frac{1}{2\pi R_1\sqrt{\mu_0\varepsilon_0}}\sqrt{(X'_{np})^2 + \left(\frac{q\pi R_1}{L_s}\right)^2} \qquad (8)$$

where n = 0,1,2,..., p = 1,2,3,…, q = 0,1,2,… for TM modes and n = 0,1,2,…, p = 1,2,3,…, q = 1,2,3,… for TE modes. $\chi_{np} = \text{zeros of } J_n(X) \text{and } X'_{np} = \text{zeros of } J'_n(X)$.

Figure 4.8 and 4.9 show the resonance frequency versus L_S; i.e. equation (7) and (8) are plotted for two different cavity diameters. The 7-inch (17.8cm) in diameter is for 2.45 GHz Reactor A and B, and the 12-inch (30.5cm) is for the proposed Reactor C. The line at 2.45 GHz shows our reactor is excited at 2.45 GHz. So if our reactor is excited with 2.45 GHz the TM_{013} mode can be excited if the cavity length, L_S, is adjusted to 21.6 cm. As shown in Figure 4.9 if the cavity diameter is increased to 30.5 cm then the reactor can be excited with the TM_{013} mode when the length, L_S, is adjusted to 19.3 cm.

This simplified theory provides the designer an approximate idea of the cavity dimensions. That is given a cavity reactor of a certain diameter it allows one to approximate the length of the cavity for TM_{013} mode excitation.

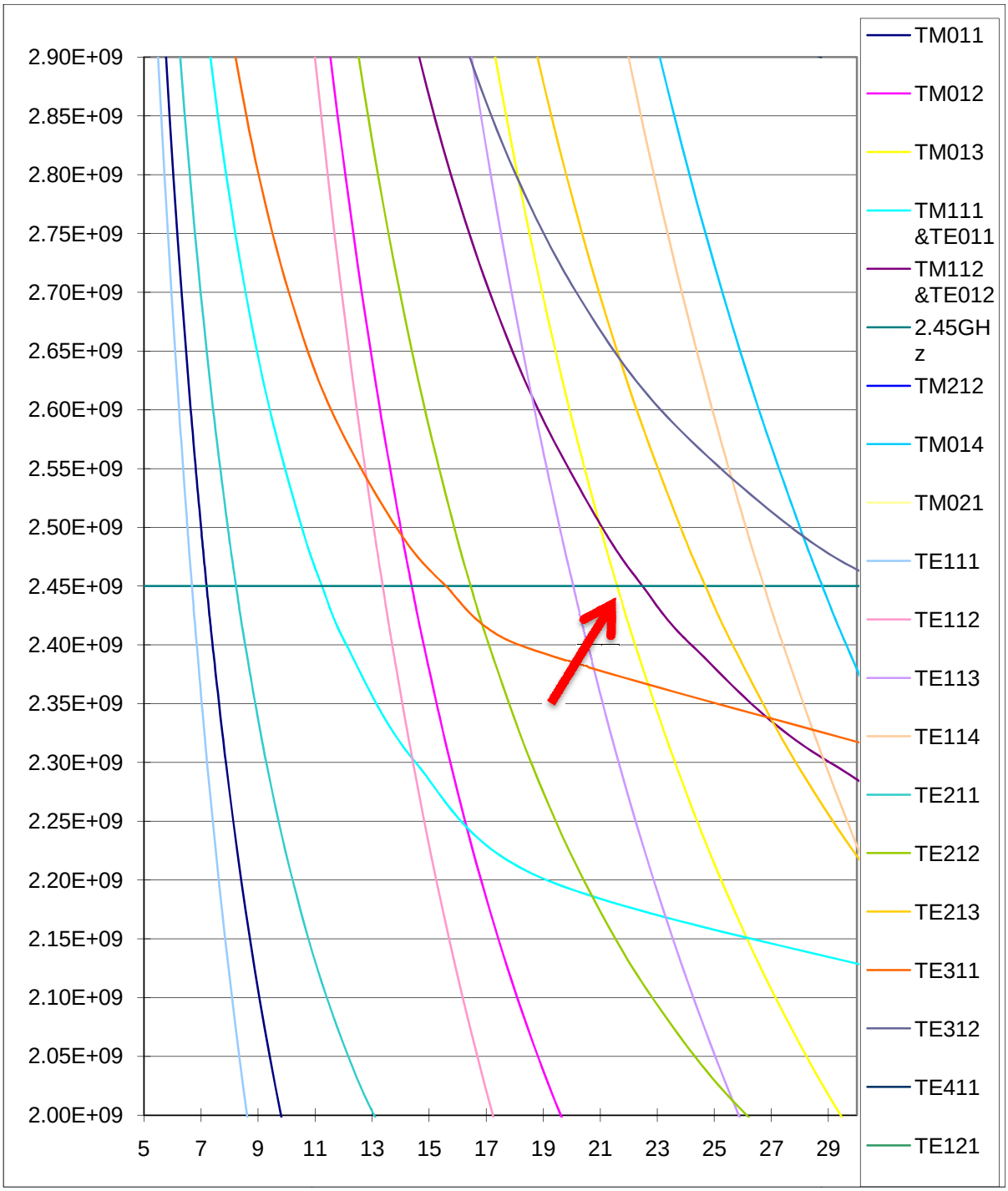

Figure 4.8 Resonant frequencies versus L_S for 7-inch cavity

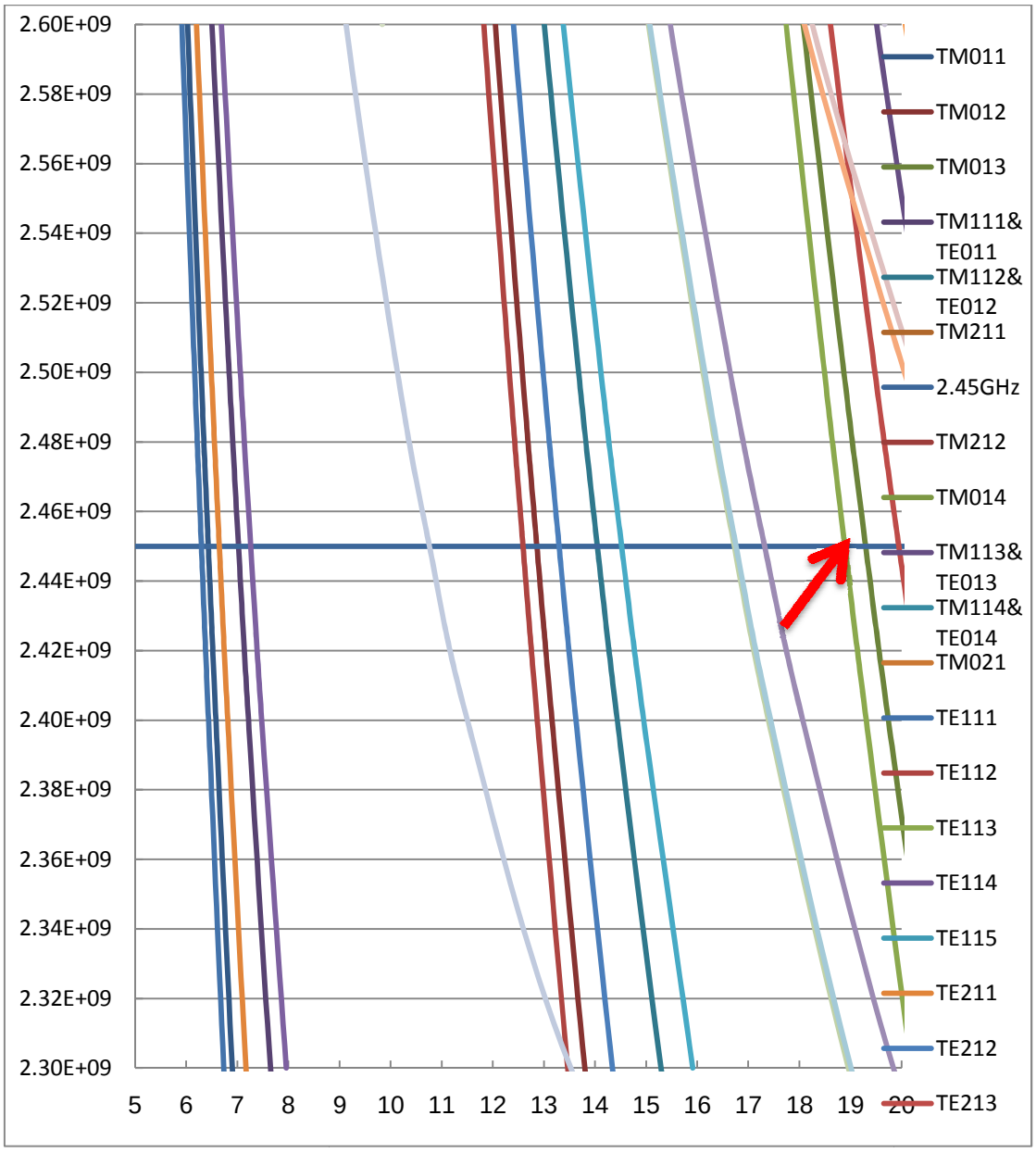

Figure 4.9 Resonant frequencies versus L_S for 12-inch cavity

4.6.2 Initial Prototype Design

This reactor was initially designed in July 2006, the first prototype reactor was built in late 2007 and then the experimental evaluation took place in MSU/FHG

CCL -C laboratories. Design and reactor construction were initiated during the 2007-2009 period and the experiments first briefly synthesized PCD over three to four inches Si wafers and were performed at low pressures (50-100 Torr) and then they were later extended to higher pressures (180-240 Torr) and synthesized thick PCD over two-inch diameter Si wafers. These results are reported in Chapter 5. The synthesis of single crystal diamond was initiated in October 2009 and SCD synthesis and the resulting SCD quality evaluation process continue through 2011. These SCD synthesis experimental results are reported in Chapter 6.

Figure 4.10 The fourth generation MSU reactor and automated system

Figure 4.10 displays the fourth generation MSU reactor and Figure 4.11 shows the drawing of the initial design of the fourth generation MSU reactor. The applicator consists of two coupled cavities, i.e. a cylindrical cavity section (z>0) and a coaxial cavity section (z<0). The plasma loaded applicator is single mode excited with the hybrid TM_{02} waveguide mode in the cylindrical section of the applicator and TEM_{001} waveguide mode in the coaxial section. The discharge is excited with the EM fields at the z=0 plane. The excited EM mode is a hybrid EM applicator mode consisting of the two waveguide modes plus evanescent modes around the Z=0 plane.

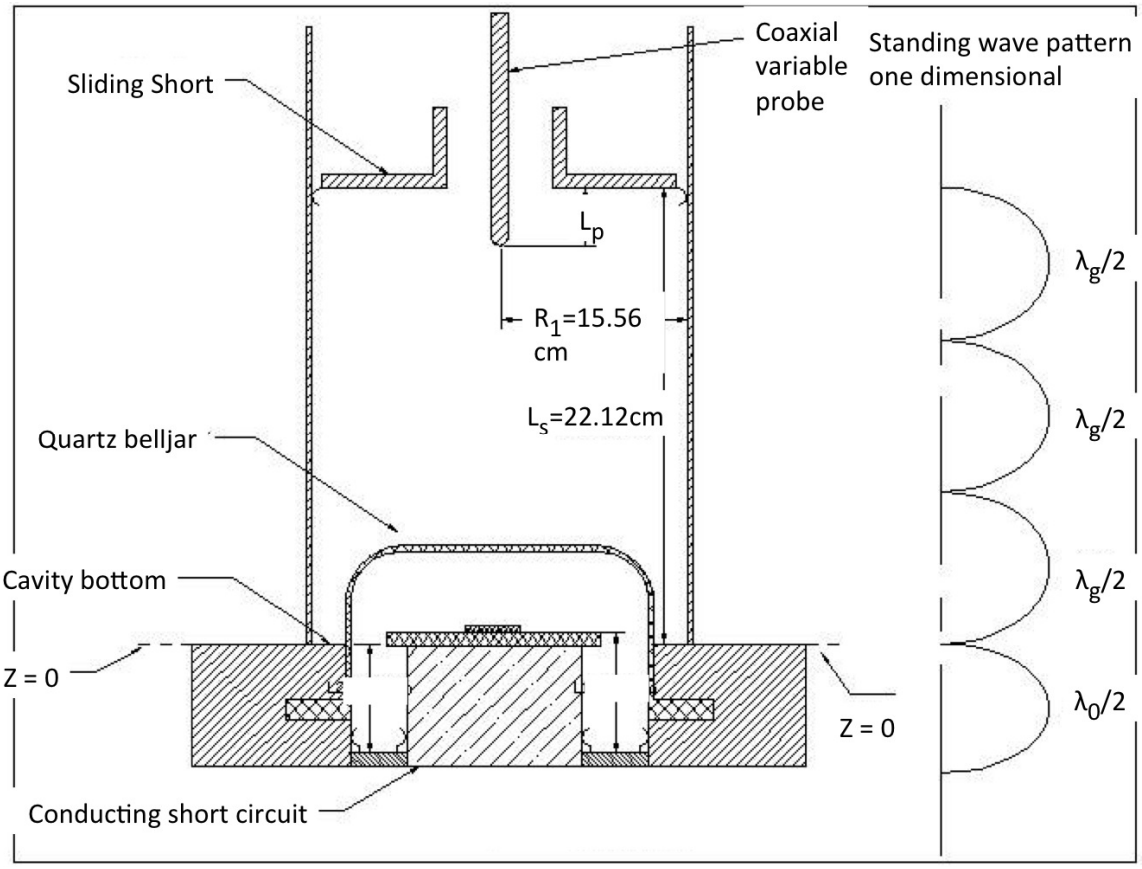

Figure 4.11 The initial design for the fourth generation MSU reactor

4.6.3 Final Prototype design

Figure 4.12 displays the cross sectional drawing of the fourth generation MSU reactor. The reactor can be considered as a special case of the generalized reactor design concept that is described in Section 4.3. As shown in Figure 4.12, it is composed of the five cylindrical sections; i.e. the input section and plus sections (1) through (4). The first, prototype realization of this design had the following dimensions; $L_p \approx 3$ cm; $L_s \approx 16.2$ cm; $R_1 = 15.24$ cm; $R_2 = 10.8$ cm; $R_3 = 1.84$ cm; $R_5 = 12.07$ cm; $L_1 = L_2 \approx 6.12$ cm; -0.8 cm $< Z_s < 0.5$ cm; and $L_3 = 7.32$ cm. It has four mechanically independent cavity applicator adjustments: (1) variable coupling probe length L_p, (2) variable substrate holder length L_1, (3) variable top plate sliding short L_s, and (4) variable conducting short plate L_2.

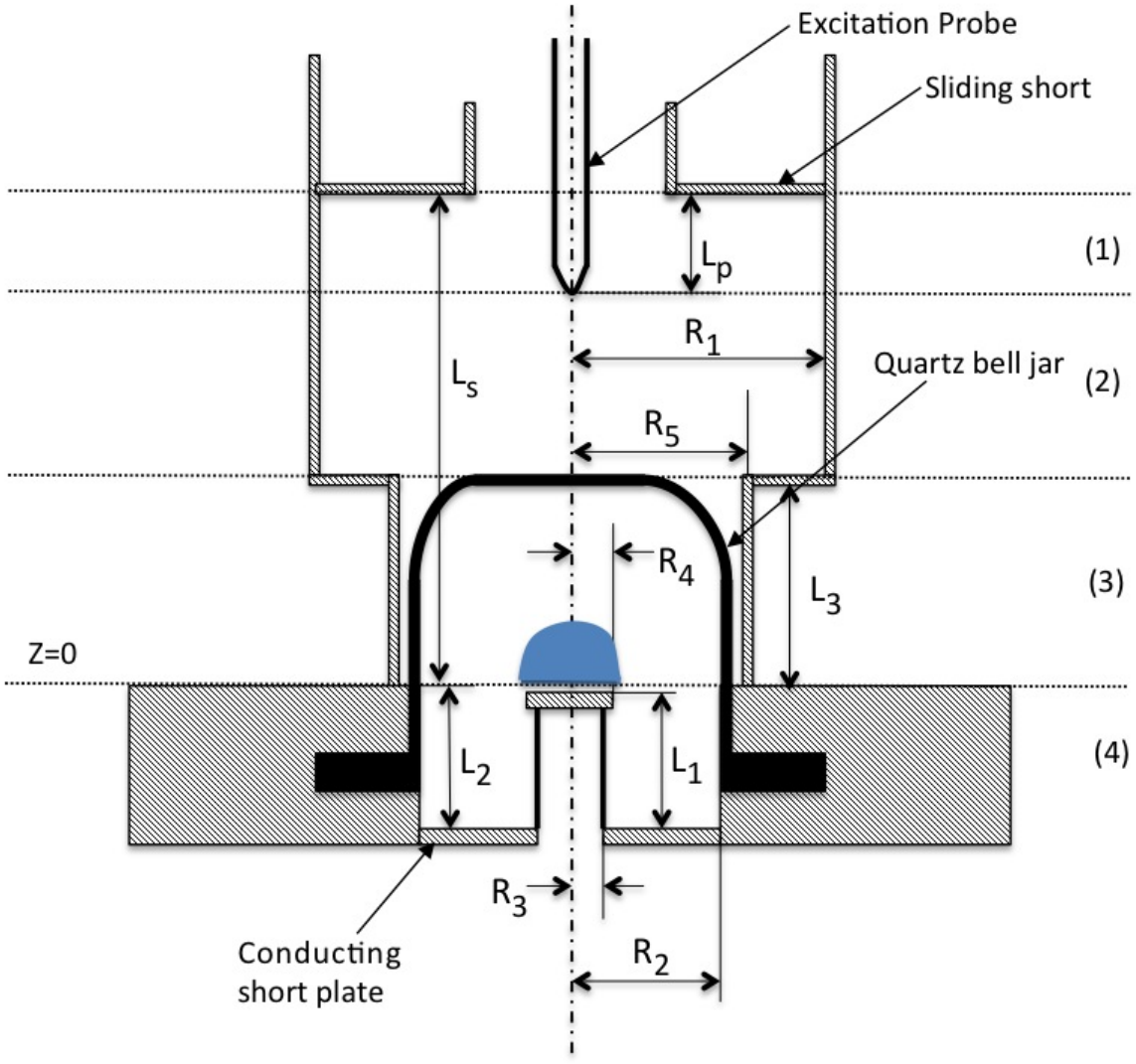

Figure 4.12 Cross section of the fourth generation MSU reactor

Therefore in Reactor C, the cavity and quartz dome wall radii were increased and the reactor was changed from the Reactor A shown in Figures 4.4 and 4.5 of Section 4.4 to a design with larger cavity wall and quartz dome radii. In particular the cylindrical cavity of Reactor A shown in Figure 4.5 was replaced with the sections (2) and (3) that are shown in Figure 4.12 above. Radius R_1 = 8.9cm of cylindrical cavity section of Figure 4.5 was replaced by sections 2 and 3 in Figure

4.12 with respective radii R_1 = 15.24 cm and R_5 = 12.07 cm. For a given input power this design change spreads out the electromagnetic field intensity over the waveguide cross section. Then at and around the Z=0 plane the time average power flux density flowing through the sections (2) and (3) is refocused onto the substrate.

4.6.4 Experimental Test (with or without plasma)

After setting up the fourth generation MSU reactor system, some initial tests were performed without plasma. At low power, a variable microwave frequency sweep of the reactor was performed. This experimental technique has been employed for over forty years at MSU to aid in the design and experimental test of new reactor designs. In order to facilitate this evaluation a rectangle waveguide was attached to the cavity entrance. The cavity/waveguide system was then attached to a circulator, and a reflected power directional coupler. The input to the circulator was connected to a HP 8350B Sweep Oscillator and Tektronix 2215A Oscilloscope. (See Figure 4.13 and 4.14)

A very small amount of variable frequency microwave power (<25mW) was input into the reactor. The power reflected from the cavity was then sampled by the reflected power directional coupler and displayed on the oscilloscope versus swept frequency as is shown on Figure 4.14. The dips in reflected power, i.e. the absorptions in reflected power were identified as the excitation of a cavity resonant mode. See Figure 4.15 and 4.16. These resonant cavity frequencies could also be enhanced by matching the cavity to the input transmission circuit

by varying L_s and L_p.

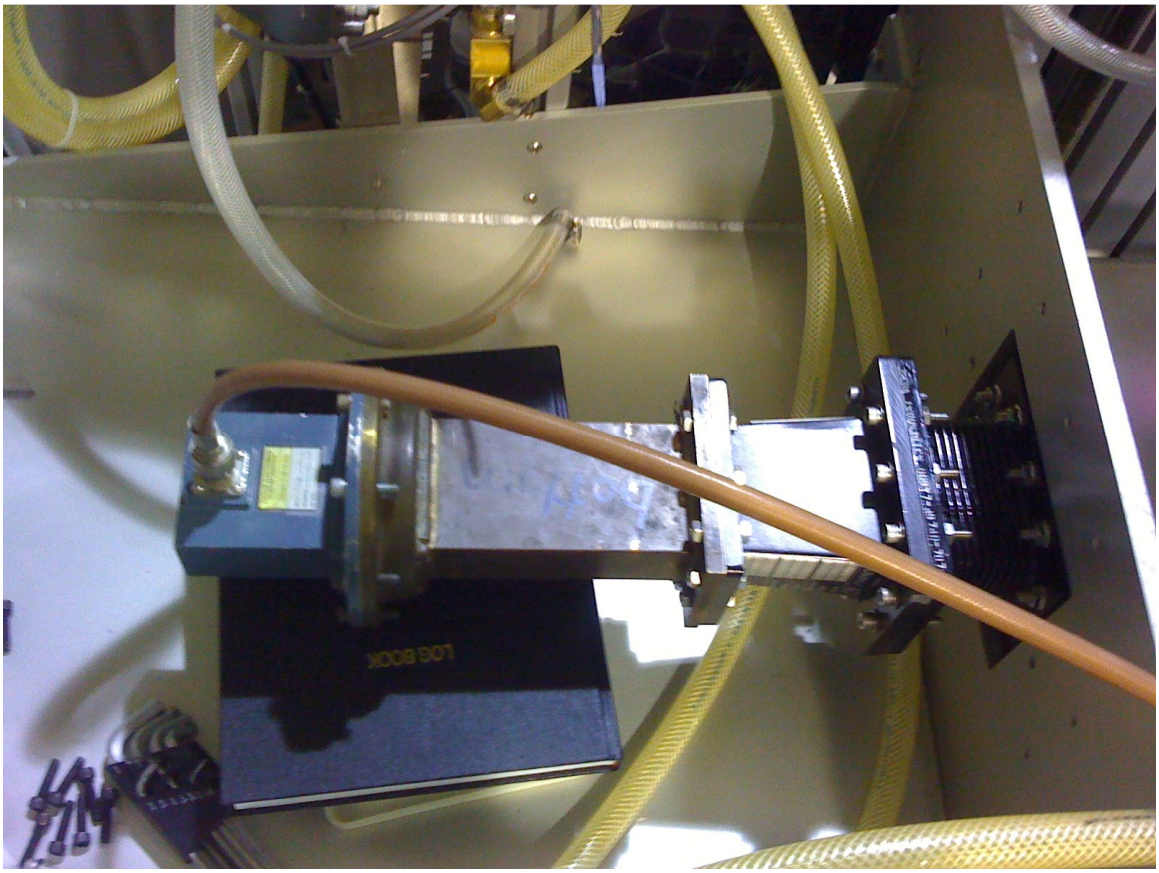

Figure 4.13 Rectangle waveguide hooked up with MPACVD reactor entrance

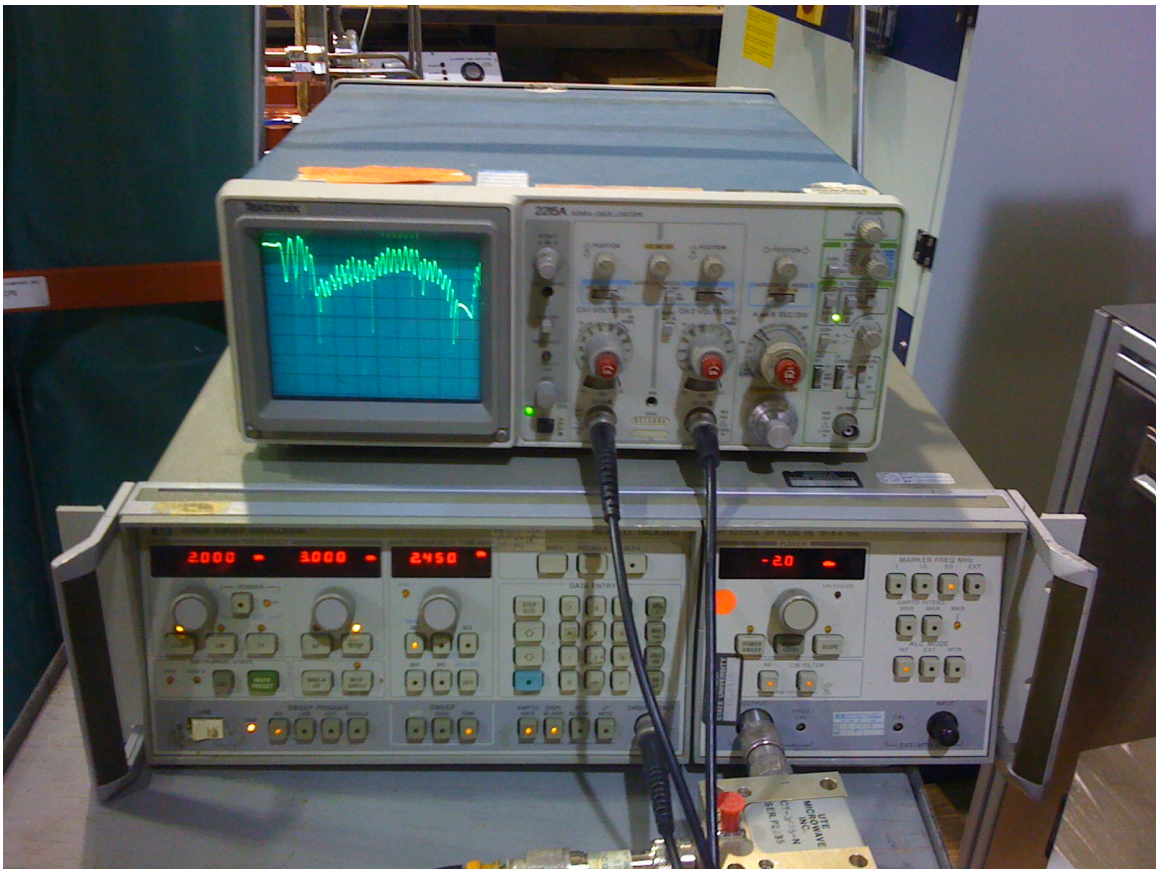

Figure 4.14 HP 8350B Sweep Oscillator and Tektronix 2215A Oscilloscope

The cavity reactor design of Figure 4.11 was first tested at low power. According to the resonance frequency calculations (see section 4.6.1), $L_{S,}$ should be 19.3 cm for a 12-inch cavity respectively, to let it excite the TM_{013} mode and resonance at 2.45 GHz. Finally when we adjust Ls to 18.36 cm, we found the cavity resonance frequency at 2.45 GHz. Figure 4.15 shows the frequency sweep range from 2.3 GHz to 2.6 GHz, and Figure 4.16 shows the frequency sweep range from 2.44 GHz to 2.46 GHz. The circuit loaded Q factor is equal to $f_0 / \Delta f = 2.45 / (2.4504-2.4495) = 2722$. L_S value is not exactly what we have

calculated because there are other structures below the substrate surface (Z surface) to affect the resonance frequency, but the simple eigenfrequency calculations of Section 4.6.1 were able to guide us to the right L_S for the TM_0 mode excitation.

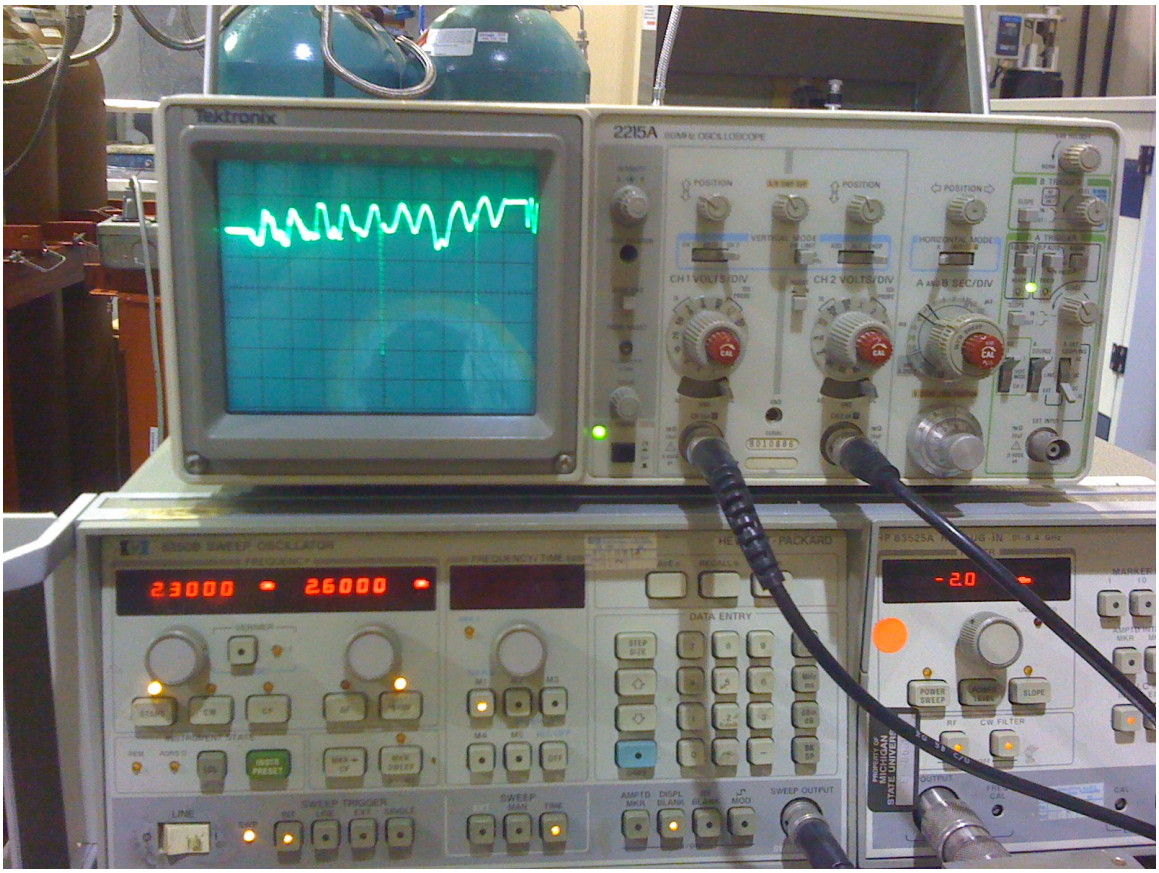

Figure 4.15 Low power sweep (2.3 – 2.6 GHz)

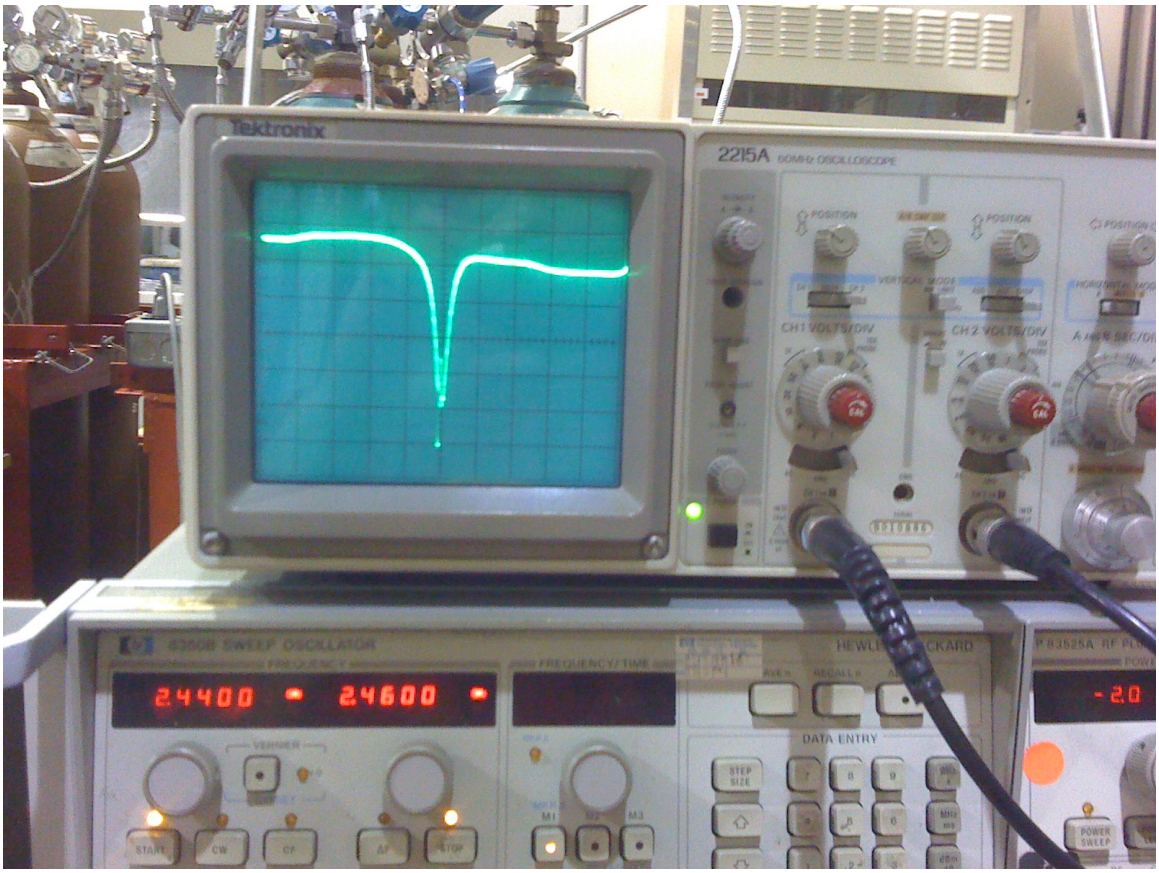

Figure 4.16 Low power sweep (2.44 – 2.46 GHz)

After we found the right L_S, the MPACVD reactor system was hooked up to the 10 kW microwave power supply and magnetron. A few exploratory diamond deposition experiments were performed to test the new system with plasma. Unfortunately there are several problems with the system including dome heating and the ignition of unwanted discharges in the coaxial cavity region ($Z < 0$ region).

Since it was desired to operate the reactor at high power densities and at high pressures, it was decided to further modify the design of Figure 4.11. This reactor design employed the same cooling stage design that was used in Reactor B. The basic idea was to divide the reactor in Figure 4.11 into 3 parts

vertically. The upper cylindrical reactor still keeps the original radius and the lower section Z<0 coaxial section employed the same substrate holder and cooling stage that reactor B utilized. A smaller diameter inner ring was also inserted into the middle section and the lower cylindrical reactor radius was reduced from 15.24 cm to 10.8 cm. The smaller radii that were used here refocused the microwave energy onto the substrate holder similar to the design of Reactor B. However a larger quartz dome was still used in order to allow the discharge to locate itself away from the reactor walls and thereby enable high pressure operation (see section 2.2).

The important dimensions of the final design (see Figure 4.12) are as follows. The radius of the fourth generation cavity applicator is R_1 = 30.48 cm. Other important dimensions and coordinates of the applicator are the coupling probe depth, L_p = 3.0 cm, the cylindrical cavity length, L_s = 16.2 cm, the cylindrical cavity radius, R_1 = 15.24 cm, the coaxial cavity radii R_2 = 10.8 cm and R_3 = 1.84 cm, the molybdenum substrate holder radius R_4 = 3.24 cm, the coaxial cavity lengths L_1 = 6.12 cm and L_2 =6.12 cm, and in particular the inner ring radius R_i = 12.07 cm and inner ring length L_i = 7.32 cm.

It was not certain whether this design would work or not at that time. However the low power swept frequency experimental evaluations identified a number of possible EM resonances. One unexpected, experimentally identified resonance was found at L_s ~ 16.2cm. This resonance was not predicted by the simple

theory presented in section 4.6.1 (see Figure 4.9) but the experimental low swept frequency measurements identified it as a possible mode to excite the cavity reactor. High power experimental evaluations as discussed in later chapters identified this resonance as the best mode EM mode to operate within the high pressure and high microwave power density regime. Thus all the experimental results reported in Chapters 5 and 6 excite this EM resonance. This new EM mode has also been investigated by numerical simulations (see Section 4.7 below).

4.7 Overview of the Numerical Simulation

Electromagnetic waves in the 2.45 GHz frequency range are used to produce plasmas for diamond deposition. In this section our microwave plasma CVD reactor is studied by numerical simulation. COMSOL Multiphysics version 3.5 is used to calculate these coupled equations. The COMSOL Multiphysics simulation environment allows us to define the reactor geometry, specify physics, meshing, solving and then post-processing results. The microwave plasma assisted cavity can be set up from the predefined model for the electromagnetic analyses. Material properties, source terms and boundary conditions can all be arbitrary functions of the dependent variables.

4.7.1 Subdomain setup and cavity dimensions

The whole cavity was divided into two different subdomains. The first

subdomain is a cylindrical cavity section (Z>0, See Figure 4.17) which is set in air with relative permittivity equal to 1. The second subdomain is a coaxial cavity section ($-L_2<Z<0$).

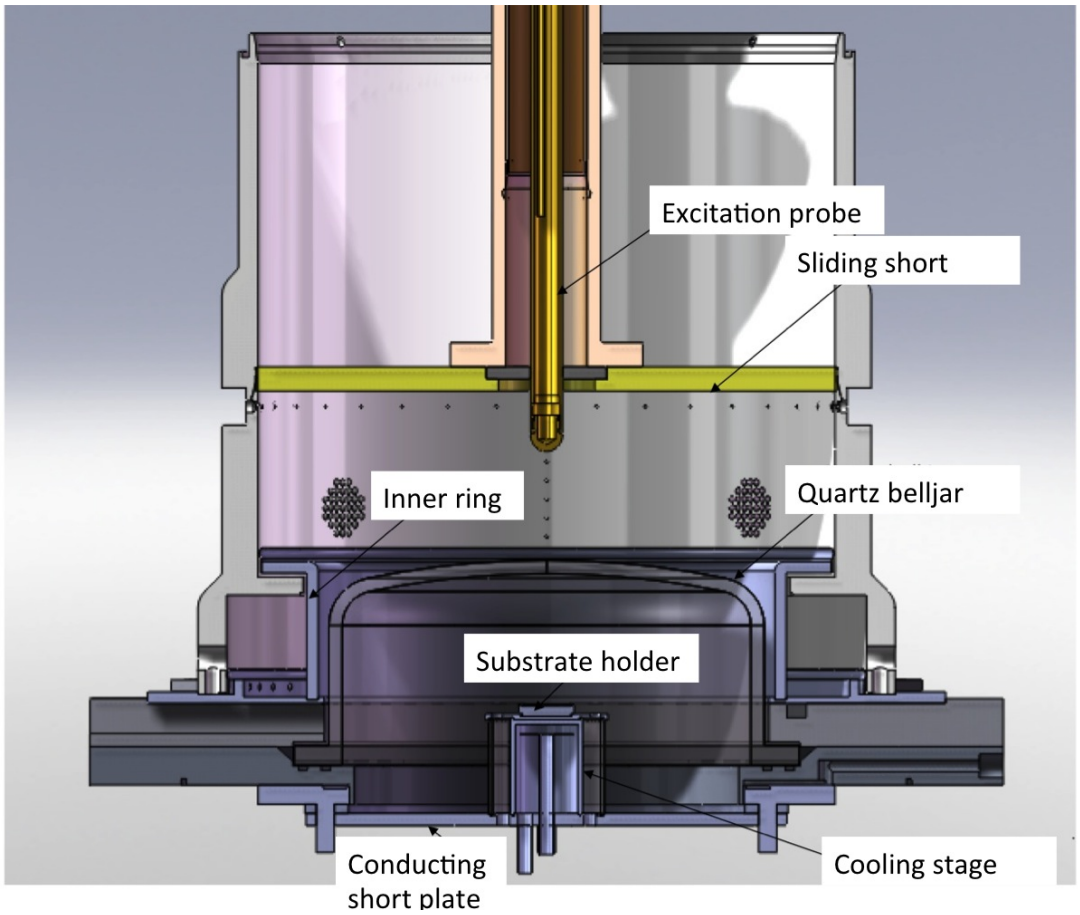

Figure 4.17 Reference microwave plasma reactor cross section

The plasma loaded applicator is excited with the hybrid TM_{013} mode in the cylindrical section of the applicator and TEM_{001} mode in the coaxial section, The discharge is excited with the electrical magnetic fields at or around the Z=0 plane. These fields consist of the two modes plus evanescent modes. This resonant

mode TM_{013} mode, which is shown in Figure 4.18 for a simple, empty, cylindrical cavity, is characterized by regions of high electric energy density on the cavity axis at the endplates, and in two annular regions circumscribing the cavity midplane. The resonant cavity is a circular cross-section waveguide shorted by two conducting endplates. One endplate contains a sliding short and excitation probe. The other one is created by an inside ring and substrate holder.

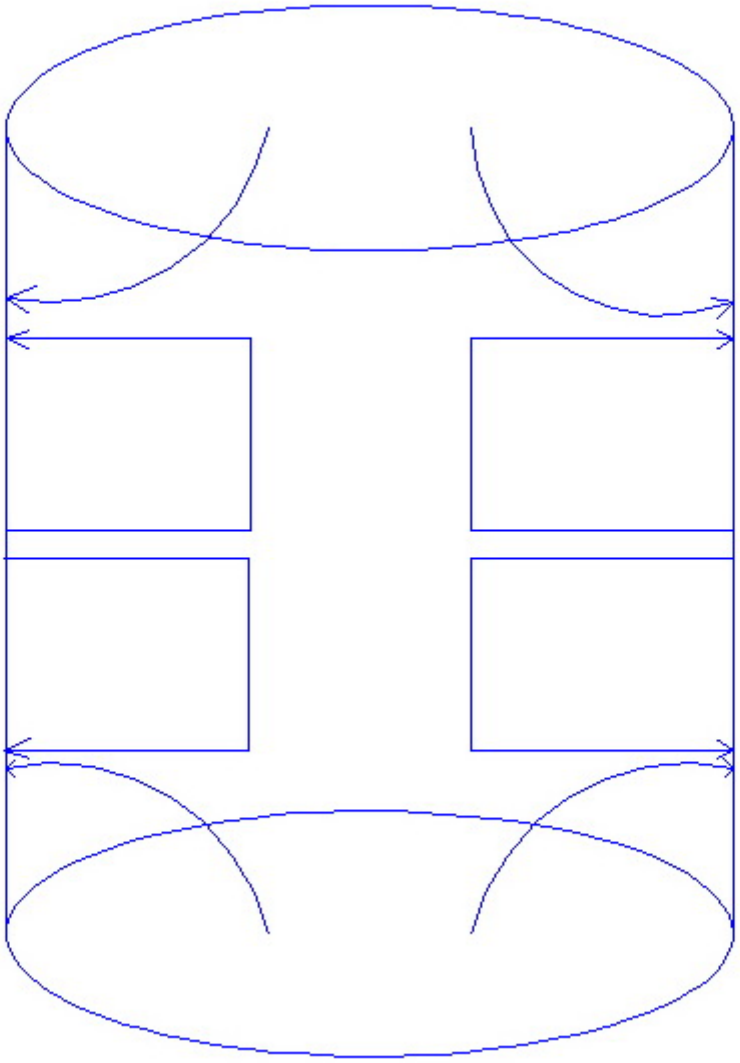

Figure 4.18 Field configuration of TM_{013} electromagnetic mode

The electromagnetic field patterns for each waveguide can be divided into transverse electric (TE) and transverse magnetic (TM) modes. There is an infinite set of discrete TE and TM modes. The TE modes have electric field components only in the plane transverse to z direction which is the direction of wave propagation, while the TM modes have magnetic field components only in a plane transverse to z direction. This microwave plasma resonant cavity operates

in the transverse magnetic TM_{013} mode, which is optimal for producing a hemisphere, free-floating plasma at bottom end of the cavity. In this mode, no magnetic field component is in the direction of propagation, but the electric field strength is high at the cavity's bottom end-plate. Proper selection of the cavity height to diameter ratio causes the electric field strength at the end-plate to be much greater than at the midplane of the cavity. The benefits for doing this are that we acquire the maximum power density at the bottom-end plate and minimum power density at the midplane to avoid the quartz dome overheating problem.

4.7.2 Numerical Modeling

The study of the electric fields focused on three different aspects: The size and shape of microwave plasma reactor and the effect of TEM_{001} mode in the coaxial region. What we are interested in is the electric field strength above the molybdenum holder and the plasma shape. A series of numerical simulations are presented here to show the electric field patterns at the applicator cavity resonant frequency.

Step 1 (Figure 4.19 and 4.20): These simulations are for a 7-inch and a 12-inch classical cylindrical cavity. The 2D picture shows half of the cross section. The left line is center line of a cylindrical cavity, so it has been set to be axially symmetric. The other boundary lines are set to be a perfect conductor, i.e. the tangential electric field is zero. The cavity is full of air which has a relative permittivity equal to 1, electric conductivity equal to 0 and relative permeability

equal to 1. Figure 4.19 displays a simplified empty cylinder with radius R_1 = 8.89 cm and height L_S = 21.59 cm (see Figure 4.17 for R_1 and L_S). With the calculated L_S, the simulation matches the field pattern of TM_{013} electromagnetic mode. We can observe from Figure 4.19 that the high field strength regions of the cavity applicator are located at the bottom, the center and at the sides of the applicator.

If we now increase the same simple cylindrical cavity radius, R_1, to 15.24 cm and height L_S to 19.29 cm and it is still resonant at 2.45 GHz. The numerical eigenfrequency simulations of the electromagnetic field patterns are shown in Figure 4.20. The interesting thing we observe is that even though the same mode is excited, i.e. TM_{013}, the EM field patterns are different. The high electric field strength regions are now located at the side of the cavity. The regions of high electric field strength in the center of the previous cavity applicator disappear. Thus one end of the cavity would not be an optimal region for excitation. However the electric region in the cavity center is greatly reduced. This result suggests that the TM_{01n} mode field patterns can be refocused by varying the cylindrical cavity diameter. In particular electric field can be moved from the center of the cylindrical cross section to the outer walls by just increasing the diameter. This is of course what is done in the final design of the reactor.

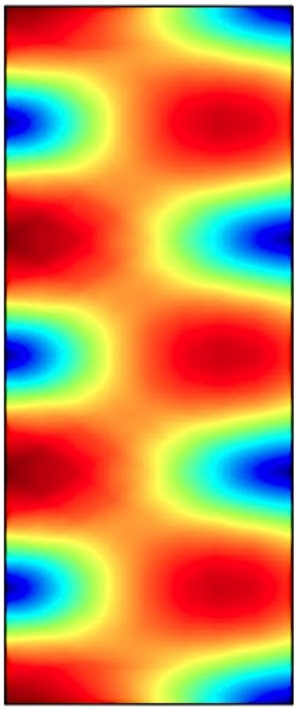

Figure 4.19 Classical Cylindrical Cavity (7-inch)

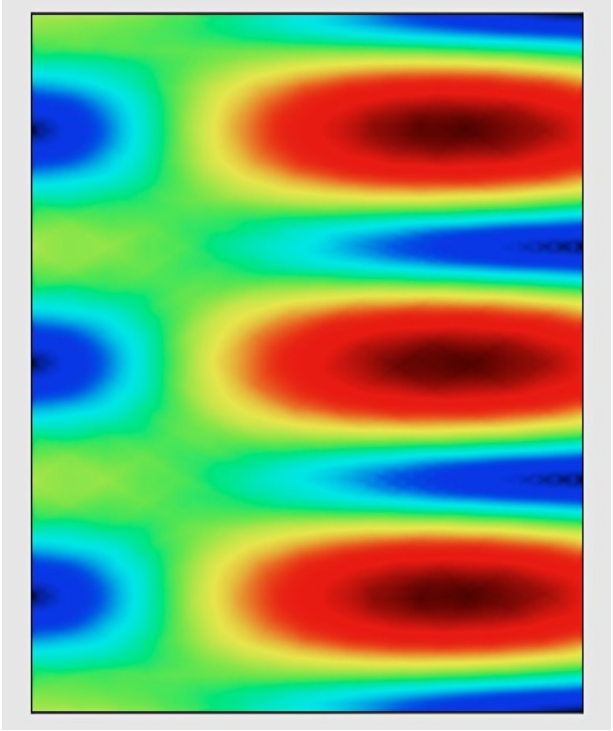

Figure 4.20 Classical Cylindrical Cavity (12-inch)

Step 2 (Figure 4.21): The numerical simulation research starts from the generic reactor. It's a 7-inch cylindrical cavity with 4.1 cm radius cooling stage and 5.1 cm radius substrate holder.

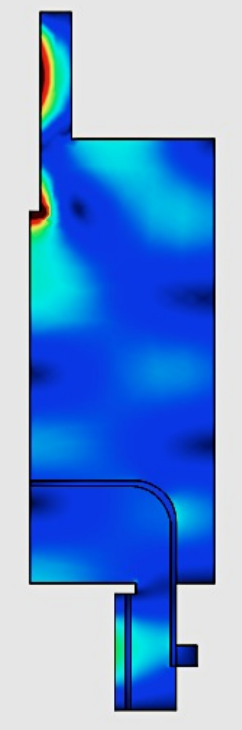

Figure 4.21 Numerical simulation for generic cavity (7-inch)

Step 3 (Figure 4.22): Figure 4.22 displays the numerical simulation for the third generation reactor. It's a 7-inch cylindrical cavity with 1.91 cm radius cooling stage and 3.24 cm radius substrate holder.

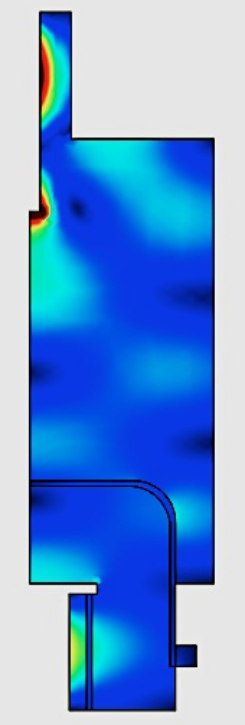

Figure 4.22 Numerical simulation for the third generation cavity (7-inch)

Step 4 (Figure 4.23): Our project is to modify an available cavity which is previously used as ECR cavity to operate CVD diamond deposition. The lower part of the cylindrical cavity's radius is 12.07 cm, less than the top cylinder's radius at 15.24 cm. This change of the shape gives us a stronger electric field at center of the bottom end plate, which is beneficial to plasma formation and diamond deposition. On left top, excitation probe is introduced. Also cooling stage and molybdenum holder are added to complete the Z<0 region where TEM_{001} mode is presented. The electric field is the greatest at the excitation probe and above molybdenum holder where the plasma will be formed. The field pattern changes a lot after a quartz dome is added to the simulation. The relative permittivity of the dome is defined as 4.2, electric conductivity as $1x10^{-14}$ S/m,

and relative permeability as 1. The electric energy density is much higher in the center of the cavity than the edge. Then a quartz tube is added. The problem of this system is although the top of the quartz dome is set to $\lambda_g/2$, the electric field near the top of the dome is too strong and if the plasma was formed it is expected to burn the dome top. To solve the burning dome top problem, we have designed an inside ring to change the geometry shape of the cavity to affect the electric field pattern.

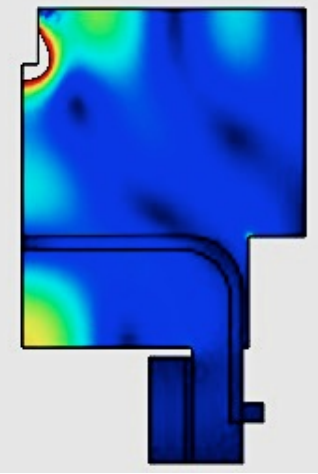

Figure 4.23 Modified Cylindrical Cavity with Inside Ring

Step 5 (Figure 4.24): We have redesigned microwave plasma reactor for different process. A big 4-inch molybdenum holder allows us to make large area CVD diamond deposition. For single crystal diamond deposition, we are looking for higher discharge power densities and higher pressures. So we reduce the molybdenum substrate holder radius and coaxial cavity inner conductor radius by the factor about 4. This modification focuses electric field energy on top of the

molybdenum substrate holder. Details will be talked about in next chapter.

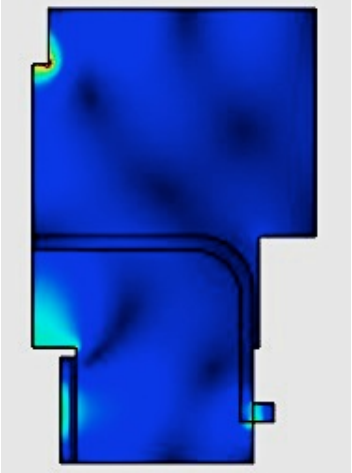

Figure 4.24 Modified Cylindrical Cavity with Smaller Stage

Step 6 (Figure 4.25-Figure 4.30): Next six simulations show us when the molybdenum holder position, Z_S, changes, how it influences the electric field pattern shape and strength. Our goal is to determine the best Z_S position where the electric field is strong on the top of the substrate. The numerical results in Figures 4.25 -4.30 indicate that the negative Z_S positions produce the most intense electric fields above the substrate. This is also observed experimentally.

Figure 4.25 Modified Cylindrical Cavity with Smaller Stage+2.5mm

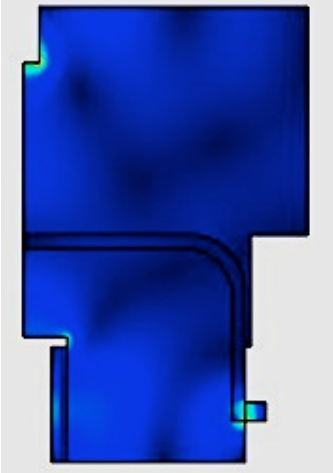

Figure 4.26 Modified Cylindrical Cavity with Smaller Stage+5.0mm

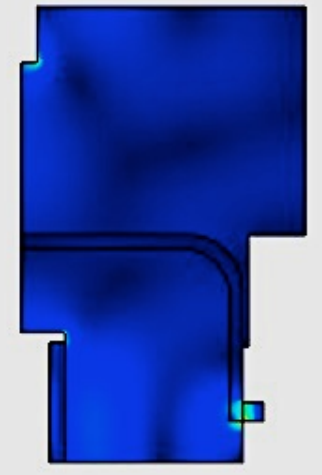

Figure 4.27 Modified Cylindrical Cavity with Smaller Stage+7.5mm

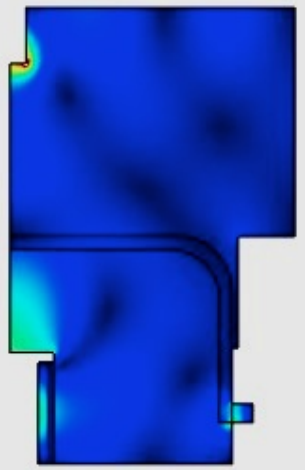

Figure 4.28 Modified Cylindrical Cavity with Smaller Stage-2.5mm

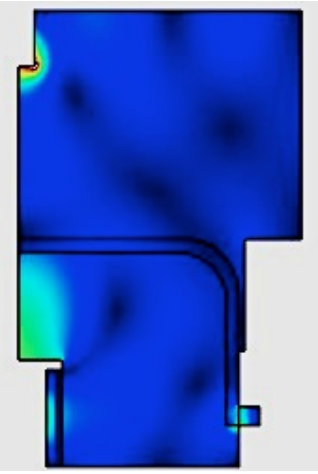

Figure 4.29 Modified Cylindrical Cavity with Smaller Stage-5.0mm

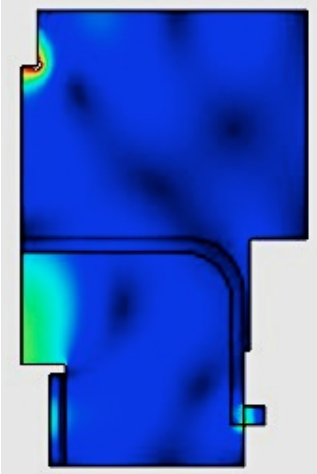

Figure 4.30 Modified Cylindrical Cavity with Smaller Stage-7.5mm

Step 7 (Figure 4.31): These four simulations use the cross section of a complete cylindrical Reactor C. For left to right, it starts from the simple cylindrical reactor. Then add the microwave power entrance and excitation probe. Then add the quartz dome. Finally add the cooling stage and quartz tube. We can see the electromagnetic field changes when we add more details of the cavity.

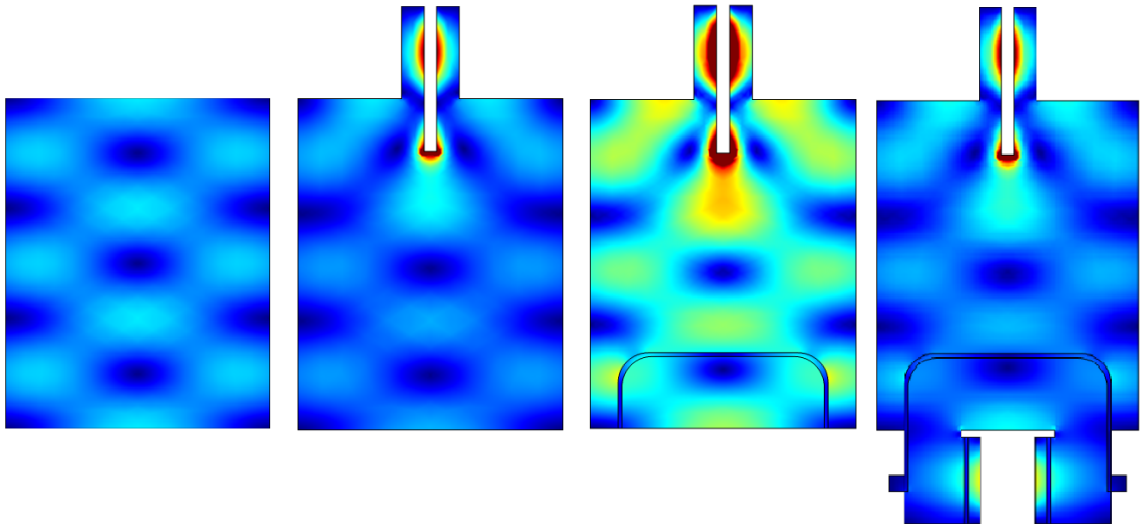

Figure 4.31 Four-stage Simulations of Cross Section of Reactor C

Step 8 (Figure 4.32): In this step, the numerical simulation of Reactor C with plasma is performed. The complex electromagnetic equations are used to calculate plasma electric conductivity σ, relative permittivity (dielectric constant includes both real and imaginary part) $\varepsilon_r = \varepsilon_r' + i\varepsilon_r''$, relative permeability μ_r, and insert these variables to COMSOL.

The average electron density in hydrogen discharge $n_e \approx$ 1E12 (1-4E11 as [62])

cm^{-3} = 1E18 m^{-3}

The electron plasma frequency is equal to

$\omega_{pe} = e/(m_e \varepsilon_0)1/2 * (ne)1/2 = 56.5\ (1E18)1/2 = 5.65E10$

$\omega = 2\pi(2.45E9) = 1.54E10$

Assume pressure p=250 Torr, and gas temperature T=3000 K

The electron-neutral collision frequency is equal to

$\gamma = 4.8E9\ p\ (300/T) = 4.8E9*250*(300/3000) = 1.2E11\ s^{-1}$

So $\varepsilon_r = 1 - (\omega_{pe}/\omega)^2 / (1-j\gamma/\omega)$

$= 1 - (5.65E10/1.54E10)^2 / (1-j1.2E11/1.54E10)$

$= 0.774 - j1.76$

Plasma electric conductivity $\sigma = \omega\ \varepsilon_0\ \varepsilon_r'' = 1.54E10*8.85E\text{-}12*1.76 = 0.24$

The relative permittivity $\varepsilon_r = 0.774 - j1.76$

The relative permeability $\mu_r = 1$

Figure 4.32 shows the numerical simulation result for Reactor C after all these calculated parameters have been inserted. The shape of the plasma has been defined as three forth of an ellipsoid which is very close to what we observed in the experiments. 1 mm sheath was added between the plasma and substrate holder. Figure 4.33 shows a close-up picture of plasma with 1-mm sheath and Figure 4.34 shows a close-up picture of plasma without 1-mm sheath.

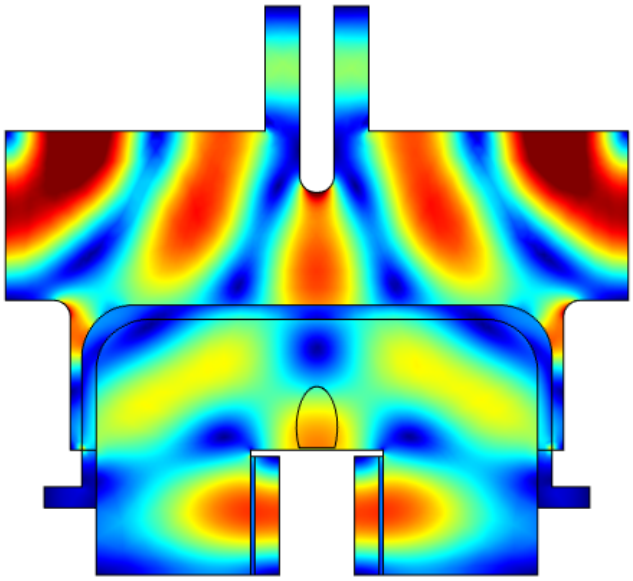

Figure 4.32 Numerical Simulation for Reactor C (all parameters)

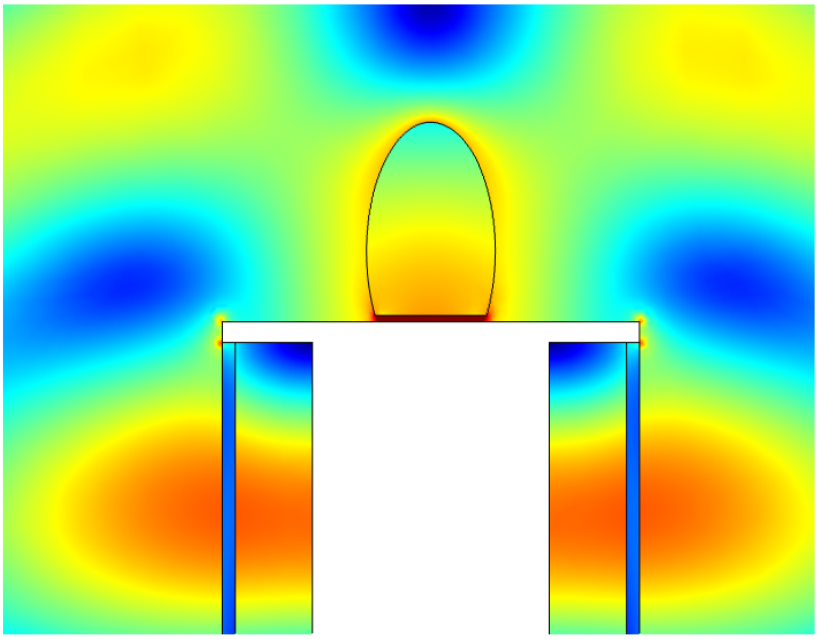

Figure 4.33 Close-up Picture of Plasma with 1-mm Sheath

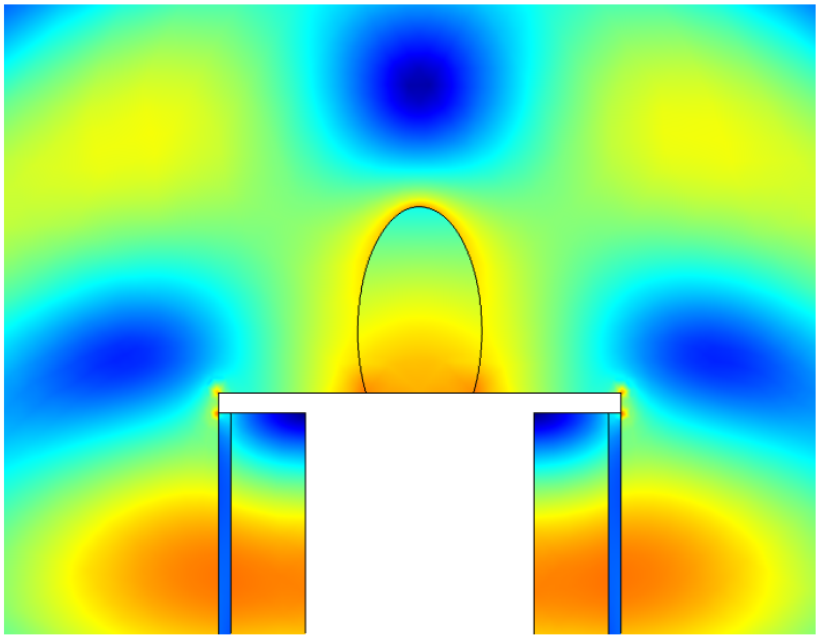

Figure 4.34 Close-up Picture of Plasma without 1-mm Sheath

4.8 Summary

A new larger reactor design was developed. This new reactor design, identified as Reactor C, has a larger diameter applicator and also a larger diameter quartz dome (over earlier reactor designs) that were expected to enable robust operation at high pressures (up to 300 Torr) and with higher power densities. The applicator diameter is varied to unfocus and then refocus the EM field as the EM energy is applied and matched into the discharge. The reactor is excited with a single hybrid EM mode. This mode was first identified experimentally and then was demonstrated to readily produce a high pressure discharge. The next two chapters experimentally evaluate this new reactor design in high pressure and high power density PCD and SCD synthesis applications.

This chapter is concluded by summarizing some of the new reactor's design principles.

First it employs a single mode microwave cavity applicator to focus the microwave energy and to create and maintain a microwave discharge above and in good contact with the substrate over a wide pressure range. In the third generation MSU reactor design the reactor is excited in the hybrid TM_{013}/TEM_{001} mode. Here in this new design because of the multiple cylindrical waveguide sections a new and quite different hybrid mode is excited. A numerical plot of the EM field patterns for the empty reactor resonant mode that is employed in our experimental reactor is shown in Figure what 4.24. As is observed in Figure 4.24, the EM field forms a standing wave field pattern as expected in an empty

resonant metallic cylindrical structure, but the observed EM fields patterns as they were in the third generation reactor. The resonant length $L_S \approx 16.2$cm is not closely related to an empty cylindrical cavity or an empty coaxial cavity resonance. However the EM field patterns do exhibit the unfocusing and refocusing of the EM energy versus Z.

Secondly it employs internal cavity impedance matching. That is it employs a moveable (variable) sliding short, i.e. a continuously variable L_S and an adjustable, continuously variable, L_p coupling probe for impedance matching. These adjustments allow efficient microwave power coupling into the variable microwave discharge load. Thus as the input variables such as pressure, power, gas mixture, and gas flow rate are varied the reactor is readily tuned to a good impedance match. Note that these impedance matching adjustments take place at the top of the applicator away from the discharge and the substrate. The discharge and substrate are located at least two half wavelengths away from the near fields associated with the coaxial coupling probe/sliding short sections. The tuning adjustments, i.e. Ls and Lp required for applicator impedance matching and the associated changes in EM near fields in the coaxial coupling section are separated from the EM focus near the substrate. Thus impedance matching of the cavity applicator does not change the spatial EM focus around the discharge/substrate region. Then as the cavity applicator is matched the special shape of the EM focus (without the discharge) does not change. Only the electric field intensity varies.

The third design principle is that it locates the substrate holder on a movable stage that is an integral part of the microwave applicator. The stage is located inside the applicator so that the electromagnetic field is intense and is focused at the stage/substrate location. The reactor tunability and the ability to adjust the position of the stage allows additional adjustment and local fine tuning/focusing of the electromagnetic fields around and directly above the substrate. This feature enables positioning of the microwave discharge above and in good contact with the substrate while operating in the high pressure and power density regime. It also appears to counter the buoyant forces that the discharge is subjected to as the operating pressure is increased --- thereby keeping the discharge in good contact with the substrate as the pressure is increased.

Fourthly the design which incorporates four tuning variables L_p, L_s, L_1, and L_2 enable the nonlinear optimization of discharge positioning, discharge size adjustment, growth rate enhancement, impedance matching, i.e. process optimization --- thereby allowing for robust and efficient processes development and an adaptable and versatile over all system operation.

A fifth design feature is the scalability of the reactor design. The EM features of the design can be directly scaled up in size by changing the excitation frequency from 2.45 GHz to 915 MHz. This principle was identified in early development in MCPR technologies. Specifically it was identified as an important principle in the early US Patents 4,507,588 and 4,585,688 concerned with MPCR ion and plasma source patents. The direct increase of the MPCR reactor size, i.e. the size scalability, versus a decrease in the EM excitation frequency is a

property of all the MCPR designs and also remains valid for the fourth generation MSU reactor. It is important to note here however, that while the MCPR design is directly scalable with respect to the EM properties, the microwave discharge has a different set of scaling laws. However the reactor EM performance CVD does scale versus size and frequency the same way as the EM performance does.

The sixth design principle, a principle that only Reactor C employs (but is also incorporated in the generalized reactor design concept) is that it incorporates the specific dimensions that allow the coupling/transfer of large amounts of microwave power into the discharge at high pressure. Specifically the dimensions of the reactor are adjusted to enable the transfer/impedance matching of high power fluxes densities of microwave energy that are required for high pressure operation from the external wave guides into the small intense high pressure discharge. It does this by unfocusing EM field in the quartz dome regions and then refocusing the microwave energy on the substrate holder/powered electrode without creating any high EM fields (standing waves) elsewhere in the cavity applicator.

The overall goal of the numerical simulation effort was to understand how the electromagnetic fields vary and behave when the reactor dimensions are varied. Since the reactor has a complex shape, one can only perform numerical electromagnetic simulations of the electric field in the resonant cavity by computer software, i.e. COMSOL Multiphysics. Cavity shape is the biggest concern to determine effects of finding the TM_{013} and TEM_{001} mode with eigenfrequency.

The results show that calculations for the simple cylindrical cavity matches the numerical result. When the cavity's shape changes, it will also change the electrical field pattern above the molybdenum holder. This can affect CVD diamond deposition process. The COMSOL simulations have been used to provide an understanding of how the EM field patterns vary inside the cavity as the size and shape of the cavity are varied.

CHAPTER 5

EXPERIMENTAL RESULTS OF POLYCRYSTALLINE DIAMOND SYNTHESIS

5.1 Introduction

Polycrystalline diamond (PCD) deposition experimental results are presented in this chapter. First the concept of the multivarible parameter space for microwave plasma assisted diamond deposition is briefly reviewed. In general, the output performance of the reactor (Y) is a function of input variables U_1, U_2, U_3 etc, i.e. $Y = f(U_1, U_2, U_3)$. The experimentally measured absorbed microwave discharge power density versus pressure is presented for Reactor C. Then the experimental results of polycrystalline diamond synthesis are presented. The

experimental results include determining the relationships between the output variables such as growth rate, uniformity, and surface morphology versus the input variables such as gas chemistry, pressure, etc. At the time of writing this thesis more than 20 exploratory PCD experiments were performed. The total growth time for all of the PCD experiments that are presented in this chapter was about 300 hours. Most of the diamond synthesis experimental results shown in this section were conducted as separate experimental runs each with duration between 8 hours to 100 hours. These 20 experiments were performed as preliminary experimental reactor design evaluation purposes, i.e. as a first test of Reactor C's ability to CVD synthesize diamond in the high, 160-300 Torr, pressure regime.

5.2 The MPACVD Experimental Subsystems Overview

5.2.1 Introduction

The fourth generation microwave plasma-assisted diamond CVD experimental system which was employed for the experimental evaluation of Reactor C is displayed in Figure 5.1. The experimental subsystems include the microwave power supply system, the microwave coupling system and reactor, the gas flow control system, the pressure control system, and the exhaust system. All these subsystems work together, generally under computer automated control, to provide the desired CVD diamond deposition environment. Several of these subsystems are described in greater detail in Section 5.2.2-5.2.5. The automated subsystems were designed previous to the beginning of

this thesis research at Michigan State University and Lambda Technologies. Reactor C and the substrate holder and associated cooling stage were designed and modified at Michigan State University (MSU) as part of the research activities described in this thesis.

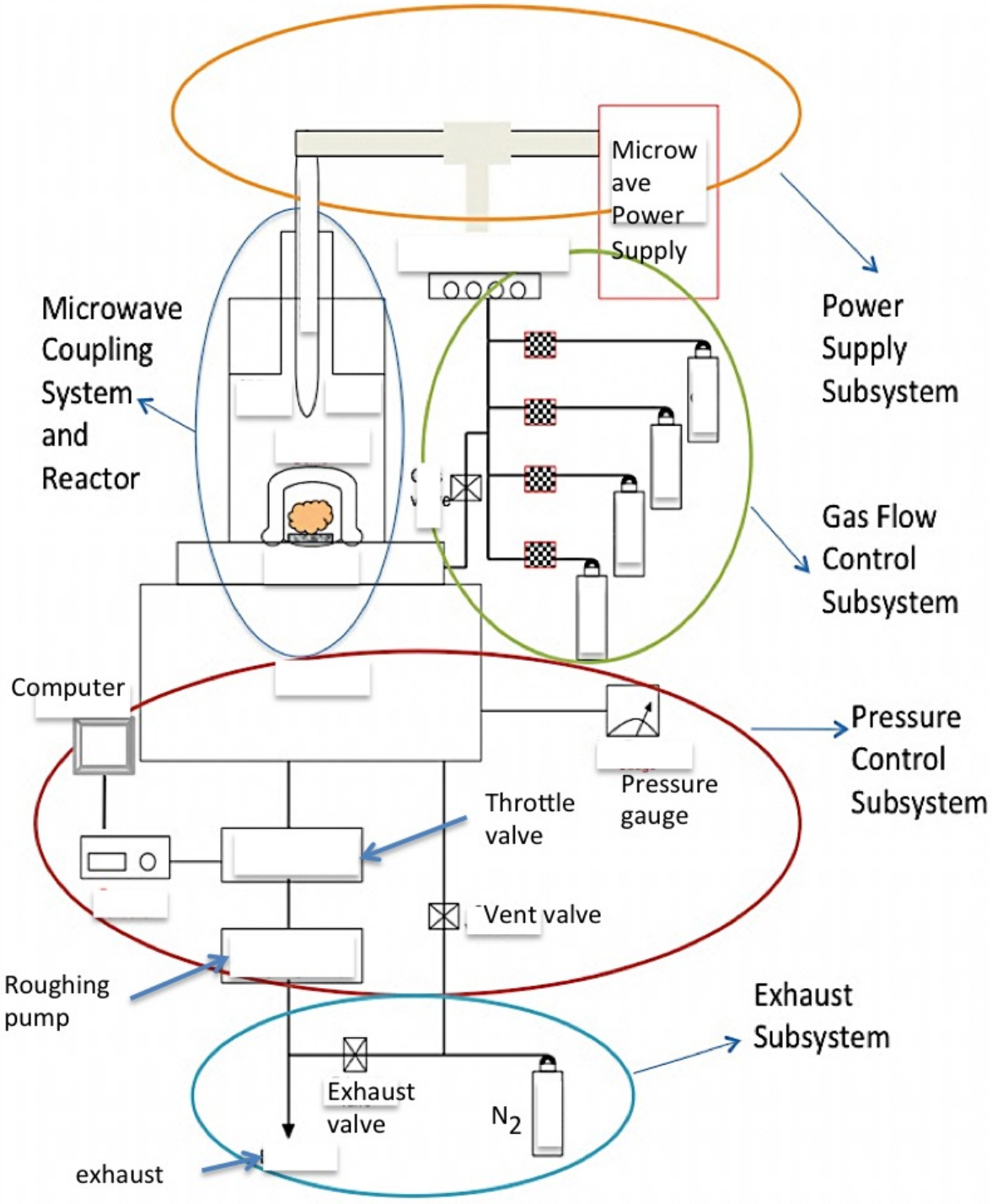

Figure 5.1 Generic microwave plasma-assisted CVD diamond system

5.2.2 Microwave Power Supply Subsystem

In a typical microwave plasma assisted CVD system, the plasma discharge is used to dissociate process gases and produce active atoms (radicals) within the process chamber. It's very important to have a highly reliable automated microwave power supply to generate and optimize microwave plasmas for CVD process. A standard microwave power supply subsystem is shown in Figure 5.2.

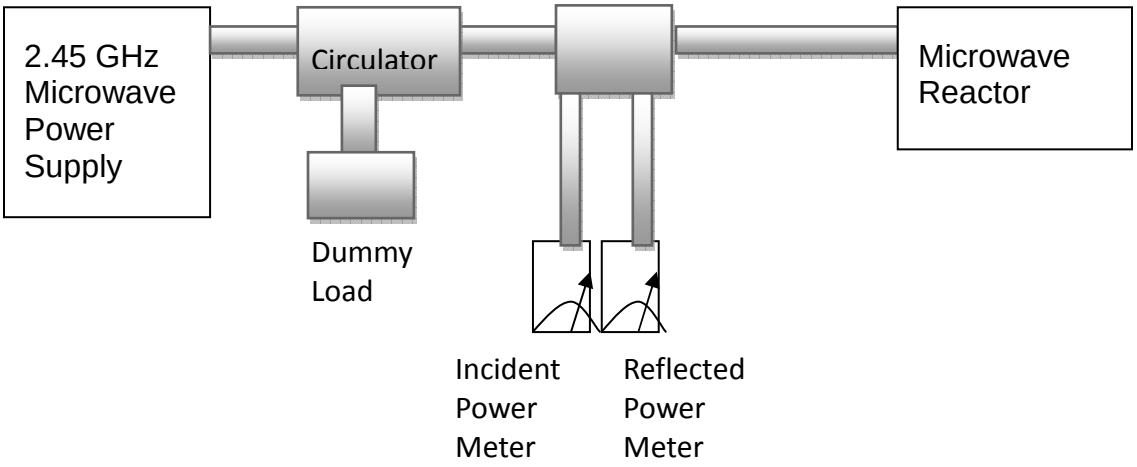

Figure 5.2 Standard microwave power supply subsystem

The continuously variable ~ 1.5 – 10 kW microwave power displayed in Figure 5.2 is generated by a magnetron power supply GENSRS10.0, consisting of MW-power supply MWPSSRS10.0 and magnetron-head MHWCS10.0, at the frequency of 2,450 MHz with a maximum 10KW HF-output. The output of the magnetron power supply is connected to a circulator that isolates and protects the power supply from any power that may be reflected from microwave reactor. The reflected power is led to a water-cooled dummy load which is impedance-matched. The absorbed power P_a is P_i - P_r, which is measured as the incident

power, P_i, minus the reflected power, P_r, is one of the major input variables. Microwave power measurements are made using dual-directional power couplers inserted in the waveguide between the circulator and microwave reactor. Typical absorbed powers, P_a, measured during the MPACVD diamond synthesis experiments range from 1 kW to 4 kW.

5.2.3 Gas Flow Control Subsystem

Four essential gases are used in the deposition process. They are nitrogen, hydrogen, methane and argon. Some other gases, like carbon monoxide, oxygen etc, are also needed for specific process. Because of the sensitivity of the process to impurities in the discharge plasma and the desire to minimize impurities in the CVD diamond, the compressed feed gases had the following compositions: 99.9995% purity (Total impurities < 5ppm, N_2 < 3ppm) for Hydrogen, 99.999% purity (Total impurities < 10ppm, N_2 < 5ppm) for Methane. Mass flow controllers (MFC) are devices used to measure and control the flow of gases. The MKS Type 1179A general purpose mass flow controller is designed and calibrated to control processing gases at a particular range of flow rates. A signal is sent to the control panel. The total flow rate ranges from tens to hundreds of sccm (standard cubic centimeters per minute) in our process. These controlled flow rate feed gases are mixed together and delivered to the discharge chamber.

5.2.4 Pressure Control Subsystem

The pressure control subsystem is used to maintain the desired pressure in the deposition chamber. During the process, the vacuum pumping system will pump the reacted gases out of the deposition chamber continuously. In this thesis diamond CVD processes operated in the pressure range of a few tens of Torr to 300 Torr. The pressure was maintained by using a mechanical roughing pump. In this research system a TRIVAC D 16 BCS two-stage rotary vane vacuum pump was used. The pressure in the deposition chamber was maintained by an automatic throttle valve located between the chamber and the pump. The pressure was measured by a pressure gauge MKS Type 141A which is a variable capacitance sensor consisting of rigidly attached capacitive electrodes located on the back or reference side of a metal diaphragm. The reference side is permanently evacuated and sealed and thus makes the pressure measurement totally independent of the gas type or composition. When pressure is applied to the diaphragm, its deflection produces a change in the distance between the electrodes and the diaphragm and a resultant capacitance change. The signal is sent to a pressure controller in main control panel. The control system automatically adjusts the throttle valve to achieve the desired pressure in the deposition chamber.

The system leak rate is an important factor for CVD diamond synthesis. The pressure-changing rate (mTorr/hr) needs to be converted to the gas flow rate in standard cubic centimeters per minute (SCCM) to estimate the residual gas, i.e.

N_2, from the leaking of the vacuum system. An example of this conversion is shown below.

$$\frac{Volume\ of\ the\ leaking\ gas\ into\ the\ chamber}{Volume\ of\ the\ chamber} = \frac{Pressure\ change\ of\ chamber}{Pressure\ of\ chamber}$$

So

the leaking gas flow rate (SCCM) =

$$\frac{Pressure{-}changing\ rate\ (\frac{mTorr}{hr}) * Volume\ of\ the\ chamber\ (cm3)}{760\ Torr}$$

In this experimental system, the leak rate was measured to be 1 mTorr/hr. The chamber volume for Reactor C is the sum of the vacuum chamber volume and quartz dome volume. The vacuum chamber is a cylinder with the radius of 16.51cm and height of 35.56cm. So the volume of the vacuum chamber is 3.04x10^4 cm^3. The quartz dome is also a cylinder with the radius of 10.8cm and height of 10.16cm. The volume of the quartz dome is 3721 cm^3. So the total volume is 3.41x10^4 cm^3. Thus we can calculate:

The leaking gas flow rate (SCCM) = $\frac{1\ \text{mTorr x}\ (1/60)\ \text{hr/min x}\ 3.41\text{x}10\ 4\ \text{cm3}}{760000\ mTorr}$ =

7.48 x10^{-4} sccm

Since the leaking gas is air and air is mostly nitrogen, we can estimate the residual nitrogen from the leaking of the vacuum system as 7.48 x10^{-4} / 400 (total flow rate in sccm) = 1.87 ppm. Thus all experiments reported in this thesis the system N_2 gas leak rate is less than 2 ppm of the total input gas flow rate.

5.2.5 Exhaust Subsystem

Safety is very important so it has been emphasized in every detail of this design. The exhaust subsystem is one of the safety precautions. A nitrogen purge is used as a dilution of the hydrogen-dominated exhaust gas at the exit of the mechanical roughing pump. Usually the flow rate of a nitrogen purge is 10 times of the total flow rate of flammable gases. The nitrogen dilution thus reduces the methane and hydrogen exhaust gas concentration to a nonflammable level at the exit of the mechanical roughing pump. The safety interlock system measures the pressure of the processing gases to prevent any over pressurizing when hydrogen is present in the system.

5.3 Microwave Plasma Reactor Process Variables And Performance Variables

In order to orderly investigate the performance of the microwave plasma assisted CVD reactor, it is essential to identify the experimental variables. These variables have been identified at MSU in earlier PhD thesis [24,52,53], and thus they are only briefly summarized here. The nonlinear relationships between the three groups of variables are presented. The three basic groups are (1) input variables, U; (2) internal variables, X; and (3) output variables, Y. A description of these variables and the relationships between these variables has already been described in Section 3.2.

The sections that follow in this section quantify the relationships between

the input variables, U, and internal variables, X_i = f(U); the input variables and output variables, Y = g(U); and the internal variables and output variables, Y= h(X). In particular, Section 5.4 describes the experimental relationship between absorbed power, substrate temperature and operation pressure; i.e. it describes the reactor roadmap. Section 5.5 presents the relationship between microwave absorbed power density and deposition pressure; Section 5.6 investigates the relationship between PCD growth rate and deposition pressure and / or gas chemistry and the quality of the synthesized PCD films as indicated by Raman measurements is briefly presented.

5.4 The Experimental Roadmap for Reactor C

When the reactor geometry, substrate size, and total gas flow are fixed, the deposition process is a function of absorbed input power, pressure, gas chemistry, and substrate temperature. The first three are input variables and the substrate temperature is an internal variable. The nonlinear relationship between these variables for a given reactor can be plotted as a set of curves called the reactor roadmap. Given a reactor design the relationship between the experimental multivariable parameter spaces is nonlinear and the best way to determine it is by experimentally measuring the substrate temperature versus absorbed power and pressure.

The experimentally measured reactor roadmap for Reactor C is displayed in Figure 5.6. The experimental variable range for the roadmap and power density measurements are listed below:

(1) Controllable input variables, U_1, which include the following

a) Deposition pressure, Variable: p = 75 - 240 Torr

b) Incident microwave power, Variable: P_i = 1.2 – 3.0 kW

c) Feed gas composition, Fixed: c = CH_4 / H_2 = 3% and no N_2 addition

d) Total flow rate, Fixed: f_t= 400 sccm

(2) Reactor geometry variables, U_2, which include the following

a) Applicator size and configuration, Fixed: Reactor C as described in Chapter 4

b) Substrate position, Fixed: Z_S = -4.8 mm (The exploratory experiments have been performed to find the right Z_S. I found when Z_S = -4.8 mm, the plasma ball is stable when adjusting the pressure from 75 to 240 Torr)

c) Cooling stage and molybdenum substrate holder design, Fixed: for 1-inch Si wafer with insert (See Figure 5.3 - 5.5).

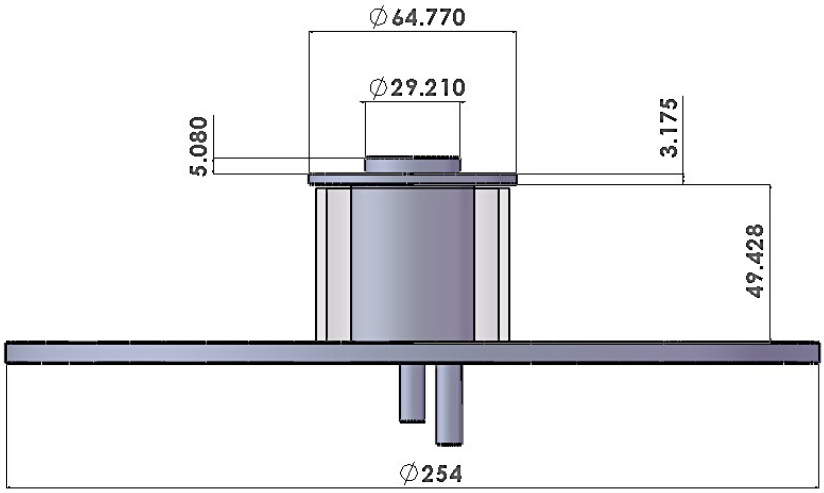

Unit: mm

Figure 5.3 Schematic drawing for the cooling stage

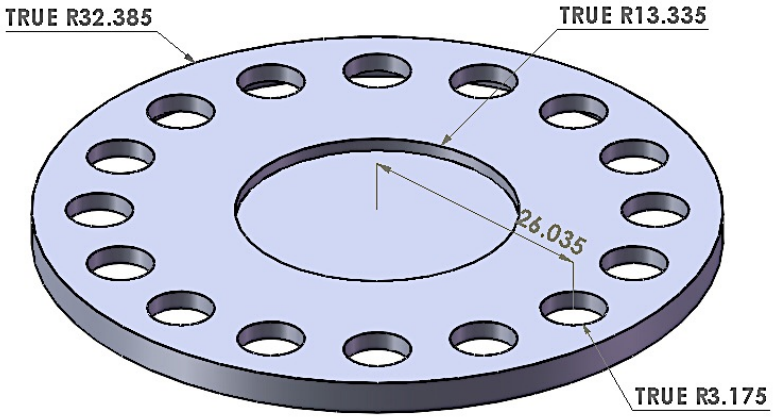

Unit: mm

Figure 5.4 Schematic drawing for the substrate holder

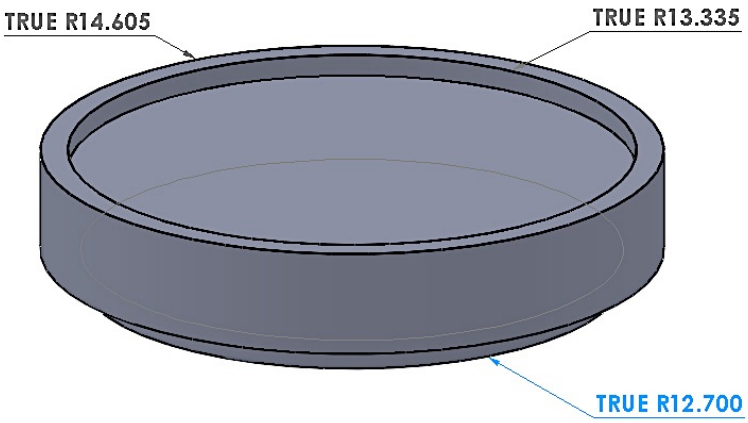

Unit: mm

Figure 5.5 Schematic drawing for the insert

d) Electromagnetic mode: Mode is fixed in all experiments as described in Chapter 4

e) Cavity tuning, Variable: L_S = 15.65-15.85 cm

f) Quartz dome geometry, Fixed: Quartz dome has been used

g) Chiller, Fixed: General ACCPS081-4B-S Air-cooled Liquid Chiller, flow rate is 1.5 GPM for the substrate holder, base plate and excitation probe; and 4.5 GPM for the magnetron. The set temperature range is 20 – 24 ℃.

(3) Deposition process variables, U_3, which include the following

a) Substrate material and size, Fixed: 1-inch silicon wafer

(4) Internal variables X_i, which include

a) Substrate temperature, Variable: $T_S \approx 650 – 1250\ ^{\circ}C$

b) Absorbed microwave power, Variable: $P_{abs} = 1.6 – 3.5$ kW

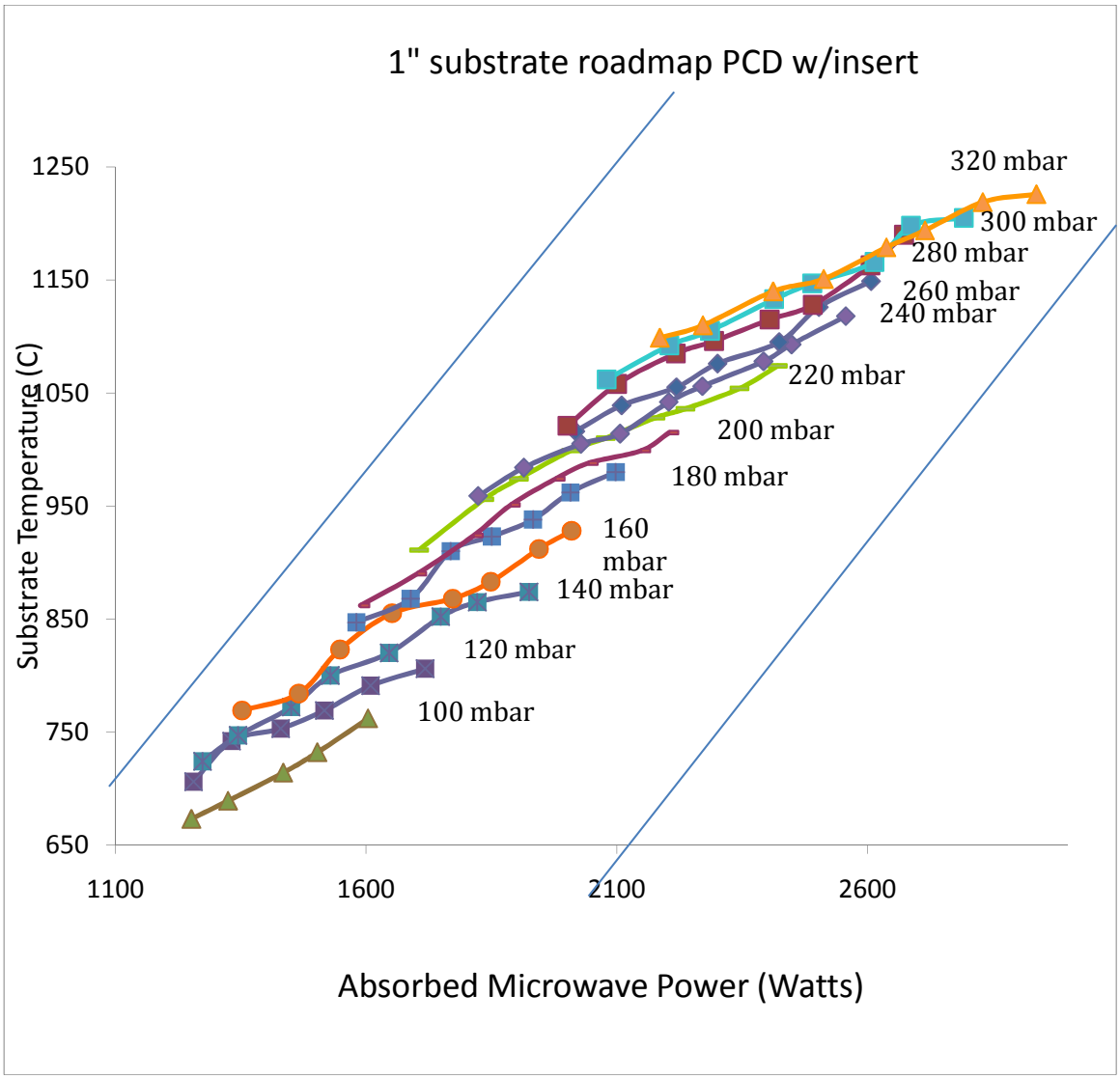

Figure 5.6 The reactor roadmap of the Reactor C, showing the substrate temperature versus absorbed microwave power (75 Torr to 240 Torr)

Figure 5.7 and 5.8 show the experimentally measured reactor roadmap for the Reactor B [53]. Figure 5.9 compares the roadmaps of Reactor B and C at 180 Torr and 240 Torr. We can see the roadmaps of two reactors are almost identical, except the Reactor C has a slightly lower substrate temperature (less than 2%, which is within experimental measurement error). This relatively close

agreement is not surprising since Reactor B and C have very similar cooling stages and molybdenum substrate holder sets.

In any of the experiments presented later in this thesis the substrate temperature at any given constant pressure may be further adjusted by changing the thickness of the molybdenum holder to enable Reactor C's substrate temperature to be adjusted to be within 900 – 1300 °C for 180 – 240 Torr. This is a similar to the design for Reactor B.

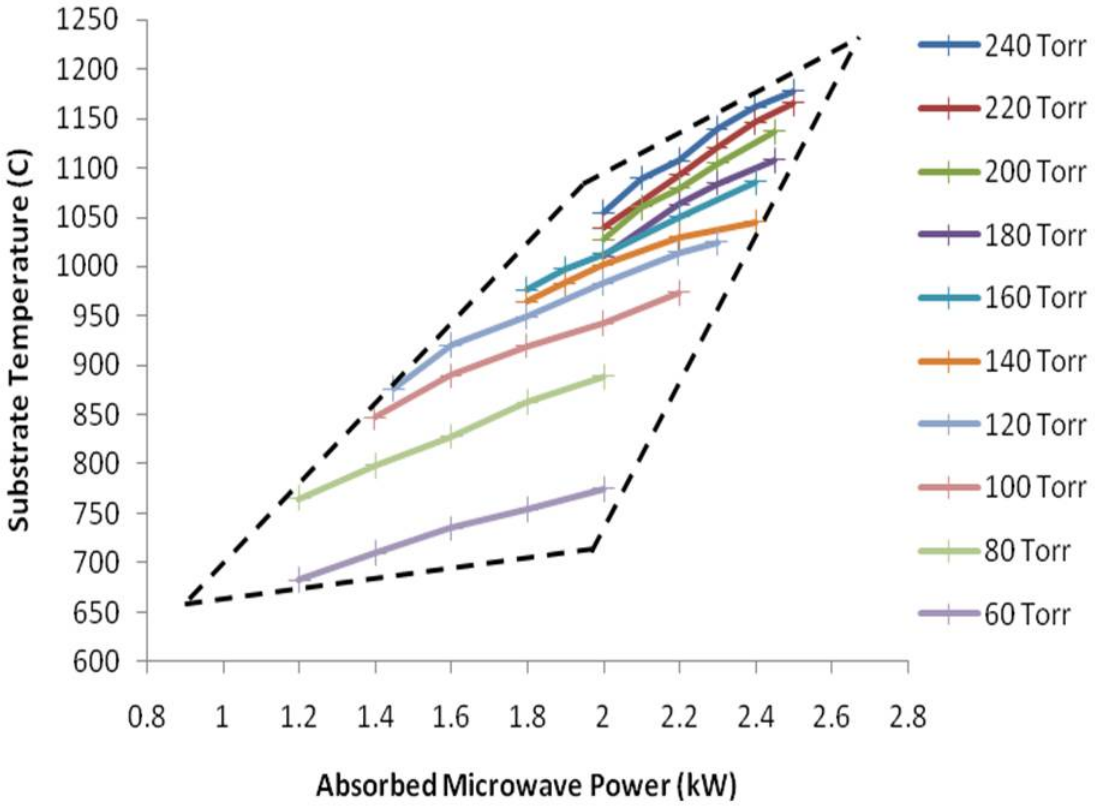

Figure 5.7 The reactor roadmap of the Reactor B, showing the substrate temperature versus absorbed microwave power (60 Torr to 240 Torr) [53]

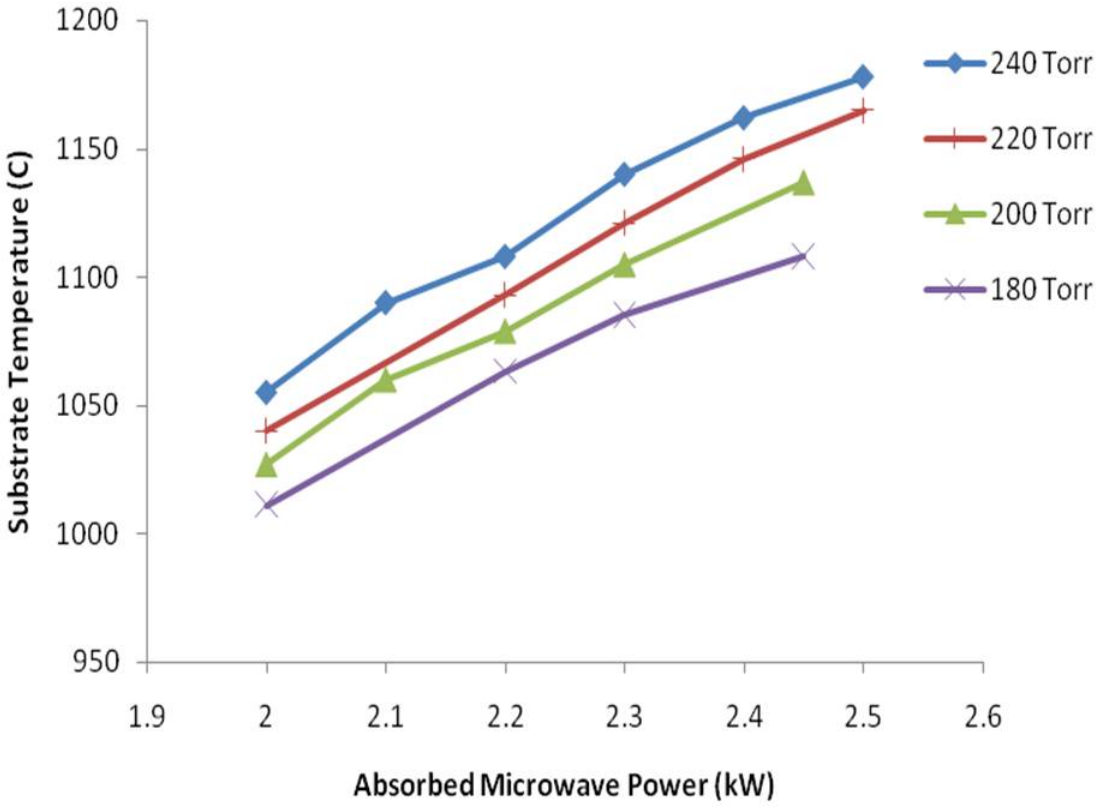

Figure 5.8 The closer view of reactor roadmap of the Reactor B, showing the substrate temperature versus absorbed microwave power (180 Torr to 240 Torr) [53]

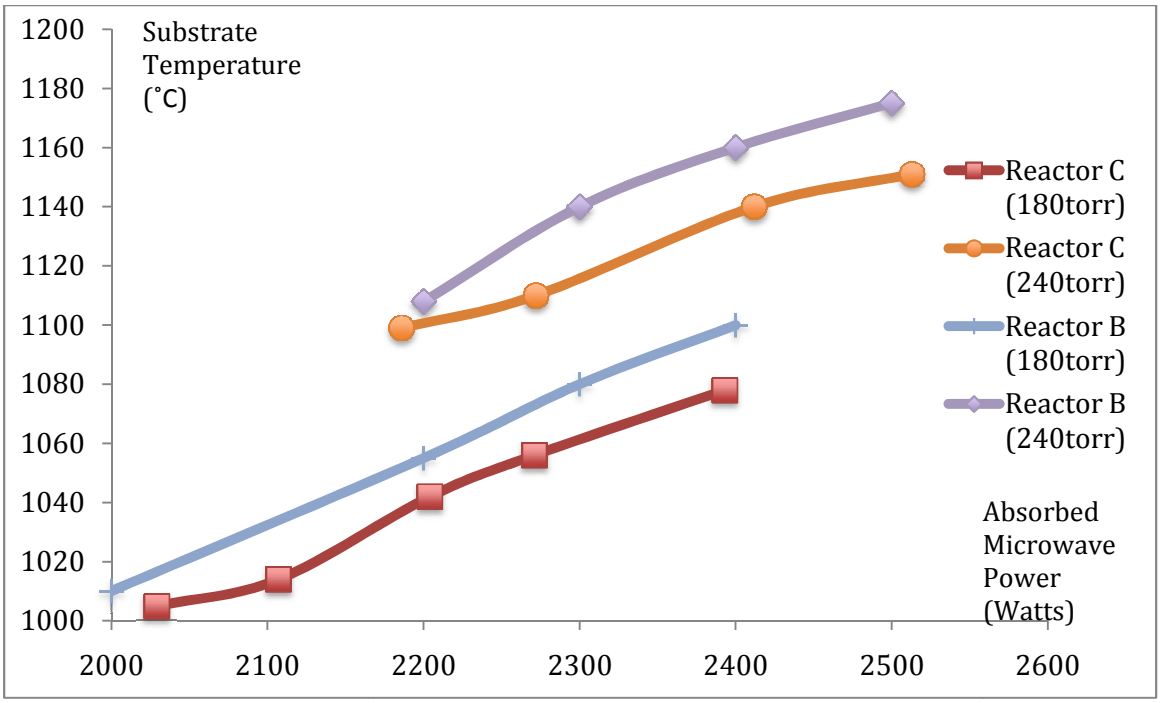

Figure 5.9 The comparison of the closer view of reactor roadmap between the Reactor B and the Reactor C

5.5 Microwave Power Density at High Pressure

An important visual difference between high pressure (>75 Torr) and low pressure (< 75 Torr) microwave discharges is that at low pressure the microwave discharge fills the quartz dome and produces a diffusion loss dominated, cold (gas temperatures are less than 1500 K), non-equilibrium plasma, while at high pressure the microwave discharge is hot (gas temperatures usually are greater than 2500 K), is volume recombination dominated and becomes a more thermal-like discharge. The photographs displayed in Figures 5.11 and 5.12 show how the plasma discharges shape, color and size vary as the operating pressures varies from 75 Torr to 240 Torr. A Canon EOS 20D Digital single-lens reflex

camera with a Canon EF wide-angle zoom lens 17-40mm F/4.0 was used to take these plasma discharge pictures. Two meshed view windows are located on the middle of the cavity wall. The picture taker stood beside the cavity, and held the camera so that the discharge was viewed through either of the reactor wall view windows at about 45 degrees against top surface of the quartz dome. The input experimental variables are the same as those that were used in the roadmap measurements (see Section 5.4). The substrate is a 1.5 mm thick, 1-inch silicon wafer. Forward power is 1900 W for the low to medium high pressures, i.e. from 75 Torr to 165 Torr, and 2700 W for the high pressure regime from 180 Torr to 240 Torr. The reason to increase the forward power is that in the high pressure regime, we need to provide more power to maintain the plasma or it will go out. This is also indicated in the reactor roadmap plots of Figure 5.6. Also at low pressure, if the forward power is too much, the plasma will expand, touch and heat the quartz walls.

The experimental average power density versus pressure can be determined from discharge photographs as those shown in Figure 5.10 and 5.11. The discharge power density is defined as the input absorbed power divided by the plasma volume. At each experimental operating condition, i.e. pressure, gas mixture, etc., the plasma volume was approximated by taking size calibrated photographs of the discharge as it is displayed in Figure 5.10 and 5.11. From the visual images of these plasma discharges during diamond deposition from 75 Torr to 240 Torr, we can see the plasma discharge constricts as pressure increases. It has also been found that at high pressure, the discharge: 1)

separates from the walls, 2) becomes volume recombination dominated, and 3) is thermally inhomogeneous.

In each photograph the discharge volume is defined as the brightest luminescence region of the discharge; i.e. the white central discharge core. The discharge volume can be then determined directly from each of the photographs. At each experimental operating condition, i.e. each photo, the discharge power density is then determined by dividing the absorbed power by the measured discharge volume.

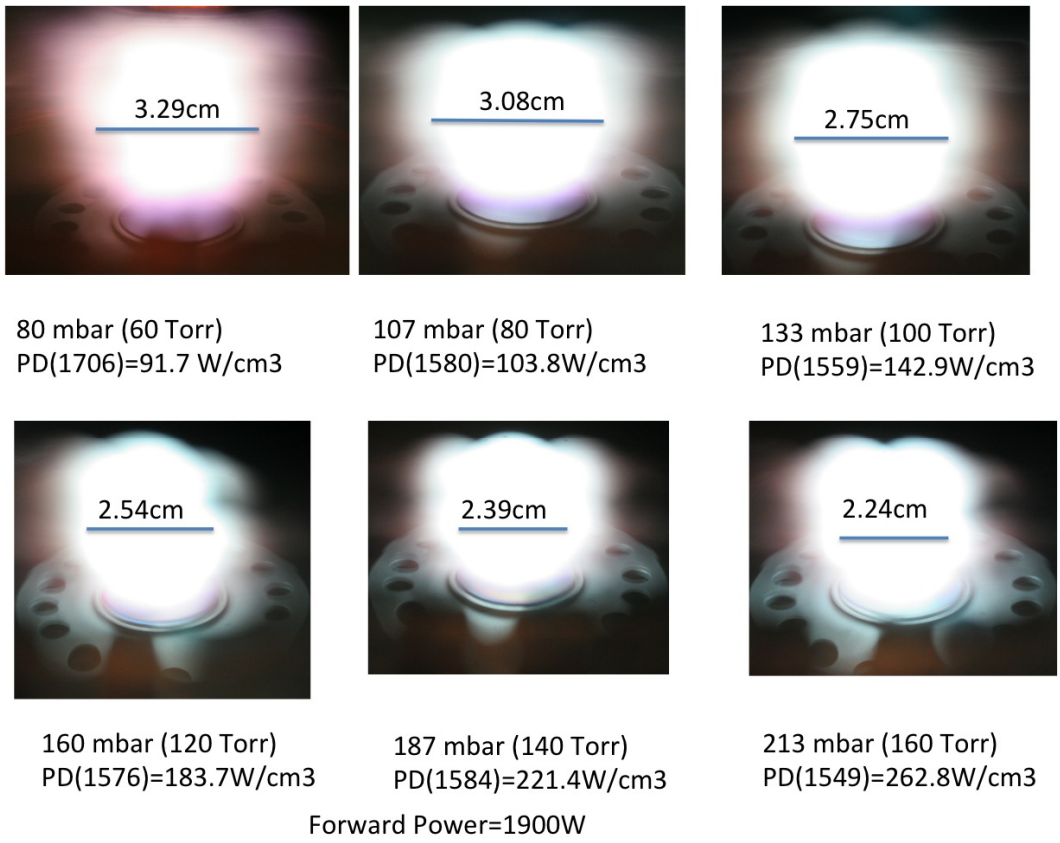

Figure 5.10 The plasma discharge at 60 Torr to 160 Torr with forward power 1900 W, Z_S = -4.8 mm, CH_4/H_2 = 3%

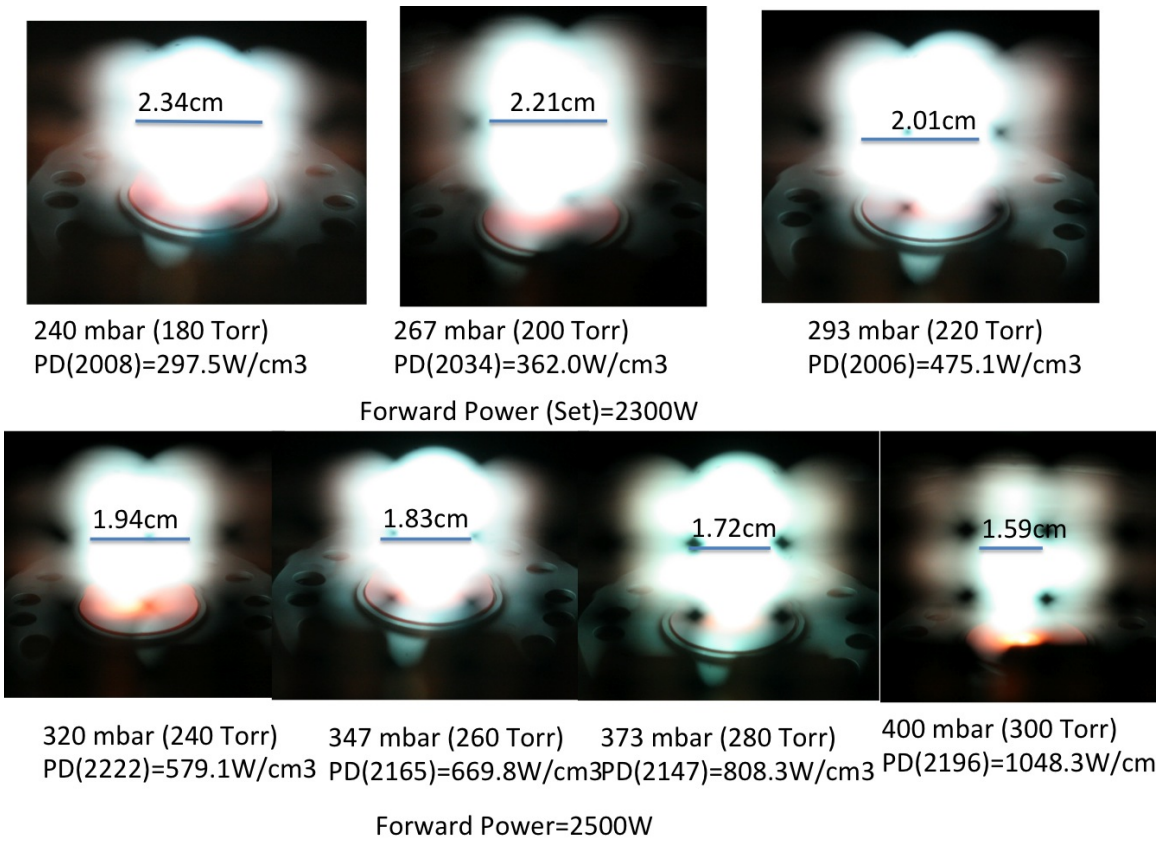

Figure 5.11 The plasma discharge at 180 Torr to 300 Torr with forward power 2500W, Z_S = -4.8 mm, CH_4/H_2 = 3%

An example of the experimentally measured discharge power density versus pressures for Reactor A, B, and C is shown in Figure 5.12. At a given operating pressure we can see that between 60 – 200 Torr Reactor C has almost 5-10% more power density than Reactor B and about 8 times more power density than Reactor A at low pressure, i.e. 80 Torr, and about 5 times at high pressure, i.e. 140 Torr. At pressures above 200 Torr, there is a much steeper rise in absorbed power density in the Reactor C than the Reactor B.

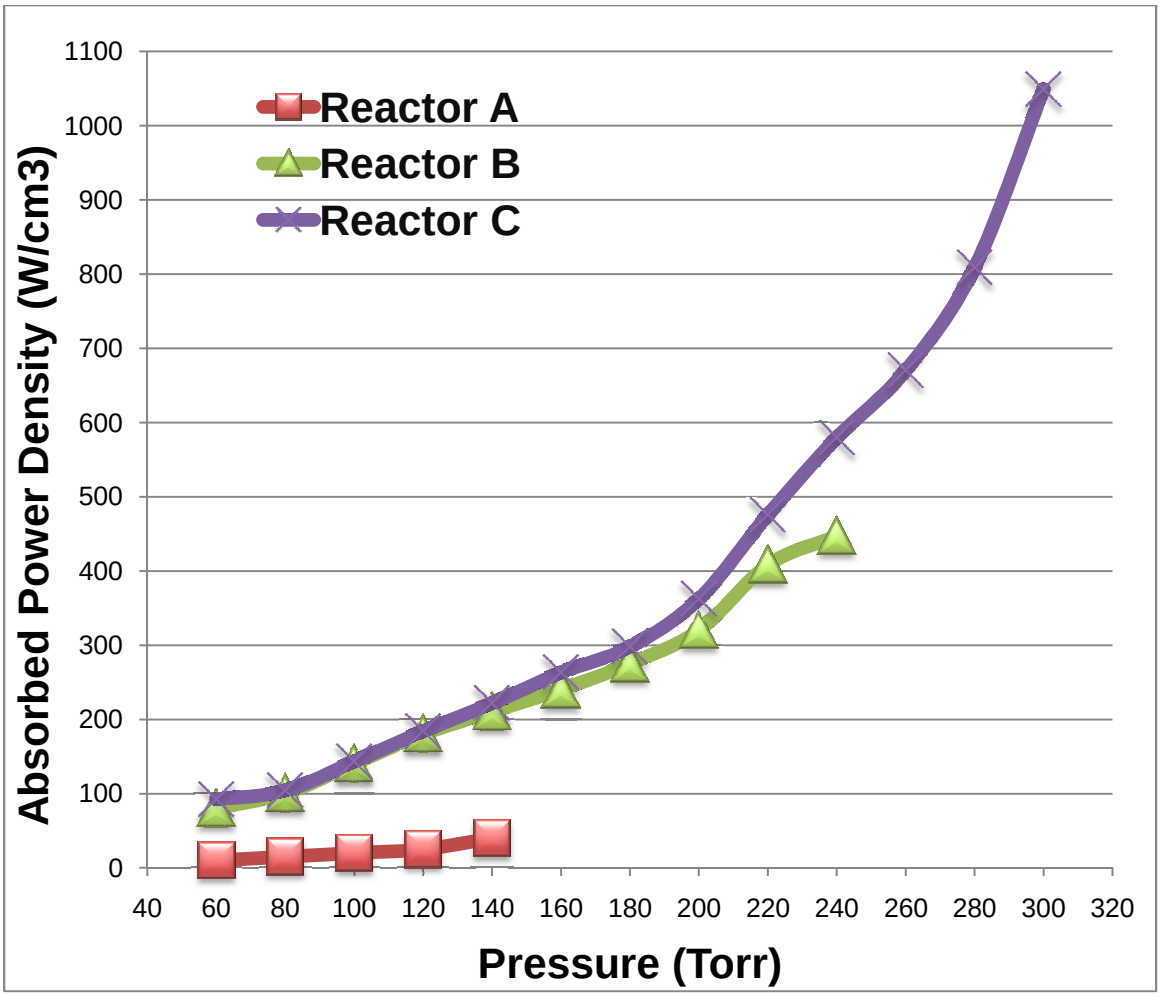

Figure 5.12 the comparison of the absorbed power density versus pressure for Reactor A, B, C

One reason the absorbed power density increases dramatically from Reactor A to either the Reactor B or C is that Reactor B and C have introduced a smaller cooling stage. This was done by reducing the substrate holder radius R_4 (See Figure 4.6) from 5.08 cm to 3.24 cm and by reducing the coaxial cavity inner conductor (cooling stage) radius R_3 from 4.13 cm to 1.91 cm. Since the electric field is normal to the top surface of the inner conductor electrode, when the

electrode diameter is reduced, the normal electric field on the electrode increases. This higher electric field creates and maintains the discharge, i.e. it is related to the electrical field that is impressed on the discharge, and thus results in higher discharge absorbed power densities in Reactor B and C.

5.6 Polycrystalline Diamond Synthesis

5.6.1 Introduction

This section presents the polycrystalline diamond deposition experimental results for Reactor C. The section begins with a description of the experimental multivariable operating parameter space, followed by discussion of experimental results of the synthesized diamond. In particular, the growth rate, surface morphology, Raman spectrum including full width half maximum (FWHM) are presented. A comparison between the growth rates and the synthesized diamond quality of Reactor B and C is presented.

5.6.2 Diamond Growth Rate

This section presents the experimental results of the output variable growth rate as a function of the operating pressure. A total of 20 experiments were conducted in polycrystalline diamond MPACVD synthesis. Polycrystalline diamond film synthesis was investigated over a range of experimental conditions and the results are shown in Figure 5.14 – 5.16 and are also compared with the results of the Reactor B. The experimental variables are listed below.

(1) Controllable input variables, U_1, which include the following

a) Deposition pressure, Variable: p = 165 - 240 Torr

b) Incident microwave power, Variable: P_i = 1.7 – 2.2 kW

c) Feed gas composition, Variable: c = CH_4 / H_2 = 2% - 5% and no N_2 addition. The residual N_2 from the input gases is no more than 3 ppm (see Section 5.2.2). The residual N_2 from the leaking of the vacuum system is 1.87 ppm, given the leaking rate 1 mTorr/hr as measured. (see Section 5.2.3) Thus the total input N_2 is ≈ 5 ppm.

d) Total flow rate, Fixed: f_t= 400 sccm

(2) Reactor geometry variables, U_2, which include the following

a) Applicator size and configuration, Fixed

b) Substrate position, Fixed: Z_S = -4.8 mm

c) Molybdenum substrate holder design, Fixed: for 1-inch silicon wafer

d) Electromagnetic mode: Mode is fixed in all experiments

e) Cavity tuning, Variable: L_S = 16.2-16.5 cm

f) Quartz dome geometry, Fixed: #1 quartz domes have been used

(3) Deposition process variables, U_3, which include the following

a) Substrate material and size, Fixed: 1-inch 1.5mm-thick silicon wafer

b) Deposition time, Variable: t = 6 - 100 Hours

(4) Internal variables X, which include

a) Substrate temperature, Variable: $T_S \approx 1020 – 1100\ ^{\circ}C$

c) Absorbed microwave power, Variable: P_{abs}= 2.0 – 2.5 kW

d) Plasma volume, Variable: V_p = 3.2 - 3.8 cm^3

e) Absorbed power density, Fixed: $\langle P_{abs} \rangle = P_{abs}/ V_p \approx 600\ W/cm^3$

The polycrystalline diamond films were deposited on 1-inch silicon wafers as pressure varied from 165 Torr to 240 Torr. The methane concentration varied from 2% to 4% with no addition of nitrogen. For each experiment, the reactor has been finely tuned to its optimized condition without changing Z_S. In all experiments for Reactor C, Z_S = -4.8 mm. For each experimental run the substrate temperature varied slightly between 1020 $^{\circ}$C to 1100 $^{\circ}$C. In order to

keep the substrate temperature in such narrow range, for example, at 240 Torr operating pressure, the absorbed microwave power was adjusted between 2.0 kW to 2.4 kW. (See Roadmaps on Figure 5.6 and 5.9) As the input power was slightly adjusted the absorbed power densities don't vary very much since T_S was adjusted to be within the deposition, 1020-1100 $^{\circ}$C, window.

Figure 5.13 shows polycrystalline diamond growth rate versus operating pressure for Reactor C. See Section 3.4.1 for the measurement of PCD growth rate. According to CVD diamond growth theories (see Section 2.2.2), CVD diamond growth rates increase as methane concentration increases or as pressure increases while all the other experimental parameters are held constant. Growth rate also increases slightly with growth time. For example, Kuo et al [23] has shown that growth rate increases by as much as 10-20% as growth time is increased from 6 hours to 100 hours. Thus the growth time is also indicated in Figure 5.14 next to each data point. Taking into account of the differences in growth times the results in Figure 5.13 match what we expect from the theory; i.e. the growth rate increases with pressure, with methane concentration and growth time.

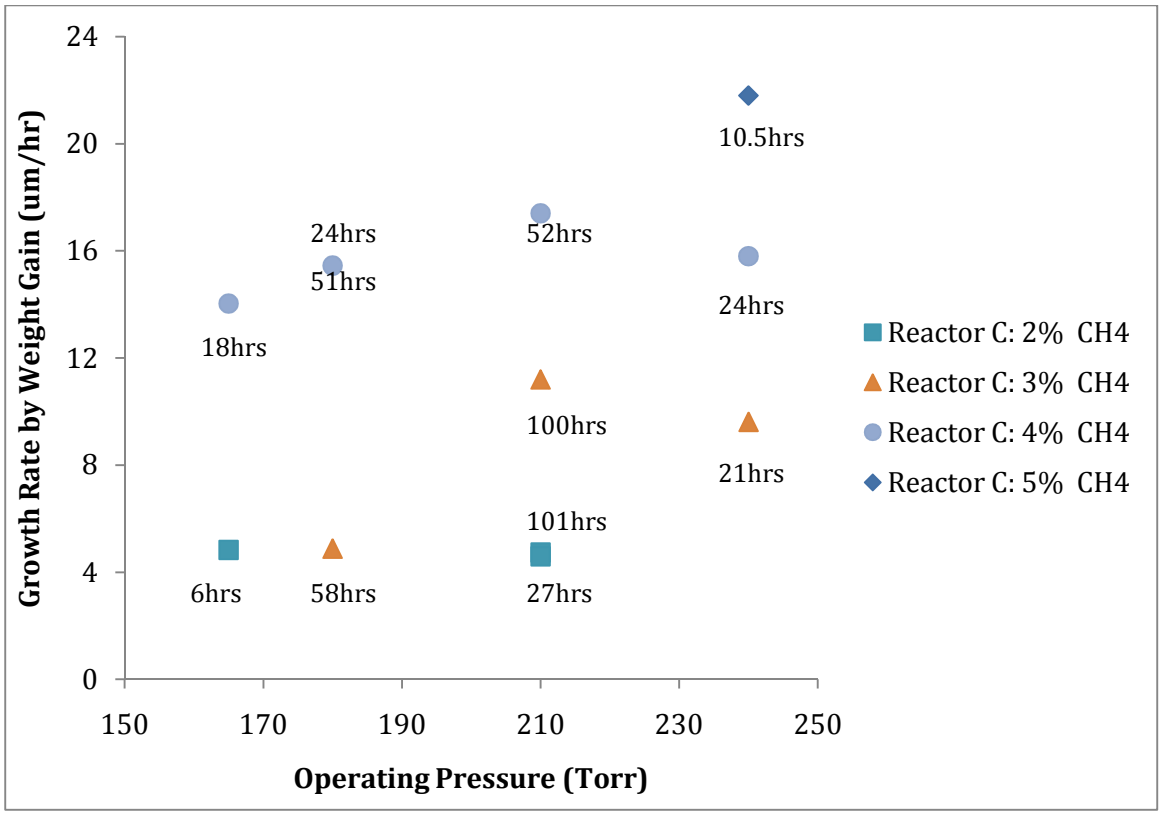

Figure 5.13 Polycrystalline diamond growth rate versus pressure of Reactor C at different CH_4 concentration

From Figure 5.14-5.16 compare the growth rate of Reactor B and C. We can see at lower methane concentrations (CH_4/H_2 = 2%) the growth rates are very close for Reactor B and C versus pressure. However when CH_4/H_2 = 4%, Reactor C's growth rates are higher than Reactor B. For example at 180 Torr, the growth rate of reactor C is about 50% more than Reactor B at 4% CH_4/H_2.

In general the experimental performance between reactors B and C is similar; that is when operating under similar experimental conditions the performances do not greatly differ. This is not surprising since the two reactors are evaluated under the same conditions and have identical substrate holder geometries. One

important difference is the performance with higher methane concentrations of 4% and 5%. Here Reactor C can operate for longer times with higher growth rates.

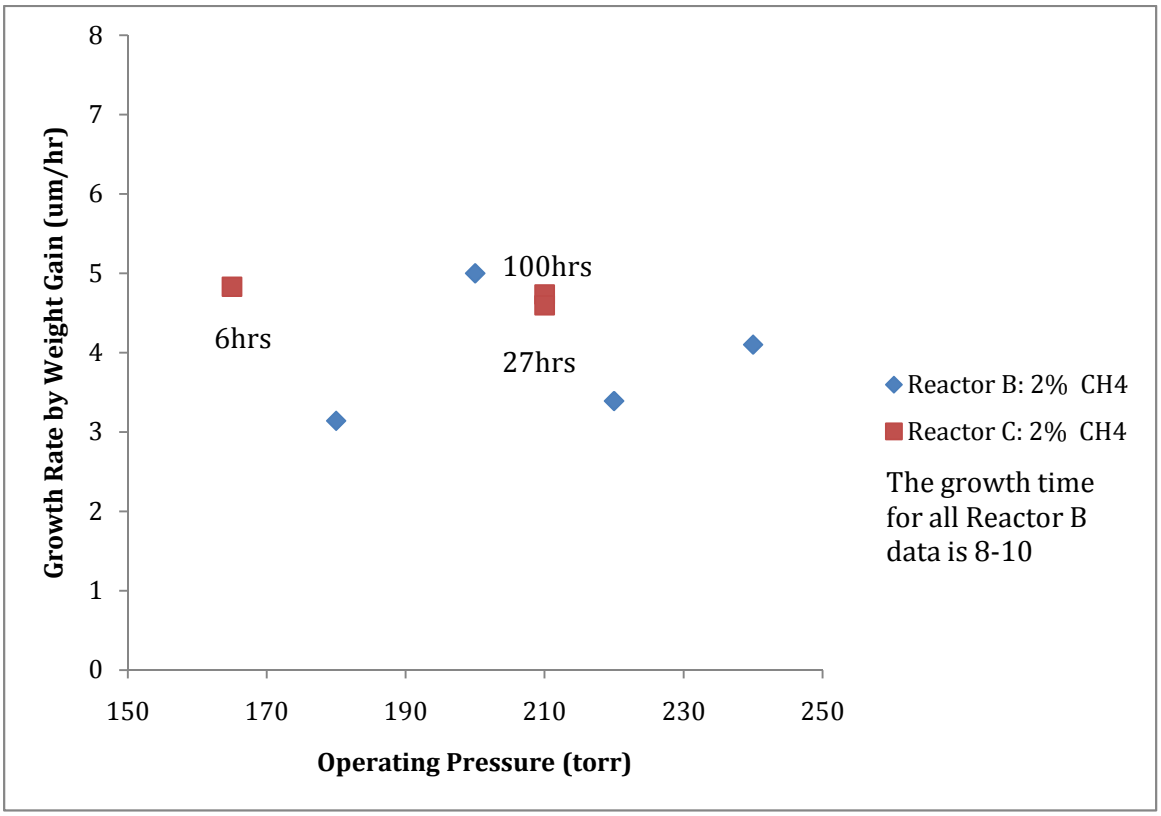

Figure 5.14 Polycrystalline diamond growth rate versus pressure of Reactor B and C at 2% CH_4/H_2

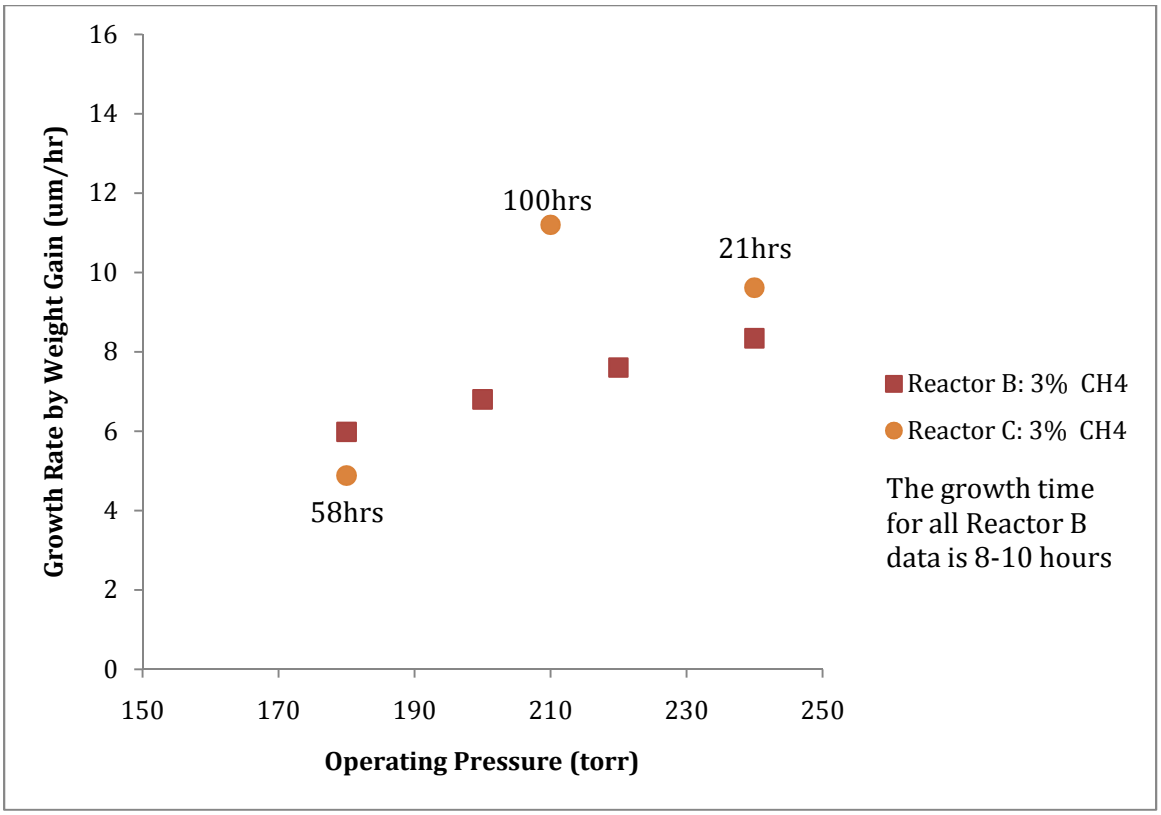

Figure 5.15 Polycrystalline diamond growth rate versus pressure of Reactor B and C at 3% CH_4/H_2

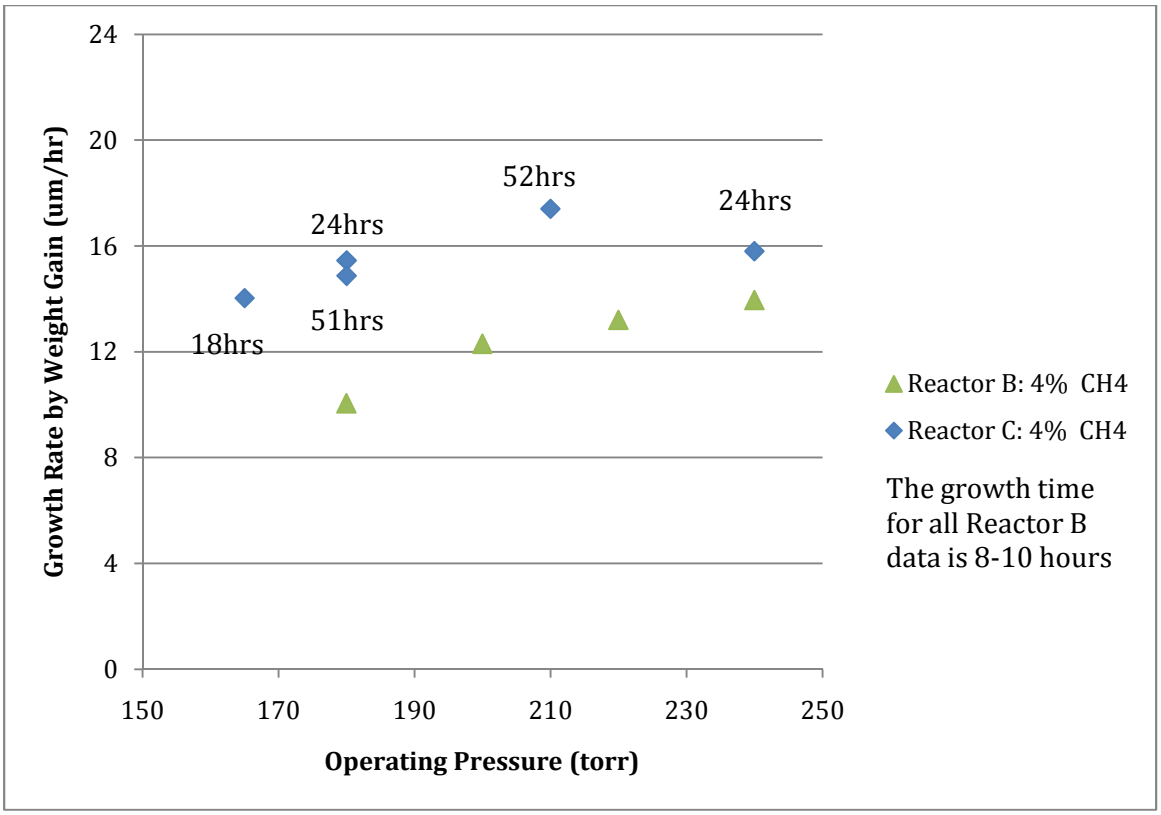

Figure 5.16 Polycrystalline diamond growth rate versus pressure of Reactor B and C at 4% CH_4/H_2

5.6.3 Diamond Surface Morphology

Figure 5.17 displays a picture of a 1.12 mm thick polycrystalline diamond plate grown on a 1-inch silicon wafer. It was grown at 3% CH_4/H_2, no N_2, 210 Torr for 100 hours resulting in an average growth rate of 11.2 μm/hr. The diamond plate has not been polished after deposition and as a result the top diamond surface is made up of many small (100-200 microns) diamond crystals.

Figure 5.17 1.12mm-thick Unpolished PCD Plate on 1” Si Wafer, grown at 3% CH_4/H_2, no N_2, 210 Torr for 100 hours results within an average growth rate of 11.2 μm/hr

Figure 5.18-5.19 displays typical synthesized PCD surface morphology at different methane concentrations and operating pressures. Since the growth time is a major factor for the crystal size, the samples have been divided into two groups. Figure 5.18 displays three samples with growth times from 6 hours to 24 hours. These growth times are considered as short run experiments. Figure 5.19 shows another three samples with long growth times of 51 to 101 hours.

The grown polycrystalline diamonds in both groups exhibits a pyramidal shape, square, and triangle structure as can be seen in the figures. These shapes are dependent on the operating pressure, gas chemistry, microwave forward power, substrate temperature, and deposition time. The crystal grain size

mostly depends on the operating pressure, gas chemistry, growth time and film thickness. Typical grain sizes shown in Figure 5.18-5.19 are 10 to 40 μm for 160 – 240 Torr, 2 – 5% CH_4/H_2 and 6-24 hours. The grain size can range as large as 80 to 200 μm for 180 – 240 Torr, 2 – 5% CH_4/H_2 for the longer, 50 - 100 hours, growth times shown in Figure 5.19.

It is well known that the grain size increases with growth time and methane concentration [63] and film thickness. Basically the film grain size increases as the film thickness increases. This is caused by the fact that some of the many initially nucleated crystals overgrow others as growth time of the film increases. Usually we can see a random orientation of small crystals at the initial film. As the film grows, the crystals that grow with their direction of fastest growth perpendicular to the surface become taller than their competitor crystals. The thicker the film the larger the crystals on the surface become. This grain size variation with deposition time and film thickness was also observed by Kuo [24], Zuo [64] and Hemawan [53]. The experimental results displayed in Figure 5.18 and 5.19 indicate the expected PCD growth behavior versus growth time, methane concentration and film thickness.

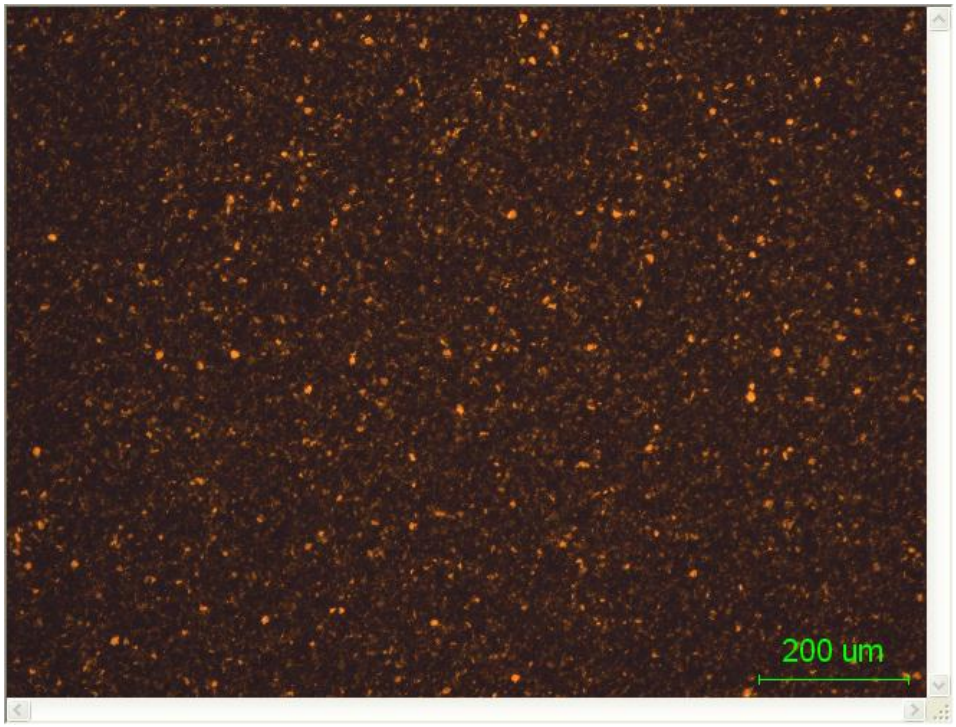

(a) GYJ016 CH_4/H_2=2% Other growth condition: growth time = 6 hours; pressure = 150 Torr; substrate temperature = 820 ℃; absorbed power = 2510 W; Z_S = -4.8 mm; growth rate = 1.87 µm/hr; film thickness (measured by weight gain) = 11.2 µm

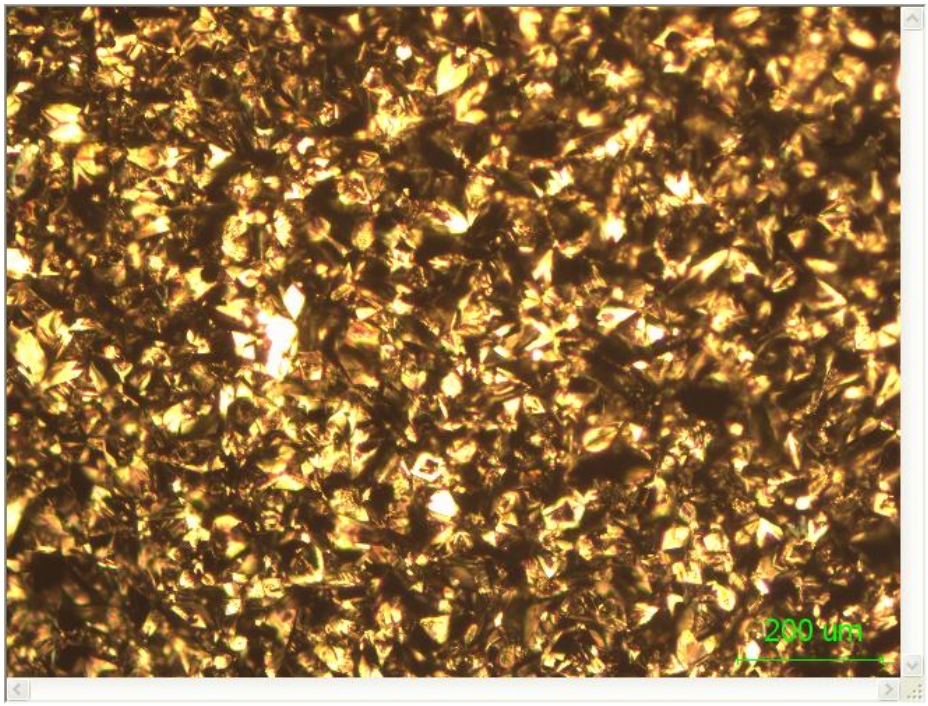

(b) GYJ036 CH_4/H_2=4% Other growth condition: growth time = 24 hours; pressure = 240 Torr; substrate temperature = 1120 ℃; absorbed power = 1870 W; Z_S = -4.8 mm; growth rate = 15.8 μm/hr; film thickness (measured by weight gain) = 379.2 μm

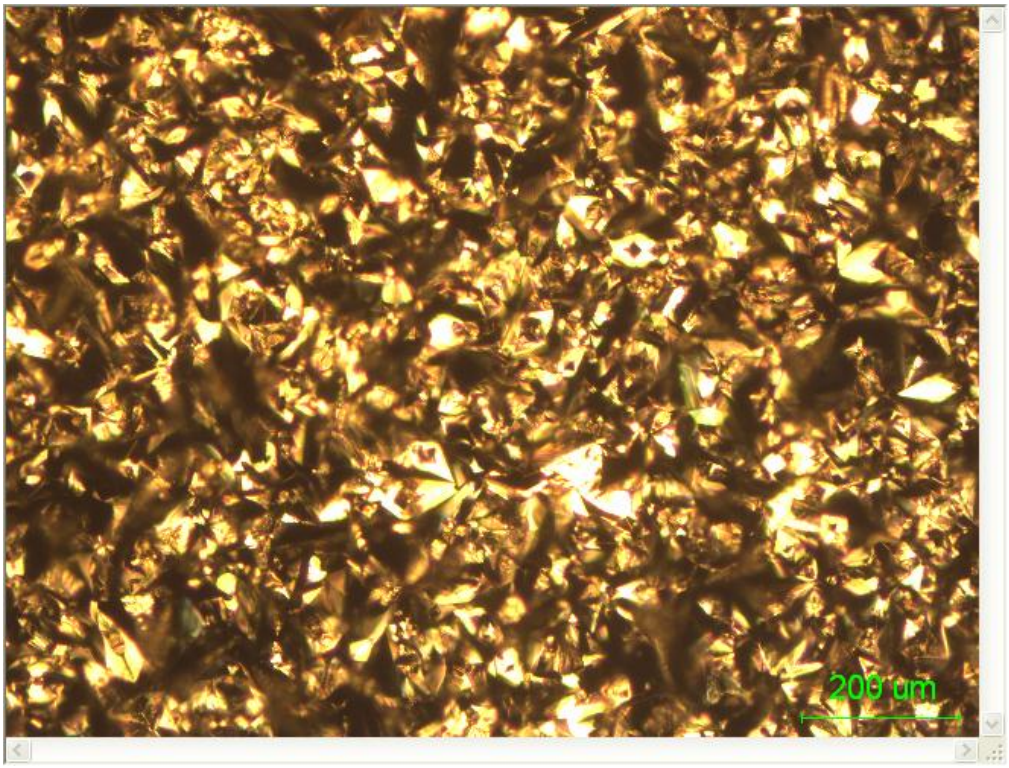

(c) GYJ037 CH_4/H_2=5% Other growth condition: growth time = 10.5 hours; pressure = 240 Torr; substrate temperature = 1127 ℃; a bsorbed power = 2115 W; Z_S = -4.8 mm; growth rate = 21.8 μm/hr; film thickness (measured by weight gain) = 228.9 μm

Figure 5.18 Surface morphology of polycrystalline CVD diamond Group #1

Below is another group which are considered as long run experiments. Figure 5.19 shows another three samples growth time from 51 hours to 101 hours.

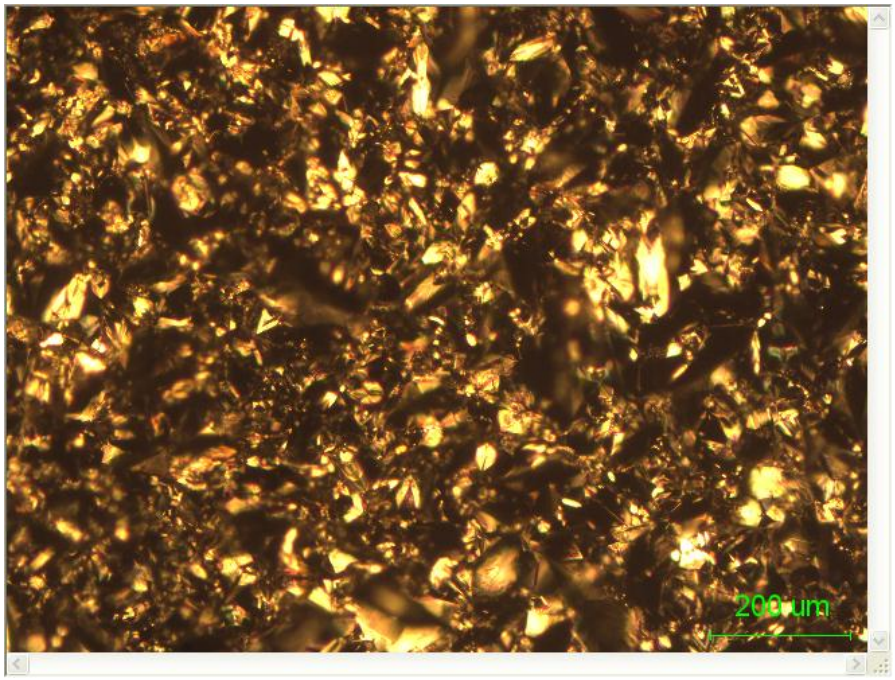

(a) GYJ031 CH_4/H_2=2% Other growth condition: growth time = 101 hours; pressure = 210 Torr; substrate temperature = 1136 ℃; absorbed power = 2327 W; Z_S = -4.8 mm; growth rate = 4.73 μm/hr; film thickness (measured by weight gain) = 477.7 μm

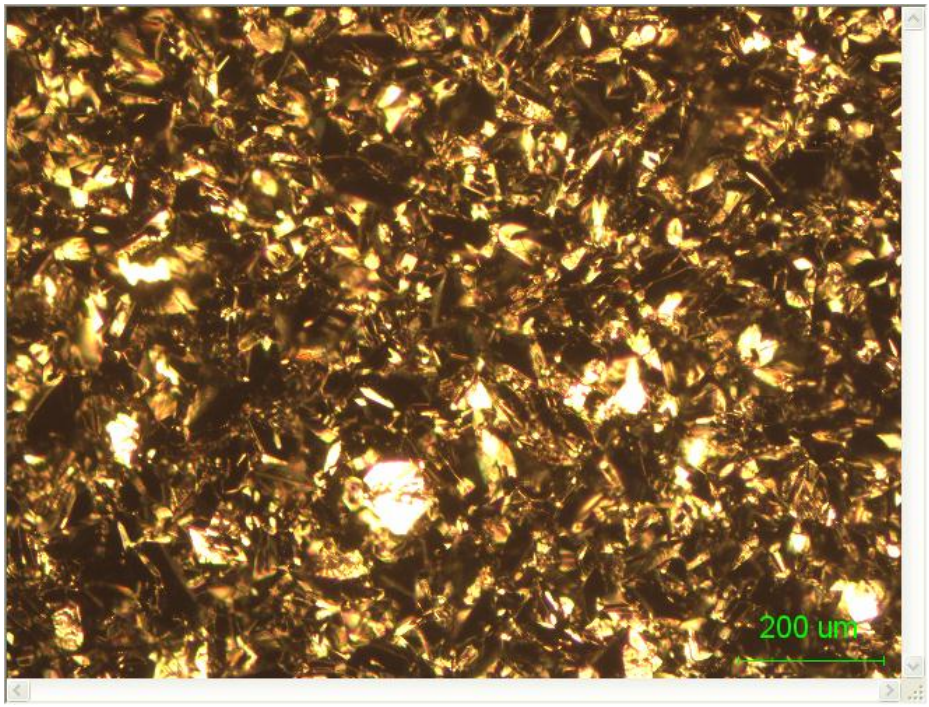

(b) GYJ027 CH_4/H_2=3% Other growth condition: growth time = 58 hours; pressure = 180 Torr; substrate temperature = 1145 ℃; absorbed power = 2219 W; Z_S = -4.8 mm; growth rate = 4.88 μm/hr; film thickness (measured by weight gain) = 283.0 μm

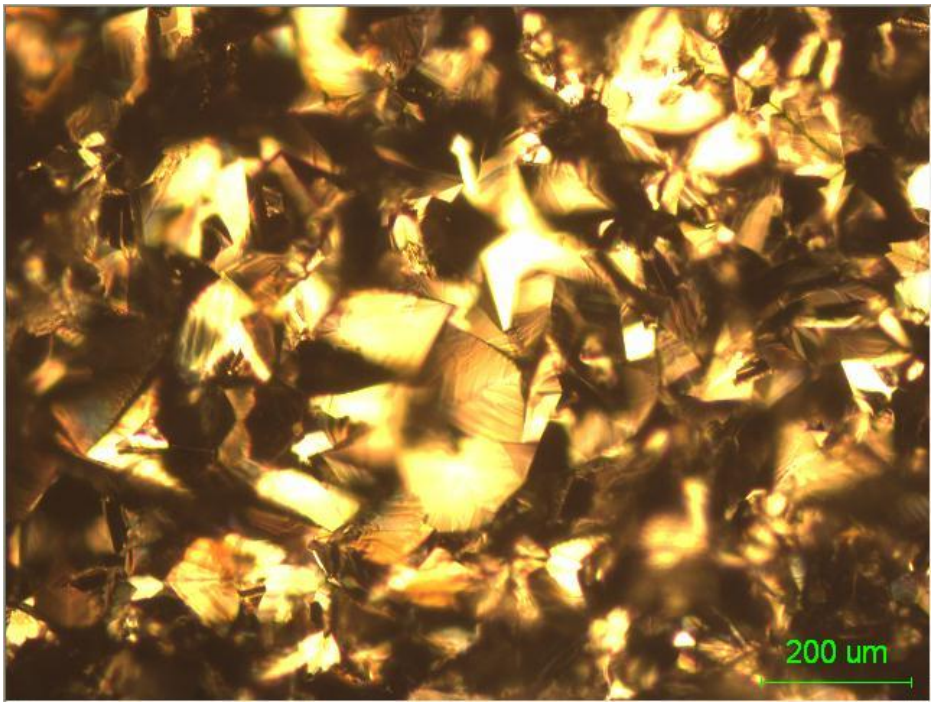

(c) GYJ026 CH_4/H_2=4% Other growth condition: growth time = 51 hours; pressure = 180 Torr; substrate temperature = 1140 ℃; absorbed power = 2207 W; Z_S = -4.8 mm; growth rate = 14.87 μm/hr; film thickness (measured by weight gain) = 758.4 μm

Figure 5.19 Surface morphology of polycrystalline CVD diamond Group #2

5.6.4 Diamond Raman FWHM Measurement

In this section, the typical Raman spectra are presented and Raman full width half maximum (FWHM) is compared between Reactor B and C. Although Reactors B and C share a lot of similarities in designs, Reactor C can be operated at higher pressure and with much longer experimental runs due to its larger reactor and quartz dome dimension (See Chapter 4). Based on the theory

presented in Chapter 2 (Section 2.2.2), microwave discharges in hydrogen and methane gas mixtures constrict at high pressure. More atomic hydrogen will be produced by thermal dissociation at higher pressure than by the direct electron-impact dissociation at lower pressure. So there will be higher densities of radical species, i.e. H and CH_3 radicals, at higher pressure. These results are shown in Figure 2.6. Also the figure shows that the diamond quality increases when the pressure increases. This has been experimentally confirmed by the previous experimental research of Zuo [64] Table 4-3 Page 188 and Kuo [23,24] Figure 2.7-2.8. So it is expected that higher quality of the CVD diamond is easier to achieve in Reactor C than at low pressure using Reactor A.

Figure 5.20 and 5.21 show typical Raman spectrums for CVD diamond films from 1100 to 1700 cm^{-1} at different experiment conditions. We can see from both results the films have Raman spectrums with a strong sp^3 bonding diamond peak around 1332 cm^{-1}. No peaks were detected for the graphite carbon peak at 1597 cm^{-1}. There are separated Raman spectrum measurements from 400 – 1000 cm^{-1} and they also display no peak for sp^2 silicon carbon (520 cm^{-1}). This indicates that the CVD polycrystalline diamond grown in Reactor C contains very little graphitic content in the film and it is a good quality polycrystalline diamond film. See the detailed Raman spectra in Appendix 3 for all polycrystalline film experiments.

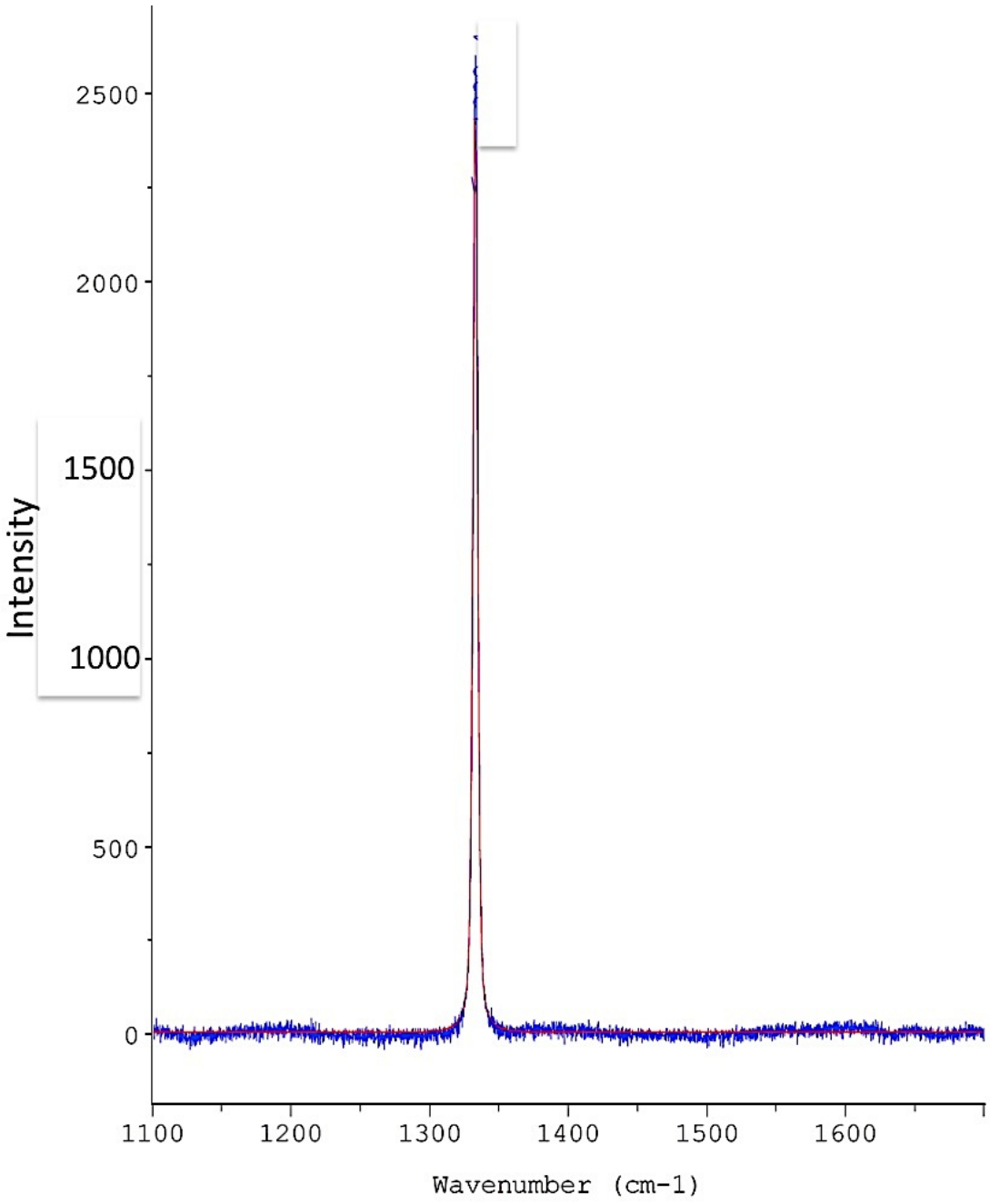

Figure 5.20 Raman spectrum for a CVD diamond film GYJ021

CH_4/H_2=4%; growth time = 18 hours; pressure = 165 Torr; substrate temperature = 1074 ℃; absorbed power = 2570 W; Z_s = -4.8 mm; growth rate = 14.03 μm/hr; film thickness (measured by weight gain) = 252.5 μm

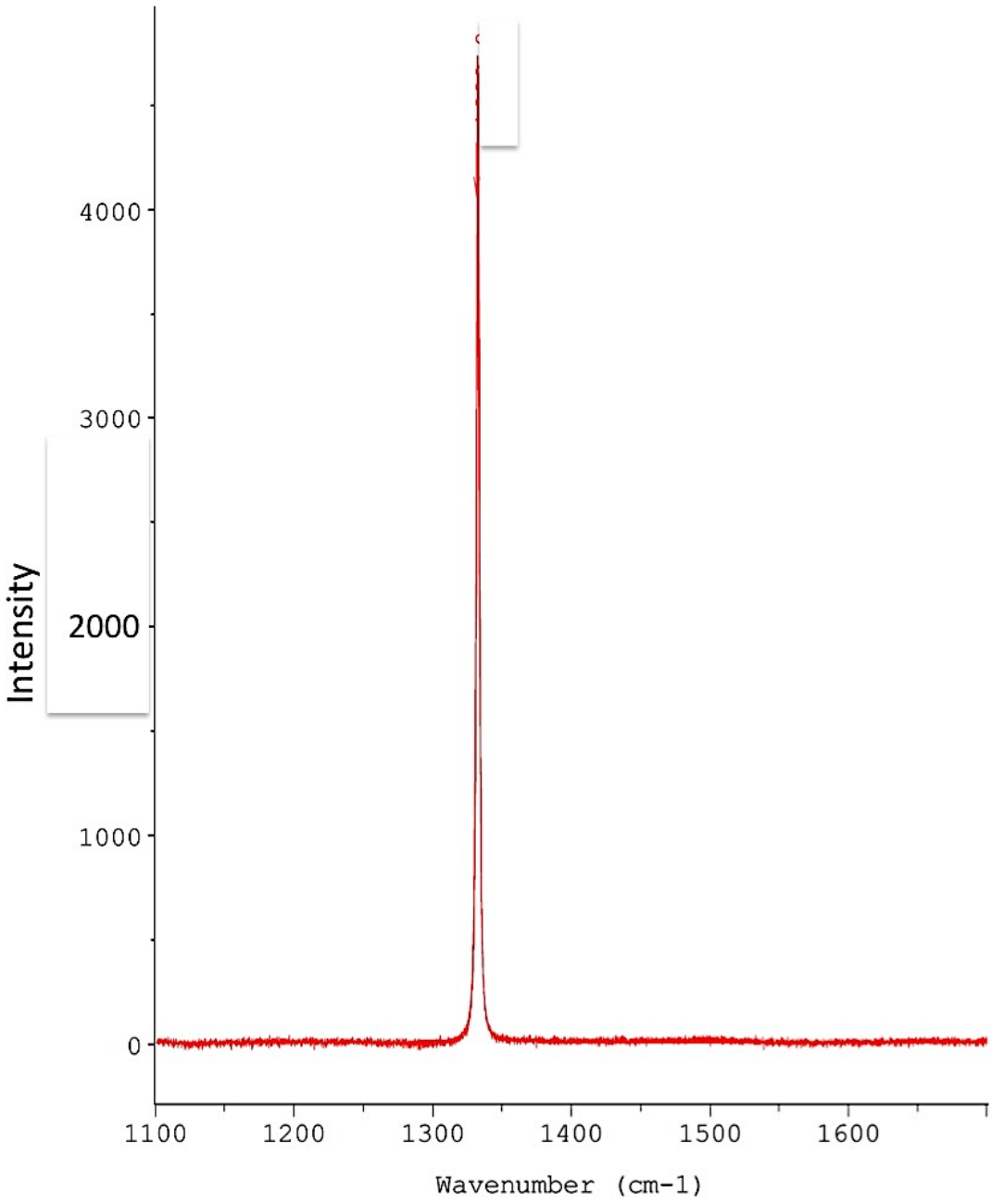

Figure 5.21 Raman spectrum for a CVD diamond film GYJ029 CH_4/H_2=4%; growth time = 52 hours; pressure = 210 Torr; substrate temperature = 1128 ℃; absorbed power = 2429 W; Z_S = -4.8 mm; growth rate = 17.4 μm/hr; film thickness (measured by weight gain) = 904.8 μm

Figure 5.22 displays Raman full width half maximum maximum (FWHM) versus pressures from 165 Torr to 240 Torr under different methane concentrations 2% - 5% CH_4/H_2 for Reactor C. These diamond films show their experimentally measured FWHM vary from 1.97 to 3.6 cm^{-1}. According to the diamond growth theories (Section 2.2.2), CVD diamond quality is expected to increase as pressure increases. Thus when the PCD Raman measurement results summarized in Figures 5.22 for Reactor C are compared with similar results from Reactor A, as expected, the film quality improves as the synthesis pressure increases. Also at higher pressure and higher power densities high quality films can be produced at higher methane concentrations than in reactor A. See in Figure 5.22 for example the FWHM values for the 4% and 5% methane data points lie between 3.2 and 2.2 cm^{-1}. This suggests very good quality PCD films even for the high, 4-5% methane concentrations. This behavior has the benefit of synthesizing high quality PCD diamond films with much higher growth rates than at lower pressures. This result is a significant performance improvement.

While the FWHM data displayed in Figure 5.22 indicates that all synthesized films are of good quality, the variations of FWHM (quality) versus methane concentrations are not consistent with expectations. For example the FWHM are higher for methane concentrations of 2-3% than with methane concentrations of 4-5%. This needs further study with additional experimental runs performed as methane concentration is varied from 2-5%.

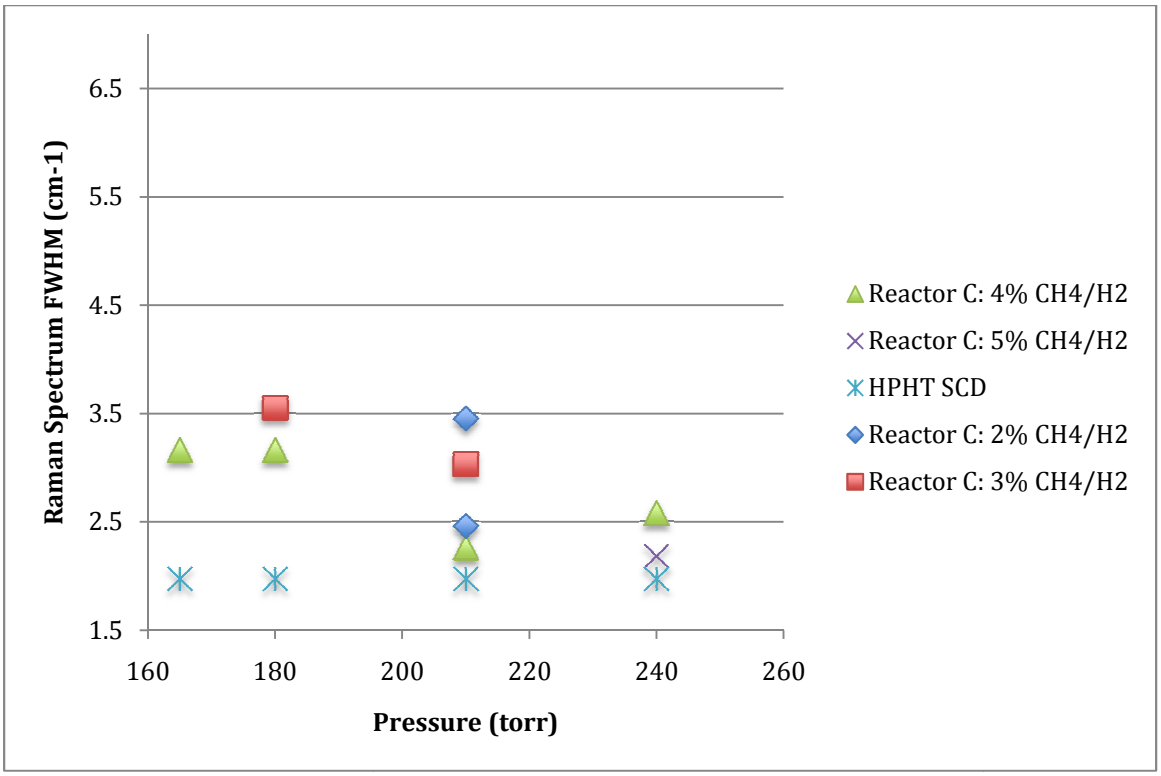

Figure 5.22 Raman spectrum full width half maximum (FWHM) versus pressures from 165 Torr to 240 Torr under different methane concentrations 2% - 5% CH_4/H_2

Shown in Figure 5.23 and 5.24 are the Raman full width half maximum (FWHM) measurements of the CVD polycrystalline diamond films synthesized at various pressures (165 – 240 Torr) and methane concentrations (2% - 5% CH_4/H_2). All experiment data have been compared with Reactor B's data measured at similar conditions [53] except for deposition time. As we can observe from Figure 5.23, at both 2% and 3% CH_4/H_2, the Raman full width half maximum of Reactor C's samples are slightly lower value than of Reactor B's. However, at 4% and 5% CH_4/H_2 (Figure 5.24), the Raman full width half

maximum of Reactor C's samples are much lower than the Reactor B's samples. So these results prove the theory in Chapter 2 that the higher quality diamond can be easier to achieve at higher pressure. Since Reactor C's CVD diamond films are thicker and the grain sizes of the films are larger than Reactor B's, this can be another factor that FWHM is lower for Reactor C's samples than Reactor B's.

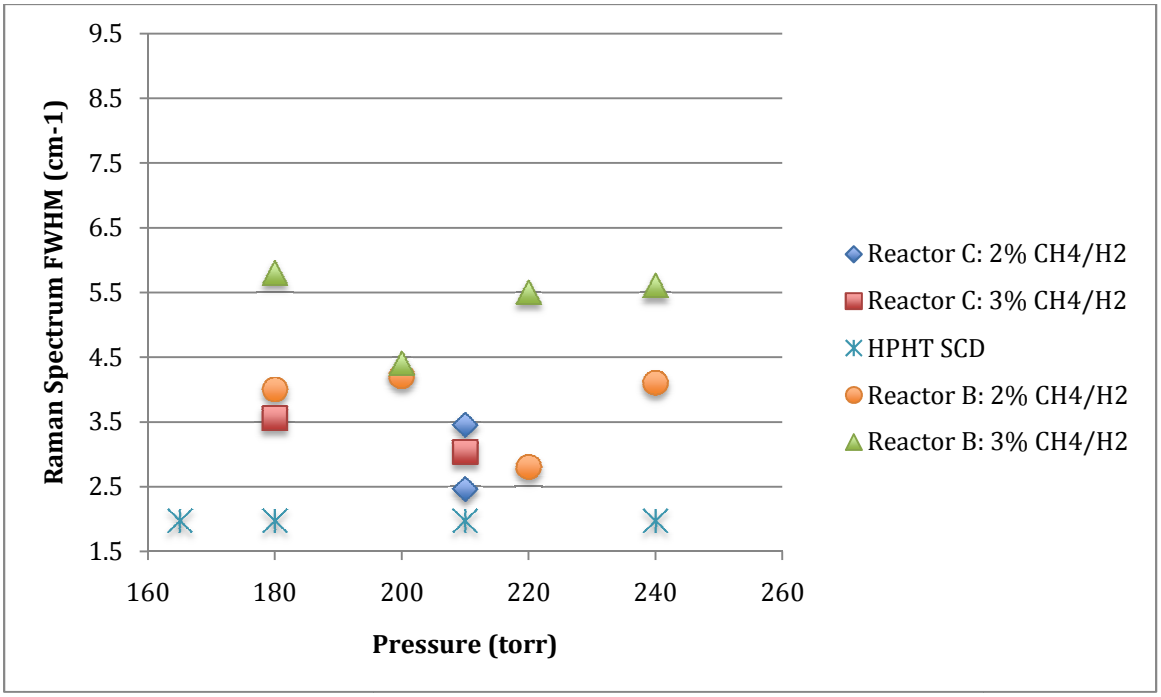

Figure 5.23 Raman spectrum full width half maximum (FWHM) versus pressures from 165 Torr to 240 Torr under methane concentrations 2% and 3% CH_4/H_2. Compared with Reactor B [53]

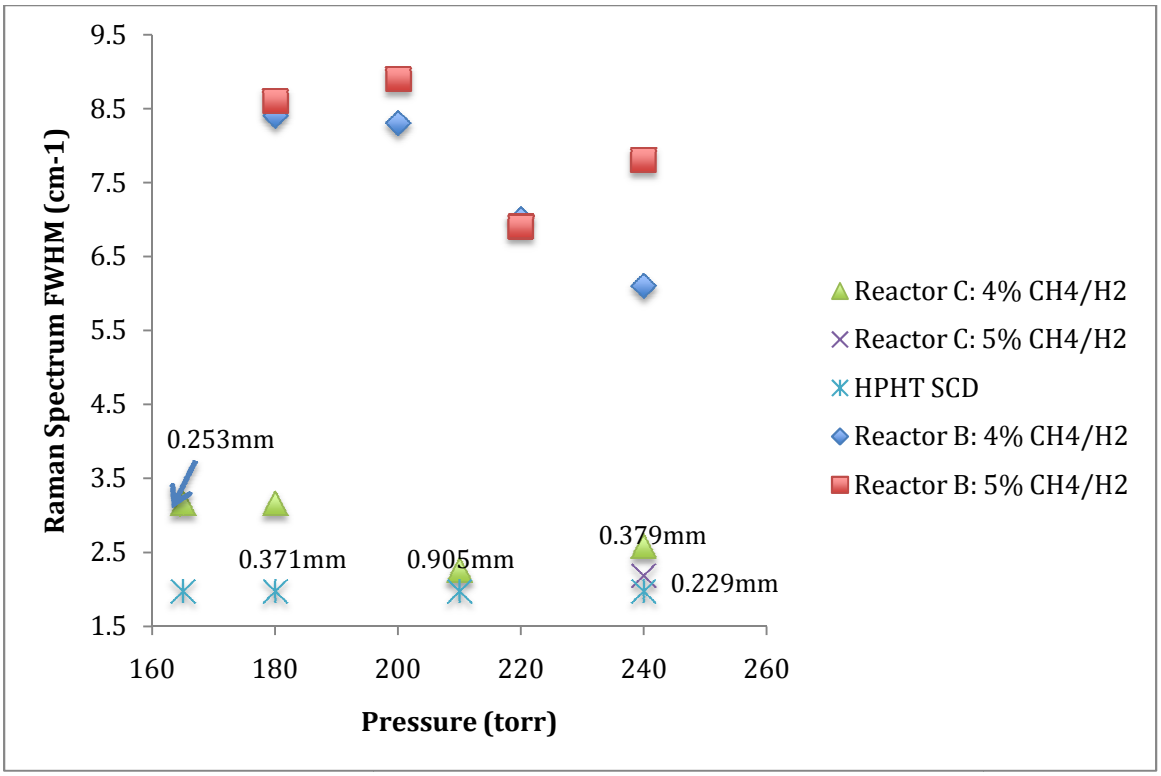

Figure 5.24 Raman spectrum full width half maximum (FWHM) versus pressures from 165 Torr to 240 Torr under methane concentrations 4% and 5% CH_4/H_2. Compared with Reactor B [53]

5.7 Summary

Reactor C was experimentally evaluated in high pressures and high power densities in a PCD synthesis application. In particular the absorbed microwave discharge power density versus pressure and reactor roadmap were measured. Then the polycrystalline diamond (PCD) deposition was performed as a set of exploratory experiments. About 20 experiments were performed as a preliminary reactor design evaluation purposes, i.e. as a first test of Reactor C's ability to

CVD synthesize PCD diamond in the high, 160-300 Torr, pressure regime.

The absorbed power density for Reactor C ranged 300 – 1000 W/cm^3 over a pressure range of 180 – 300 Torr. The growth rate varied from 4.2 - 21.8 μm/hr which is much higher than growth rates for MSU Reactor A (see Chapter 3). The growth rate for Reactor C is slightly higher than Reactor B under similar conditions, but Reactor C is able to operate at higher CH_4/H_2 concentrations at higher pressures and also was able to continuously run for over 100 hours without reactor maintenance. Using the maximum growth rate of 21.8 μm/hr over a 1-inch Si wafer yields a specific yield of 54 kW-h/g. This is approximately 10 kW-h/Ct. Recognizing that additional CVD diamond was deposited beyond the 1-inch wafer out to at least 1 ½ inches the total process specific yield is even lower. The Raman spectrum full width half maximum (FWHM) is 1.97 – 3.6 cm^{-1}. It shows the diamond films from Reactor C have considerably better quality than Reactor B at the higher 4-5% methane concentrations.

After redesigning the reactor, i.e. changing its size and shape, the cooling stage, the quartz dome size and the substrate holder, Reactor C produces higher absorbed power density plasma and operates in a reliable, stable fashion in the high pressure regime (180 – 300 Torr). At a given pressure the plasma shape and position can be adjusted for good to excellent PCD synthesis. The general evaluation of these experimental results can provide additional guidance to further optimize the MSU reactor design for operation at even higher pressures and higher power densities.

CHAPTER 6

REACTOR EXPERIMENTAL EVALUATION: SINGLE CRYSTAL DIAMOND SYNTHESIS

6.1 Introduction

The experimental results of single crystal diamond (SCD) synthesis using the MSU MPACVD Reactor C are presented and analyzed in this chapter. The performance of a microwave plasma assisted CVD (MPACVD) reactor depends on many experimental variables. The concept of the multivariable experimental parameter space for microwave plasma assisted diamond deposition, which has been presented in Section 5.3, continues to be used here. The output performance (Y) of the reactor is a function of input variables U_1, U_2, U_3 etc, i.e. $Y = f(U_1, U_2, U_3)$. The relationship between output variables Y such as growth rate, optical quality versus the input variables such as gas chemistry, gas flow

rate, pressure, etc. are presented as the experimental results for Reactor C synthesizing SCD. At the time of writing this thesis more than 100 exploratory SCD deposition experiments were performed using Reactor C. The total growth time for all of the SCD experiments that are presented is over 2200 hours.

6.2 How to understand reactor performance behavior?

Understanding reactor performance behavior is very difficult not only because of so many variables but also because the relationships between the input and output variables are nonlinear and complex. Currently there are no models that can describe and predict reactor behavior over a wide range of input experimental conditions. Thus this PhD thesis research will experimentally explore the relationships between the input variables and output variables. First, examples of the ranges of experimental variation of the input and output variables that are presented in this chapter are listed below along with expected, experimental ranges.

(1) Controllable input variables, U_1, which include the following

a) Deposition pressure, Variable: p=240 / 260 / 280 / 300 / 320 Torr

b) Incident microwave power, Variable: P_i = 1.7 – 3.0 kW

c) Feed gas composition, Variable: c = CH_4/H_2 = 3% / 5% / 7% / 9% and N_2 = 0 / 5 / 10 / 15 / 20 ppm

d) Total flow rate, Variable: f_t= 200 / 400 / 600 / 700 sccm

(2) Reactor geometry variables, U_2, which include the following

a) Applicator size and configuration, Fixed: Reactor C except in Section 6.12 where Reactor C's performance is compared with the performance of Reactor B.

b) Substrate position, Variable: Z_S = -8 to 0 mm

c) Substrate holder design, Variable: All substrate holders used in the experiments were the same holders used in PCD experiment shown in Figure 5.4. The "generic" insert for SCD experiment is shown in Figure 6.1. The differences between inserts were the pocket dimensions and thicknesses. The substrate deposition temperature, T_s, was varied by varying the insert thickness. The detailed drawing of the insert is shown in Appendix D.

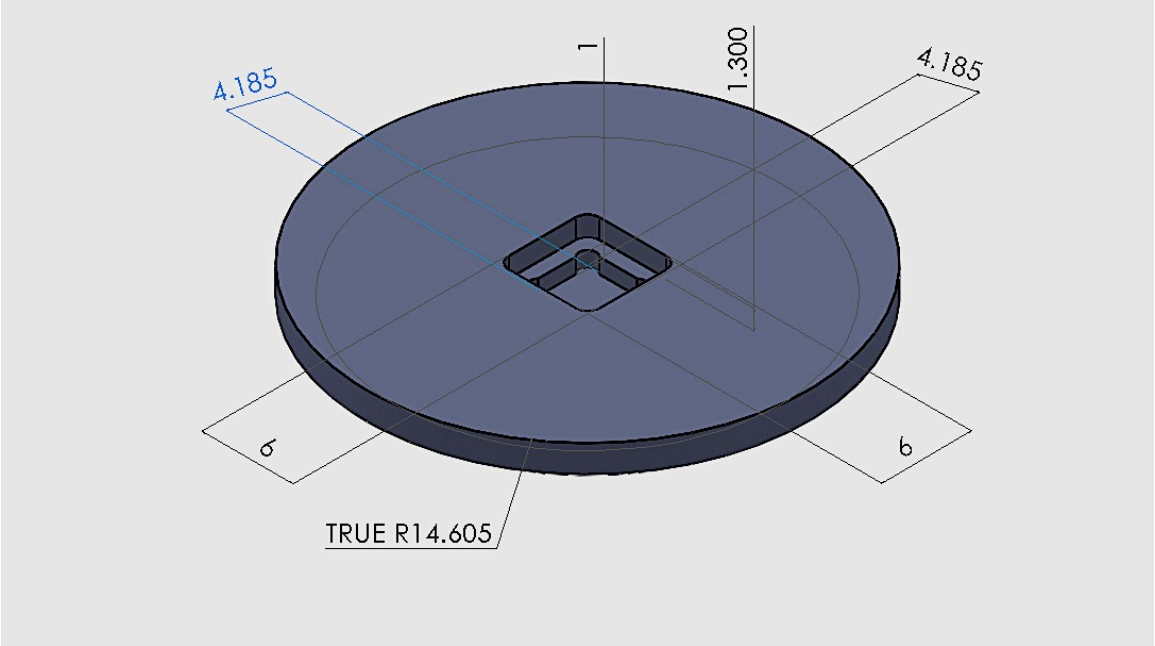

Figure 6.1 Side cross sectional view of generic pocket holder (unit: mm)

d) Electromagnetic mode: The EM mode, which is described in Chapter 4, is fixed in all experiments

e) Cavity tuning, Variable: L_S = 15.5 – 16.5 cm

f) Quartz dome geometry, Variable: four quartz domes have been used #1 / #2 / #3 / #4 (the dome height varies slightly within 1mm due to manufacturer).

(3) Deposition process variables, U_3, which include the following

a) Substrate material and size, Variable: Width*Length*Height=3.5mm*3.5mm*1.4mm HPHT diamond (S);

4.8mm*4.8mm*1.5mm HPHT diamond (M); and

7.0mm*7.0mm*1.2mm HPHT diamond (L)

b) Deposition time, Variable: t = 6 – 100 Hours

c) Substrate cleaning procedure and Reactor start-up, shutdown procedures as is described in Sections 6.3.1 and 6.3.2, respectively.

(4) Internal variables X, which include

a) Substrate temperature, Variable: T_S = 900 – 1400 $^{\circ}$C

b) Absorbed microwave power, Variable: P_{abs}= 1.4 – 2.4 kW

c) Plasma volume, Variable: V_p = 4 - 10 cm^3

d) Absorbed power density, Variable: $<P_{abs}>$ = P_{abs}/ Volume of plasma = 300 – 1000 W/cm^3

(5)Output variables, Y, which can be divided into two groups.

I. Reactor performance, Y_1 includes

a) Linear growth rate: 16 – 100 μm / hr as measured by linear encoder

b) Total growth rate by weight gain: 100– 650 mg / hr

c) Carbon conversion efficiency (CCE): 3 - 10% (See how to calculate CCE at Section 3.4.2)

d) Specific yield (SY): 100-3000 kW-h/g (See how to calculate SY at Section 3.4.3)

It is important to note that both carbon conversion efficiency and specific yield calculations employed in this Chapter assume that the SCD deposition on the top surface area of the diamond seed substrate is the only diamond deposited. However in each experimental run presented in this chapter there is, in addition to the SCD deposited on the HPHT diamond seed, considerable PCD diamond is deposited on the top surface of the molybdenum substrate holder. In this chapter this assumption leads to a much smaller carbon conversion efficiency and higher SY in this Chapter than those calculated for PCD in Chapter 5. Thus the CCF and SY calculated in this chapter should only be compared with each other.

The deposition of PCD on the substrate holder often covers an annular region over an area of an inch or more in diameter. Later in the summary section of this chapter a different CCE and SY is calculated for Reactor C that approximately accounts for this extra synthesized PCD. These adjusted “Figures of Performance”, i.e. CCE and SY, for Reactor C can then be directly compared with other reactor performance “Figures of Merit” that are presented in Chapters 3 and 5.

II. CVD diamond characteristics, Y_2, which include the following

a) Structural quality: FWHM = 1.6 – 1.8 cm^{-1} (Raman), SIMS, transmission measurement from IR to UV

b) Morphology and texture: Microscope images

In order to experimentally explore the relationships between the input variables and output variables, a number of the many variables will be held fixed and then one at a time selected input variables are individually varied. For example looking at the reactor variables, the reactor design/size is held fixed and Reactor C is only excited with the “newly discovered” hybrid mode as described in Section 4.6. Then Reactor C is experimentally evaluated with this fixed geometry and fixed EM mode excitation. Then the experimental investigation is initiated at some well defined “initial benchmark experimental SCD growth condition” and then varies one input variable at a time.

During the proposed experiments several reactor variables are held approximately constant: (1) cavity tuning, L_S and L_p, and (2) generic substrate holder design. Major input variables that are individually varied are the pressure, input absorbed power, total gas flow rate, and feed gas concentrations such as percentage of methane concentration and nitrogen feed gas composition. A reactor variable that is varied is substrate position. Since the reactor is always excited with the same hybrid mode the cavity reactor tuning is held approximately fixed. Important internal variables are substrate temperature and discharge power density. Important output variables are diamond synthesis/ deposition rates, diamond quality, and reactor efficiency such as specific yield.

As indicated above the relationships between these variables are nonlinear and can only be determined by experimental measurement. Given a particular substrate holder design the first experiments will, given a particular substrate holder design, establish the relationship between the input absorbed discharge power density, the operating pressure and the substrate temperature. This measurement has already been performed and has been reported in Chapter 5. See Figures 5.6 and 5.13 in Sections 5.4 and 5.5, which relates the pressure, discharge power density and the internal variable substrate temperature. This measurement establishes the reactor roadmap and thereby establishes the new reactor's useful and safe experimental operating regime. It also establishes the "initial benchmark experimental growth conditions" which in this thesis operate from and vary around a pressure of 240 Torr.

Starting with the initial benchmark experimental SCD growth conditions a set of exploratory experiments is then performed where the performance of the Reactor C is investigated over a large experimental operating space. These experiments are summarized in Figures 6.2-6.35 below and demonstrate that the new reactor is indeed robust and safe to operate over a large experimental operating space. Eight sets of experiments have been performed in the sequence as is described in Section 6.4 – 6.11. The first experiments described in Section 6.4 investigate the variation of growth rate versus flow rate. These experiments identify the "best flow rate" conditions in which to perform the rest of the experiments. Then operating with these "best flow rate" conditions the substrate position, Z_S, is varied as described in Section 6.5. The optimum

substrate position, Z_S, is then determined from these experiments. In Section 6.6 the growth rate versus time is investigated. Then the rest of the experiments, growth rate versus pressure, substrate temperature, methane concentration etc., are performed with the flow rate and substrate position held constant at their "best" conditions and for a fixed deposition time of 24 hours.

6.3 Substrate Cleaning Procedures and Reactor Start-up and Shutdown Procedures

6.3.1 Substrate Cleaning Procedures

High pressure high temperature (HPHT) diamond seeds are used as the substrate in all CVD single crystal diamond synthesis. The cleaning procedures are described as follows:

Acidic Cleaning

1) Nitric Acid (40 ml) + Sulfuric Acid (40 ml) in Pyrex beaker, on the heater (set to Maximum, about 200 ℃) for 20 minutes .
2) Rinse sample in DI water (dip the sample in water container for a second)
3) Hydrochloric Acid (60 ml) in Pyrex beaker, on the heater (set to Maximum, about 200 ℃) for 20 minutes.
4) Rinse sample in DI water (dip the sample in water container for a second)

5) Ammonium Hydroxide (80 ml) in Pyrex beaker, on the heater (set to Maximum, about 200 ℃) for 20 minutes.
6) Rinse sample in DI water (dip the sample in water container for a second)

Ultrasonic Cleaning

1) Ultrasonic bath cleaning with Acetone (40 ml) in Pyrex beaker for 15 minutes.
2) Ultrasonic bath cleaning with Methanol (40 ml) in Pyrex beaker for 15 minutes.

Final Rinsing and Drying

1) Rinse sample with DI water for 5 minutes
2) Blow Nitrogen (or Air) on the sample to remove water
3) Place sample in a clean petri dish

6.3.2 Reactor Start-up and Shutdown Procedures

The general start-up and shutdown procedures are described as follows:

Sample Pre-load

1) The prepared sample (after cleaning procedure described in Section 6.3.1) is manually loaded onto the substrate holder then placed in the discharge chamber at the right position.
2) The system is pumped down to 0.5 mTorr (usually overnight).

Start-up Procedures

1) Open the valves for all processing gases.
2) Turn on microwave power supply and chiller.
3) Adjust the short L_s and excitation probe L_p to the right position.
4) Set H_2 flow rate to 1500 sccm.
5) Set pressure to 8 Torr.
6) Turn on the microwave power by setting the incident microwave power as 1 kW when the pressure is greater than 3 Torr. The plasma should be lit at this point.
7) Set pressure to the experimental pressure (i.e. 240 Torr).
8) Slowly increase the incident microwave power as the pressure increases to the desired incident power (i.e. 2.4 kW).
9) If necessary, adjust the short L_S and excitation probe L_p to maintain the minimum reflected power.
10) When reaching the desired pressure, set H_2 flow rate to 400 sccm.

During Experiment

1) Use H_2 only plasma for pre-etching for 3 hours.
2) After pre-etching turn on other processing gases (i.e. CH_4, N_2) for CVD single crystal diamond synthesis.

Shutdown Procedures

1) Turn off all processing gases except H_2.

2) Slowly drop the power to 1 kW when dropping the pressure to 75 Torr with a step of 15 Torr.
3) Turn off the microwave power when the pressure is at 75 Torr.
4) Turn off H_2 gas.
5) Pump down the system to 1 mTorr.
6) Wait until at least 30 minutes for the system to cool down, then set the chamber pressure to atmosphere pressure.
7) Unload the grown diamond sample.
8) Turn off microwave power supply and chamber.
9) Turn off the valves for all processing gas.

6.4 The Role of Total Gas Flow Rate (f_t=100/200/400/600/700 sccm)

6.4.1 Introduction

This section presents the experimental results of the output variable Y as a function of total gas flow rate. A total of five experiments were conducted to verify the role of total gas flow rate in SCD MPACVD synthesis. The experiments start at the initial “benchmark experimental SCD growth conditions” as described in Section 6.4.2 and then carefully vary the flow rate. First the initial “benchmark experimental SCD growth conditions are introduced in this Section 6.4.2. Then the relationship between total gas flow rate and output variables Y, such as linear

growth rate, total growth rate by weight gain, carbon conversion efficiency, specific yield, surface morphology and structural quality is described.

6.4.2 Initial Benchmark Experimental Variables

(1) Controllable input variables, U_1, which include the following

a) Deposition pressure, Fixed: p = 240 Torr

b) Incident microwave power, Variable: P_i = 1.7 – 2.2 kW

c) Feed gas composition, Fixed: c = CH_4/H_2= 5% and N_2 = 5 ppm

d) Total flow rate, Variable: f_t= 100 / 200 / 400 / 600 / 700 sccm

(2) Reactor geometry variables, U_2, which include the following

a) Applicator size and configuration, Fixed

b) Substrate position, Fixed: Z_s = -4.8 mm

c) Substrate holder design, Fixed: Adjust and redesign for size S seeds

d) Electromagnetic mode: Mode is fixed in all experiments

e) Cavity tuning, Variable: L_s = 16.2-16.5 cm

f) Quartz dome geometry, Fixed: 8.5” quartz domes

(3) Deposition process variables, U_3, which include the following

a) Substrate material and size, Fixed: 3.5mm*3.5mm*1.4mm HPHT diamond (S)

b) Deposition time, Fixed: t = 24 Hours

(4) Internal variables X, which include

a) Substrate temperature, Fixed: $T_s \approx 1000\ ^{\circ}C$

b) Absorbed microwave power, Variable: P_{abs}= 1.6 – 1.9 kW

c) Plasma volume, Variable: V_p = 3.2 - 3.8 cm^3

d) Absorbed power density, Fixed: $<P_{abs}>$ = P_{abs}/ Volume of plasma ≈ 600 W/cm^3

6.4.3 Growth Rate vs. Total Gas Flow Rate

The linear growth rate and total growth rate variation versus the total flow rate are shown in the Figures 6.2 and 6.3 below. In the figures each experimental run has the substrate growth temperature listed next to each data point. The substrate temperature varies slightly from run to run varying from 971-1018 ℃.

As shown the growth rate decreases as the total gas flow rate increases.

CVD diamond growth is a very complex process. The feed gas is undergoing many chemical reactions during the CVD diamond deposition process (See Section 2.2.2). When the total input gas flow rate increases, it means higher carbon radical species content may be available in the gas phase for diamond synthesis than at lower flow rates. However as shown in Figure 6.2 the growth rate decreases as the flow rate increases. This may be caused because more of the input gas by passes the discharge reactor zone at the higher flow rates than at the lower flow rates.

It has been observed by others that lower diamond quality is produced at low flow rate (100/200 sccm) [12]. This is because the associated longer gas residence times allows the gas leaking into the vacuum system to become a more important fraction of the "total input gas flow". Thus chamber wall erosion and vacuum system leaks lead to larger gas impurity concentrations, like N_2, in the reactor synthesis gases and thus may contribute to the growth rate increase and diamond quality decrease as flow rate is decreased.

Thus looking at the experimental results in Fig. 6.2 and also noting what has been used in other MSU reactor investigations [Kadek, Kou, Stanley] a total flow rate of ~ 400 sccm was determined to be the "best flow rate" to use for the rest of the experiments. This flow rate was high enough to minimize the vacuum system impurity problem but it is not so high as to reduce the growth rate and thereby waste input gases. Thus all experiments in Sections 6.5 – 6.12 described below are performed with a total flow rate held constant at ~400 sccm. The substrate

temperature is kept approximately constant by adjusting the input power. The experiment is repeatable.

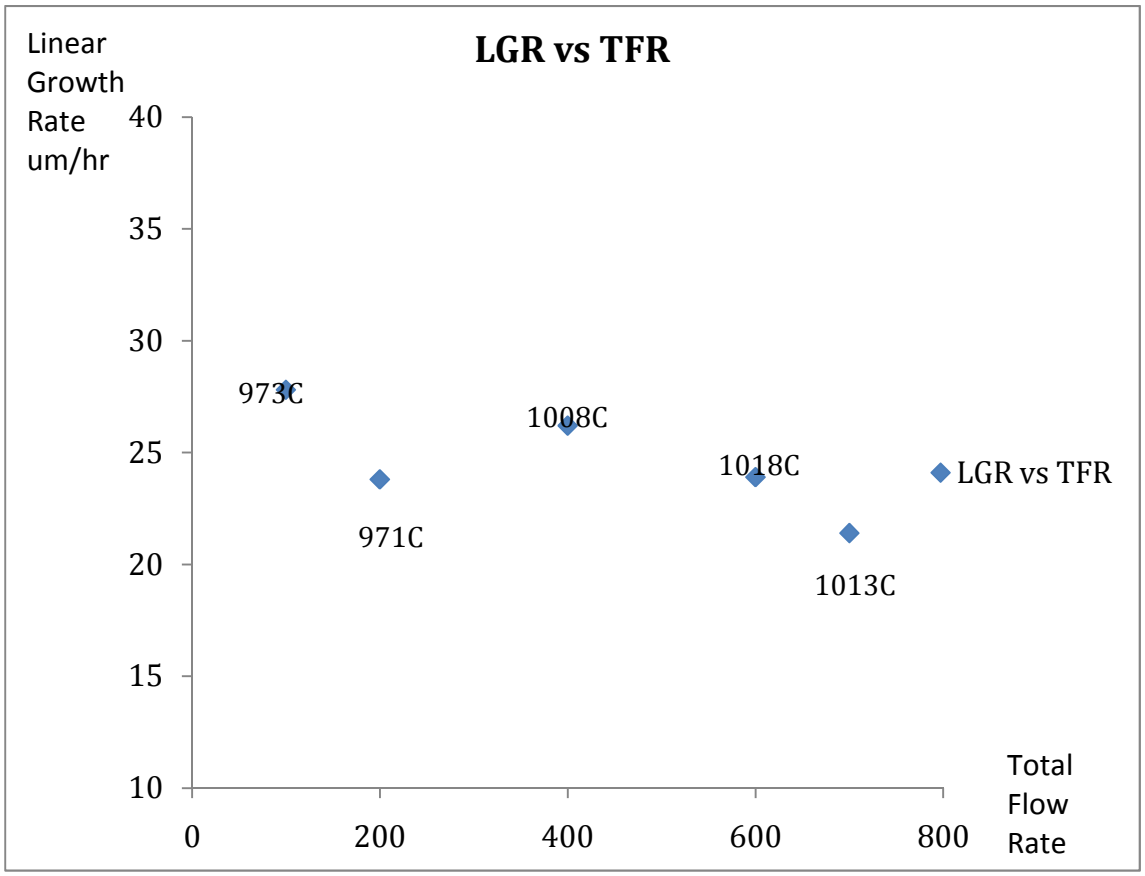

Figure 6.2 Linear growth rate vs. total gas flow rate for Reactor C

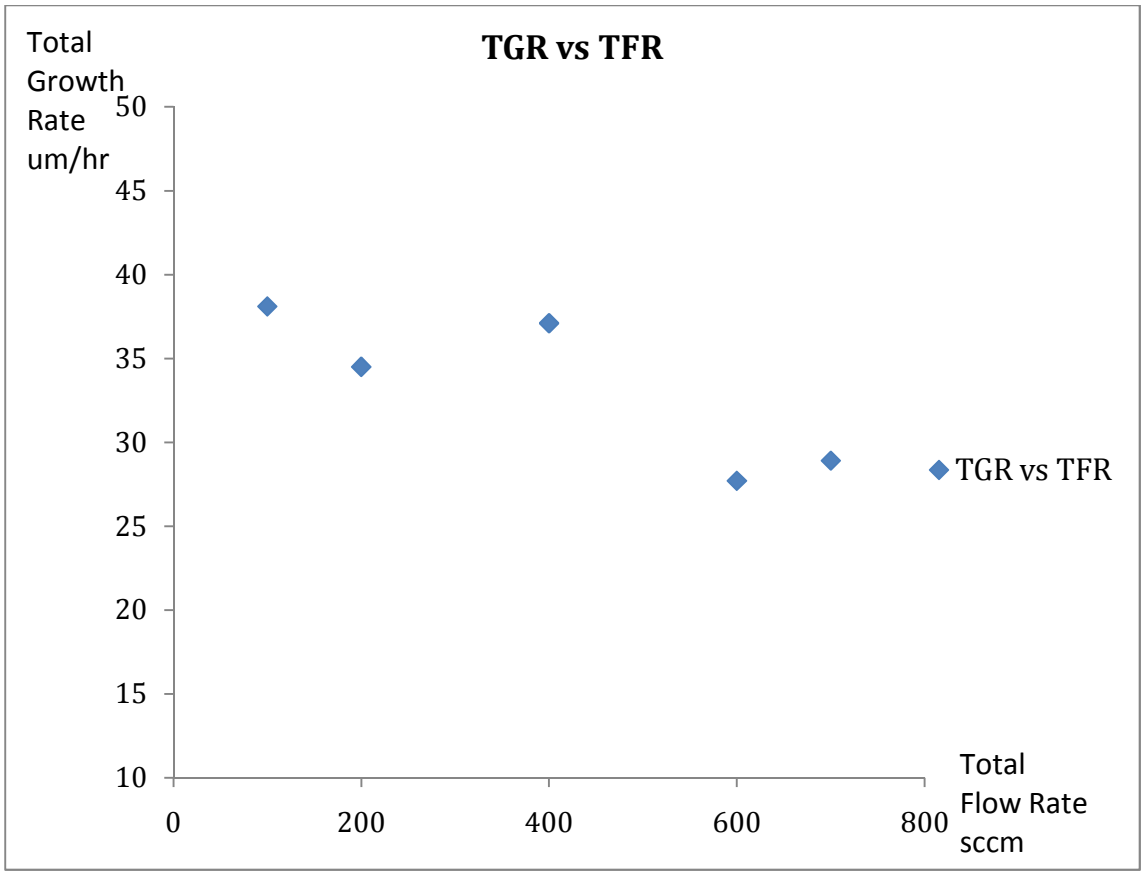

Figure 6.3 Total growth rate vs. total gas flow rate for Reactor C

6.4.4 Carbon Conversion Efficiency vs. Total Gas Flow Rate

Before we explore the relationship between carbon conversion efficiency (CCE) and total gas flow rate, a very important parameter which is the residence time of the feed gas in the deposition chamber, is defined. The residence time, t, is given by

$$t = V_c / F \qquad (1)$$

where V_c is the discharge chamber volume and F is the flow rate scaled to the pressure in the chamber. Typical residence times in a discharge chamber

range from 1 second to a few minutes. For Reactor C, the quartz dome is a cylinder with the radius of 10.8 cm and height of 10.16 cm. The volume of the quartz dome is 3721 cm^3. A 400-sccm flow is 1250 cc/min at 240 Torr. So the residence time t is about 3 minutes.

Carbon conversion efficiency tells us how much of the carbon in the input feed gas is deposited on the diamond surface. As expected the carbon conversion efficiency is higher at lower total flow rates than at higher flow rates as shown in Figure 6.4.

According to equation (1), we get longer gas residence times when gas flow rate is lower since the discharge chamber volume is fixed. Because of the longer gas residence times during the diamond growth, the exit gas composition can be considered a close approximation of the carbon mole fraction in the chamber. Hence lower gas flow rates are equivalent to lower carbon concentrations.

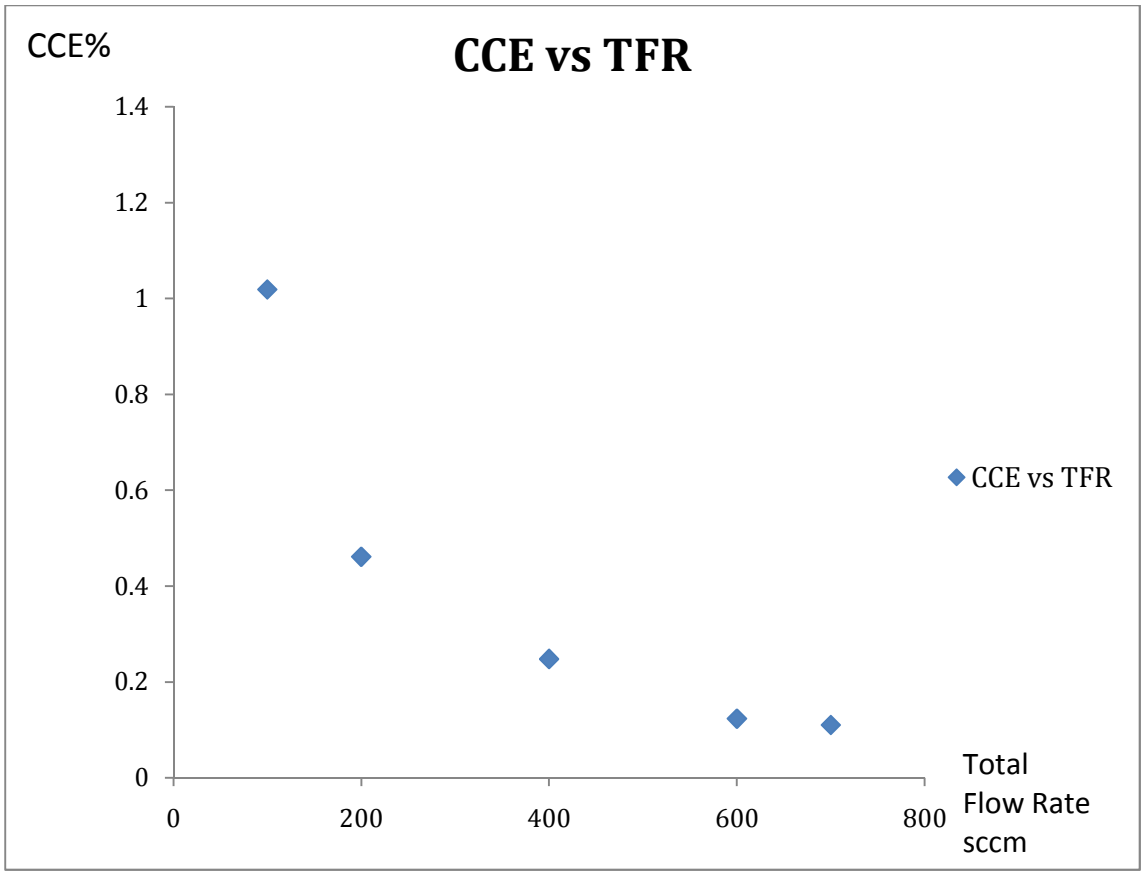

Figure 6.4 Carbon conversion efficiency vs. total gas flow rate for Reactor C

6.4.5 Specific Yield vs. Total Gas Flow Rate

Specific yield (SY) is defined as the absorbed power input (p_a) per diamond total growth rate in the units of kW-h/g. It is a measure of the electric deposition efficiency. As shown in Figure 6.5 the specific yield slightly increases as the total flow rate increases. This behavior is just the inverse of the growth rate. Thus the deposition system becomes less electrically efficient and less total gas handling efficient at the high total input gas flow rates.

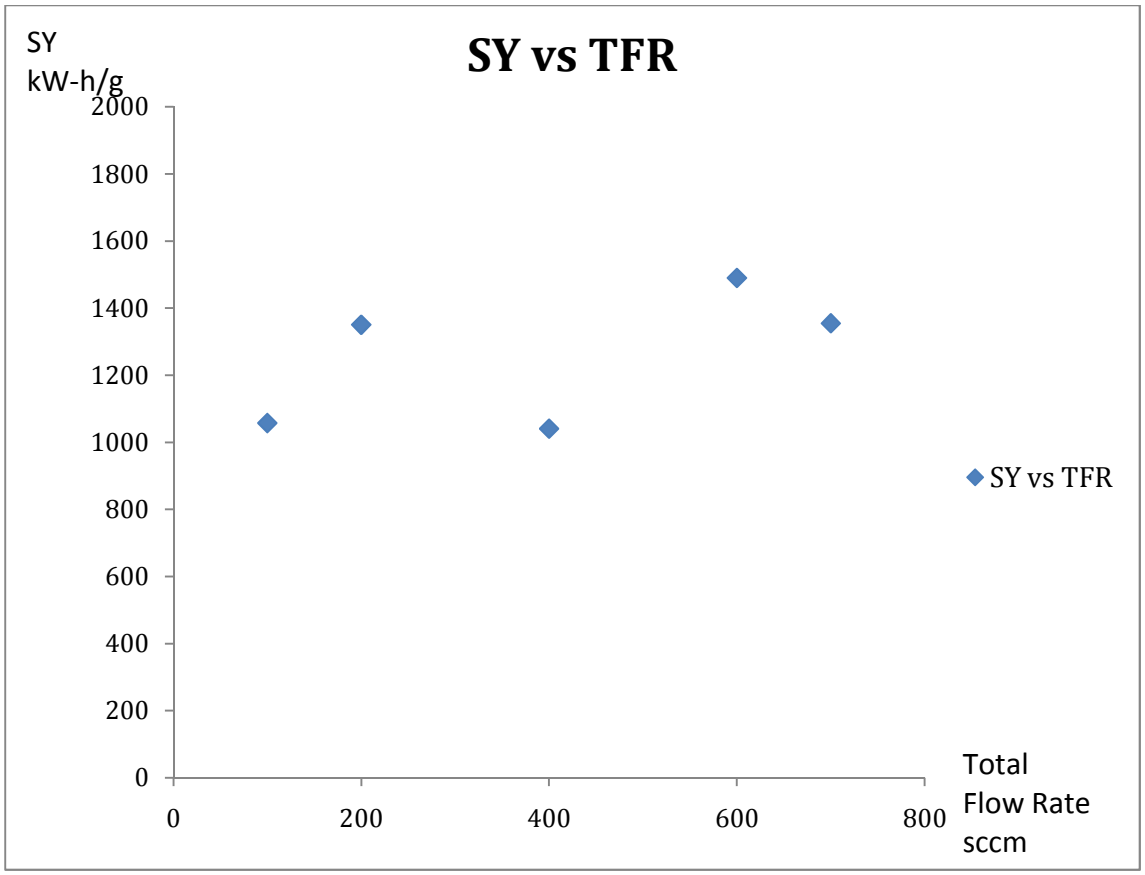

Figure 6.5 Specific yield vs. total gas flow rate for Reactor C

6.5 The Role of Substrate Holder Position (Z_S = -6 mm to 0 mm)

6.5.1 Introduction

This section presents the experimental results of the output variable Y as a function the substrate holder location, Z_S, is varied from -6 – 0 mm. A total of six experiments were conducted to verify the role of substrate holder location on single crystal diamond MPACVD synthesis. The experiments were started by

operating the reactor at the initial “benchmark experimental SCD growth conditions” and then Z_S was carefully experimentally varied. The optimized SCD growth conditions are described in Section 6.5.2. Then the relationships between substrate holder location, Z_S, and output variables Y, such as linear growth rate, total growth rate by weight gain, carbon conversion efficiency, and specific yield are presented in Sections 6.5.3 – 6.5.5.

6.5.2 Initial Benchmark Experimental Variables

(1) Controllable input variables, U_1, which include the following

a) Deposition pressure, Fixed: p = 240 Torr

b) Incident microwave power, Variable: P_i = 1.7 – 2.2 kW

c) Feed gas composition, Fixed: c = CH_4 / H_2 = 5% and N_2 = 5 ppm

d) Total flow rate, Fixed: f_t = 400 sccm

(2) Reactor geometry variables, U_2, which include the following

a) Applicator size and configuration, Fixed

b) Substrate position, Variable: Z_S = -6 - 0 mm

c) Substrate holder design, Fixed: Adjust and redesign for size S seeds

d) Electromagnetic mode: Mode is fixed in all experiments

e) Cavity tuning, Variable: L_S = 16.2-16.5 cm

f) Quartz dome geometry, Fixed: #3 quartz domes have been used

(3) Deposition process variables, U_3, which include the following

a) Substrate material and size, Fixed: 3.5mm*3.5mm*1.4mm HPHT diamond (S)

b) Deposition time, Fixed: t = 24 Hours

(4) Internal variables X, which include

a) Substrate temperature, Fixed: $T_S \approx 1000\ ^{\circ}C$

b) Absorbed microwave power, Variable: P_{abs} = 1.6 – 1.9 kW

c) Plasma volume, Variable: V_p = 3.2 - 3.8 cm^3

d) Absorbed power density, Fixed: $< P_{abs} > = P_{abs}$ / Volume of plasma ≈ 600 W/cm^3

6.5.3 Growth Rate vs. Substrate Holder Position

The substrate holder is sitting on a movable cooling stage with a reduction of holder area by four times over Reactor A. The ability to adjust the position of the stage allows additional adjustment and local fine tuning of the electromagnetic field and the discharge around and above the substrate. It also appears to counter the buoyant microwave discharge as pressure increases. The experimental results are displayed in Figures 6.6 and 6.7 below. The highest linear growth rate occurs at Z_S = -4.8 mm. Thus this substrate position was used for the experiments presented in this thesis.

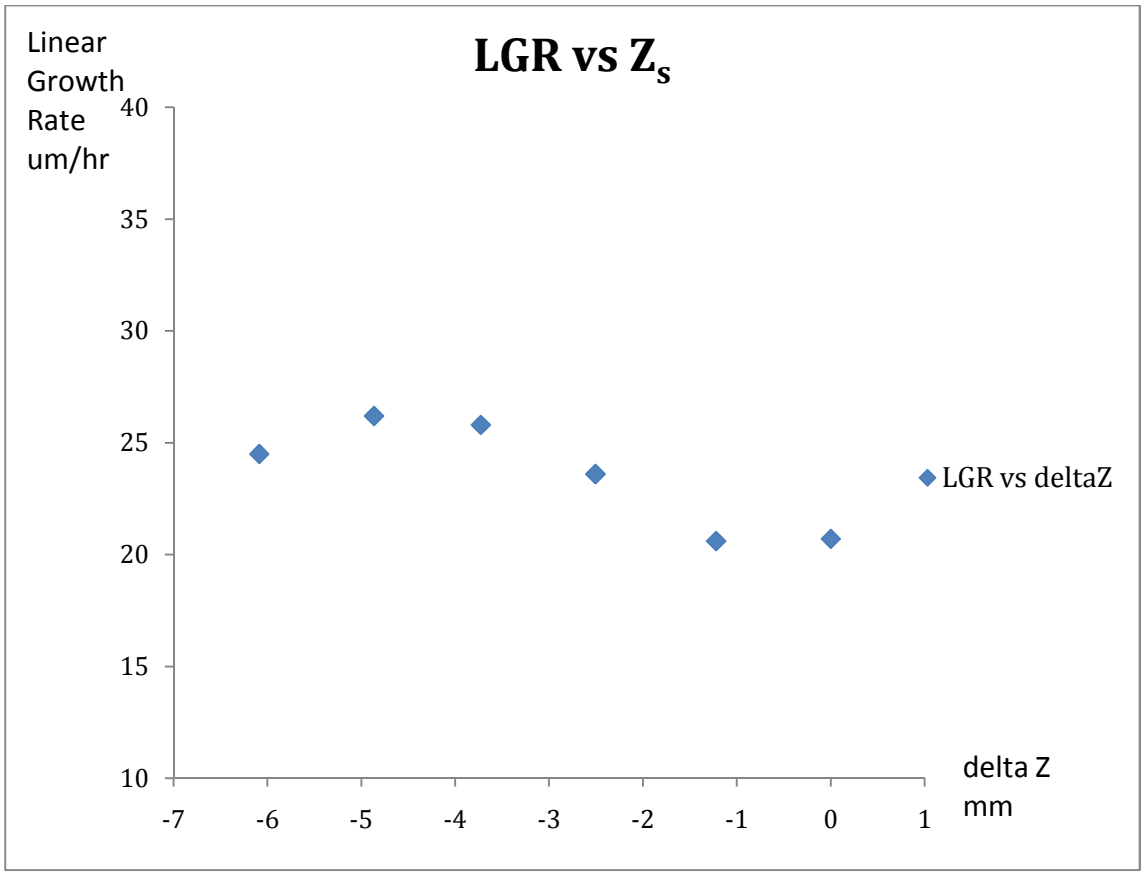

Figure 6.6 Linear growth rates vs. substrate holder location for Reactor C

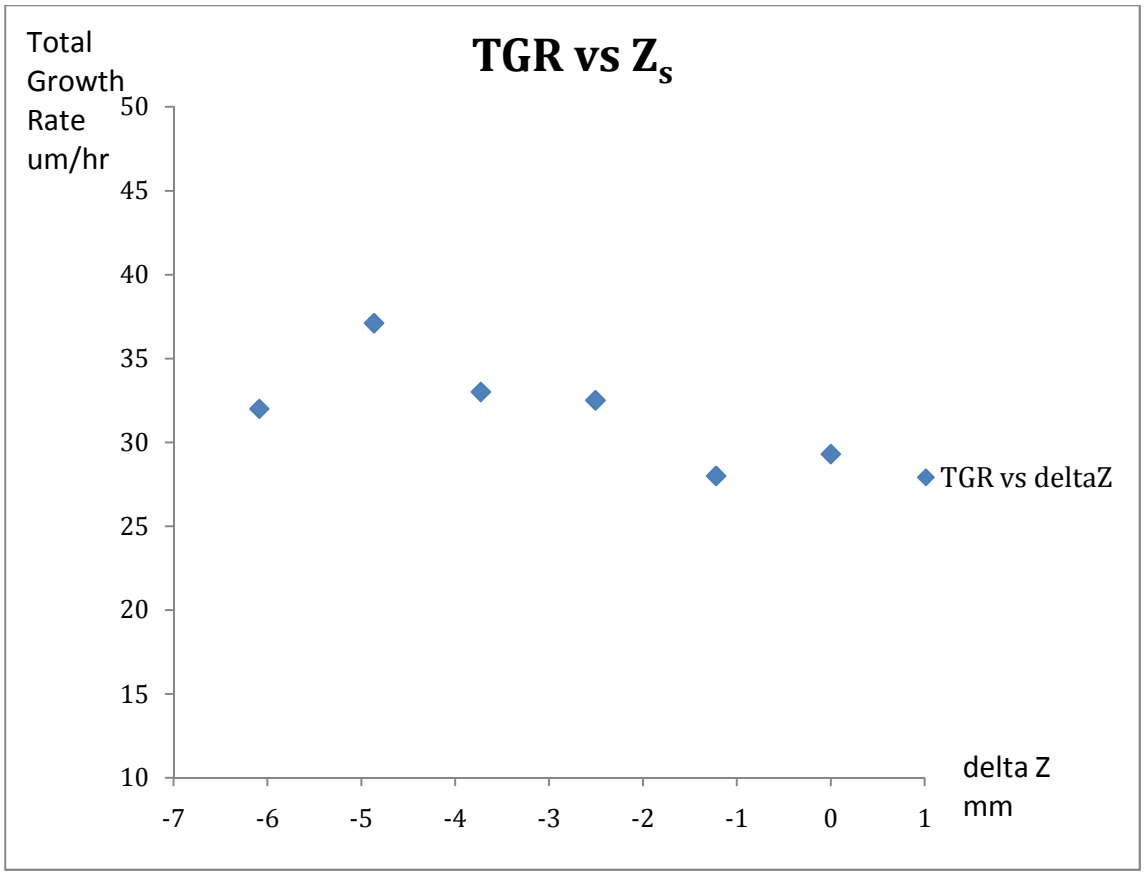

Figure 6.7 Total growth rate vs. substrate holder location for Reactor C

6.5.4 Carbon Conversion Efficiency vs. Substrate Holder Position

Since the methane concentrations and substrate sizes were not changed in this set of the experiments, carbon conversion efficiency versus Z_S has as expected the same variation versus position as the total growth rate versus Z_S that is shown in Figures 6.6 and 6.7.

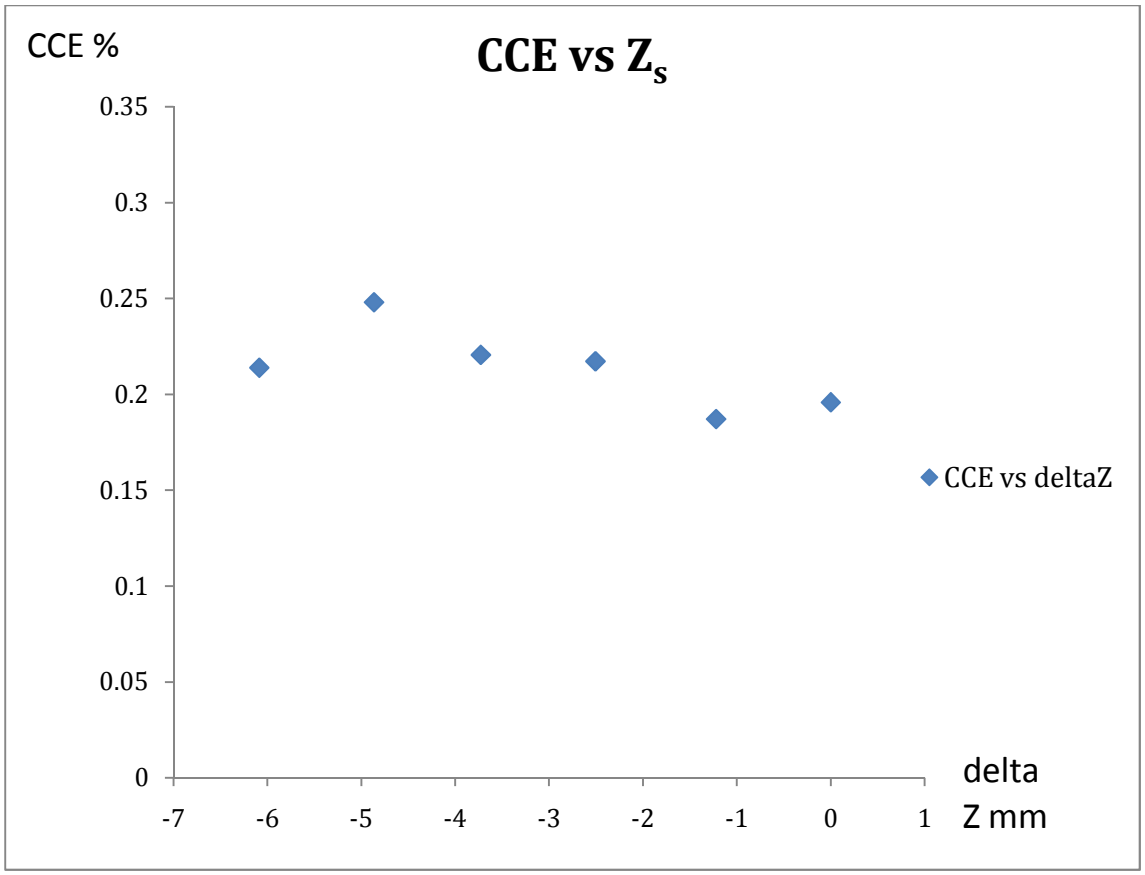

Figure 6.8 Carbon conversion efficiency vs. substrate holder location for Reactor C

6.5.5 Specific Yield vs. Substrate Holder Position

Since specific yield is defined as the absorbed power input per diamond film total growth rate, and the absorbed power input in this set of experiments is held approximately constant, the specific yield versus Z_S is inversely proportional to the total growth rate versus Z_S as expected.

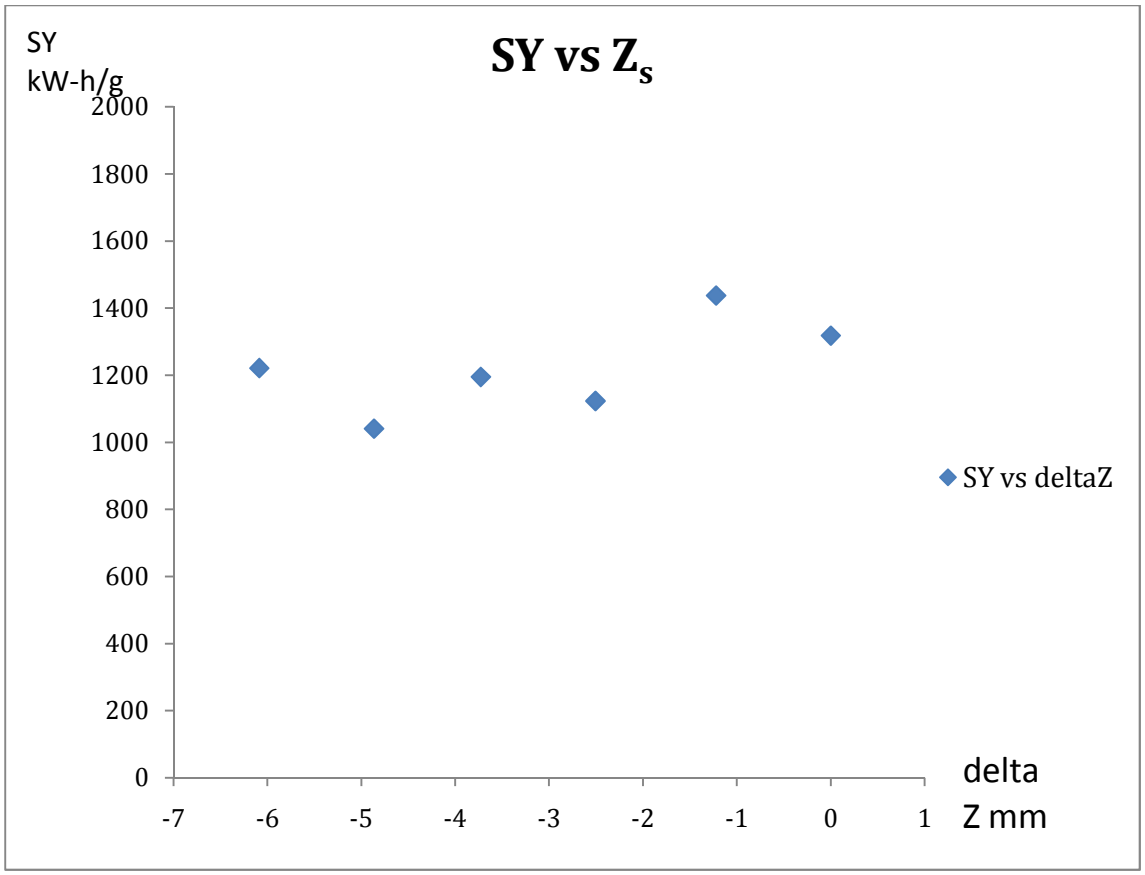

Figure 6.9 Specific yield vs. substrate holder location for Reactor C

6.6 The Role of Deposition Time (t = 15 – 70 hours)

6.6.1 Introduction

This section presents the experimental results of the output variable Y as a function of deposition time t. A total of six experiments were conducted to verify the role of deposition time in SCD MPACVD synthesis. The experiments start at the initial "benchmark experimental SCD growth conditions" and then time was varied from 15 – 70 hours. The initial benchmark SCD growth conditions are introduced in Section 6.6.2. Then the relationships between deposition time and

output variables Y, such as linear growth rate, total growth rate by weight gain, carbon conversion efficiency, and specific yield, are presented in Sections 6.6.3 – 6.6.5.

6.6.2 Initial Benchmark Experimental Variables

(1) Controllable input variables, U_1, which include the following

a) Deposition pressure, Fixed: p = 240 Torr

b) Incident microwave power, Variable: P_i = 1.7 – 2.2 kW

c) Feed gas composition, Fixed: c = CH_4/H_2= 5% and N_2 = 5 ppm

d) Total flow rate, Fixed: f_t = 400 sccm

(2) Reactor geometry variables, U_2, which include the following

a) Applicator size and configuration, Fixed

b) Substrate position, Fixed: Z_S = -4.8 mm

c) Substrate holder design, Fixed: Adjust and redesign for size S seeds

d) Electromagnetic mode: Mode is fixed in all experiments

e) Cavity tuning, Variable: L_S = 16.2-16.5 cm

f) Quartz dome geometry, Fixed: #3 quartz domes have been used

(3) Deposition process variables, U_3, which include the following

a) Substrate material and size, Fixed: 3.5mm*3.5mm*1.4mm HPHT diamond (S)

b) Deposition time, variable: t = 15 - 70 Hours

(4) Internal variables X, which include

a) Substrate temperature, Fixed: $T_s \approx 1000\ ^{\circ}C$

b) Absorbed microwave power, Variable: P_{abs} = 1.6 – 1.9 kW

c) Plasma volume, Variable: V_p = 3.2 - 3.8 cm^3

d) Absorbed power density, Fixed: $< P_{abs} > = P_{abs}$ / Volume of plasma ≈ 600 W/cm^3

6.6.3 Growth Rate vs. Deposition Time

Figures 6.10 and 6.11 display the linear growth rate and total growth rate versus time. As shown the growth rate increases as time increases. Over the 15-70 hour time period the growth rate increase can be approximated as a straight

line with a slope of 0.83 microns / hr^2. Thus over this time period the longer runs yield the fastest growth rates. The reason for this growth rate increase is not understood. However one possible explanation is that as deposition time increases the SCD growth surface grows from inside the substrate holder pocket further into the discharge. Thus as the CVD diamond is added to the diamond seed surface the plasma boundary layer between the diamond surface and position occupied by the intense discharge is modified in such a manner that more growth radicals are available for diamond synthesis. That is, as the diamond thickness increases the growth surface moves into a more higher density radical species region resulting in higher growth rates. This explanation is very similar to growth rate versus d_{ave} explanation given in Figure 2.37 and reference [49].

Longer synthesis times result in higher growth rates and thus it was desirable to perform the basic experiments in this study with the longer growth times of 60-70 hours. However in order to place a limit on the total experimental run time required to perform this investigation the basic experiments in this investigation were limited to run times of 24 hours. It is recognized that in all the experiments presented in the sections below that higher deposition rates can be achieved with deposition times greater than 24 hours.

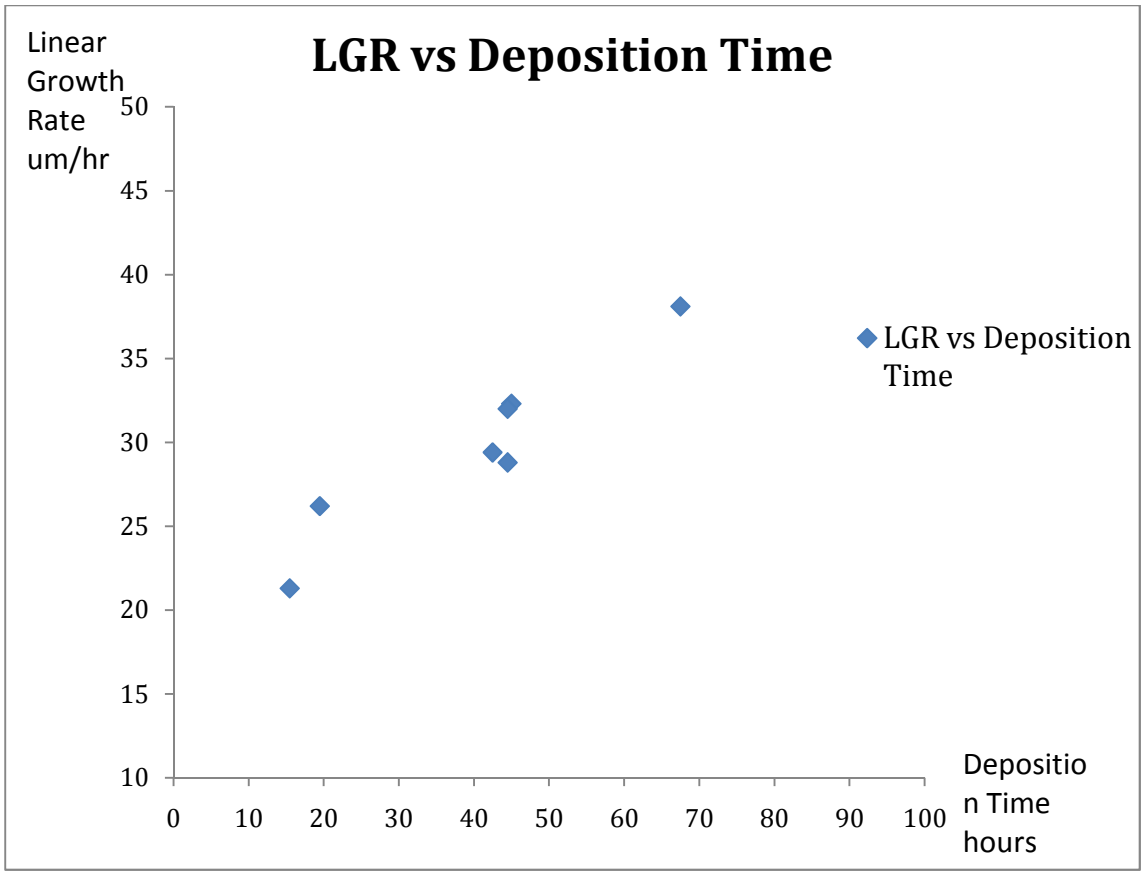

Figure 6.10 Linear growth rate vs. deposition time for Reactor C

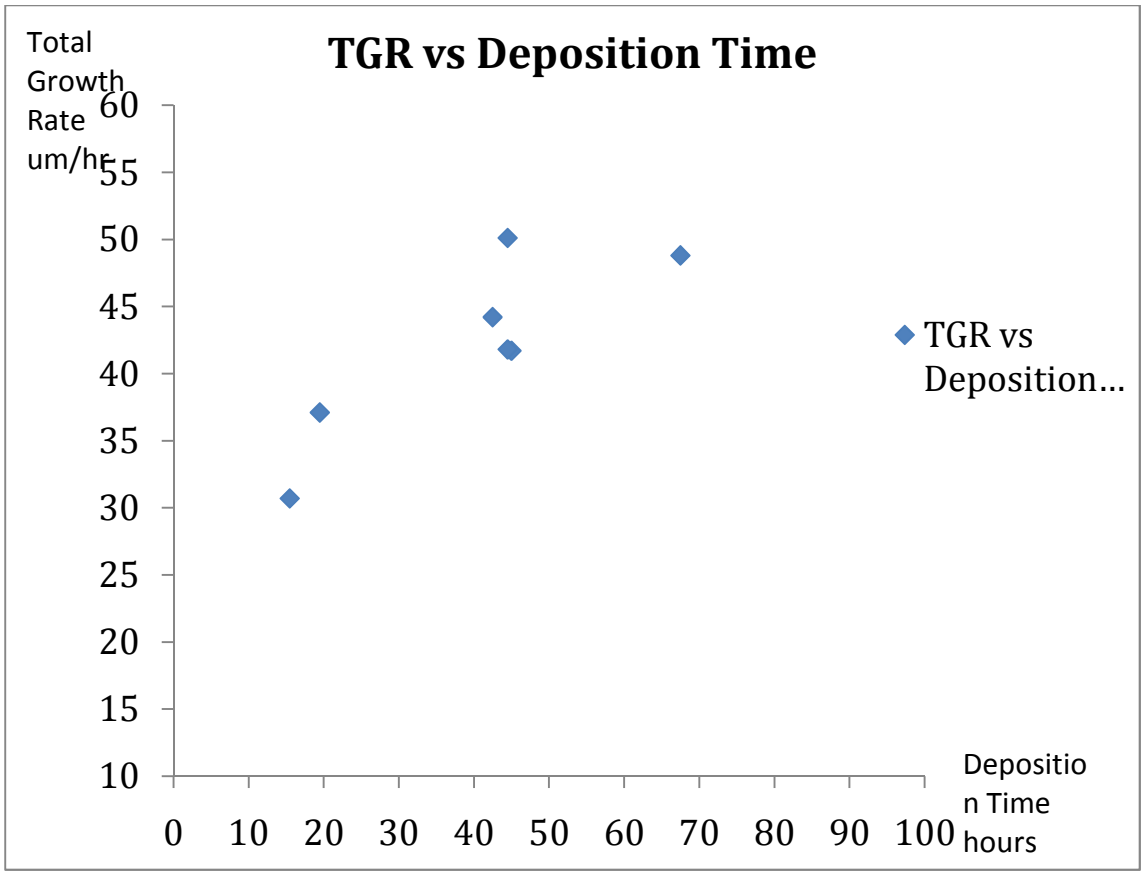

Figure 6.11 Total growth rate vs. deposition time for Reactor C

6.6.4 Carbon Conversion Efficiency vs. Deposition Time

Since the methane concentrations and substrate sizes are not changed in this set of the experiments, carbon conversion efficiency versus deposition time as is shown in Figure 6.12 is expected to have a curve with a similar shape as the total growth rate versus deposition time that is displayed in Figure 6.11.

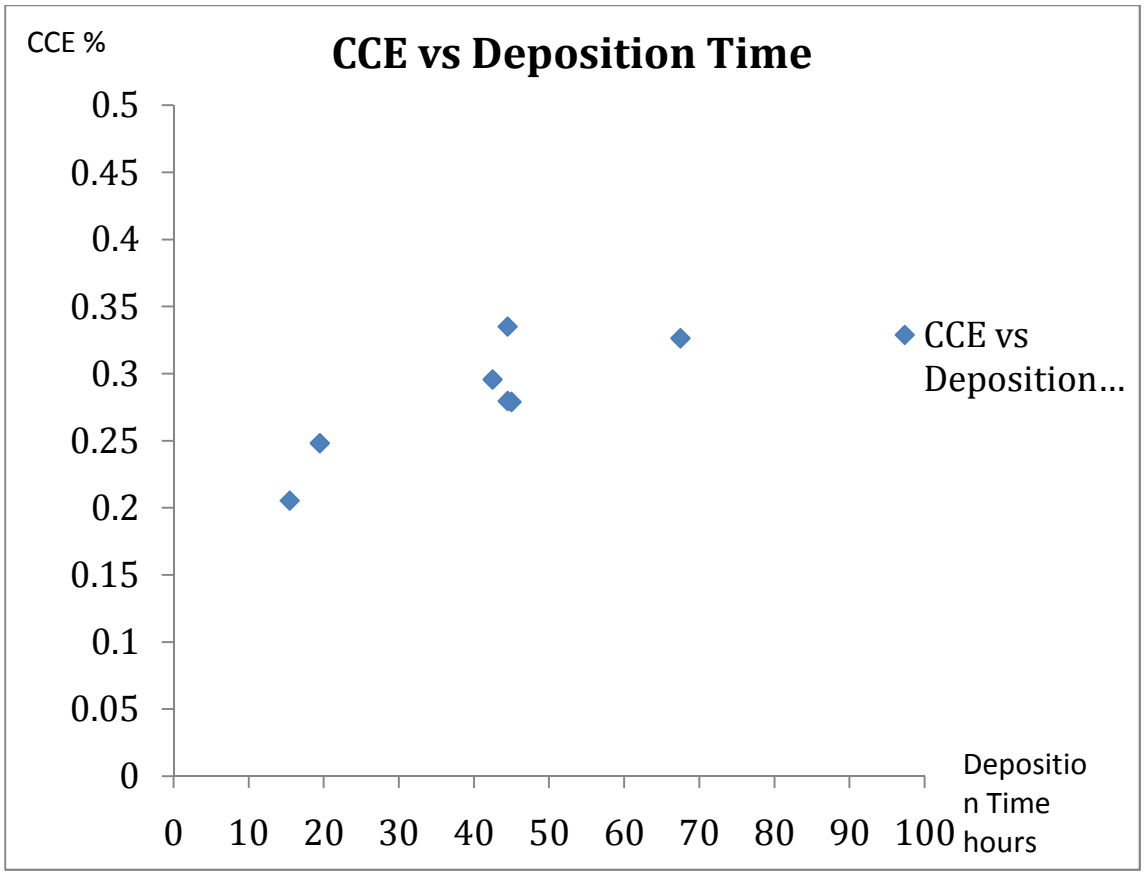

Figure 6.12 Carbon conversion efficiency vs. deposition time for Reactor C

6.6.5 Specific Yield vs. Deposition Time

Since specific yield is defined as the absorbed power input per diamond film total growth rate, and the absorbed power input in this set of experiments remains approximately constant, the specific yield versus deposition time is inversely proportional to the total growth rate. This is displayed in Figure 6.13. Thus as the deposition time increases the electrical efficiency increases.

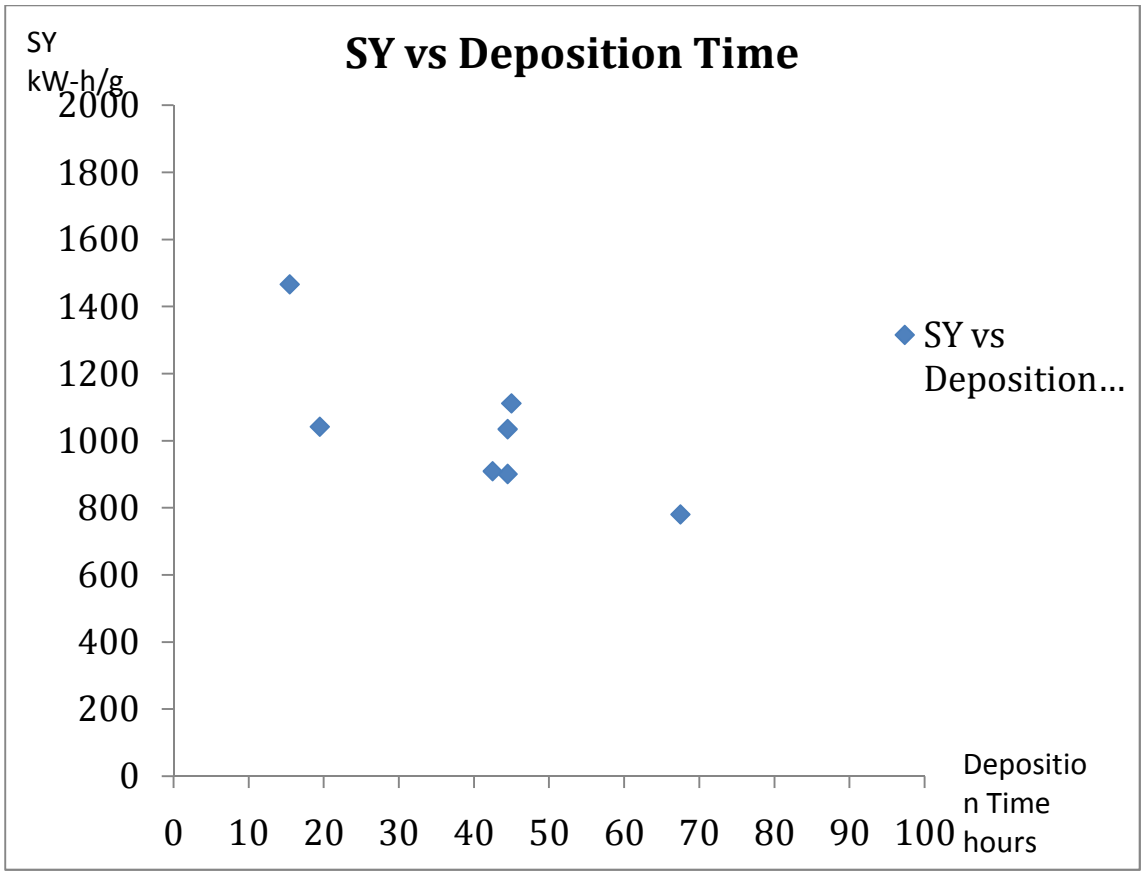

Figure 6.13 Specific yield vs. deposition time for Reactor C

6.7 The Role of Deposition Pressure (p = 240 / 260 / 280 / 300 / 320 Torr)

6.7.1 Introduction

This section presents the experimental results of the output variable Y as a function of deposition pressure p. A total of six experiments were conducted to verify the role of deposition pressure in SCD MPACVD synthesis. The experiments start at the initial "benchmark experimental SCD growth conditions" and then pressure is varied incrementally. The initial SCD growth conditions are

described in Section 6.7.2. Then the relationships between deposition pressure and output variables Y, such as linear growth rate, total growth rate by weight gain, carbon conversion efficiency, and specific yield are presented in Sections 6.7.3 – 6.7.5.

6.7.2 Initial Benchmark Experimental Variables

(1) Controllable input variables, U_1, which include the following

a) Deposition pressure, Variable: p = 240 / 260 / 280 / 300 / 320 Torr

b) Incident microwave power, Variable: P_i = 1.7 – 2.2 kW

c) Feed gas composition, Fixed: c = CH_4/H_2= 5% and N_2 = 5 ppm

d) Total flow rate, Fixed: f_t = 400 sccm

(2) Reactor geometry variables, U_2, which include the following

a) Applicator size and configuration, Fixed

b) Substrate position, Fixed: Z_s = -4.8 mm

c) Substrate holder design, Fixed: Adjust and redesign for size S seeds

d) Electromagnetic mode: Mode is fixed in all experiments

e) Cavity tuning, Variable: L_S = 16.2-16.5 cm

f) Quartz dome geometry, Fixed: #3 quartz domes have been used

(3) Deposition process variables, U_3, which include the following

a) Substrate material and size, Fixed: 3.5mm*3.5mm*1.4mm HPHT diamond (S)

b) Deposition time, Fixed: t = 24 Hours

(4) Internal variables X, which include

a) Substrate temperature, Fixed: $T_S \approx 1000\ ^{\circ}C$

b) Absorbed microwave power, Variable: P_{abs}= 1.6 – 1.9 kW

c) Plasma volume, Variable: V_p = 3.2 - 3.8 cm^3

d) Absorbed power density, Fixed: $<P_{abs}>$ = P_{abs}/ Volume of plasma ≈ 600 W/cm^3

6.7.3 Growth Rate vs. Deposition Pressure

The formation of microwave discharges at high pressures was first observed and investigated many years ago [65-67], and high pressure microwave discharges have been applied as plasma sources for electrothermal thruster

space engines [62,68,69] and as high pressure microwave discharge light sources [70]. A visual example of how a microwave discharge behaves as pressure increases is displayed in Figure 5.11 and 5.12. As shown, as the pressure increases the discharge shrinks and constricts and becomes more intense.

At pressures of 100 Torr or more, microwave discharges in hydrogen and methane gas mixtures separate from the reactor walls. They become freely floating and assume shapes that are related to the shape of the impressed electromagnetic (EM) fields. At very high pressures microwave discharges become very non-uniform, intense and “arc like”. They may even move about the discharge chamber as they react both to buoyant forces and to convective forces caused by the gas flows around and within the discharge. Plasma densities for 2.45 GHz hydrogen discharges operating at 100-200 Torr pressure regime are estimated to be 10^{11} cm^{-3} to 10^{13} cm^{-3} [62,63]. At pressures greater than 150 Torr, microwave discharges in hydrogen and methane gas mixtures have neutral gas temperatures in excess of 2500 K. These discharges have high densities of radical species, i.e. H and CH_3 radicals, which enable increased diamond growth rates at high pressures [19].

Since high pressure microwave plasma discharges behave very differently from the typical lower pressure discharges they require methods of discharge control and microwave applicator and plasma reactor design that take into account their distinctly unique nature. As pressure increases the size, the spatial location and the shape of the very hot, non-uniform plasma must be controlled so

that optimal CVD diamond synthesis is achieved. Thus in our designs we provide substrate position adjustments that enable the discharge to be positioned up into and in good contact with the substrate as pressure is varied. This enables the optimal, independent positioning of the substrate with respect to the discharge as pressure varies, and yields high deposition rates. At high pressures the independent positioning of the discharge with respect to the substrate position becomes an additional experimental variable. However, all the experimental results presented in this section hold the substrate position constant at the maximum growth rate position, Z_S= -4.8 mm, that was identified by the experiments that were described in Section 6.5.3. This value may not be the optimized growth rate position for all the experiments presented here, but it was believed that it is also relatively close to the maximum growth rate positions for all the pressure conditions. This assumption should be checked further in future experimental investigations.

From Figure 6.14, a continuous increase of linear growth rate is observed when the pressure increases from 240 Torr to 320 Torr. This increase in growth rate versus pressure was expected since the discharge absorbed power density also increases versus pressure (see Figure 5.12) and as discussed in Chapter 2 the growth rate is expected to increase as pressure increases since the growth radical increase with pressure.

It is believed that in the future additional experiments can be operated at even higher pressures if the substrate holder/ cooler configuration is additionally designed to maintain an appropriate steady substrate temperature at these

higher pressures. In addition for safety reasons the reactor dome must be cooled with pure nitrogen gas.

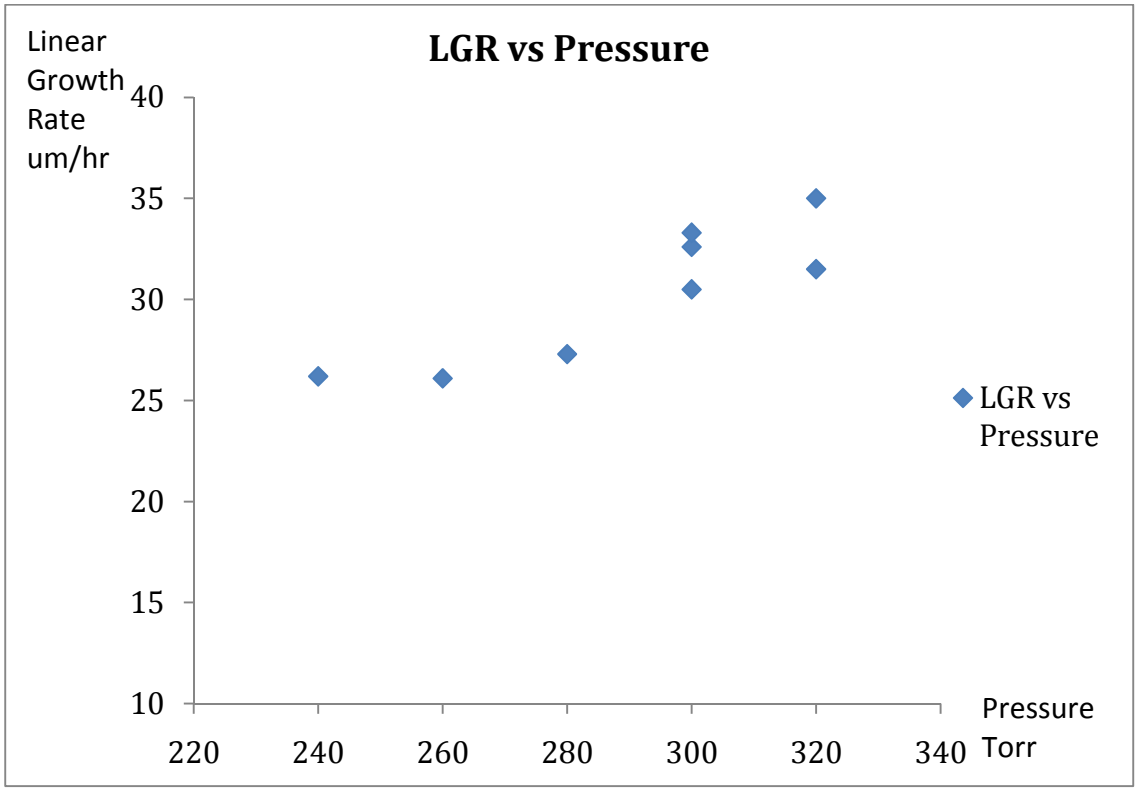

Figure 6.14 Linear growth rate vs. deposition pressure for Reactor C

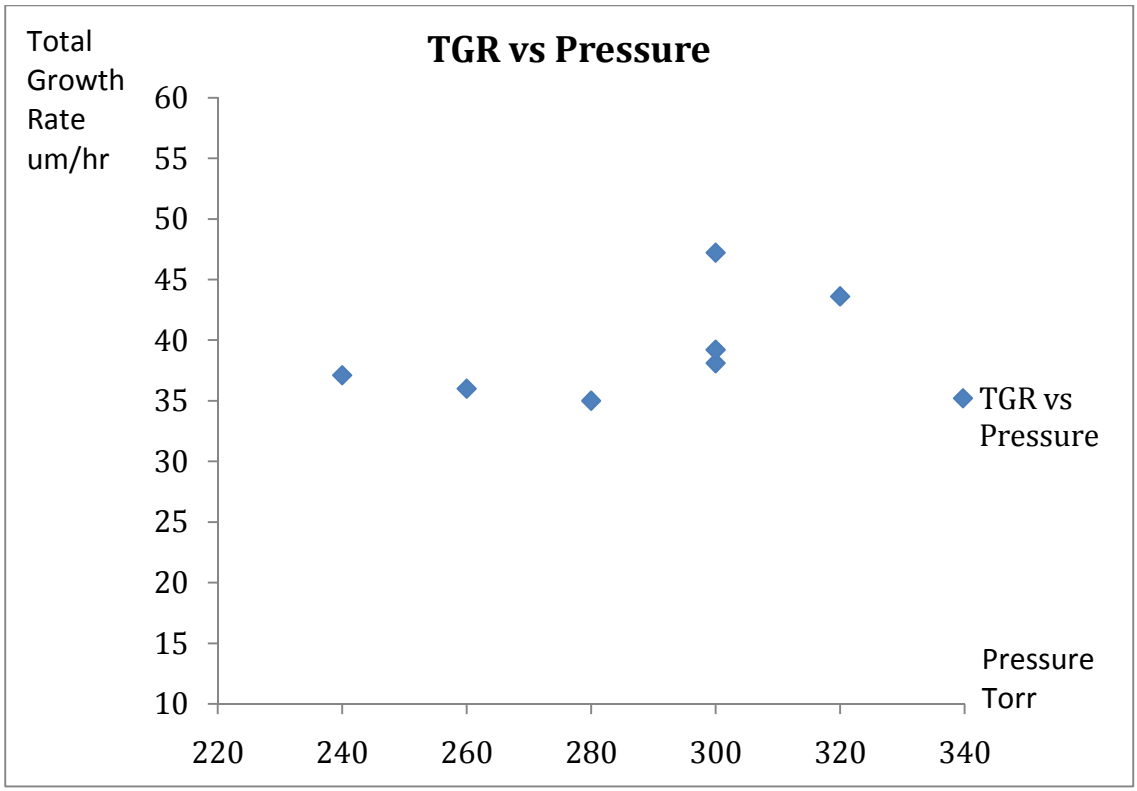

Figure 6.15 Total growth rate vs. deposition pressure for Reactor C

6.7.4 Carbon Conversion Efficiency vs. Deposition Pressure

Since the methane concentrations and substrate sizes are not changed in this set of the experiments, carbon conversion efficiency versus deposition pressure has, as is shown in Figure 6.16, the same shaped curve as the total growth rate versus deposition pressure.

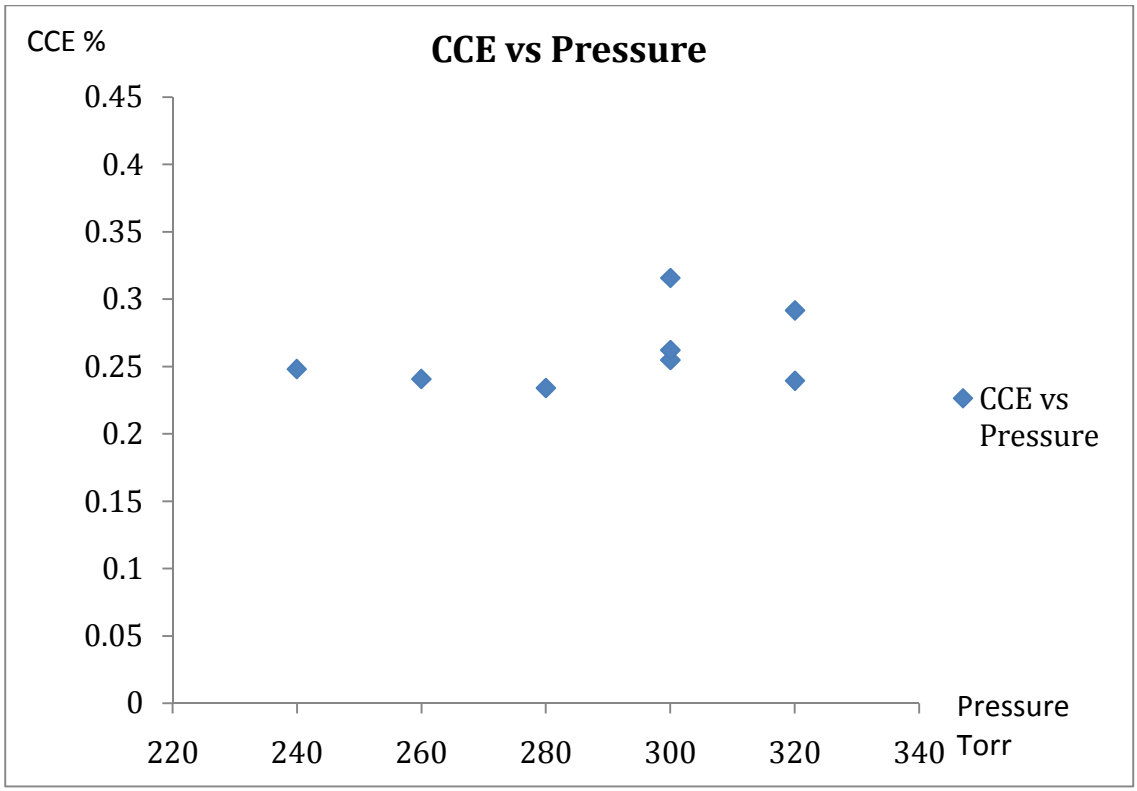

Figure 6.16 Carbon conversion efficiency vs. deposition pressure for Reactor C

6.7.5 Specific Yield vs. Deposition Pressure

Since specific yield is defined as the absorbed power input per diamond film total growth rate, and the absorbed input power in this set of experiments slightly increases with pressure, the specific yield versus deposition pressure is not exactly inversely proportional to the total growth rate versus pressure as expected.

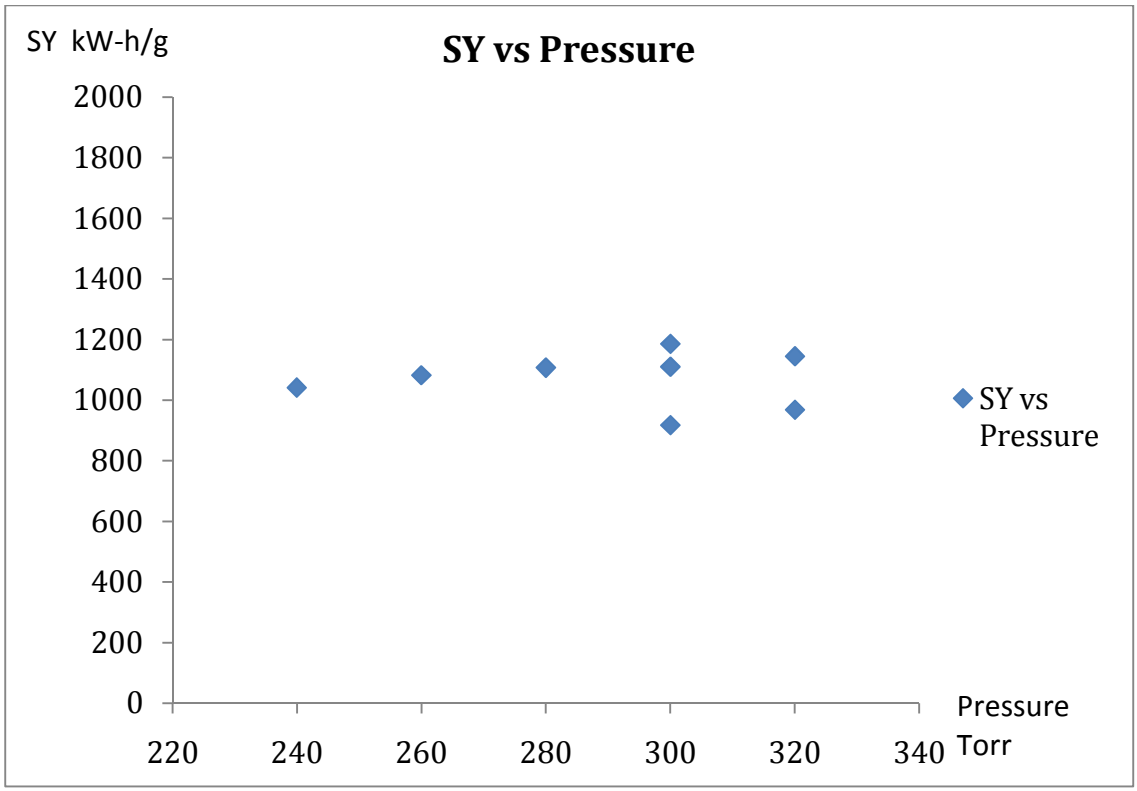

Figure 6.17 Specific yield vs. deposition pressure for Reactor C

6.8 The Role of Substrate Temperature (Ts = 900 – 1200 ℃)

6.8.1 Introduction

This section presents the experimental results of the output variable Y as a function of substrate temperature T_S. A total seven experiments were conducted to verify the role of substrate temperature in SCD MPACVD synthesis. The experiments start with the initial benchmark experimental SCD growth conditions outlined in Section 6.8.2 and then substrate temperature is varied by adjusting the input power and also the substrate holder design. Then the relationships

between substrate temperature and output variables Y, such as linear growth rate, total growth rate by weight gain, carbon conversion efficiency, and specific yield are experimentally determined. These relationships are presented in Sections 6.8.3 – 6.8.5.

6.8.2 Initial Benchmark Experimental Variables

(1) Controllable input variables, U_1, which include the following

a) Deposition pressure, Fixed: p = 240 Torr

b) Incident microwave power, Variable: P_i = 1.7 – 2.2 kW

c) Feed gas composition, Fixed: c = CH_4 / H_2 = 5% and N_2 = 5 ppm

d) Total flow rate, Fixed: f_t = 400 sccm

(2) Reactor geometry variables, U_2, which include the following

a) Applicator size and configuration, Fixed

b) Substrate position, Fixed: Z_S = -4.8 mm

c) Substrate holder design, Fixed: Adjust and redesign for size S seeds

d) Electromagnetic mode: Mode is fixed in all experiments

e) Cavity tuning, Variable: L_S = 16.2-16.5 cm

f) Quartz dome geometry, Fixed: #3 quartz domes have been used

(3) Deposition process variables, U_3, which include the following

a) Substrate material and size, Fixed: 3.5mm*3.5mm*1.4mm HPHT diamond (S)

b) Deposition time, Fixed: t = 24 Hours

(4) Internal variables X, which include

a) Substrate temperature, Variable: $T_S \approx 900 - 1200\ ^{\circ}C$

b) Absorbed microwave power, Variable: P_{abs}= 1.6 – 1.9 kW

c) Plasma volume, Variable: $V_p = 3.2 - 3.8\ cm^3$

d) Absorbed power density, Fixed: $< P_{abs} > = P_{abs}$ / Volume of plasma ≈ 600 W/cm^3

6.8.3 Growth Rate vs. Substrate Temperature

The linear growth rate as a function of substrate temperature is shown in Figure 6.18. The substrate holder is located on top of a water cooling stage (Figure 5.3) to control the substrate temperature. The schematic drawings of the

substrate holder and insert are shown in Figure 5.4 and 6.1. Additional schematic insert drawings of different thicknesses and pocket sizes insert are shown in Appendix D. The substrate temperature can be studied independently without varying any input variables such as deposition pressure, feed gas composition etc.

Figure 6.18 shows the maximum growth rate versus substrate temperature is in the temperature range 1000 $^{\circ}$C - 1150 $^{\circ}$C. PCD synthesis experimental results [24, 57, 71] have shown a similar shaped growth curve versus pressure and that the maximum growth rate temperature, T_{max}, increases gradually with deposition pressure. The SCD synthesis growth results shown in Figure 6.18 and 6.19 indicate a similar growth behavior versus temperature.

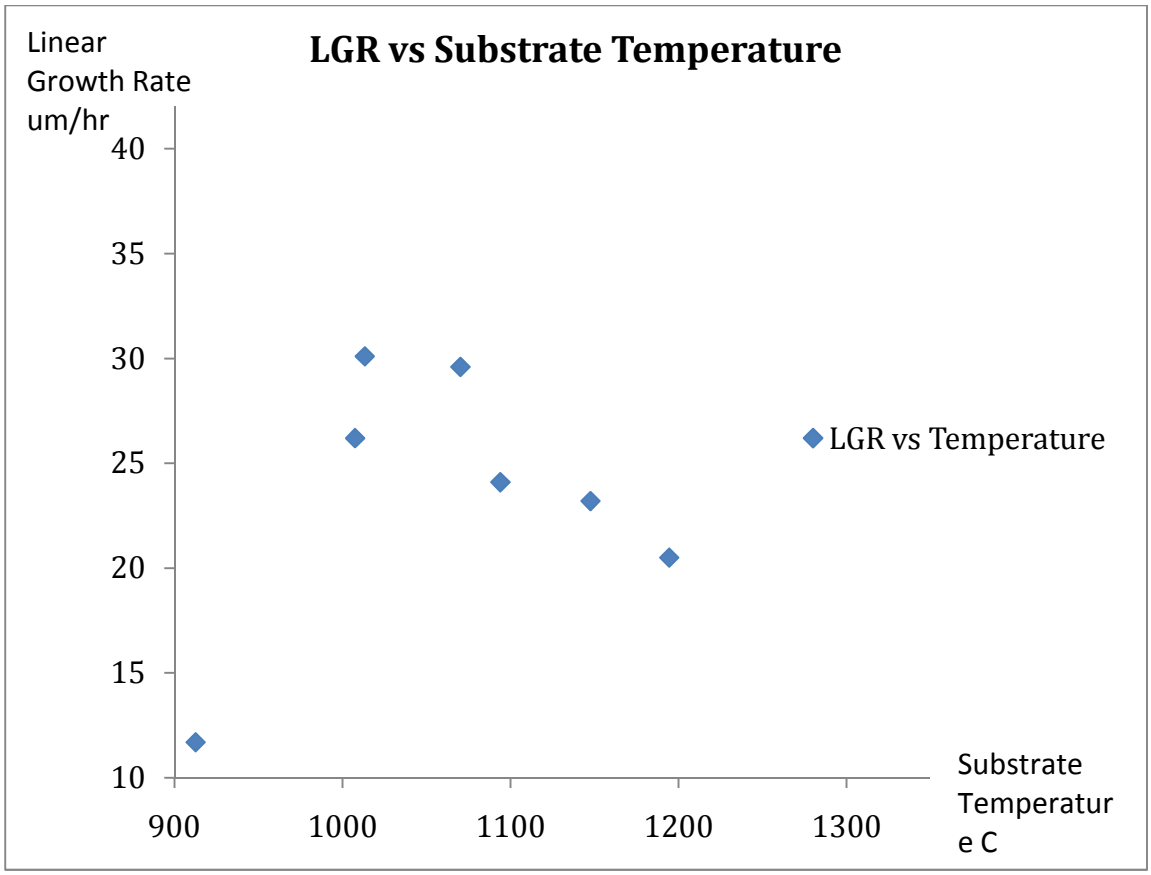

Figure 6.18 Linear growth rate vs. substrate temperature for Reactor C

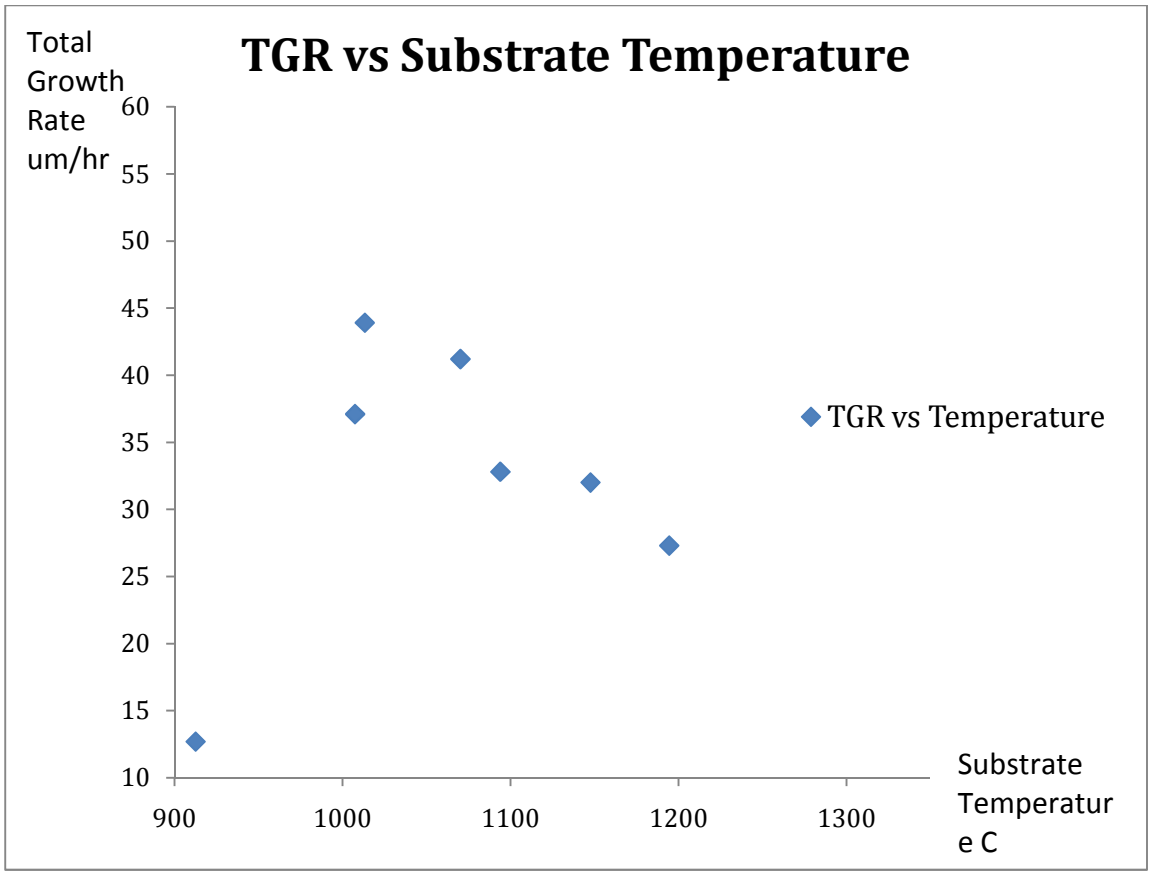

Figure 6.19 Total growth rate vs. substrate temperature for Reactor C

6.8.4 Carbon Conversion Efficiency vs. Substrate Temperature

Since the methane concentrations and substrate sizes are not changed in this set of the experiments, carbon conversion efficiency versus substrate temperature is expected to have the same shaped curve as the total growth rate versus substrate temperature.

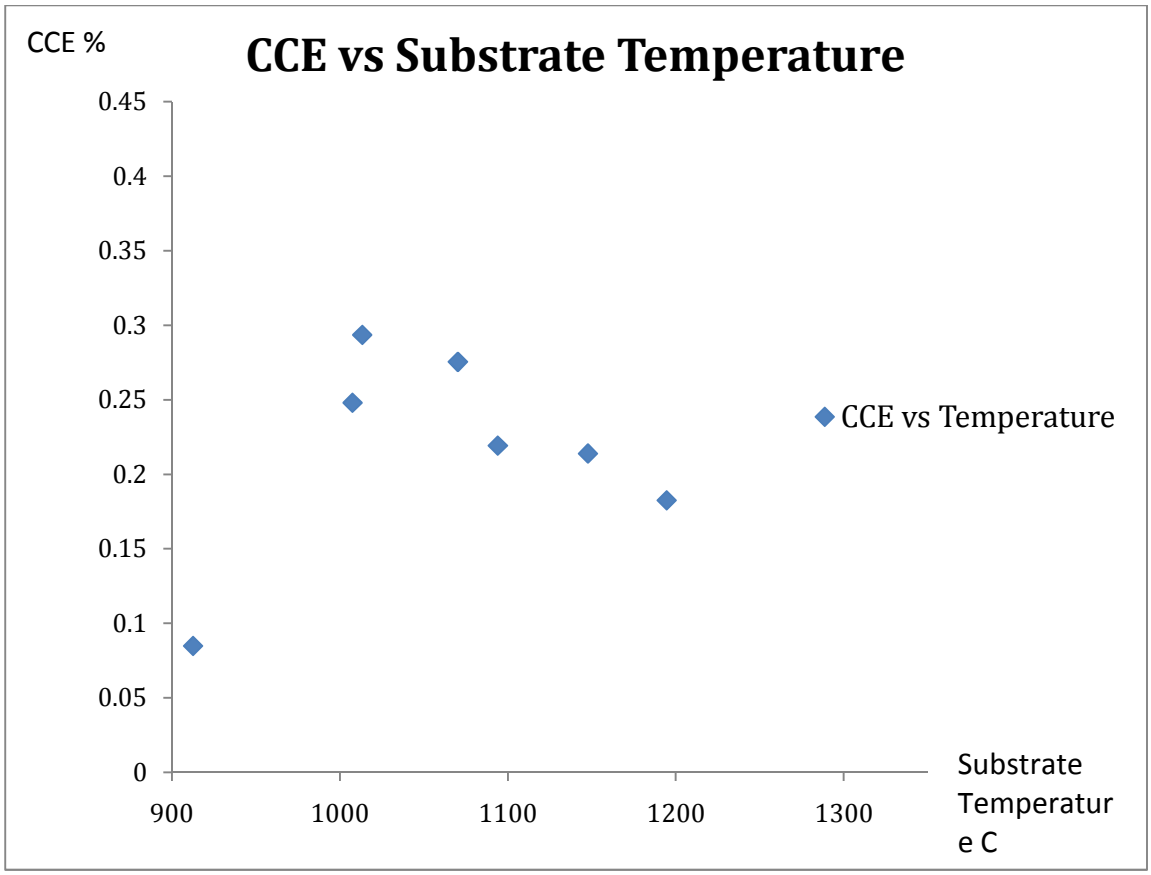

Figure 6.20 Carbon conversion efficiency vs. substrate temperature for Reactor C

6.8.5 Specific Yield vs. Substrate Temperature

Since specific yield is defined as the absorbed power input per diamond film total growth rate, and the absorbed power input in this set of experiments remain close, the specific yield versus substrate temperature is inversely proportional to the total growth rate versus substrate temperature as expected.

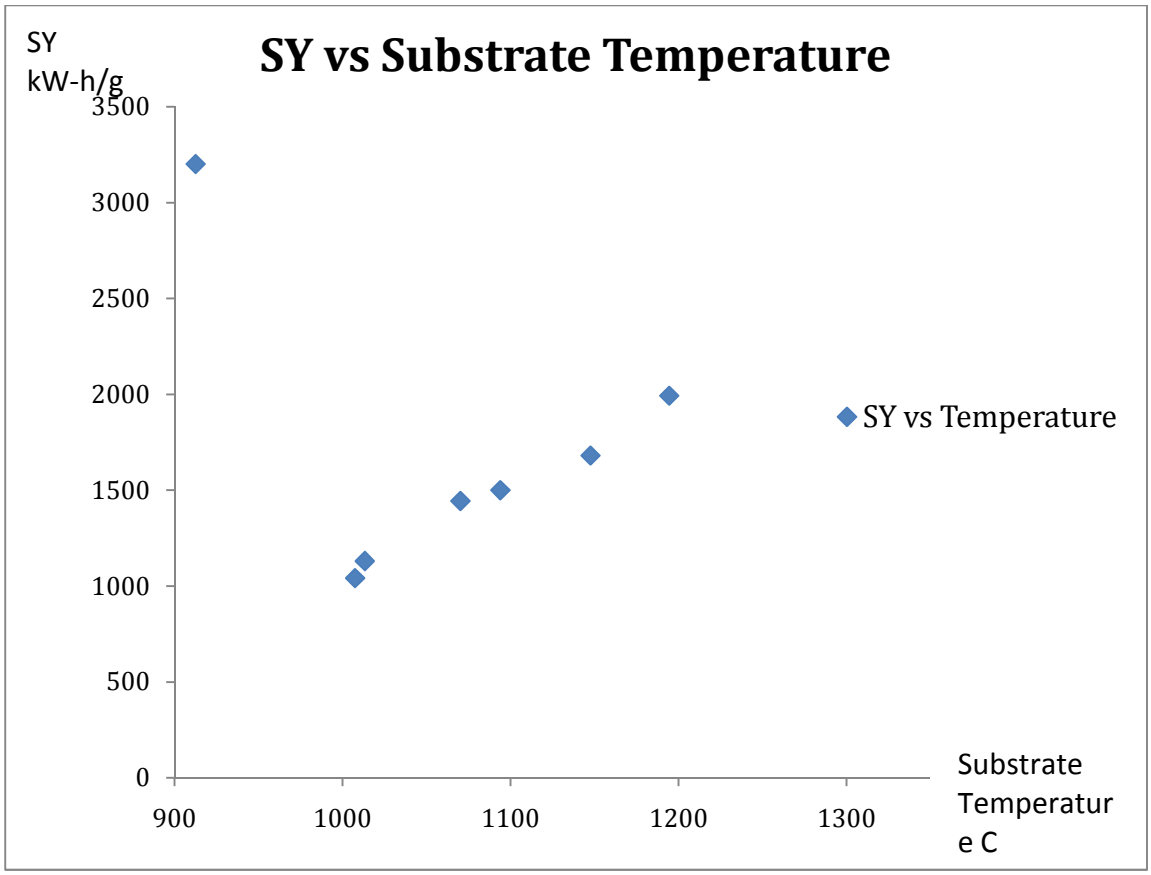

Figure 6.21 Specific yield vs. substrate temperature for Reactor C

6.9 The Role of Methane Concentration (CH_4 / H_2 = 3% / 5% / 7% / 9%)

6.9.1 Introduction

This section presents the experimental results of the output variable Y as a function of methane concentration. A total of four experiments were conducted to verify the role of methane concentration in single crystal diamond MPACVD synthesis. The experiments began at the initial benchmark experimental SCD growth conditions and then carefully varied the methane concentration. The SCD

growth conditions are described in Section 6.9.2. The relationships between methane concentration and output variables Y, such as linear growth rate, total growth rate by weight gain, carbon conversion efficiency, and specific yield, are described in Section 6.9.3 – 6.9.5.

6.9.2 Initial Benchmark Experimental Variables

(1) Controllable input variables, U_1, which include the following

a) Deposition pressure, Fixed: p = 240 Torr

b) Incident microwave power, Variable: P_i = 1.7 – 2.2 kW

c) Feed gas composition, Variable: c = CH_4/H_2= 3% / 5% / 7% / 9% and Fixed: N_2 = 5 ppm

d) Total flow rate, Fixed: f_t = 400 sccm

(2) Reactor geometry variables, U_2, which include the following

a) Applicator size and configuration, Fixed

b) Substrate position, Fixed: Z_S = -4.8 mm

c) Substrate holder design, Fixed: Adjust and redesign for size S seeds

d) Electromagnetic mode: Mode is fixed in all experiments

e) Cavity tuning, Variable: L_S = 16.2-16.5 cm

f) Quartz dome geometry, Fixed: #3 quartz domes have been used

(3) Deposition process variables, U_3, which include the following

a) Substrate material and size, Fixed: 3.5mm*3.5mm*1.4mm HPHT diamond (S)

b) Deposition time, Fixed: t = 24 Hours

(4) Internal variables X, which include

a) Substrate temperature, Fixed: $T_S \approx 1000\ ^{\circ}C$

b) Absorbed microwave power, Variable: P_{abs} = 1.6 – 1.9 kW

c) Plasma volume, Variable: V_p = 3.2 - 3.8 cm^3

d) Absorbed power density, Fixed: $< P_{abs} >$ = P_{abs} / Volume of plasma ≈ 600 W/cm^3

6.9.3 Growth Rate vs. Methane Concentration

The linear growth rate increases as expected when methane concentration

increases for low methane concentrations as shown in Figure 6.22. This is, as described in Section 2.2.2, because the carbon related radical growth species, i.e. CH_3 and H_2, in the plasma are expected to increase as the methane concentration increases resulting in higher growth rates and higher quality diamond. However, the increase of linear growth rate stops at 7% (CH_4/H_2) and decreases at 9%. The reason for this is once the methane concentration becomes large enough at high CH_4/H_2ratios, other reactions within the reactor, such as the formation of soot in the gas phase, and also reactions on the reactor walls which result in wall coating, become important. For example when growing at 9% (CH_4/H_2) graphic layers (black) were found on the top of the deposited SCD when the substrate was taken out of the reactor after the run was finished. It is not known if this graphite formation occurred during the synthesis process or as the reactor was shut down. Additionally at methane concentrations > 7%, the reactor walls also become coated with a dark carbon containing film thereby limiting the length of the deposition process. These wall and gas phase reactions reduce the growth rate and contaminate the deposited diamond and also limit the deposition time.

This series of experiments ended at 9% (CH_4/H_2) because the quartz dome gets badly coated when the methane concentration is too high. The maximum deposition time is limited to 8 hours if the methane concentration is more than 7%. However it is believed that the formation of soot can be modified, and hence reduced, by adjusting the cooling of the reactor walls. This needs more

experimental investigation in future studies.

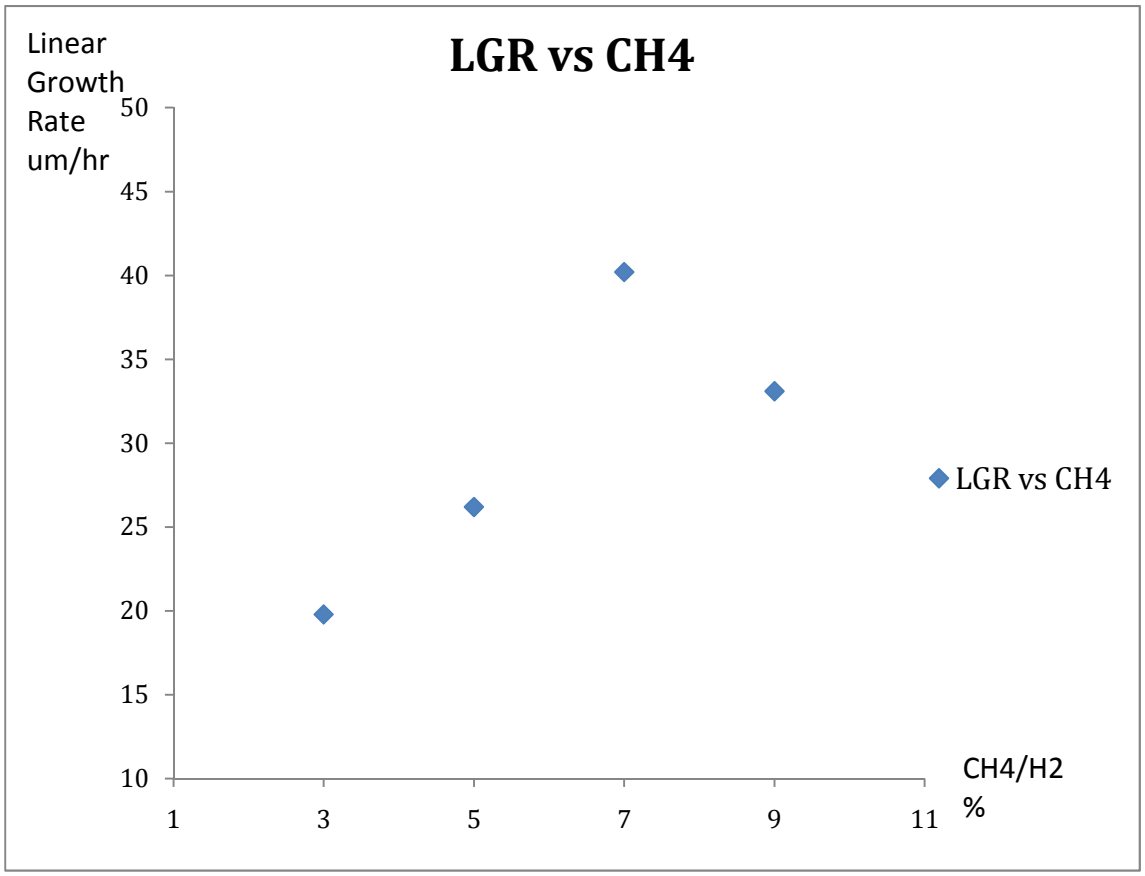

Figure 6.22 Linear growth rate vs. methane concentration for Reactor C

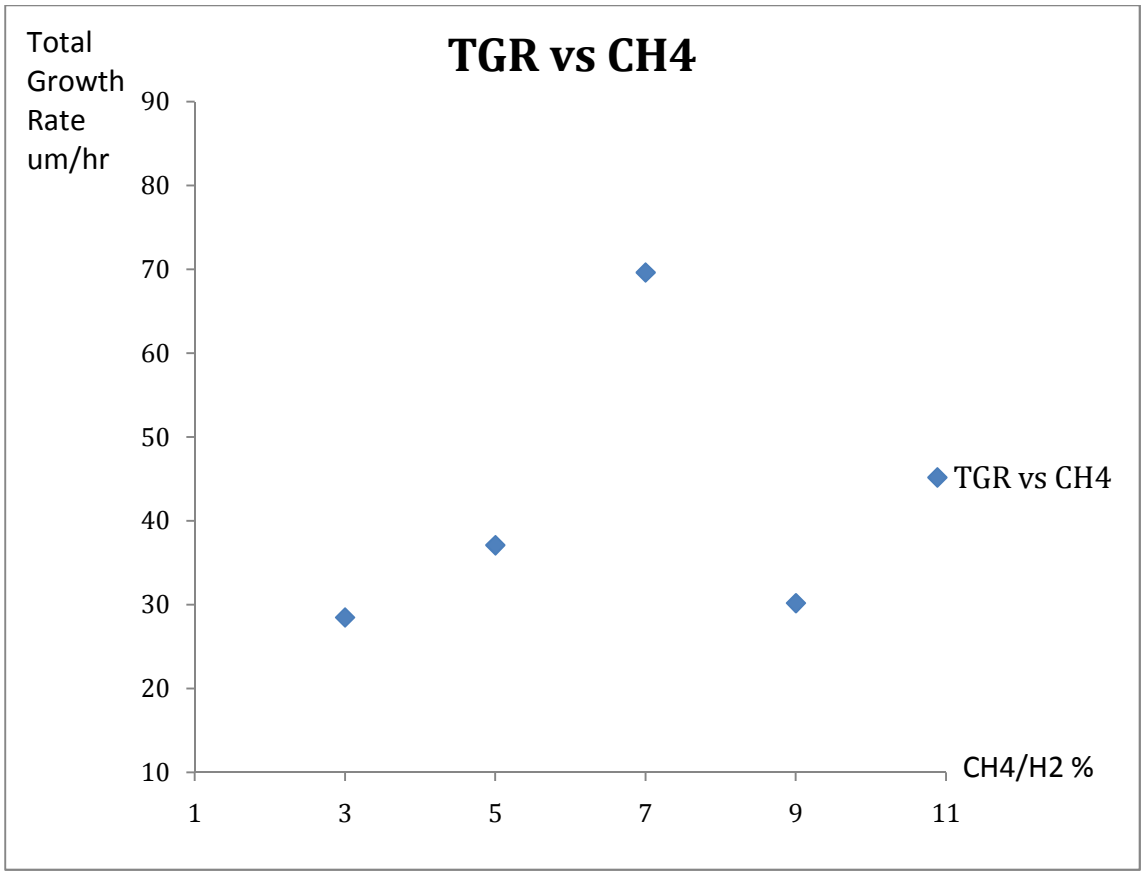

Figure 6.23 Total growth rate vs. methane concentration for Reactor C

6.9.4 Carbon Conversion Efficiency vs. Methane Concentration

As shown in Figure 6.24, carbon conversion efficiency reaches maximum when the growth rate is highest at $CH_4/H_2$is 7%. The CCE drops significantly at 9% because the possible soot formation happens in the gas phase to slow down the CVD diamond deposition. Under these conditions the some of input carbon is being lost in the formation of soot and also in unwanted reactor wall reactions.

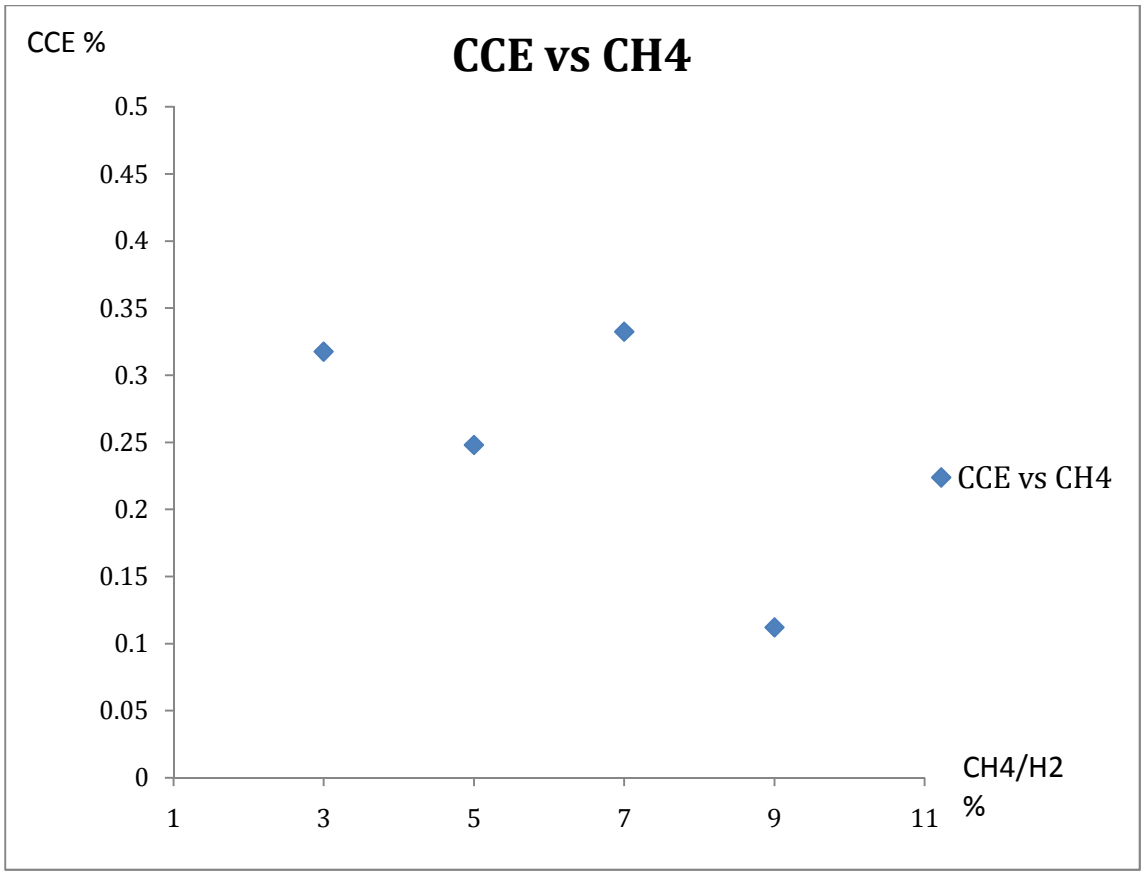

Figure 6.24 Carbon conversion efficiency vs. methane concentration for Reactor C

6.9.5 Specific Yield vs. Methane Concentration

Since specific yield is defined as the absorbed power input per diamond film total growth rate, and the absorbed power input in this set of experiments is slightly varied within a very limited range of 1.7 – 2 kW, the specific yield versus methane concentration is almost inversely proportional to the total growth rate versus methane concentration as expected.

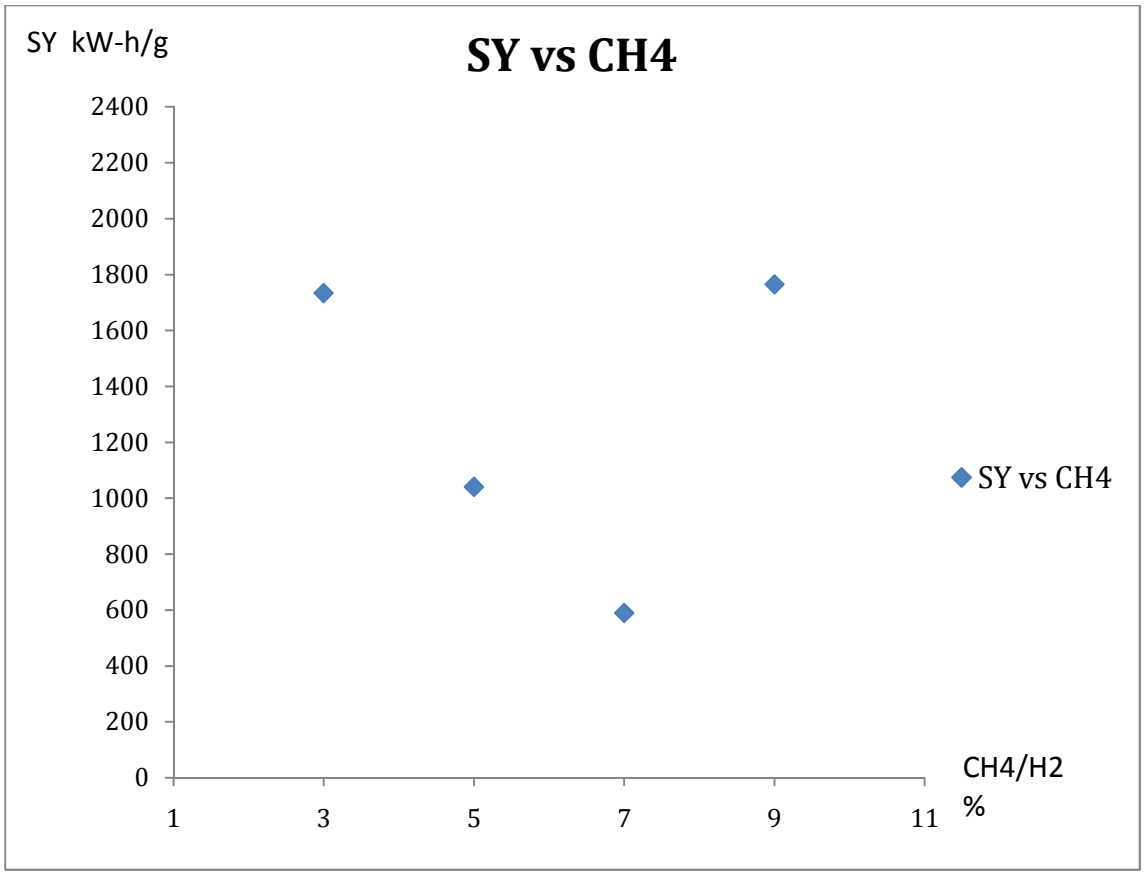

Figure 6.25 Specific yield vs. methane concentration for Reactor C

6.10 The Role of Nitrogen Concentration (N_2 / H_2 = 0 / 5 / 10 / 15 / 20 ppm)

6.10.1 Introduction

This section presents the experimental results of the output variable Y as a function of nitrogen concentration. A total of five experiments were conducted to verify the role of nitrogen concentration in SCD MPACVD synthesis. The experiments start with the benchmark SCD growth conditions and then the total nitrogen content is varied from 5 ppm to 25 ppm. The initial SCD growth

conditions are presented in Section 6.10.2. Then the relationships between the input nitrogen concentration and output variables Y, such as linear growth rate, total growth rate by weight gain, carbon conversion efficiency, and specific yield are presented in Section 6.10.3 – 6.10.5.

6.10.2 Initial Benchmark Experimental Variables

(1) Controllable input variables, U_1, which include the following

a) Deposition pressure, Fixed: p = 240 Torr

b) Incident microwave power, Variable: P_i = 1.7 – 2.2 kW

c) Feed gas composition, Fixed: c = CH_4/H_2= 5% and variable: N_2 = 5 / 10 / 15 / 25 ppm

d) Total flow rate, Fixed: f_t = 400 sccm

(2) Reactor geometry variables, U_2, which include the following

a) Applicator size and configuration, Fixed

b) Substrate position, Fixed: Z_s = -4.8 mm

c) Substrate holder design, Fixed: Adjust and redesign for size S seeds

d) Electromagnetic mode: Mode is fixed in all experiments

e) Cavity tuning, Variable: L_S = 16.2-16.5 cm

f) Quartz dome geometry, Fixed: #3 quartz domes have been used

(3) Deposition process variables, U_3, which include the following

a) Substrate material and size, Fixed: 3.5mm*3.5mm*1.4mm HPHT diamond (S)

b) Deposition time, variable: t = 42 - 82 Hours

(4) Internal variables X, which include

a) Substrate temperature, Fixed: $T_S \approx 1000\ ^{\circ}C$

b) Absorbed microwave power, Variable: P_{abs} = 1.6 – 1.9 kW

c) Plasma volume, Variable: V_p = 3.2 - 3.8 cm^3

d) Absorbed power density, Fixed: $< P_{abs} >$ = P_{abs} / Volume of plasma ≈ 600 W/cm^3

6.10.3 Growth Rate vs. Nitrogen Concentration

It has been demonstrated experimentally over last two decades that the addition of small amounts of nitrogen to the methane-hydrogen diamond

synthesis gas has an important impact on CVD diamond synthesis [72-74]. For example, the addition of 5-50 ppm of nitrogen can have a beneficial effect on growth rate. So using the experience of past experiments the linear growth rate is expected to increase as the nitrogen concentration increases. This has been observed in other experiments such as Jing [75] and it also has been observed in the recent published literature [76,77].

Figures 6.26 and 6.27 display the experimental variation of growth rate versus input nitrogen gas concentration. A shown in Figure 6.26 the growth rate increases linearly from about 17 microns/hr with 5 ppm nitrogen to over 40 microns/hr for 25 ppm of nitrogen concentration. It is important to note that the 5 ppm data point is the amount of nitrogen input that results from the input feed gas impurities and vacuum leaks. The 5 ppm nitrogen input is an estimated maximum impurity level.

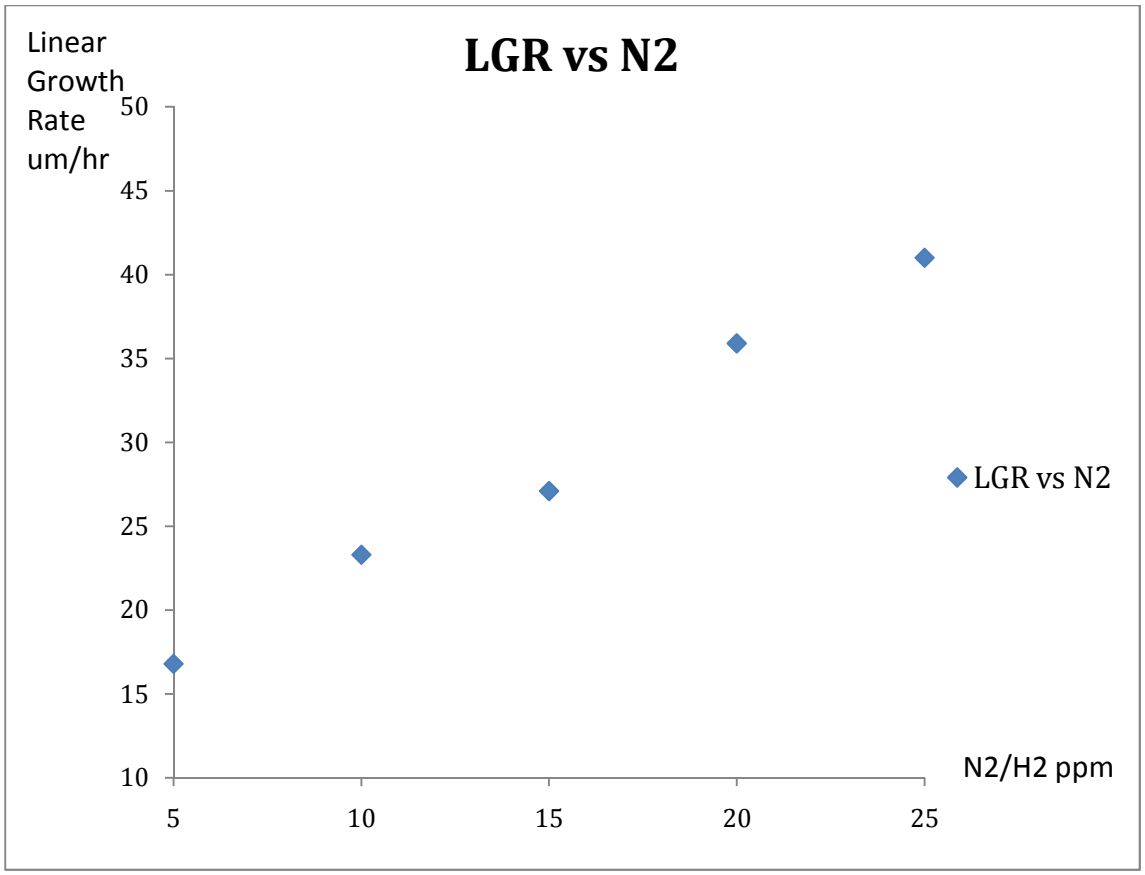

Figure 6.26 Linear growth rate vs. nitrogen concentration for Reactor C

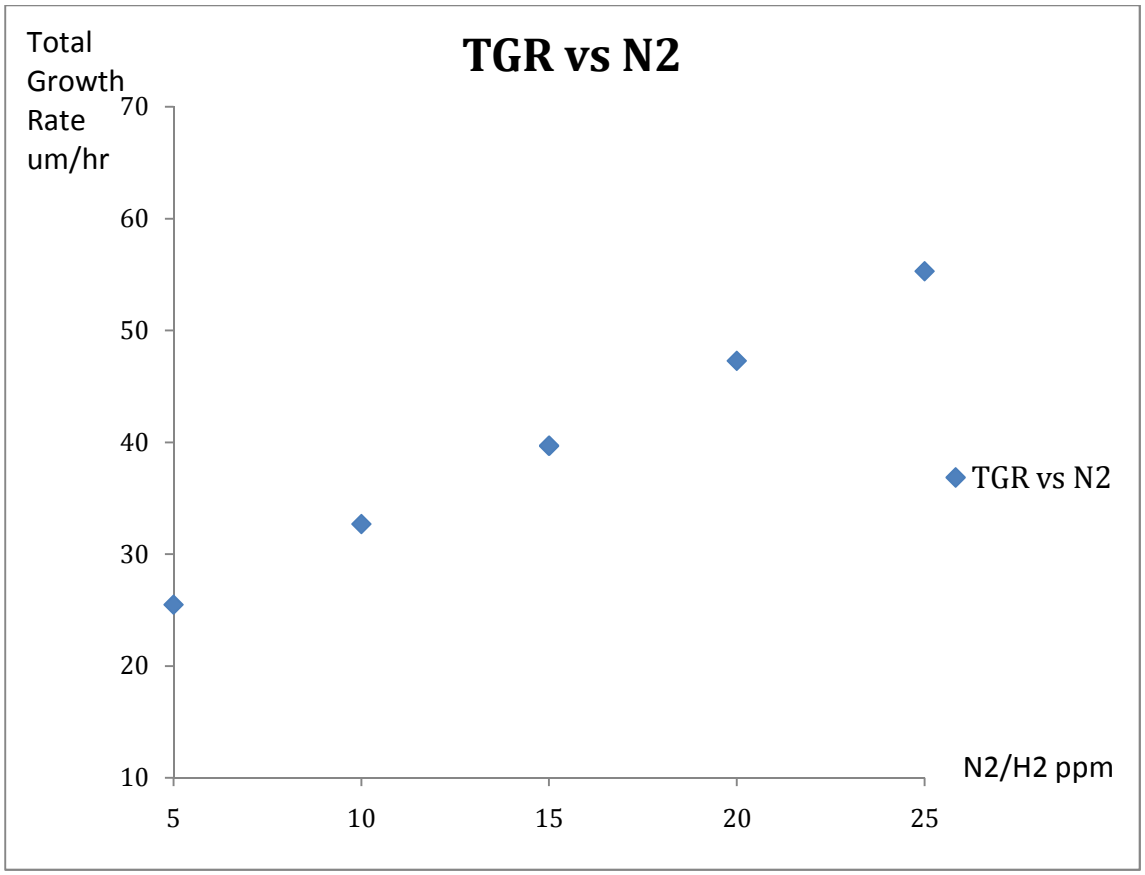

Figure 6.27 Total growth rate vs. nitrogen concentration for Reactor C

6.10.4 Carbon Conversion Efficiency vs. Nitrogen Concentration

Since the methane concentrations and substrate sizes are not changed in this set of the experiments, carbon conversion efficiency versus nitrogen concentration is expected to have the same shaped curve as the total growth rate versus nitrogen concentration.

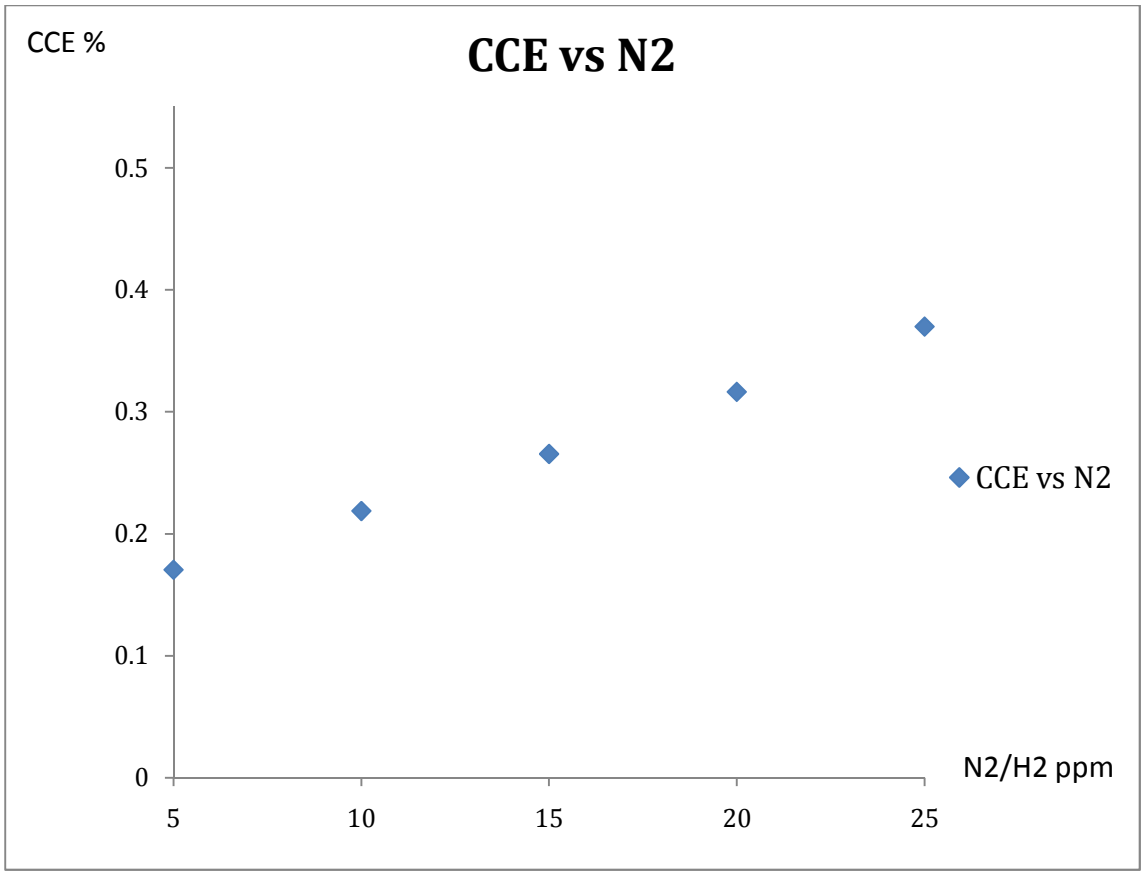

Figure 6.28 Carbon conversion efficiency vs. nitrogen concentration for Reactor C

6.10.5 Specific Yield vs. Nitrogen Concentration

Since specific yield is defined as the absorbed power input per diamond film total growth rate, and the absorbed power input is limited to the narrow range of 1.6-1.9 kW, the specific yield versus nitrogen concentration is in inverse proportion of the total growth rate versus nitrogen concentration as expected.

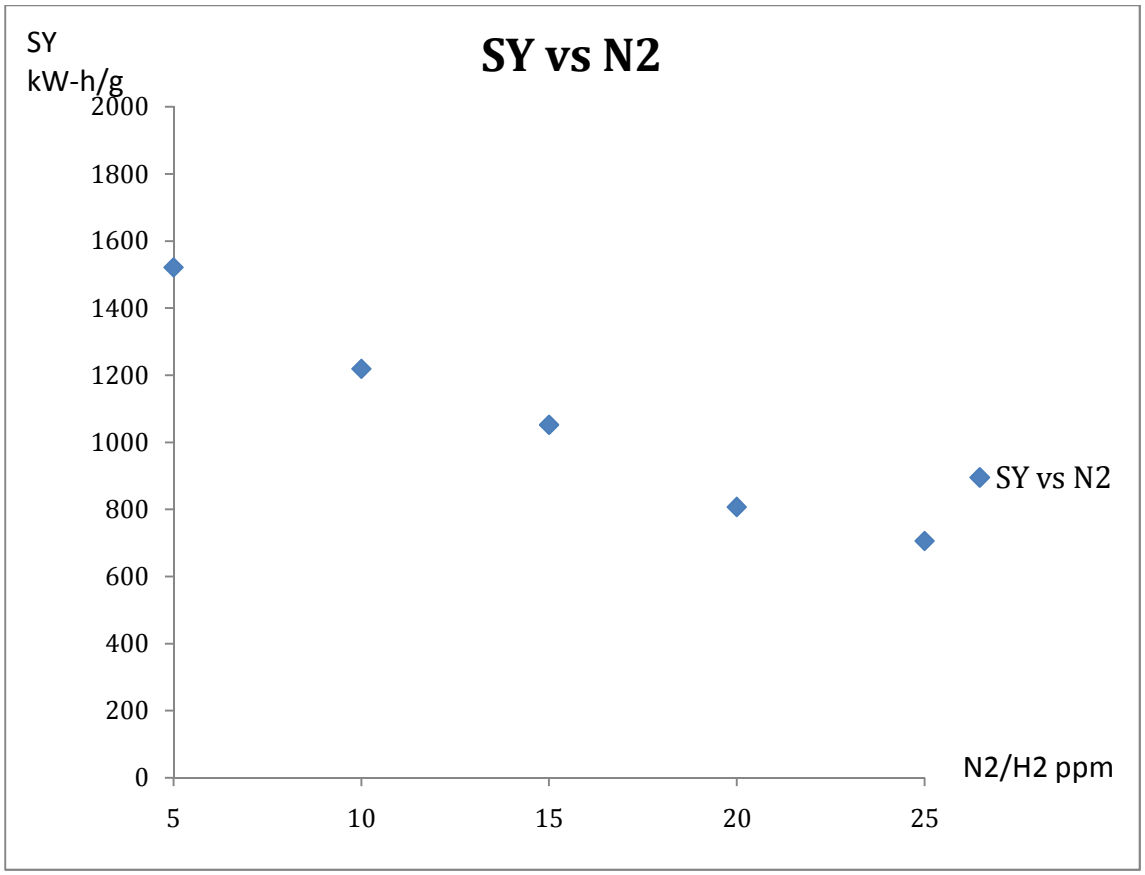

Figure 6.29 Specific yield vs. nitrogen concentration for Reactor C

6.11 The Role of Substrate Size (S / M / L)

6.11.1 Introduction

This section presents the experimental results of the output variable Y as a function of substrate size. Total three experiments were conducted to understand the role of substrate size in SCD MPACVD synthesis. The experiments start with the initial benchmark experimental SCD growth conditions and then substrate size was varied from 3.5mm*3.5mm, to 4.8mm*4.8mm and then to 7mm*7mm. The initial benchmark experimental SCD growth conditions are introduced in

Section 6.11.2. Then the relationships between substrate size and output variables Y, such as linear growth rate, total growth rate by weight gain, carbon conversion efficiency, and specific yield are presented in Sections 6.11.3 – 6.11.5. It is important to note that each substrate size has its own substrate holder set design. The holder for each substrate size is very similar to the holder shown in Fig. 6.1 except the pocket area in the molybdenum holder is adjusted to accommodate the different diamond seed substrate areas. Thus these experiments have in addition to the variation of seed substrates may have another variable; i.e. the molybdenum holder itself.

6.11.2 Initial Benchmark Experimental Variables

(1) Controllable input variables, U_1, which include the following

a) Deposition pressure, Fixed: p = 240 Torr

b) Incident microwave power, Variable: P_i = 1.7 – 2.2 kW

c) Feed gas composition, Fixed: c = CH_4/H_2= 5% and N_2 = 5 ppm

d) Total flow rate, Fixed: f_t= 400 sccm

(2) Reactor geometry variables, U_2, which include the following

a) Applicator size and configuration, Fixed

b) Substrate position, Fixed: Z_S = -4.8 mm

c) Substrate holder design, Variable: Adjust and redesign for size S / M / L seeds

d) Electromagnetic mode: Mode is fixed in all experiments

e) Cavity tuning, Variable: L_S = 16.2-16.5 cm

f) Quartz dome geometry, Fixed: #3 quartz domes have been used

(3) Deposition process variables, U_3, which include the following

a) Substrate material and size, Variable: 3.5mm*3.5mm*1.4mm HPHT diamond (S), 4.8mm*4.8mm*1.5mm HPHT diamond (M) and 7.0mm*7.0mm*1.2mm HPHT diamond (L)

b) Deposition time, fixed: t = 24 Hours

(4) Internal variables X, which include

a) Substrate temperature, Fixed: $T_S \approx 1000$ ˚C

b) Absorbed microwave power, Variable: P_{abs} = 1.6 – 1.9 kW

c) Plasma volume, Variable: V_p = 3.2 - 3.8 cm^3

d) Absorbed power density, Fixed: $< P_{abs} > = P_{abs}$ / Volume of plasma ≈ 600 W/cm^3

6.11.3 Growth Rate, Carbon Conversion Efficiency and Specific Yield vs. Substrate Size

From Figure 6.30, it is observed that the linear growth rates have the lowest growth rate for medium size substrate and are similar for small and large size substrates. However considering that the SCD growth rates are dependent on the substrate holder geometry the variation between all three runs is not significant. It is believed that the growth rate variation shown in Figures 6.30 – 6.31 is probably due to the variation in substrate holder design from one size substrate to another and thus there is little variation in growth rate versus size over the 10 -50 mm^2 variation in substrate area displayed in Figures 6.30 and 6.31. Figures 6.32 and 6.33 display the carbon conversion efficiency and specific yield versus substrate area.

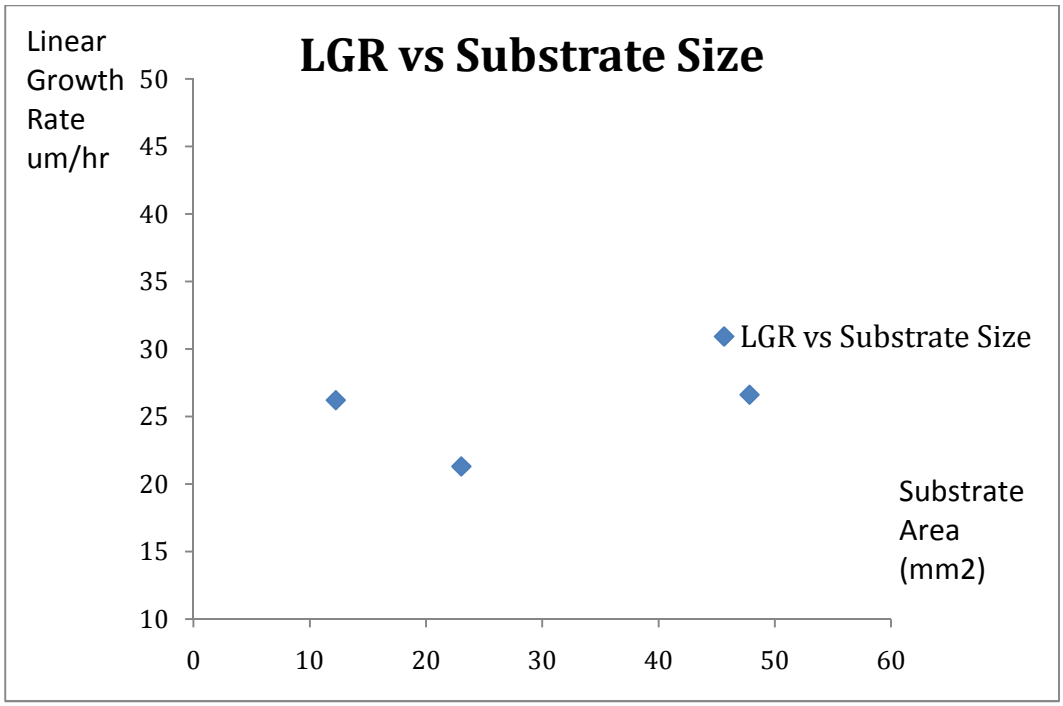

Figure 6.30 Linear growth rate vs. substrate size for Reactor C

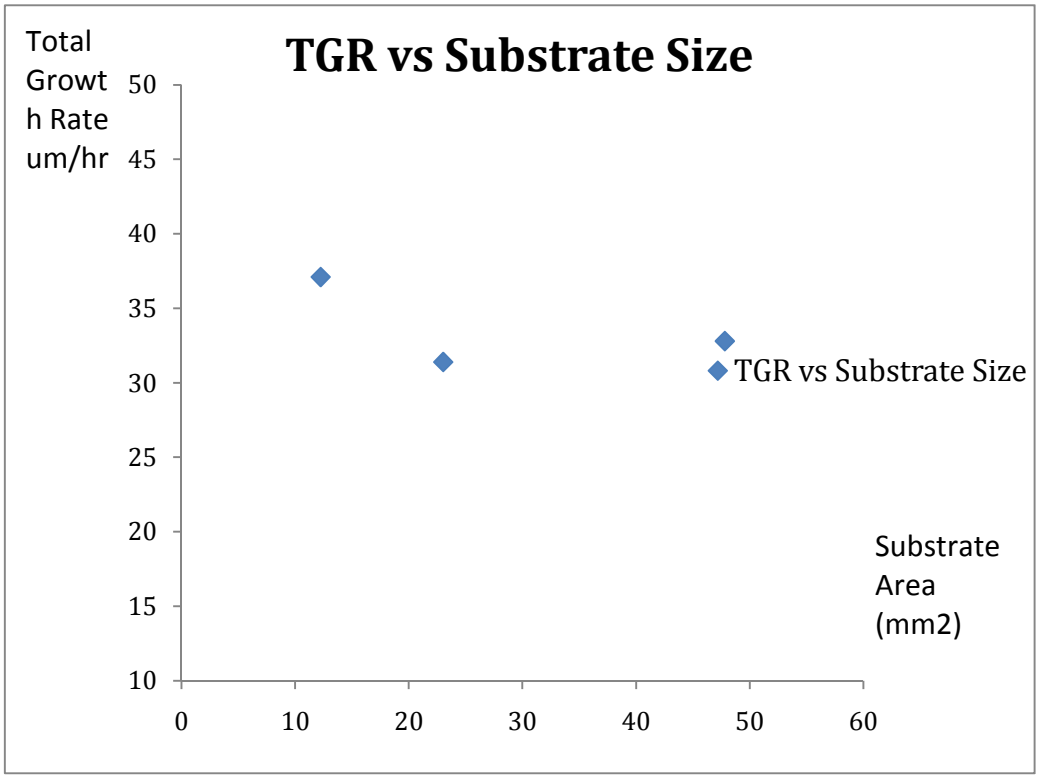

Figure 6.31 Total growth rate vs. substrate size for Reactor C

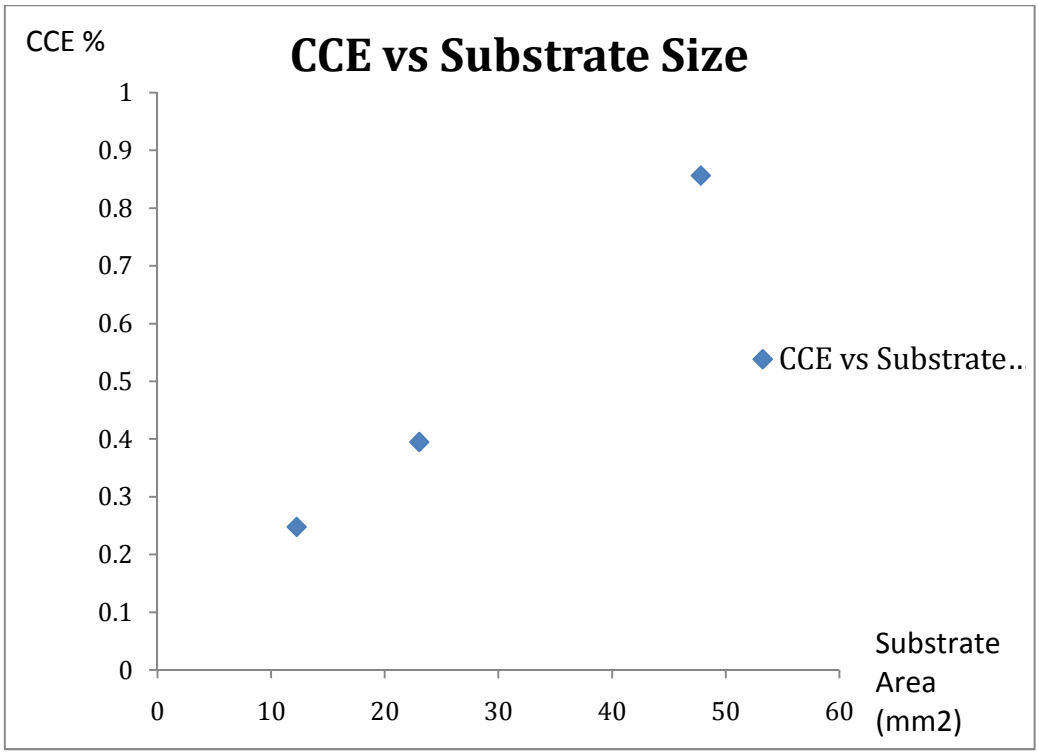

Figure 6.32 Carbon conversion efficiency vs. substrate size for Reactor C

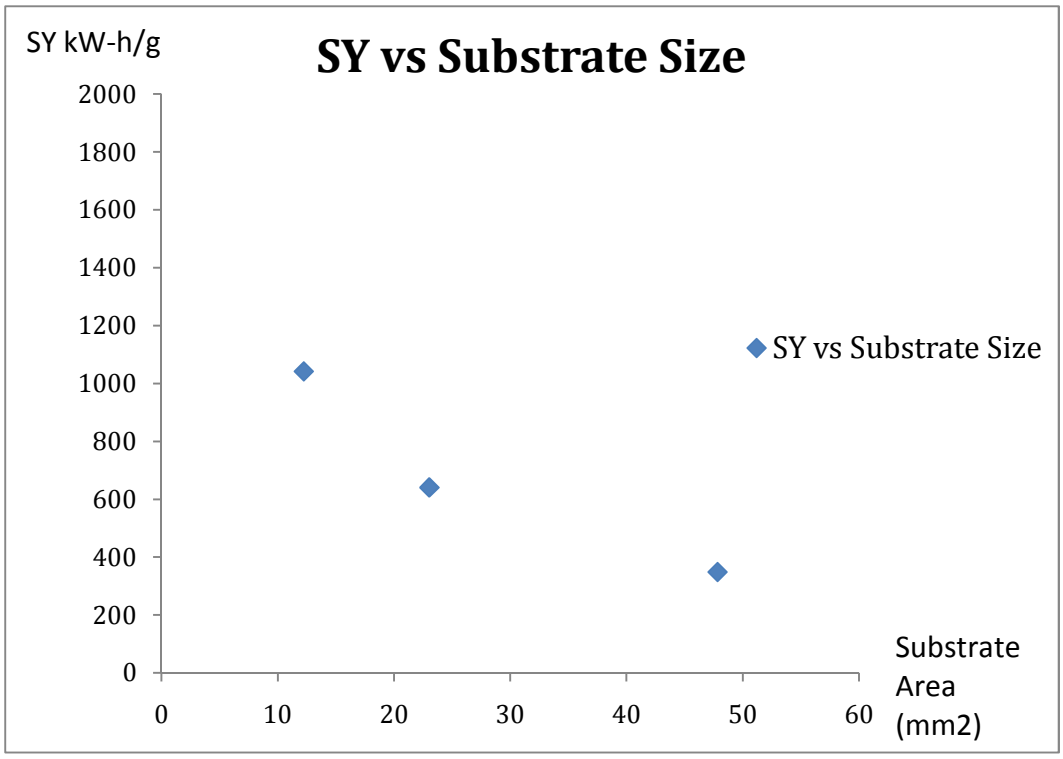

Figure 6.33 Specific yield vs. substrate size for Reactor C

6.12 The Comparison of the Performance of Reactor C with Earlier Reactor Designs

A series of exploratory experiments of SCD growth rate versus pressure, were performed in Reactors A, B and C and the results are displayed in Figure 6.34. Clearly the maximization of the growth rate at each data point is a multivariable optimization problem. At each of the data points shown in Figure 6.34 the total flow rate was held at ~ 400 sccm and the substrate position, $Z_{S,}$ for each reactor was held constant at an optimized (high growth rate) position. The optimized Z_S position for Reactor B is ~ -3.6 mm and for Reactor C are -4.8 mm. The input powers ranged from 3 kW for Reactor A, between 2.1-2.3 kW for Reactor B and 1.9-2.1 kW for Reactor C. The exploratory experimental data in Figure 6.34 shows that there are important increases in SCD growth rates for Reactors B and C over the growth rates of Reactor A at lower pressures. If we compare Figure 5.12 and Figure 6.34, it suggests that the increased growth rates in Reactor C are related in part to the increased discharge power density due to both the smaller substrate holder and to the operation at higher pressures.

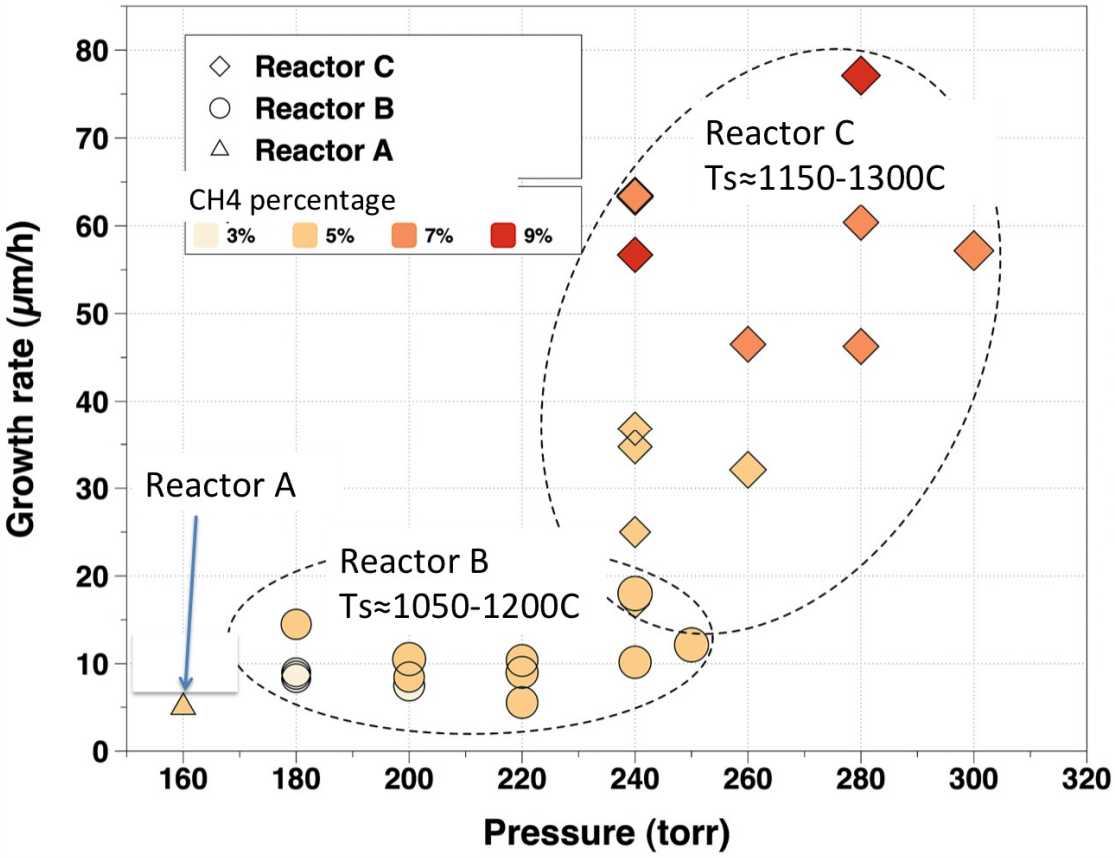

Figure 6.34 Linear growth rate comparison among Reactor A, B and C vs. deposition pressure

After we compare linear growth rate versus pressure for Reactor A, B and C, a more precise comparison between reactors B and C is made in Figure 6.35 where the performance of the reactors is compared under similar experimental conditions. For each experimental data point there are at least eight important experimental variables: (1) pressure, (2) substrate temperature, (3) substrate position, Z_S, (4) substrate holder configuration, (5) methane concentration, (6) flow rate, (7) absorbed power density, and (8) reactor design/geometry. In the comparison between Reactors B and C shown in Figure 6.35 both reactors were

operated under the same input variable conditions, i.e. 240 torr, fixed Z_S, the fixed generic substrate holder configuration shown in Figure 6.1, CH_4/H_2= 5%, and a constant total flow rate of ~ 400 sccm. Under these input conditions a series of experiments versus substrate temperature were performed for both reactors B and C operating with the approximate absorbed power density conditions that are indicated in Figure 5.12. Figure 6.35 identifies a SCD growth window between 1000 ℃ -1300 ℃, where the growth r ate exhibits a maximum between 1125 ℃ -1225 ℃. Under these conditions the maximum growth rate for Reactor B is about 25 microns/hr at 1200 ℃, and is 38 m icrons/hr at 1150 ℃ for Reactor C. Within this growth window the growth rates for Reactor C are 1.2-2.5 times greater than the corresponding growth rates for Reactor B. This suggests that the higher power densities of Reactor C (see Figure 5.12) result in higher deposition rates; i.e. changes in reactor design/configuration result in higher power densities and also higher deposition rates.

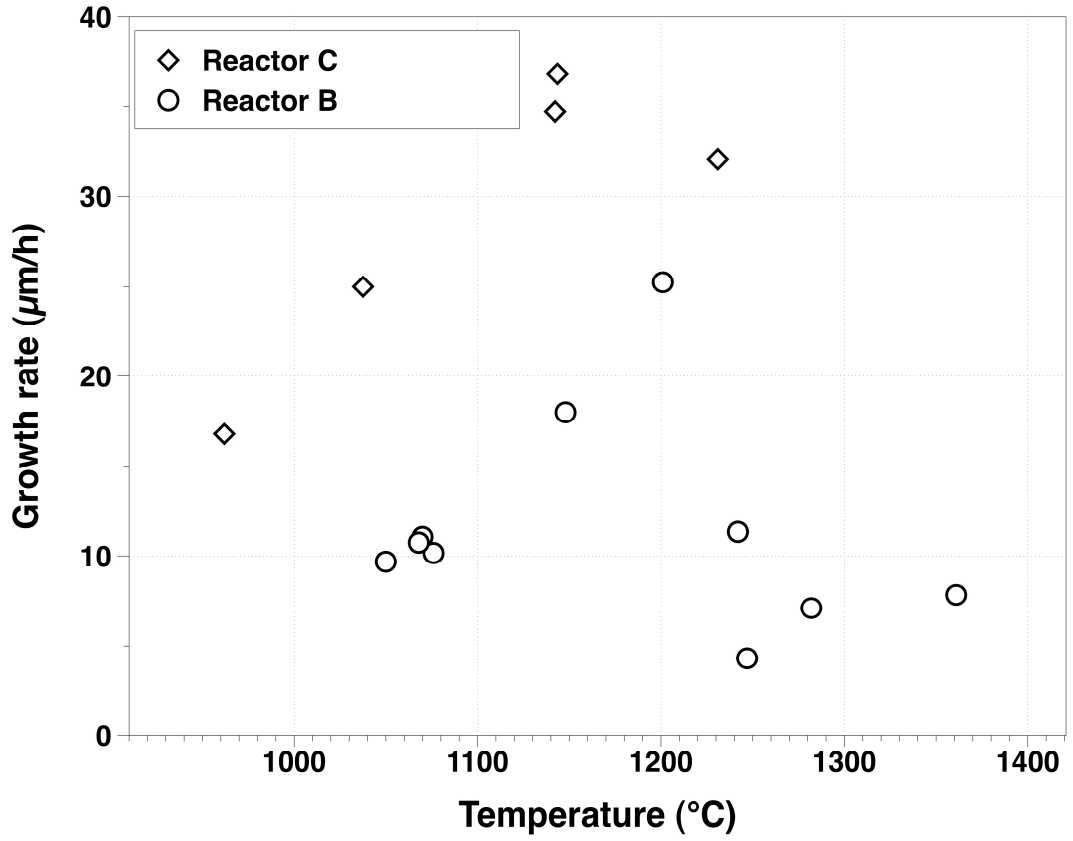

Figure 6.35 SCD growth rate versus temperature for Reactors B and C

6.13 Diamond Quality Assessment

6.13.1 Visual Inspection of the Diamond Surface

After each experimental run the CVD synthesized SCD diamond substrate was visually inspected with an optical microscope (Nikon Eclipse ME600) and a group of photographs were taken as part of the experimental record for this investigation. Examples of several of the microscope photo images of the grown single crystal diamond surface are shown in Figure 6.36-6.37. These two samples were grown under similar conditions, i.e. 5% CH_4/H_2, 240 Torr. These

two images indicate that the diamond process may vary during a long experiment. Sample GYJ118 grew for 24 hours at a relatively high temperature 1013 ℃. The image shows it grew in thin layers starting from the outer edges and moving inward. Some conical round hillocks can be seen on the right side of the surface. Sample GYJ087 also grew for the same methane concentration and pressure, but at lower temperature and a longer growth time of 67.5 hours. In this photograph it appears that the growth surface becomes more even when it grows longer and at a lower temperature and top surface now grows from inside out. Thus as the diamond becomes thicker the growth changes from initially growing from the edges inward to growth from the inside out. Substrate temperature also may play a role in the growth process. This phenomenon needs additional investigation. It is recognized that growth from the inside out produces diamond plates with a minimal PCD boundary.

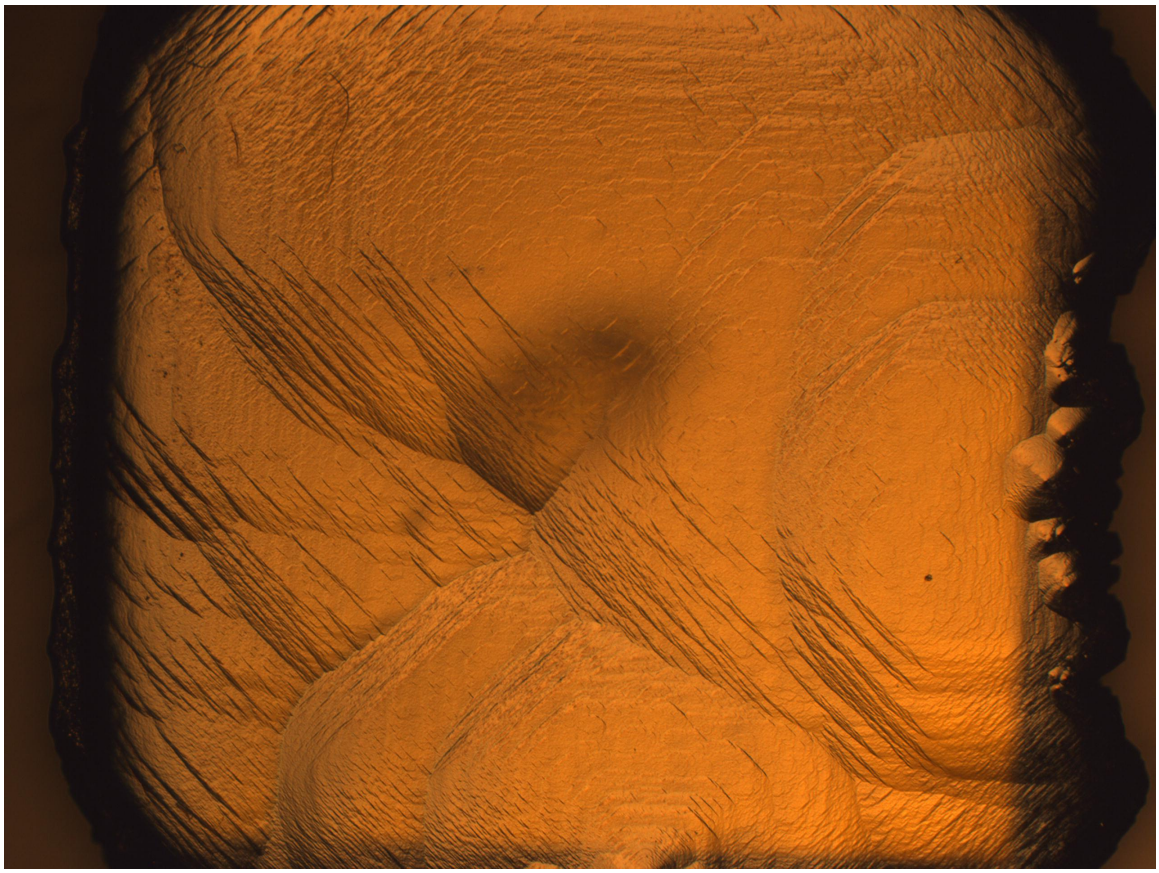

Figure 6.36 Unpolished SCD sample GYJ118: CH_4/H_2=5%, pressure=240 Torr, Growth time=24 hours, 5ppm N_2, substrate temperature=1013 ℃, absorbed power = 2133 W, growth rate=30.1 μm/hr, film thickness = 722.4 μm

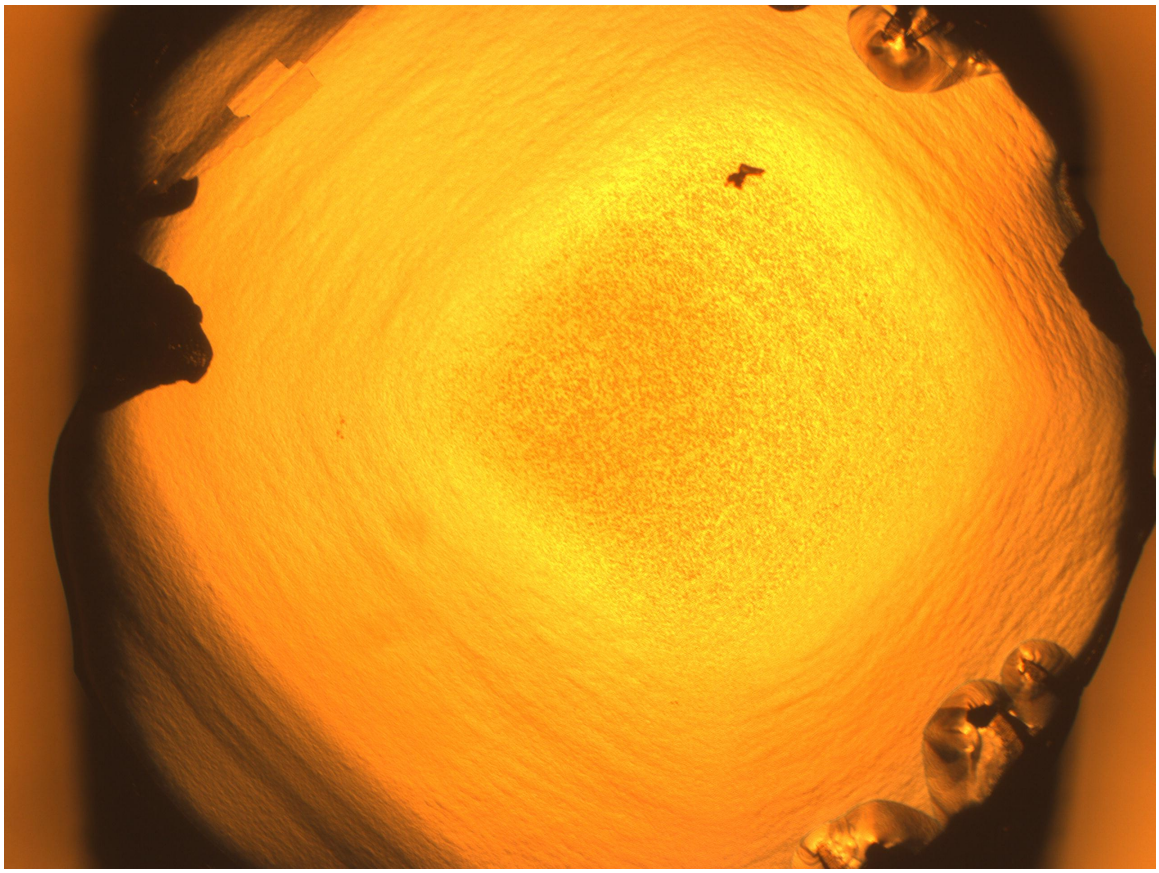

Figure 6.37 Unpolished SCD sample GYJ087: CH_4/H_2=5%, pressure=240 Torr, Growth time=67.5 hours, 5ppm N_2, substrate temperature=974 ℃, absorbed power = 1637 W, growth rate=38.1 μm/hr, film thickness = 2572 μm

Figures 6.38 – 6.40 show some examples of the defects on the grown single crystal diamond surface. Figure 6.38 displays some dark particles at the corner of sample GYJ051. This could be caused by the fact that soot was formed in the high temperature high power density plasma and fell down on the diamond surface or even more likely the defects in the corner probably originated at the seed surface and then propagated and enlarged as the growth proceed and the film became thicker. Figure 6.39 shows a conical round hillock on the smoothly

grown surface of sample GYJ125.

The high pressure high temperature (HPHT) diamond seed itself contains imperfections or defects prior to deposition. For example it usually contains more than 100 ppm N content and consists of several HPHT growth domains that have different impurity levels. Also depending on how the manufacturer fabricates and cuts the HPHT diamond seed, the top surface may not perfectly on [100] direction. Thus many of the defects that have been observed probably originate on the seed substrate surface. An example of one such defect is shown in Figure 6.40. It has been observed that in some cases these defects are overgrown as the process proceeds and under other conditions the defect becomes more pronounced as the process proceeds.

The identification, the origin and understanding of growth defects require much additional study and were not the topic of this thesis. Thus the benchmark processes/conditions that were employed here in this investigation were known to produce few defects and a goal was to produce thick (> 250 μm) diamond plates.

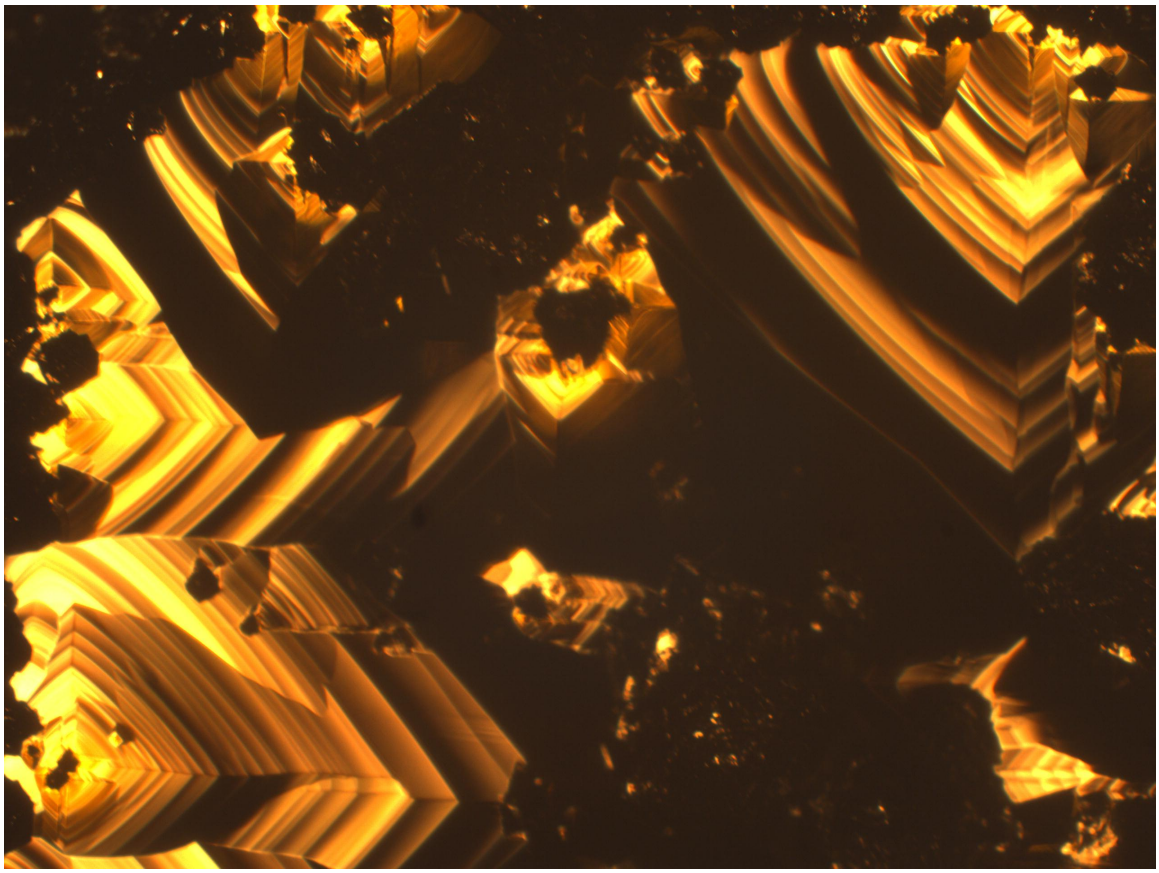

Figure 6.38 Unpolished SCD sample GYJ051: CH_4/H_2=5%, pressure=240 Torr, Growth time=12.5 hours, No N_2, substrate temperature=1172 ℃, absorbed power = 1841 W, growth rate=22 μm/hr, film thickness = 275.3 μm

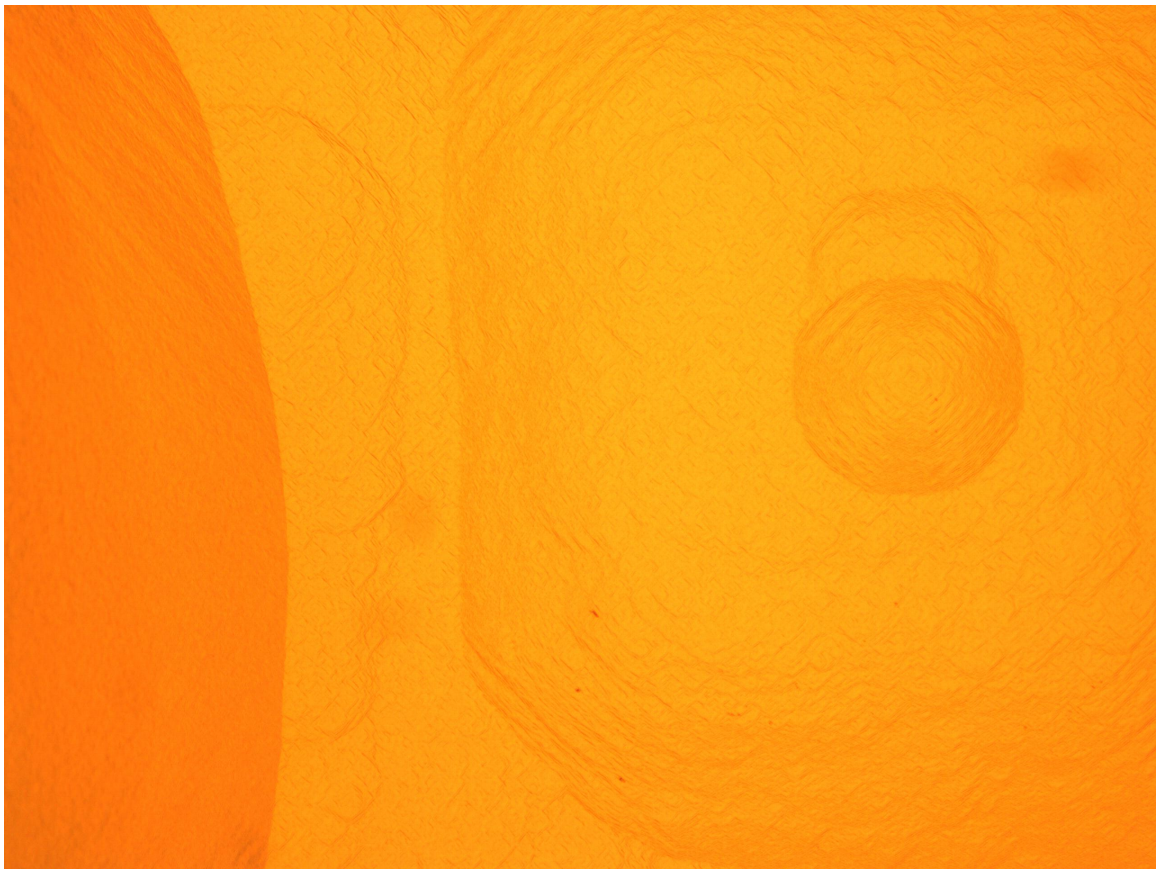

Figure 6.39 Unpolished SCD sample GYJ125: CH_4/H_2=5%, pressure=300 Torr, Growth time=24 hours, 5ppm N_2, substrate temperature=987 ℃, absorbed power = 1862 W, growth rate=33.3 μm/hr, film thickness = 799.2 μm

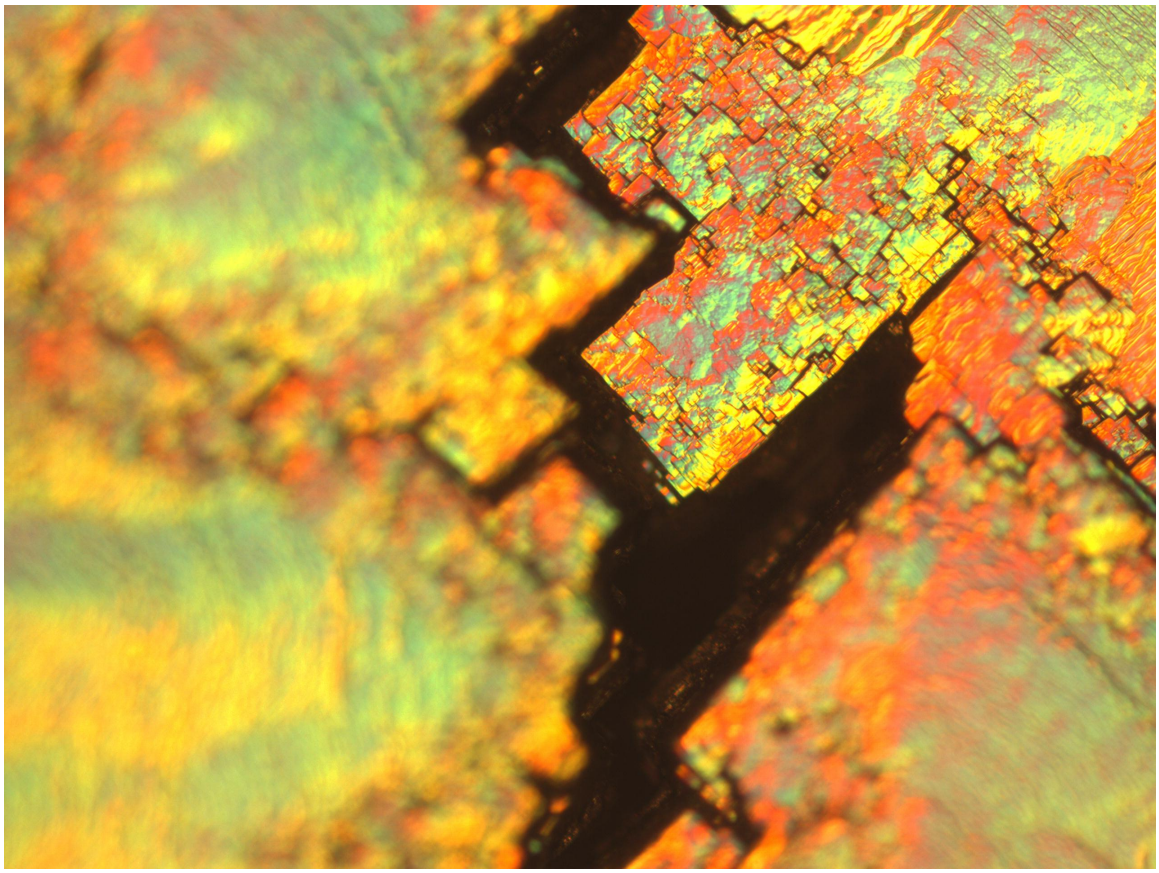

Figure 6.40 Unpolished SCD sample GYJ054: CH_4/H_2=5%, pressure=240 Torr, Growth time=51.5 hours, 10ppm N_2, substrate temperature=1153 ℃, absorbed power = 1876 W, growth rate=38 μm/hr, film thickness = 1956 μm

Diamond plates were fabricated by first removing the SCD CVD synthesized diamond from the seed by laser cutting and then also the PCD rims were removed by laser cutting. Then the plates were mechanically polished. Typical examples of these plates are shown in Figure 6.41. Some of the plates shown were synthesized in Reactor A and some contain different but small amounts nitrogen. However they are all type IIa CVD single crystal diamond

plates.

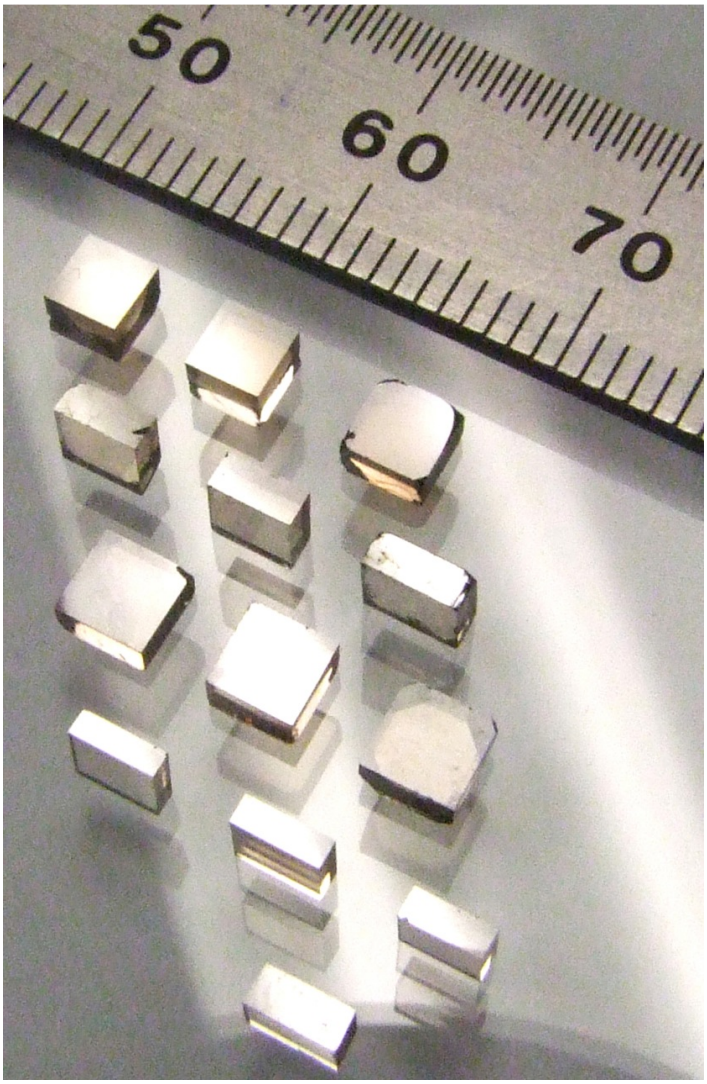

Figure 6.41 Examples of CVD diamond plates: GYJ069 (row 4 column 1) CH_4/H_2=5%, pressure=240 Torr, Growth time=42 hours, 5ppm N_2, substrate temperature=962 ℃, absorbed power = 1668 W, growth rate=16.8 μm/hr, film thickness = 705.6 μm; GYJ075 (row 3 column 3) CH_4/H_2=5%, pressure=240 Torr, Growth time=44.5 hours, 10ppm N_2, substrate temperature=982 ℃, absorbed power = 1859 W, growth rate=28.8 μm/hr, film thickness = 1282 μm

6.13.2 Diamond Raman Spectroscopy and Stress Measurements

Raman spectroscopy is a spectroscopic technique commonly used for the identification of a wide range of substances, i.e. solids, liquids, and gases. In general a sample is illuminated with a laser beam. A spectrometer is used to examine the light from the illuminated spot.

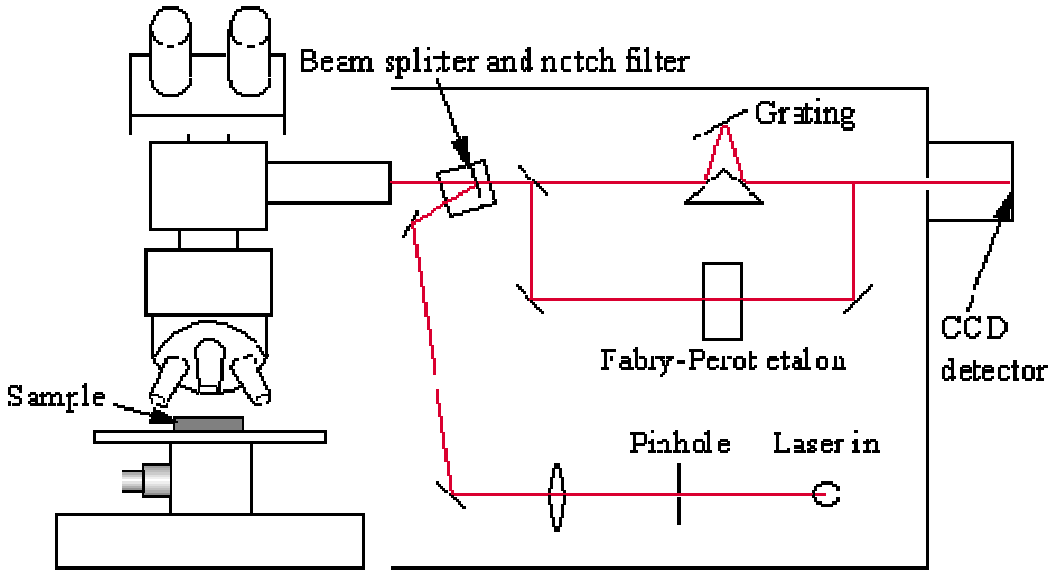

Figure 6.42 Schematic diagram of a Raman spectrometer.

As shown in Figure 6.42 is a schematic diagram of a typical Raman spectrometer. Lasers are used as a photon source due to their highly monochromatic nature, and high beam fluxes. Raman spectrometer for CVD material characterization uses a microscope to focus the laser beam to a small

spot. The light from the illuminated spot passes through the microscope optics to the spectrometer. Raman shifted radiation can be detected with a charge coupled device (CCD) detector. Computer is used to collect the data. The data is post-processed with software to fit the curve and calculate full width half maximum (FWHM). FWHM is the difference between two values ($X_2 – X_1$) at the half of its dependent variable's maximum value ($1/2 * f_{max}(x)$). It is used to describe a measurement of the width of the diamond peak. The low values of FWHM imply good quality of diamond.

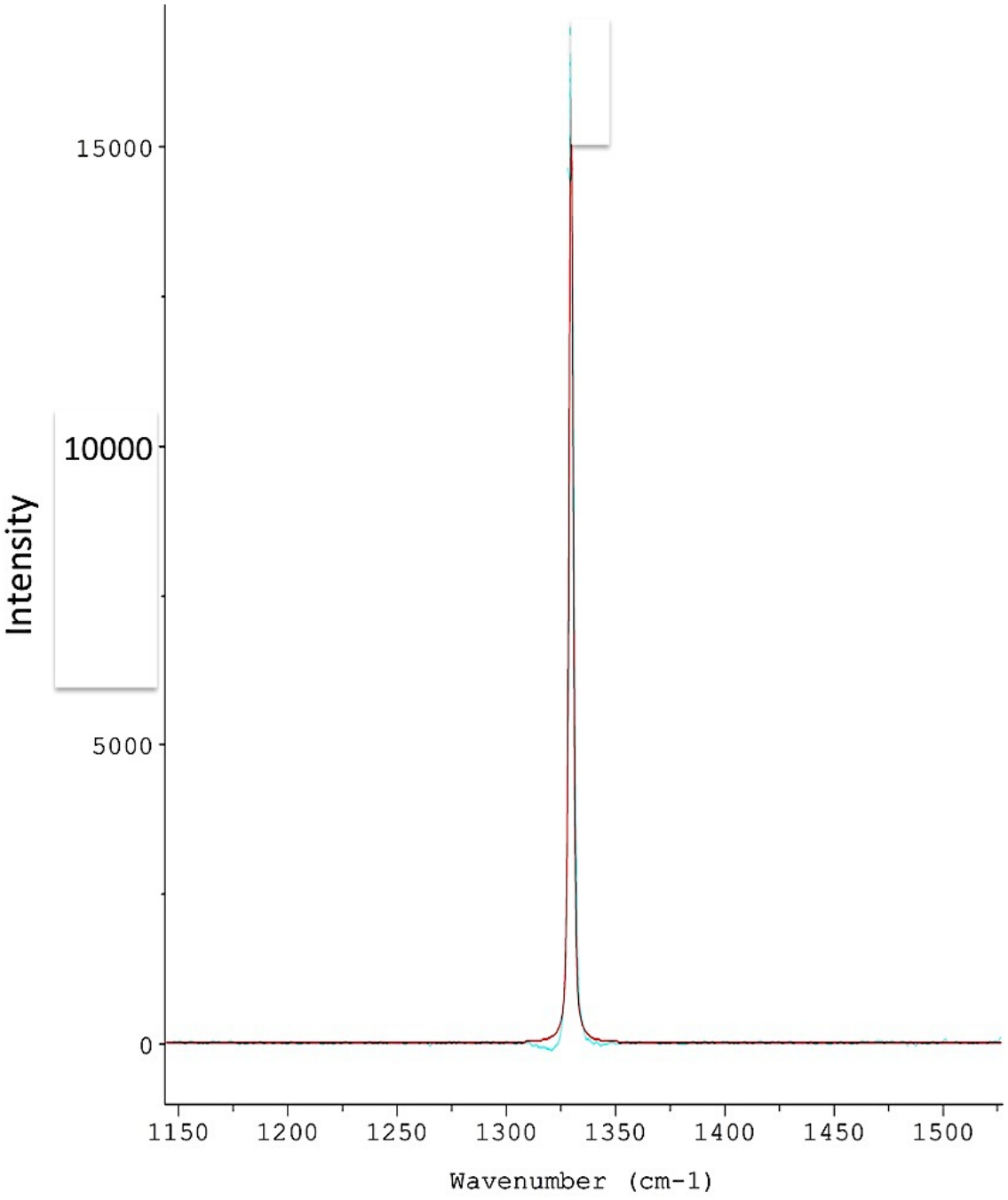

Figure 6.43 Raman spectrum of SCD (GYJ084), showing the main peak at 1332 cm^{-1}. FWHM is 1.93 cm^{-1}. The intensity is in arbitrary units.

Good quality diamond usually shows one Raman spectrum peak around

1332 cm^{-1} [78] and FWHM is typically less than 2 cm^{-1}. An example of a Raman spectrum for the CVD SCD samples synthesized by Reactor C is shown in Figure 6.43. The FWHM is 1.93 cm^{-1}. An Element Six type IIIa diamond sample was also used as a reference sample for these measurements and its Raman FWHM was 1.64 cm^{-1}. FWHM Raman measurements were made on nine experimental SCD runs with input nitrogen concentrations of only < ~ 5ppm. The FWHM of these samples ranged from 1.62 to 1.70 cm^{-1} indicating good quality diamonds were synthesized. The experimental data for these samples are listed in Appendix B.

Another example of the measured Raman spectrum is displayed in Figure 6.44. The data presented in the figure are the measured Raman FWHM versus nitrogen concentrations for five experiments shown in Figure 6.26. Note that the nitrogen concentration in gas phase includes the residual nitrogen calculated in Section 5.2.4, which is 2 ppm plus the nitrogen impurity (<3 ppm) in the hydrogen gas bottle. As shown, the FWHM of the synthesized SCD increases as the input nitrogen increases from 5 ppm to 25 ppm. At 5 ppm the FWHM is about 1.6 cm^{-1} and the FWHM gradually increases to 2.07 cm^{-1} as the nitrogen concentration is increased from 5ppm to 25ppm. As shown in Figure 6.44 the SCD synthesized by Reactor C is of good quality.

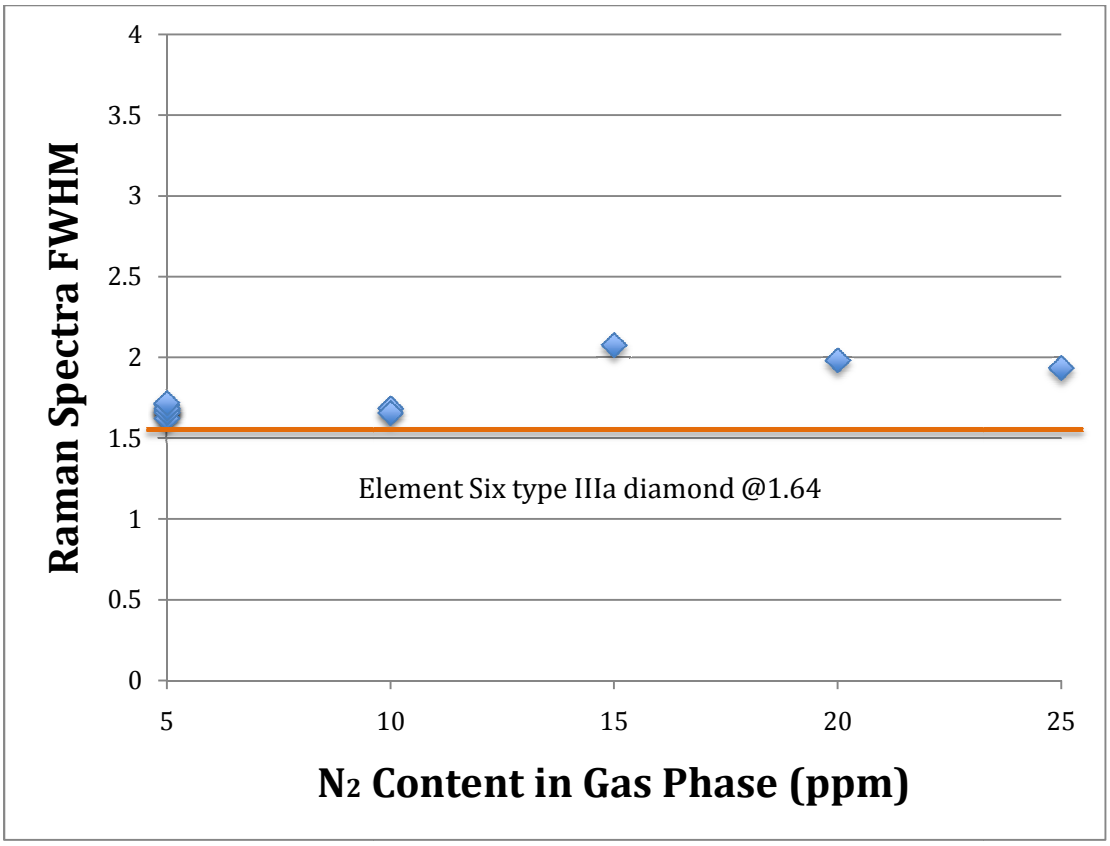

Figure 6.44 Raman spectra FWHM vs. N_2 content for Reactor C

Figure 6.45 displays Raman spectra FWHM versus substrate temperature. Although all of SCD samples show excellent quality with very low FWHM, we can see relatively higher FWHM for the SCD grown above 1300 ℃ or below 1000 ℃. This matches the experimental data shown in Section 9.7.3 where the good diamond growth window was identified from 1000 ℃ to 1300 ℃.

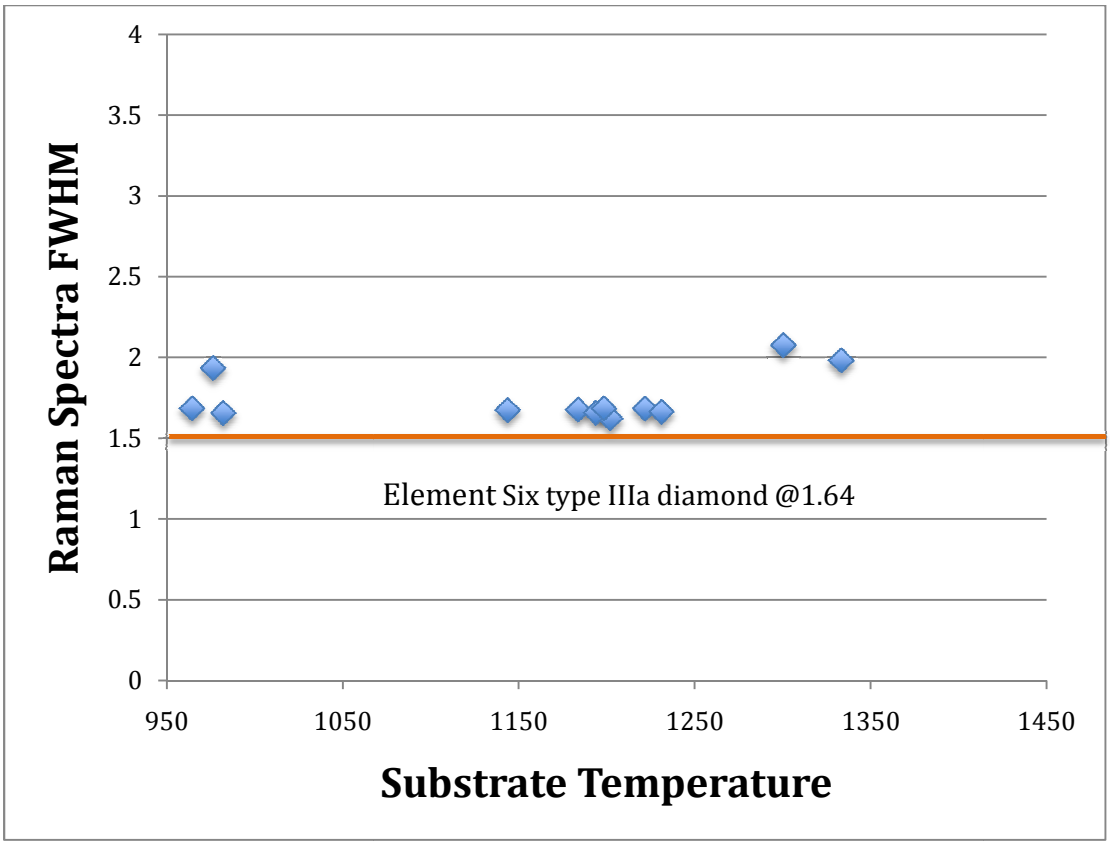

Figure 6.45 Raman spectra FWHM vs. substrate temperature for Reactor C

Local stress analyses are also calculated via Raman spectrum shift by Muehle et al. [79]. Figure 6.46 shows the internal stress versus nitrogen concentration. The red X samples were SCD synthesized in Reactor C and the blue X samples were synthesized in Reactor A at 160 Torr with 5% methane. The following equation, by Ager et al. [80], is used for stress calculation.

(1)

where is the local stress, is equal to 1332 cm^{-1} for diamond. To calculated maximum internal stress inside the diamond,

(2)

As shown in Figure 6.46, the first impression is that the nitrogen concentration in the crystal doesn't increase internal stress. However, according to Lang et al. [81] 10 to 100 ppm nitrogen in the crystal increase the lattice parameter significantly, thus leads to local stress. One possible reason is that since both CVD SCD and HPHT SCD are compared in Figure 6.46, CVD SCD are more affected by incorporated nitrogen than HPHT SCD. If only CVD SCD internal compressive stress versus nitrogen concentration are compared, the diamond samples from Reactor C (called DS IV in the figure) shows relatively lower stress level as compared to Reactor A (called DS II in the figure) and the literature values for CVD diamond stress from several GPa [80] to -0.25 GPa [82,83].

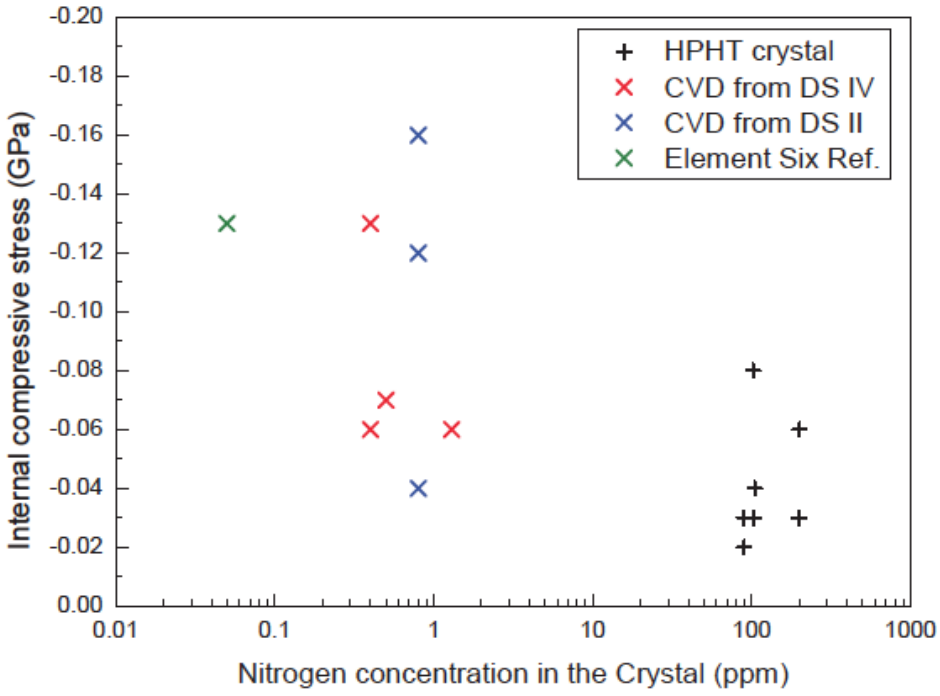

Figure 6.46 Internal compressive stress versus nitrogen concentration in different types of diamond [79]

6.13.3 Diamond SIMS Measurement

Secondary ion mass spectrometry (SIMS) is another commonly used technique to analyze the composition of solid surfaces or thin films. A focused primary ion beam (usually an inert gas such as Ar^+) generated by ion gun in Figure 6.47 is sputtered to the sample surface. These high energy ions damage the sample surface as seen in Figure 6.48. Then a mass spectrometer is used to collect and analyze the mass of species sputtered off the surface. SIMS is a more sensitive surface analysis technique than Raman, but due to its high-cost, a

limited number of samples from Reactor C have been sent for SIMS analysis.

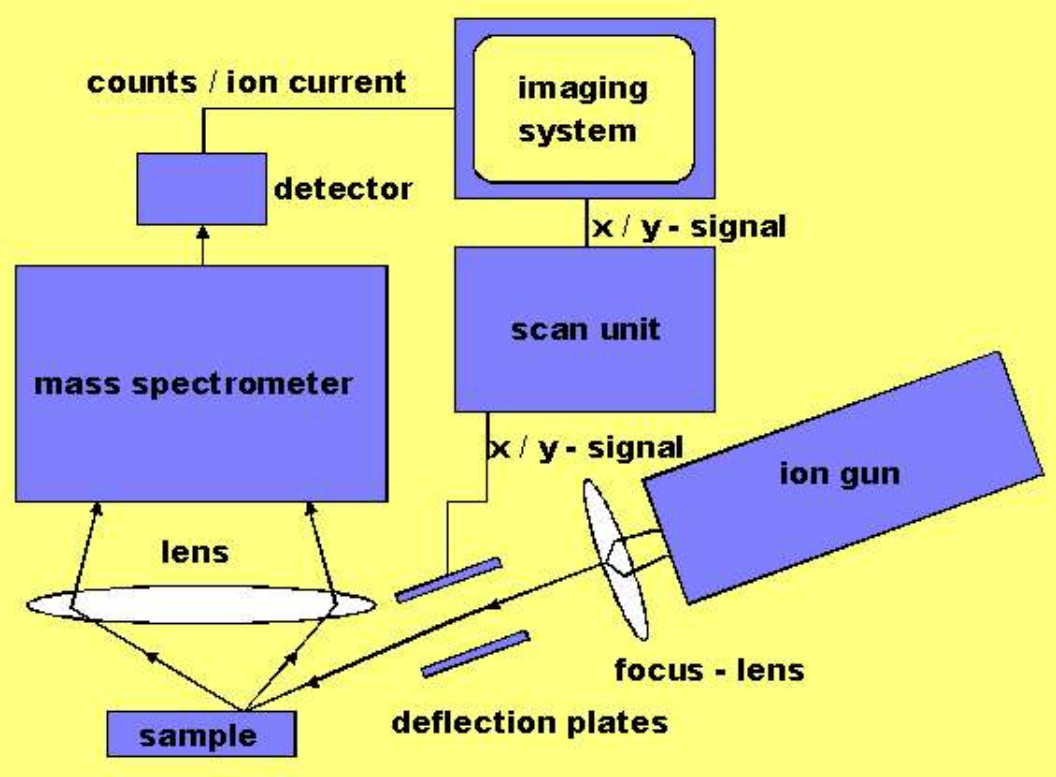

Figure 6.47 Schematic diagram of a secondary ion mass spectrometry [84]

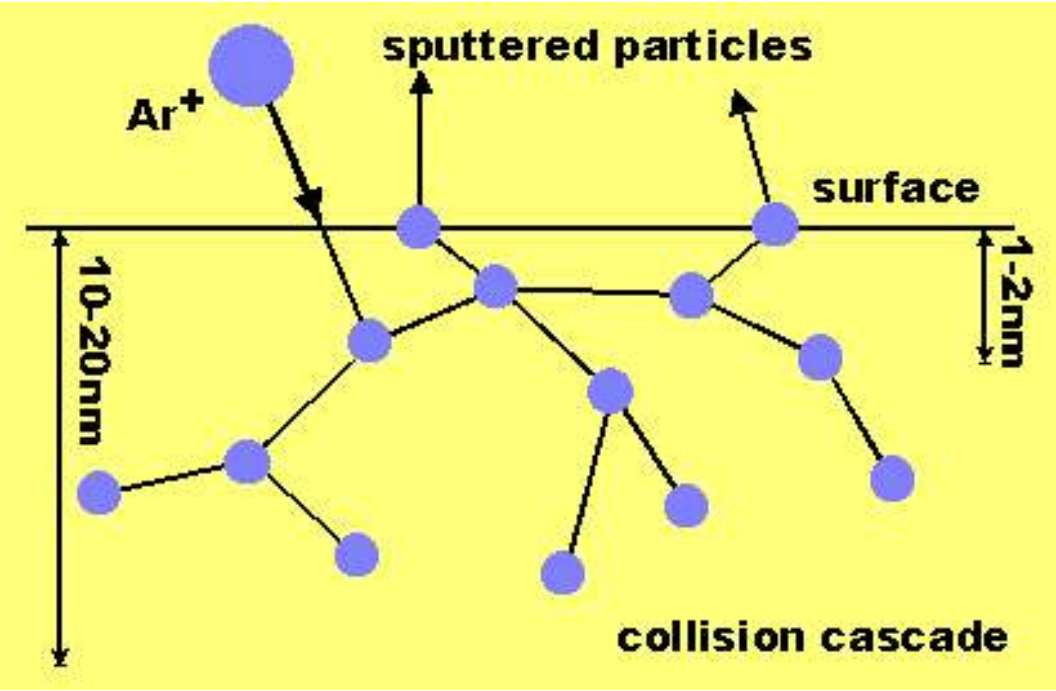

Figure 6.48 Collision on the sample surface [84]

Nitrogen content by SIMS vs. N_2 content in gas phase for Reactor C is shown in Figure 6.49. The SIMS result shows that 400-500 ppb N in the synthesized diamond when residual N_2 was less than or equal to 5ppm in the gas phase (see Section 5.2.4). When the N_2 content in gas phase increases to 10 and 20 ppm, N content by SIMS also increase to 1.3 and 1.7 ppm. The increase is not linear. Experimental data points included in Figure 6.49 are listed in the Appendix B.

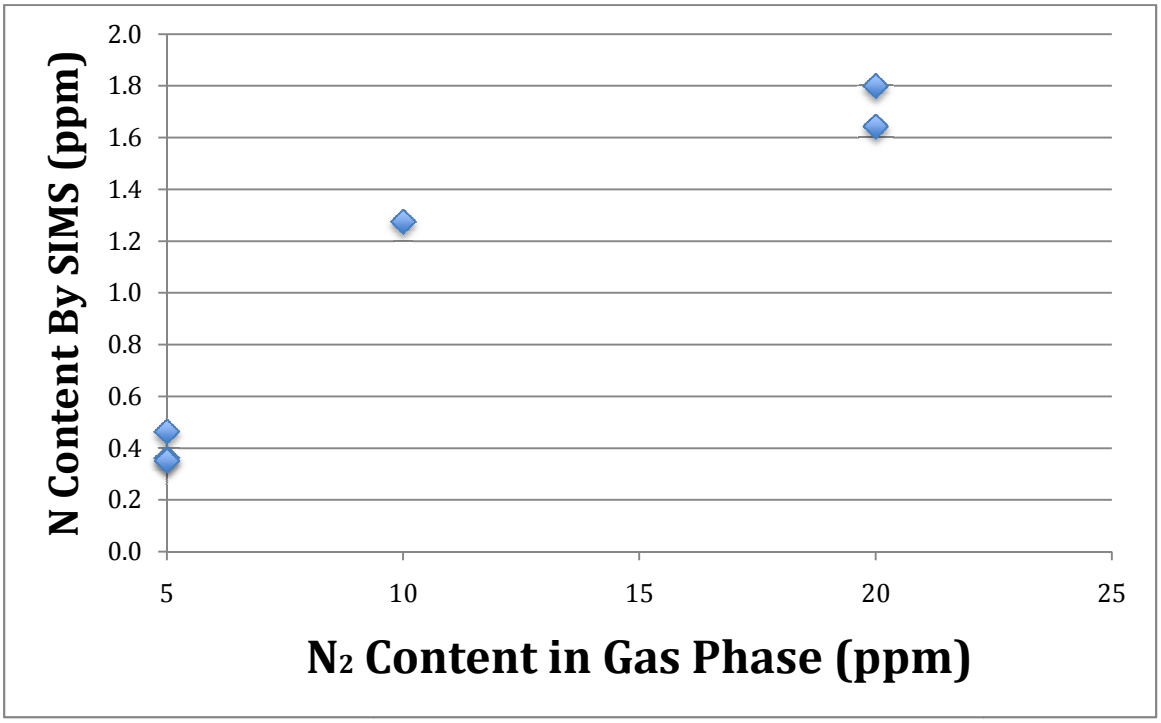

Figure 6.49 N content by SIMS vs. N_2 content in gas phase for Reactor C

6.13.4 Diamond Transmission Measurements

Fourier transform infrared spectroscopy (FTIR) is commonly used to obtain an infrared spectrum of absorption of a solid, liquid or gas. IR radiation is passed through a sample in the measurement. Some of the infrared radiation is absorbed by the sample and some is transmitted and collected by the detector (Figure 6.50). Fourier transform is required to convert the collected raw data into the actual spectrum. This technique can determine the quality of a diamond sample by comparing it with the known good-quality diamond.

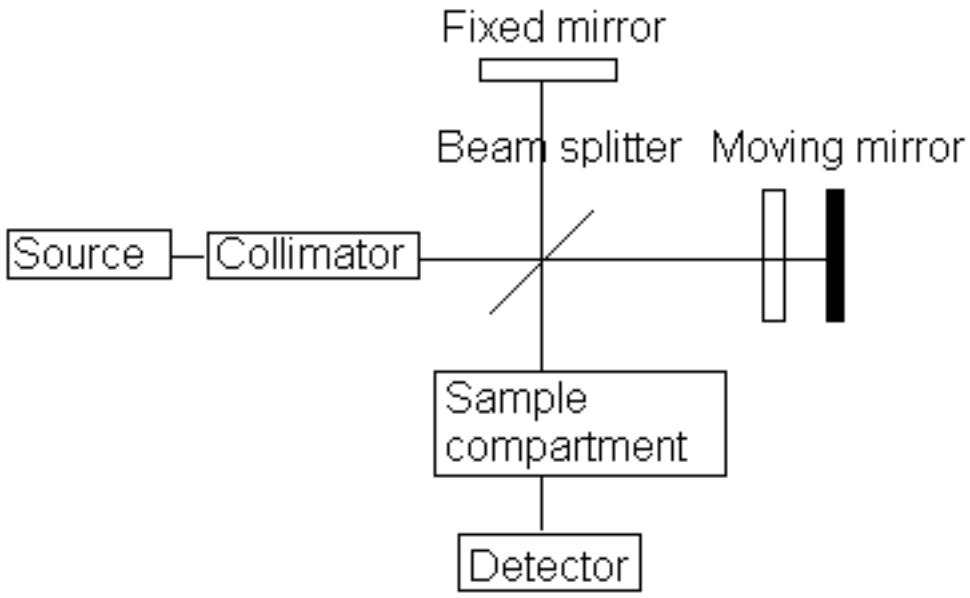

Figure 6.50 Schematic diagram of a FTIR measurement setup [85]

Before comparing the diamond sample from Reactor C with other good quality diamond, we need to understand the absorption coefficient. First let's consider an optical beam of intensity I_0 normally incident on the surface of a

diamond sample [12]. So the optical intensity at depth d in this case is,

$$I(d) = I_0 (1-R)\exp(-\alpha d) \quad (1)$$

where R is the reflection coefficient at the front surface given by

$$R = \left(\frac{n_a - n_d}{n_a + n_d}\right)^2 \quad (2)$$

Where n_a and n_d are the refractive indices of air and diamond, respectively.

α used in equation (1) is called absorption coefficient. The lower value of α means less optical beam is absorbed by the diamond sample. Figure 6.51 shows the comparison among samples from Reactor A, C and Element Six of absorption coefficient versus wavelength from 0 to 10000 nm. Figure 6.52 is a close-up image for wavelength from 200 to 800 nm. The IR transmission for all samples was similar to that associated with type IIa diamond and the sub-band gap ultraviolet optical absorption coefficients for the SCD synthesized with Reactor C were comparable to that reported for type IIa [12]; i.e. the absorption coefficient at 250 nm is between 4 and 7 cm^{-1}. Thus Reactor C is capable of synthesizing type IIa diamond.

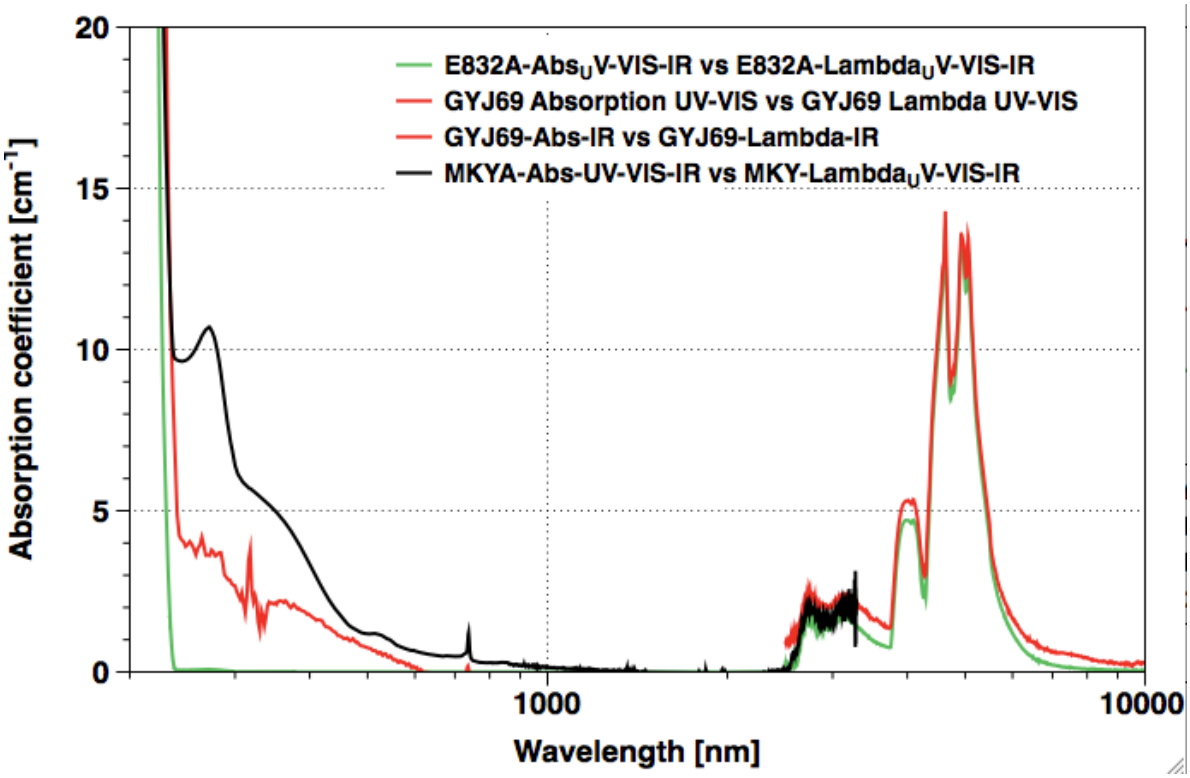

Figure 6.51 Optical absorption comparison among samples from Reactor A, C and Element Six (wavelength from 1 to 10000 nm)

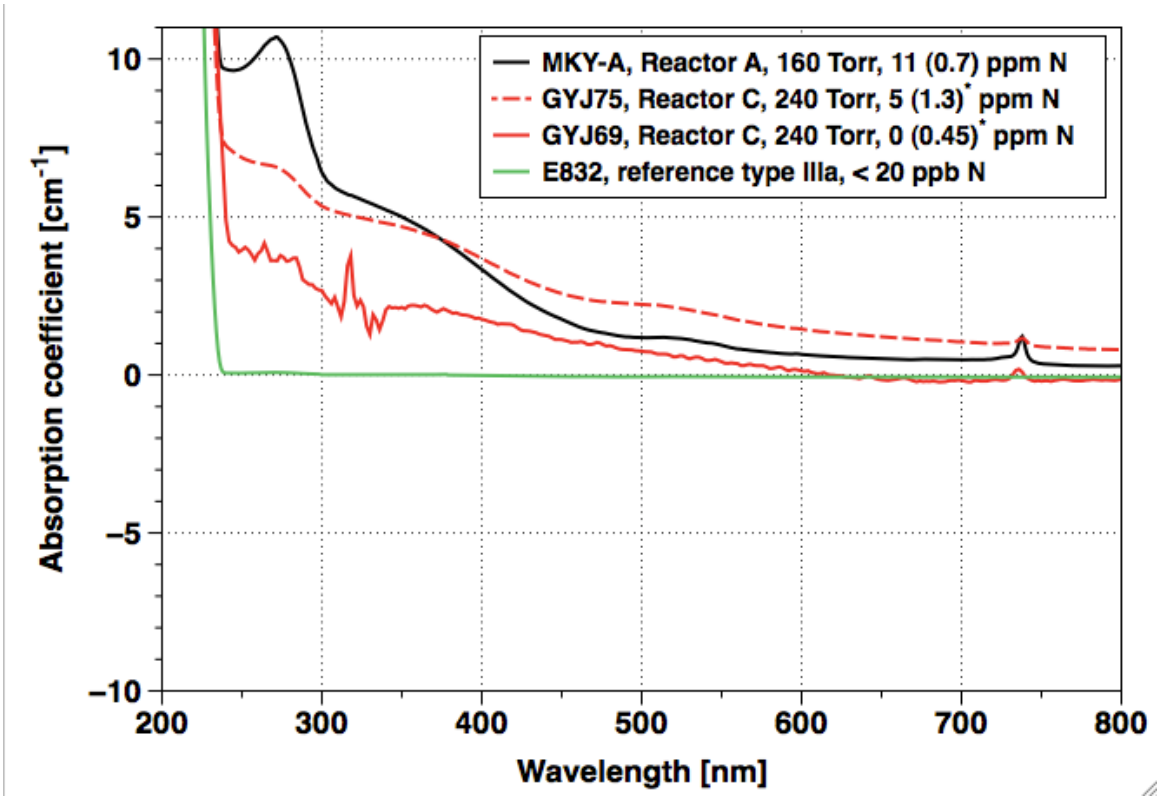

Figure 6.52 Optical absorption comparison among samples from Reactor A, C and Element Six (wavelength from 200 to 800 nm)

6.14 Summary

Reactor C was experimentally evaluated in high pressure and high power density in a SCD synthesis application. After the examples of the ranges of experimental variation of the input and output variables were presented, eight sets of exploratory experiments were performed with the initial benchmark experimental SCD growth conditions. These experiments included determining the output variables, i.e. linear growth rate, total growth rate, carbon conversion efficiency, and specific yield, versus variety of input variables, i.e. total flow rate, substrate holder position, deposition pressure, substrate temperature, methane

concentration, nitrogen concentration, growth time, and substrate size. These experiments show that the new Reactor C is indeed robust and safe to operate over a large experimental operating space. The performance of Reactor C was compared to early reactor designs, i.e. Reactor A and B via growth rate versus pressure and substrate temperature. Reactor C shows better growth rate over Reactor A and B due to both the smaller substrate holder and to the operation at higher pressures.

Finally selected CVD SCD samples from Reactor C were characterized by Raman spectroscopy, SIMS, transmission measurement and visual surface inspections. The Raman spectrum peak and FWHM indicates that SCD of Reactor C are of good quality as compared to Element Six type IIIa diamond. SIMS results shows a very small amount (400-500 ppb) of the nitrogen content in the samples when the samples were grown with less than 5ppm nitrogen in the gas phase. For transmission measurement, the absorption coefficient for SCD synthesized with Reactor C were comparable to that reported for type IIa. Thus again the diamond quality measurements have demonstrated that Reactor C operating under high pressure and high power density conditions is capable of synthesizing type IIa diamond with very good growth rates. After laser cutting and mechanical polishing high quality, type IIa, CVD SCD plates of thicknesses of 0.25 – 3.3 mm were produced.

CHAPTER 7

CONCLUSIONS

7.1 Introduction

It is widely understood that CVD synthesized diamond quality and growth rates can be improved by using high power density microwave discharges operating at pressures above 160 Torr. In order to take advantage of the improved deposition chemistry and physics that exist at high pressure, we have designed, developed and experimentally evaluated this new generation MSU microwave plasma assisted reactor and associated process methods that are both robust and are optimized for high pressure and high power density operation. This reactor can operate in the 160-320 Torr pressure regime contiguously for more than 100 hours.

7.2 Summary of Research Accomplishments

Using information available in the published literature a review of all commercially available MPACVD diamond synthesis reactor designs was performed. The five commercial reactor designs/systems that are currently available are offered by the following manufactures/organizations: (1) MSU/ Wavemat/Lambda, (2) AsTex/SEKI, (3) FHG IAP/AIXTRON (4) French/LIMHP/PLASSYS and (5) iplas.

The five different reactor designs have a number of design similarities. First, all applicators have an axially symmetric, phi independent cylindrical shape except for the AIXTRON which has an ellipsoidal phi independent shape. Secondly, microwave energy is coupled into the reactor by a coaxial coupling probe except for the iplas which uses a rectangular wave guide which is toroidally wrapped around the cylindrical reactor side walls and coupling takes place via a small gap in the applicator side walls. Additionally all reactors excite a phi symmetric TM_0 electromagnetic waveguide mode. Specific electromagnetic mode excitations of the more advanced designs are the TM_{01n} (SEKI 1st gen), the TM_{012} (iplas), the hybrid TM_{013} +TEM_{001} (MSU A and B), the TM_{023} (LIMHP) and the ellipsoidal TM_{012} (AIXTRON). All the reactor designs can be readily scaled up by a factor of 2.67 in size by dropping the excitation to 915MHz.

Important reactor design differences are: (1) external matching (SEKI, iplas, and AIXTRON) versus internal matching (MSU/Lambda, PLASSYS/LIMHP); (2) the reactor vacuum barrier is provided by (a) a quartz dome (MSU/Lambda, AIXTRON, LIMHP 1st and 3rd gen), (b) a quartz plate (SEKI 1st gen, LIMHP 2nd

gen), (c) a cylindrical quartz tube (iplas), and (d) a quartz ring located in the coaxial input system under the fixed coupling probe/substrate holder; and (3) a variable substrate position (MSU/Lambda) versus a fixed substrate position (SEKI 3rd gen, AIXTRON, iplas, PLASSYS/LIMHP) .

Using experimental data available in the reviewed published literature a comparison of the performance of the difference reactor designs was performed. MPACVD synthesis of diamond is a multi-dimensional experimental problem and a carful comparison of reactor performance requires the knowledge of all the experimental variables. However the experimental data presented for each commercial reactor that is available in the reviewed literature is not complete enough to make a careful, exact comparison between most of the reactor designs. However there are two exceptions: (1) the SEKI reactor and (2) the MSU reactor. Much data is available in the reviewed published literature on the performance of the MSU reactors, and additional unpublished experimental data is also available directly from experiments that have been performed in the MSU laboratories. The SEKI reactors also have considerable experimental data available in the literature. Thus an approximate comparison was made (1) between the 2.45 GHz and 915MHz excited reactors of the same design, and (2) between the SEKI reactor and the MSU reactor designs. In each comparison the reactors are operating approximately under similar experimental conditions.

The various reactors were compared by calculating the (1) growth rate, (2) the discharge absorbed power density and (3) specific yield.

When the SEKI Reactors were compared to the MSU/Lambda Reactors

the growth rate for the MSU and SEKI reactors were within 30% of each other and the discharge absorbed power densities for the SEKI reactor were smaller at 2.45 GHz but were greater at 915 MHz than the corresponding absorbed power densities for the MSU reactor. The specific yield for the MSU reactors are considerably lower than the specific yield for SEKI reactors. For example, for 2.45 GHz, the specific yield for the MSU design is 70 kW-h/g and specific yield for the SEKI design is 272 kW-h/g. Thus the 2.45 GHz MSU Reactor A is about 4 times more electrically efficient than the 2.45 GHz SEKI 1^{st} and 2^{nd} generation reactor. For 915 MHz excitation, the specific yield for the MSU design is about 20 kW-h/g and specific yield for the SEKI 915 MHZ design is 208 kW-h/g. Thus the MSU 915 MHz reactor is about 10 times more electrically efficient than the 915 MHz design.

It was observed when comparing the 2.45GHz MSU Reactor A to the 915 MHz MSU scaled up reactor that when operating under similar conditions, i.e. from 100-160 Torr, (1) that the scale up the MSU reactor design via 915 MHZ excitation improved the SY from 70 kW-h/g to 20kW-h/g, and reduced the discharge absorbed power density from 32-45 W/cm^3 to 7.7 W/cm^3 while the growth rates remained approximately the same .

An improved high pressure, high power density reactor was designed, built and experimentally evaluated by synthesizing PCD and SCD diamond over 180-320 Torr pressure regime. The design features of the new design were (1) single electromagnetic mode excitation, (2) internal cavity applicator impedance matching, (3) variable substrate position, (4) four independent process tuning

variables, L_S, L_p, L_1 and L_2, and (5) the ability to scale up the design. As with earlier designs the substrate holder diameter was reduced by a factor of two and it incorporated position/length tuning to enable the substrate position to be adjusted to enable process optimization. Major differences in the design over earlier designs was the larger diameter applicator and quartz dome diameters in order to locate the reactor walls away from the high intensity high pressure discharge. Another design difference was the variation in applicator diameter versus the axial position. This enabled the unfocusing and then refocusing the microwave energy as it passes through the reactor applicator and it is delivered to the discharge zone. These improvements enabled higher pressure operation and also longer synthesis runs and less dome maintenance.

The new rector design, identified in this thesis as Reactor C, was first experimentally evaluated by synthesizing PCD over one inch diameter silicon substrates in the high pressures regime. The experimentally measured absorbed power density for Reactor C ranged 300 – 1000 W/cm^3 over a pressure range of 180 – 300 Torr. The growth rate varied from 4.2 - 21.8 μm/hr as pressure was increased from 180 Torr to 300 Torr, which is much higher than growth rates for MSU Reactor A. The PCD growth rate for Reactor C was slightly higher than Reactor B under similar conditions, but Reactor C was able to operate at higher CH_4/H_2 concentrations at higher pressures and also was able to continuously run for over 100 hours without reactor maintenance. Using the maximum growth rate of 21.8 μm/hr over a 1-inch Si wafer yielded a specific yield of 54 kW-h/g. If a deposition area of 1.5 inches is assumed then and the same growth is assumed

over the entire wafer, then the specific yield is reduced to 26 kW-h/g or 5kW-h/carat. This is a considerable improvement in efficiency over the specific yield of Reactor A. The quality of the PCD films was investigated via Raman spectroscopy. The Raman spectrum did not indicate the presence of and appreciable amount of graphite in the films. The Raman spectrum full width half maximum (FWHM) was 2 – 3.6 cm^{-1}. These Raman measurements indicated that the PCD films that were synthesized in Reactor C produced under the same growth conditions; i.e. 240 Torr, CH_4/H_2 = 4-5%, have considerably better quality than PCD films produced in Reactor B.

Reactor C was also experimentally evaluated operating at high pressures of 180-320 Torr and at high power densities of 400 W/cm^3 to 1000 W/cm^3 in the application of SCD synthesis. This SCD experimental investigation consisted of over 100 separate experimental runs as reactor investigated the multidimensional experimental variable space resulting in a total exploratory process time of well over 2200 hours. These experiments required little operational maintenance other than dome cleaning after each run, and thus demonstrated that Reactor C is indeed robust and safe to operate over a large high pressure experimental operating space. Growth rates of 25-80 microns/h were achieved as the synthesis pressure was varied from 240-320 Torr and the methane concentration was varied from 3-9%. If this deposition rate was maintained over a one-inch diameter single crystal area the specific yield of Reactor C would be approximately 50 - 15 kW-h/g.

Then the performance of Reactor C was compared to early reactor

designs, i.e. Reactor A and B via growth rate versus pressure and substrate temperature. When operating at 240 Torr and with an input with a methane concentration of 5%, a high quality SCD growth window was identified between 1000 ℃ -1300 ℃. Within this growth window the grow th rate exhibited a maximum between 1125 ℃ -1225 ℃. Under these condit ions the maximum growth rate for Reactor B was about 25 microns/hr at 1200 ℃, and was 38 microns/hr at 1150 ℃ for Reactor C. Within this growth window the growth rates for Reactor C are 1.2-2.5 times greater than the corresponding growth rates for Reactor B. This suggests that the higher power densities of Reactor C result in higher deposition rates; i.e. the Reactor C design results in higher power densities and also produces higher growth rates than those in Reactor B.

Diamond plates were fabricated by first removing the SCD CVD synthesized diamond from the seed by laser cutting and then also the PCD rims were removed by laser cutting. The quality of these SCD plates was investigated by Raman, SIMS and transmission measurements. The Raman spectroscopy displayed a strong and narrow Raman signal with a FWHM of 1.6-1.7 cm^{-1}. This is comparable to a reference Raman spectrum from a type IIIa CVD grown diamond sample from Element Six. SIMS measurements indicted that when the SCD is synthesized with 5ppm nitrogen concentration in the gas phase the nitrogen concentration in the synthesized diamond is 400-500 ppb. Single crystal diamond IR to UV transmission spectra measurements displayed spectra similar to or better than that of a type IIa diamond or better. In particular the IR transmission for all samples was similar to that associated with type IIa diamond

and the sub-band gap ultraviolet optical absorption coefficients for the SCD synthesized with Reactor C were comparable to that reported for type IIa [12]; i.e. the absorption coefficient at 250 nm is between 4 and 7 cm^{-1}. Thus Reactor C is capable of synthesizing type IIa diamond.

In summary an improved high pressure, high power density reactor, i.e. Reactor C, was designed, and built, and was successfully experimentally tested by synthesizing PCD and SCD diamond over a high, 180-320 Torr, pressure and high, 200-1000 W/cm^3, discharge power density regime. Reactor C demonstrated reliable MPACVD PCD and SCD synthesis operation operating over long (> 100 hrs.) deposition times and with little run to run maintenance. The Reactor C design has been disclosed to the MSU IP office and a patent has been submitted to the US patent office.

Also both the PCD and SCD experimental results presented in this thesis support the initial hypothesis that as the MPACVD diamond synthesis process is moved to higher pressures: (1) the diamond growth rates increase (up to 25-80 microns/h) and (2) high quality diamond can be synthesized over an expanded range (1-9%) of input methane concentrations.

7.3 Recommendations for Future Research

I. One of the design features of the fourth generation MSU MPACVD reactor is to locate the substrate holder on a movable stage that works as an integral part of the microwave applicator. The ability to adjust the position of the stage allows additional adjustment and

local fine tuning/focusing of the electromagnetic fields around and directly above the substrate. This feature enables the positioning of the microwave discharge above and in good contact with the substrate while operating in the high pressure and power density regime. It also appears to counter the buoyant forces that the discharge is subjected to as the operating pressure is increased --- thereby keeping the discharge in good contact with the substrate as the pressure is increased. But the current stage is movable by manually adding a shim set before experiment starts. So it only allows discrete height option for the substrate holder. A mechanically movable cooling stage can be built in the future design to allow continuous height position for the substrate holder. So even when experiment has already starts, we still can adjust the stage position for the best diamond synthesis conditions.

II. According to Section 6.8, substrate temperature plays a very important role in CVD diamond synthesis. To grow a diamond with better quality, we would like to keep the substrate temperature steady. So one or more thermal detectors can be installed in the system. The control software can adjust the input power due to the increase of substrate temperature at the different growth stages.

III. In order to apply CVD diamond technology in industry, multi-seed CVD diamond synthesis has to be investigated. The main challenge is the coverage of microwave plasma on 2x2 or even 3x3 multi-

seed layout. The only way to increase the plasma size is to increase the absorbed microwave power but maintain the same substrate cooling condition. It will require a redesign for the cooling stage and substrate holder.

Appendix

APPENDIX A CVD Polycrystalline Diamond Synthesis Experimental Data

Sample Number	GYJ016-2	GYJ031	GYJ033	GYJ027	GYJ030	GYJ034	GYJ021	GYJ022	GYJ026
Total Thickness (μm)	29.0	478.1	124.1	283.0	1120	201.9	252.5	370.8	758.4
Growth Rate (μm/hr)	4.8	4.7	4.6	4.9	11.2	9.6	14.0	15.5	14.9
Growth Time (hr)	6	101	27	58	100	21	18	24	51
P_{abs} (W)	2410	2327	2020	2219	2338	2008	2570	2484	2207
Sub.Temp. (℃)	1044	1136	1135	1145	1128	1125	1074	1136	1140
ΔZ (mm)	-4.8	-4.8	-4.8	-4.8	-4.8	-4.8	-4.8	-4.8	-4.8

Table A.1 CVD Polycrystalline Diamond Synthesis Experimental Data 1

Table A.1 CVD Polycrystalline Diamond Synthesis Experimental Data 1 (Cont,d)

Pressure (Torr)	165	210	210	180	210	240	165	180	180
CH_4/H_2 %	2	2	2	3	3	3	4	4	4
H_2 (sccm)	400	400	400	400	400	400	400	400	400
Si Thickness (mm)	1.5	1.5	1.5	1.5	1.5	1.5	1.5	1.5	1.5
SiWafer Dia. (inch)	1	1	1	1	1	1	1	1	1

Sample Number	GYJ029	GYJ036	GYJ037
Total Thickness (μm)	904.8	379.2	228.9
Growth Rate (μm/hr)	17.4	15.8	21.8
Growth Time (hr)	52	24	10.5
P_{abs} (W)	2429	1870	2115
Sub.Temp. (℃)	1128	1120	1127
ΔZ (mm)	-4.8	-4.8	-4.8
Pressure (Torr)	210	240	240
CH_4/H_2 %	4	4	5

Table A.2 CVD Polycrystalline Diamond Synthesis Experimental Data 2

Table A.2 CVD Polycrystalline Diamond Synthesis Experimental Data 2 (Cont,d)

H_2 (sccm)	400	400	400
Si Thickness (mm)	1.5	1.5	1.5
SiWafer Dia. (inch)	1	1	1

APPENDIX B CVD Single Crystal Diamond Synthesis Experimental Data

Sample Number	GYJ085	GYJ092	GYJ095	GYJ097	GYJ098	GYJ099	GYJ100	GYJ101	GYJ102
Total Thickness (μm)	510.9	549.7	513.6	667.2	547.4	606.3	566.4	473.8	496.8
Growth Rate (μm/hr)	26.2	23.9	21.4	27.8	23.8	25.8	23.6	20.6	20.7
Growth Time (hr)	19.5	23	24	24	23	23.5	24	23	24
P_{abs} (W)	1661	1775	1684	1733	2004	1696	1570	1731	1661
Sub.Temp. (℃)	1008	1018	1013	973	971	981	991	978	978
ΔZ (mm)	-4.8	-4.8	-4.8	-4.8	-4.8	-3.7	-2.5	-1.2	0

Table B.1 CVD Single Crystal Diamond Synthesis Experimental Data 1

Table B.1 CVD Single Crystal Diamond Synthesis Experimental Data 1 (Cont,d)

Pressure (Torr)	240	240	240	240	240	240	240	240	240
N_2/ H_2 ppm	5	5	5	5	5	5	5	5	5
CH_4/H_2 %	5	5	5	5	5	5	5	5	5
H_2 (sccm)	400	600	700	100	200	400	400	400	400
Seed Area (mm^2)	12.25	12.25	12.25	12.25	12.25	12.25	12.25	12.25	12.25

Sample Number	GYJ103	GYJ104	GYJ110	GYJ119	GYJ121	GYJ122	GYJ125
Total Thickness (μm)	588	626.4	627.9	244	504	260.8	799.2
Growth Rate (μm/hr)	24.5	26.1	27.3	30.5	31.5	32.6	33.3
Growth Time (hr)	24	24	23	8	16	8	24
P_{abs} (W)	1681	1675	1666	1942	1762	1871	1862
Sub.Temp. (℃)	973	978	988	984	989	991	987
ΔZ (mm)	-6.1	-4.8	-4.8	-4.8	-4.8	-4.8	-4.8
Pressure (Torr)	240	260	280	300	320	300	300
N_2/ H_2 ppm	5	5	5	5	5	5	5
CH_4/H_2 %	5	5	5	5	5	5	5

Table B.2 CVD Single Crystal Diamond Synthesis Experimental Data 2

Table B.2 CVD Single Crystal Diamond Synthesis Experimental Data 2 (Cont,d)

H_2 (sccm)	400	400	400	400	400	400	400
Seed Area (mm^2)	12.25	12.25	12.25	12.25	12.25	12.25	12.25

Sample Number	GYJ126	GYJ112	GYJ113	GYJ115	GYJ116	GYJ117	GYJ118
Total Thickness (μm)	280	280.8	556.8	492	590.5	710.4	722.4
Growth Rate (μm/hr)	35	11.7	23.2	20.5	24.1	29.6	30.1
Growth Time (hr)	8	24	24	24	24.5	24	24
P_{abs} (W)	1815	1748	2312	2339	2115	2557	2133

Table B.3 CVD Single Crystal Diamond Synthesis Experimental Data 3

Table B.3 CVD Single Crystal Diamond Synthesis Experimental Data 3 (Cont,d)

Sub.Temp. (℃)	987	913	1148	1195	1094	1070	1013
ΔZ (mm)	-4.8	-4.8	-4.8	-4.8	-4.8	-4.8	-4.8
Pressure (Torr)	320	240	240	240	240	240	240
N_2/ H_2 ppm	5	5	5	5	5	5	5
CH_4/H_2 %	5	5	5	5	5	5	5
H_2 (sccm)	400	400	400	400	400	400	400
Seed Area (mm^2)	12.25	12.25	12.25	12.25	12.25	12.25	12.25

Sample Number	GYJ061	GYJ128	GYJ130	GYJ069	GYJ076	GYJ080	GYJ081	GYJ084
Total Thickness (μm)	261.3	475.2	264.8	705.6	1735.9	1327.9	2584.8	3341.5
Growth Rate (μm/hr)	40.2	19.8	33.1	16.8	23.3	27.1	35.9	41
Growth Time (hr)	6.5	24	8	42	74.5	49	72	81.5
P_{abs} (W)	1766	2125	2292	1668	1714	1796	1642	1679
Sub.Temp. (℃)	10000	967	1030	962	990	976	964	982
ΔZ (mm)	-4.8	-4.8	-4.8	-4.8	-4.8	-4.8	-4.8	-4.8
Pressure (Torr)	240	240	240	240	240	240	240	240
N_2/ H_2 ppm	5	5	5	0	5	10	15	20

Table B.4 CVD Single Crystal Diamond Synthesis Experimental Data 4

Table B.4 CVD Single Crystal Diamond Synthesis Experimental Data 4 (Cont,d)

CH_4/H_2 %	7	3	9	5	5	5	5	5
H_2 (sccm)	400	400	400	400	400	400	400	400
Seed Area (mm^2)	12.25	12.25	12.25	12.25	12.25	12.25	12.25	12.25

Sample Number	GYJ065	GYJ066	GYJ067	GYJ068	GYJ075	GYJ087	GYJ079	GYJ124-2
Total Thickness (μm)	1453.5	330.2	1424	1249.5	1281.6	2571.8	340.8	638.4
Growth Rate (μm/hr)	32.3	21.3	32	29.4	28.8	38.1	21.3	26.6
Growth Time (hr)	45	15.5	44.5	42.5	44.5	67.5	16	24
P_{abs} (W)	1992	1935	1940	1727	1859	1637	1626	1918
Sub.Temp. (℃)	1024	1022	982	979	982	974	975	1004
ΔZ (mm)	-4.8	-4.8	-4.8	-4.8	-4.8	-4.8	-4.8	-4.8
Pressure (Torr)	240	240	240	240	240	240	240	240
N_2/ H_2 ppm	5	5	5	5	5	5	5	5

Table B.5 CVD Single Crystal Diamond Synthesis Experimental Data 5

Table B.5 CVD Single Crystal Diamond Synthesis Experimental Data 5 (Cont,d)

CH_4/H_2 %	5	5	5	5	5	5	5	5
H_2 (sccm)	400	400	400	400	400	400	400	400
Seed Area (mm^2)	12.25	12.25	12.25	12.25	12.25	12.25	23.04	47.82

APPENDIX C Raman Spectra of CVD Polycrystalline Diamond

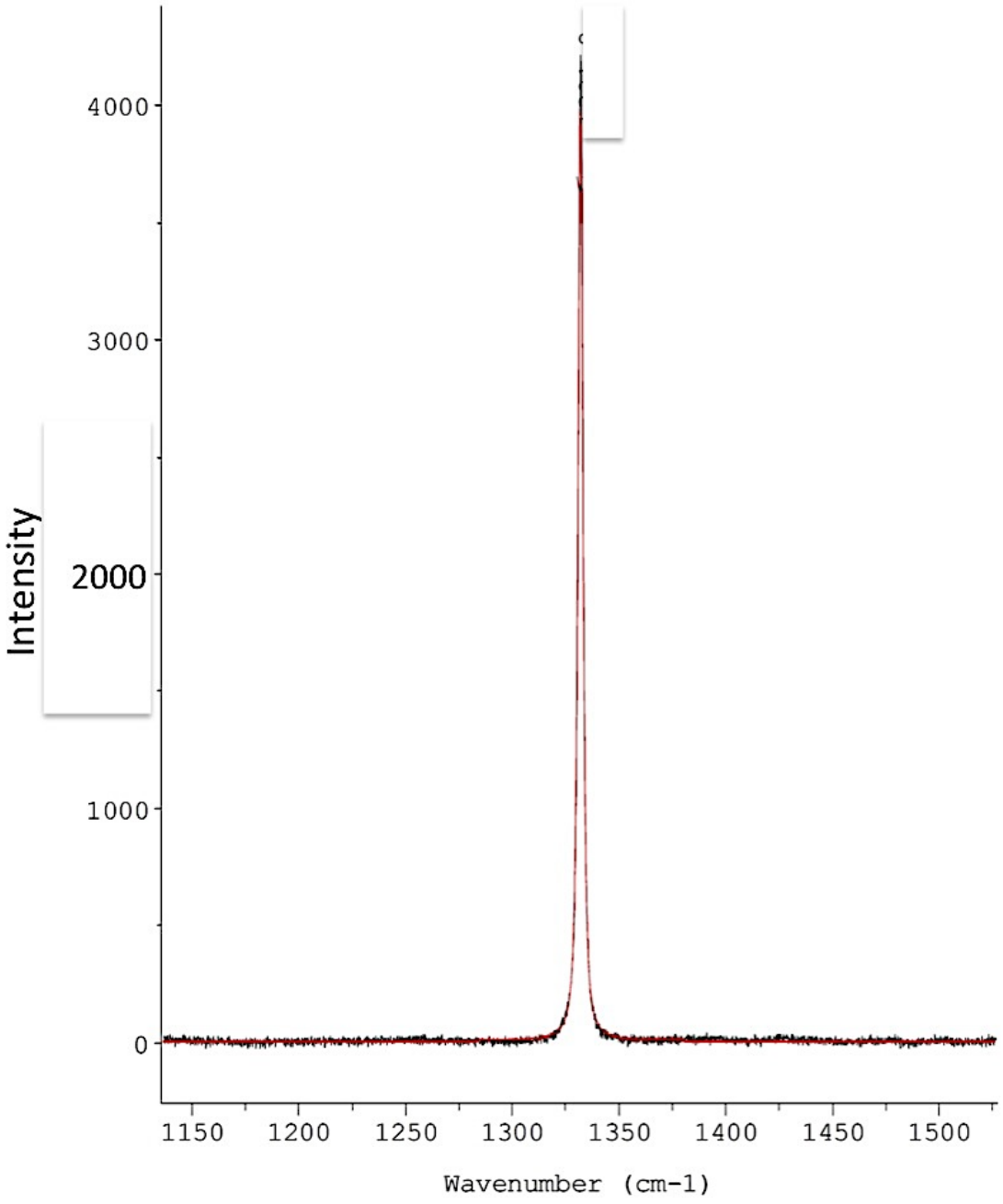

Figure C.1 Sample GYJ031 2% CH_4/H_2, 210 Torr, T_S=1136 ℃, P_{abs}=2327 W, Growth Time=101 hours, Growth Rate=4.7 μm/hr, Total Thickness=478.1 μm

APPENDIX D Additional Drawings for the Substrate Holder and Insert

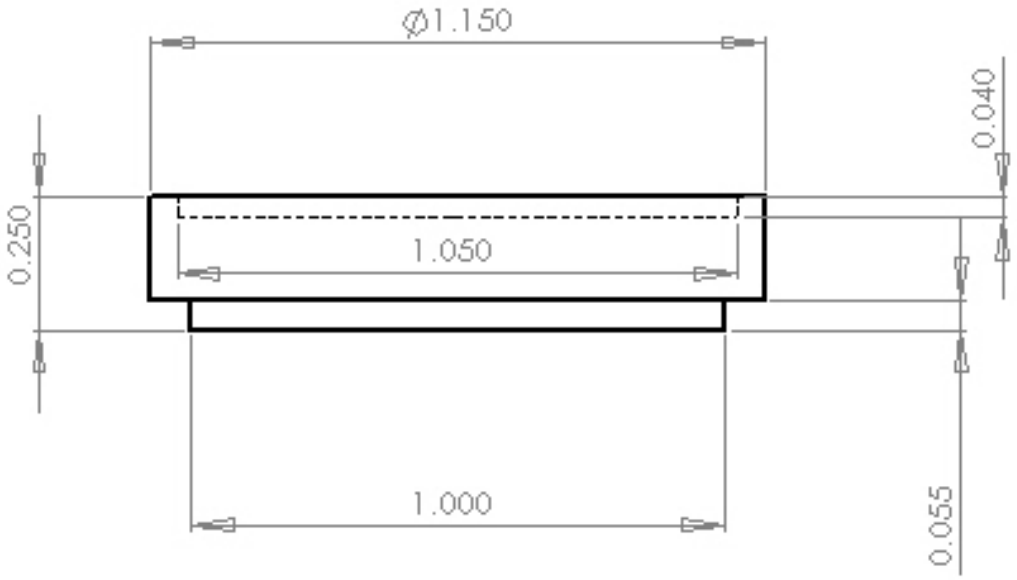

Figure D.1 Additional drawing for the moly insert (PCD)

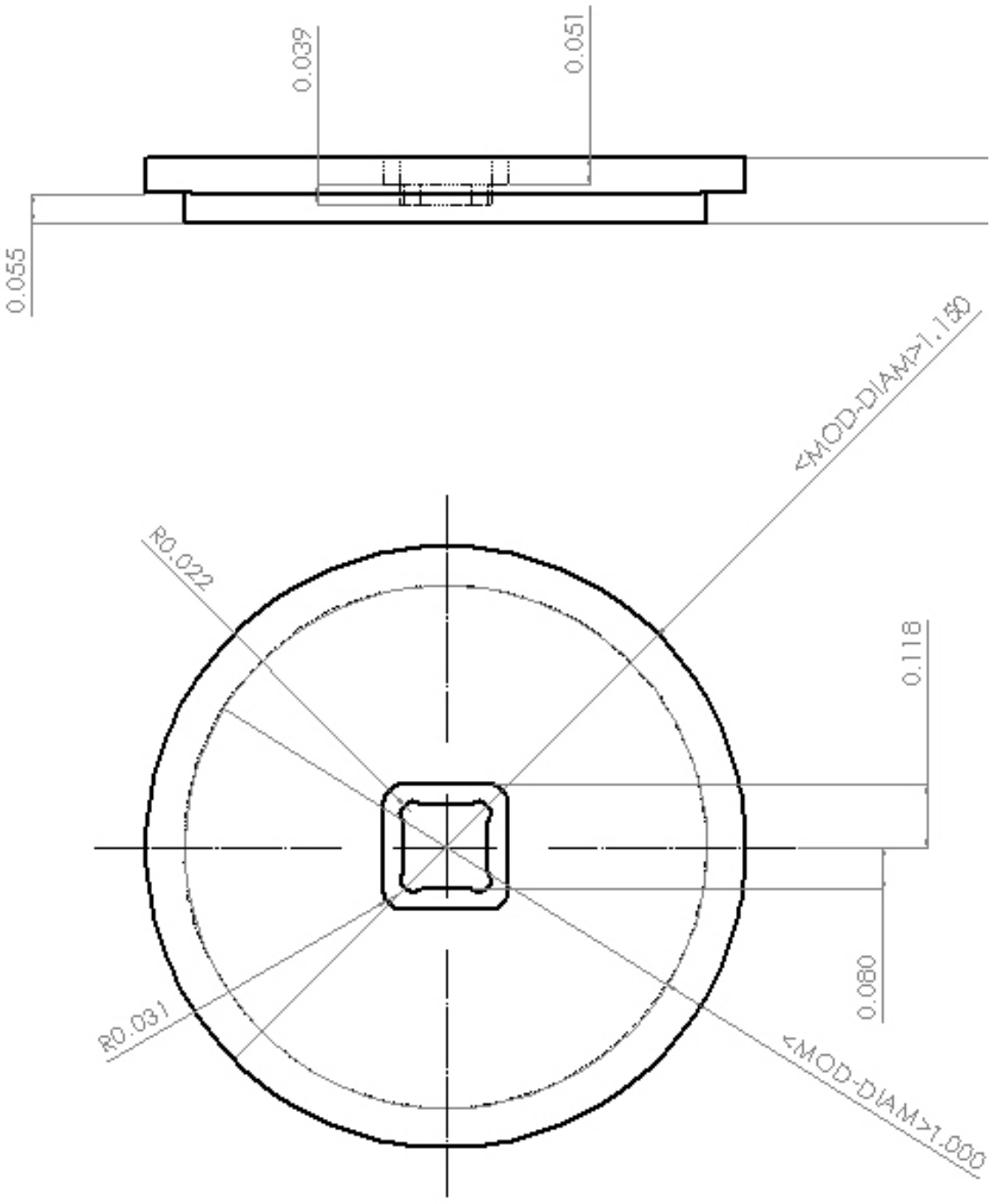

Figure D.2 Additional drawing for the moly insert (thin, SCD)

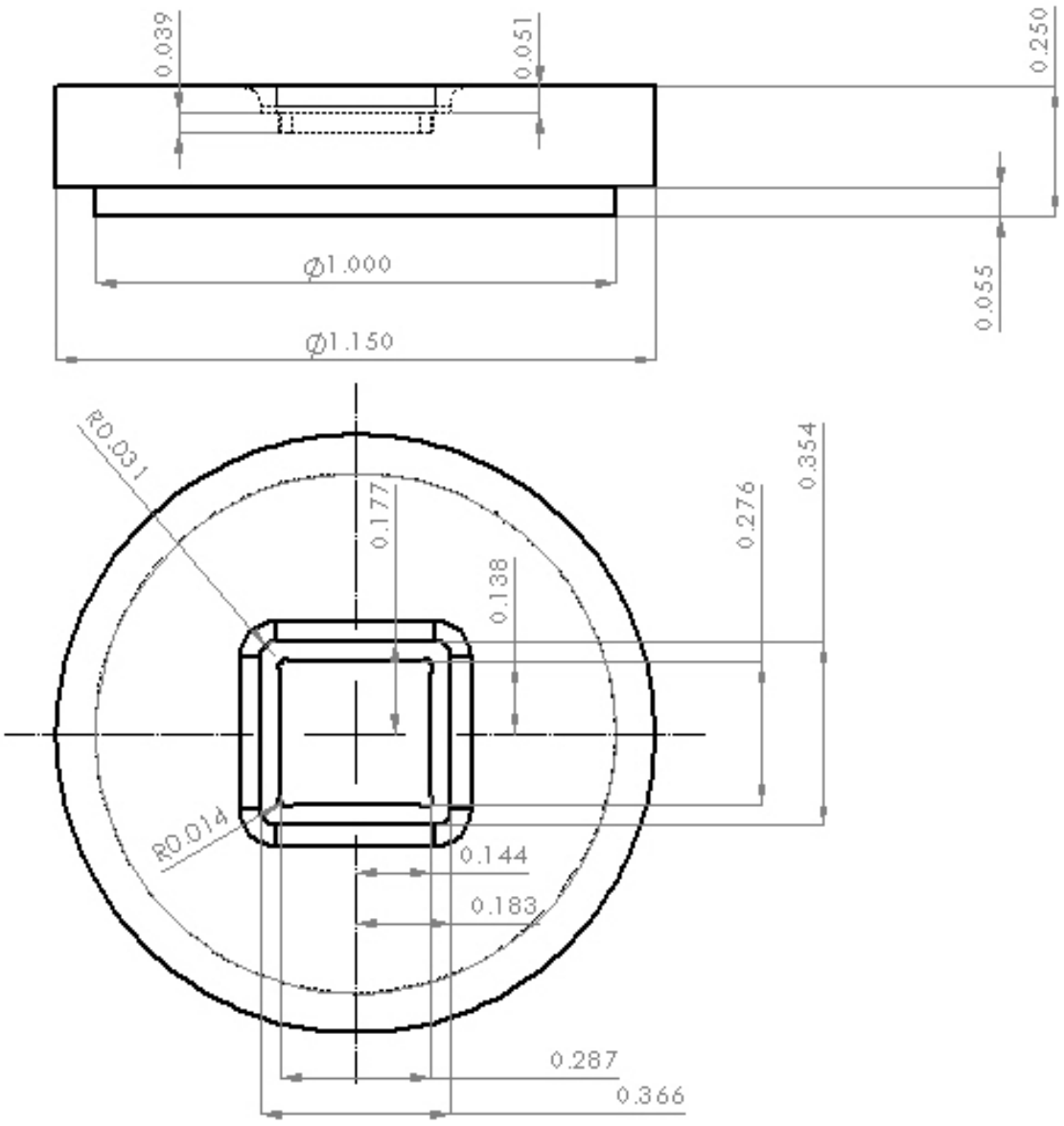

Figure D.3 Additional drawing for the moly insert (thick, SCD)

REFERENCES

REFERENCES

1. J. Angus and C. Hayman Low-pressure, metastable growth of diamond and diamondlike phases, Science 241 913-21, 1988

2. W. Yarbrough and R. Messier Current issues and problems in the chemical vapor deposition of diamond, Science 247 688-96, 1990

3. J. Butler and H. Windischmann Developments in CVD-diamond synthesis during the past decade, MRS Bull. 23 22-7, 1998

4. W. Wang, T. Moses , R. Linares, J. Shigley, M. Hall and J. Bulter Gem-quality synthetic diamonds grown by a chemical vapor deposition (CVD) method, Gems Gemol. 39 268-83, 2003

5. C. Yan, Y. Vohra, H. Mao and R. Hemley, Very high growth rate chemical vapor deposition of single crystal diamond, Proc. Natl Acad. Sci. USA 99 12523-5, 2002

6. G. Bogdan, K. De Corte, W. Deferme, K. Haenen and M. Nesladek, Thick single crystal CVD diamond prepared from CH_4-rich mixtures, Phys. Status Solidi a, 203 3063-9, 2006

7. WIKIPEDIA, The Encyclopedia, internet based

8. V. Blank, Ultrahard and superhard phases of fullerite C60: comparison with diamond on hardness and wear, Diamond and Related Materials 7: 427, 1998

9. M. Wever, Handbook of optical materials, CRC Press, p. 119, 2002

10. J. Field, C. Freeman, Strength and fracture properties of diamond, Philosophical magazine A 43 (3): 595-618, 1981

11. P. Read, Gemology (2^{nd} edition), Butterworth-Heinemann, Great Britain, P. 52,53,275,276, ISBN 0-7506-4411-7, 1999

12. J. Asmussen, D. K. Reinhard, Diamond Films Handbook, Marcel Dekker, 2002

13. S. Koizumi, C. Nebel, M. Nesladek, Physics and Applications of CVD diamond, Wiley VCH. Pp. 200-240. ISBN 3527408010, 2008

14. L. Wei, P. Kuo, R. Thomas, T. Anthony, W. Banholzer, Thermal conductivity of isotropically modified single crystal diamond, Physical Review Letters, 70 (24): 3764-3767, 1993-02-16

15. G. Davies and T. Evans, Graphitization of Diamond at Zero Pressure and at a High Pressure, Proceedings of the Royal Society a Mathematical Physical and Engineering Sciences 328: 413, 1972

16. T. Evans, P. James, A study of the transformation of diamond to graphite, Proc. Roy. Soc. A 277: 260, 1964

17. J. Asmussen, K. Hemawan, J. Lu, Y. Gu, T. Grotjohn, M. Yaran, T. Schuelke, Microwave Plasma Reactor Design for Diamond Synthesis at High Pressures and High Power Densities, 37th IEEE ICOPS, 2010

18. J. Butler, Y. Mankelevich, A. Cheesman, J. Ma, M. Ashfold, Understanding the chemical vapor deposition of diamond: recent progress, J. Phys.: Condens. Matter 21 (2009) 364201 (20pp)

19. F Silva, K Hassouni, X Bonnin and A Gicquel, Microwave engineering of plasma-assisted CVD reactors for diamond deposition, J. Phys.: Condens. Matter 21 (2009) 364202 (16pp)

20. D. G. Goodwin, J. Appl. Phys. 74(11) (1993) 6888

21. K. V. Ravi, C. A. Koch, H. S. Hu, A. Joshi, J Mater Res 5:2356, 1990

22. K. Hirabayashi, Y. Hirose, Diamond Relat Mater 5:48, 1996

23. K. Kuo, J. Asmussen, Diamond and Related Materials 6 (1997) 1097-1105

24. K. Kuo, Microwave assisted plasma CVD of diamond films using thermal-like plasma discharge, thesis, MSU 1997

25. J. Asmussen, J. Root, Ion generating apparatus and method for the use thereof, U.S. Patent No. 4,507,588, March 26, 1985

26. J. Asmussen, S. Nakanishi, J. Malinkey and S. Whitehair, Microwave electrothruster, patent applied for by NASA-Lewis

27. J. Asmussen, D. K. Reinhard, Method for treating a surface with a microwave plasma and improved apparatus, U.S. Patent No. 4,585,688, Apr. 29, 1986

28. J. Asmussen, D. K. Reinhard, Microwave or UHF plasma and improved apparatus, U. S. Patent NO. 4,630,566, Dec. 23, 1986

29. T. Ropple, D. K. Reinhard and J. Asmussen, Dual Plasma microwave apparatus and method for treating a surface, U.S. Patent No. 4,691,662, Sept. 8, 1987

30. J. Asmussen, D. K. Reinhard and M. Dahimene, Improved plasma generating apparatus using magnets and method, U.S. Patent No. 4,727,293, Feb. 23, 1988

31. J. Asmussen, Method for treating a material using radiofrequency waves, U.S. Patent No. 4,777,336, Oct. 11, 1988

32. J. Asmussen, Improved microwave apparatus, U.S. Patent No. 4,792,772, Dec.20, 1988; also Canadian Letters Patent No. 1,287,666, Aug. 13, 1991

33. J. Asmussen, D. K. Reinhard, Improved plasma reactor apparatus and method for treating a substrate, U.S. Patent No. 4,943,345, July 24, 1990

34. J. Asmussen, J. Zhang, Apparatus for the coating of material on a substrate using a microwave or UHF plasma, U.S. Patent No. 5,311,103, May 10, 1994

35. F. C. Sze, Design And Experimental Investigation Of A Large Diameter Electron Cyclotron Resonant Plasma Source, thesis, MSU 1993

36. F. C. Sze et. al., J. of Vac. Sci. Technology B8(6) 1759, 1990

37. D. King, Scaling the microwave plasma-assisted chemical vapor diamond deposition process to 150-200 mm substrates, Diamond and Related Materials 17 (2008) 520-524

38. K. Hemawan, T. Grotjohn, D. Reinhard, J. Asmussen, Improved microwave plasma cavity reactor for diamond synthesis at high pressure and high power density, Diamond and Related Materials, In Press, Available online Aug. 14, 2010

39. K. W. Hemawan, C. Yan, Q. Liang, J. Lai, S. Krasnicki, Y. Meng, H. Mao, R. Hemley, “Simulation of Microwave Plasma Discharge in 915 MHz CVD Reactor for Single Crystal Diamond Deposition”, ICOPS 2011

40. www.sekitech.com/product/DiamondCVD/MicroCVD/productline.html

41. M. Besen, E. Sevillano, D. Smith, Microwave Plasma Reactor, US patent 5,501,740

42. Y. Ando, T. Tachibana, K. Kobashi, Growth of diamond films by a 5-kW microwave plasma CVD reactor, Diamond and Related Materials 10 (2001)

312-315

43. V. Ralchenko, I. Sychov, I. Vlasov, A. Vlasov, V. Konov, A. Khomich, S. Voronina, Quality of diamond wafers grown by microwave plasma CVD: effects of gas flow rate, Diamond and Related Materials 8 (1999) 189-193

44. K. Kobashi, R&D of diamond films in the frontier carbon technology project and related topics, Diamond and Related Materials 12 (2003) 233-240

45. T. Tachibana, Diamond films grown by a 60-kW microwave plasma chemical vapor deposition system, Diamond and Related Materials 10 (2001) 1569-1572

46. E. Woerner, C. Wild, W. Mueller-Sebert, P. Koidl, “CVD-diamond optical lenses”, Diamond Relat. Mater. Vol. 5, pp688, 1996

47. www.cyrannus.com/

48. www.plassys.com/plassysf2/pageuk/machines/diamant/depot_diamant.html

49. Y. Mokuno, A. Chayahara, Y. Soda, Y. Horino, F. Fujimori, Diamond and related materials, 14 (2005) 1743 – 1746

50. Y. Mokuno, A. Chayahara, H. Yamada, N. Tsubouchi, Diamond and related materials, 18 (2009) 1258 – 1261

51. H. Yamada, A. Chayahara, Y. Mokuno, N. Tsubouchi, S. Shikata, N. Fujimori, Diamond and related materials, 20 (2011) 616 – 619

52. J. Zhang, PhD Dissertation, MSU 1993

53. K. Hemawan, PhD Dissertation, MSU 2010

54. X.J. Li, W.Z. Tang, F.Y. Wang, C.M. Li, L.F. Hei, F.X. Lu, “A Compact Ellipsoidal Cavity Type Microwave Plasma Reactor For Diamond Film Deposition”, Diamond & Related Materials 20 (2011) 374-379

55. T. Grotjoh, R. Liske, K. Hassouni, J. Asmussen, “Scaling behavior of microwave reactors and discharge size for diamond deposition”, Diamond & Related Materials 14 (2005) 288-291

56. Y. Ando, Y. Yokota, T. Tachibana, A. Watanabe, Y. Nishibayashi, K. Kobashi, T. Hirao, K. Oura, “Large area deposition of <100>-textured diamond films by a 60-kW microwave plasma CVD reactor”, Diamond and Related Materials 11 (2002) 596-600

57. J. Asmussen, T.A. Grotjohn, T. Schuelke, M. Becker, M. Yaran, D. King, S. Wicklein, D. Reinhard, “Multiple substrate microwave plasma-assisted chemical vapor deposition single crystal diamond synthesis”, Applied Physics Letters 93, 031502 (2008)

58. S. S. Zuo, M. K. Yaran, T. A. Grotjohn, D. K. Reinhard, J. Asmussen, Inverstigation of diamond deposition uniformity and quality for freestanding film and substrate applications, Diamond and Related Materials, 17,3 March 2008, pp. 300-305

59. J. Asmussen, Y. Gu, “Improved Hybrid Electromagnetic Mode Microwave Plasma Reactor”, Pub. No: MSU 4.1-921, 2011

60. M. Kamo, H. Yurimuto, Y. Sato, “Epitaxial growth of diamond on diamond substrate by plasma assisted CVD”, Applied Surface Science 33/34, 553-560 (1988)

61. L.D. Landau, “The Classical Theory of Fields”, Oxford, 1987 ISBN 0-08-018176-7

62. T.A. Grotjohn, J. Asmussen, J. Sivagnaname, D. Story, A.L. Vikharev, A. Gorbachev, A, Kolysko, Diamond and Related Materials, 9 (2000) 322.

63. RE Clausing, Diamond morphology. In: MA Prelas, G. Popovici, LK Bigelow, eds. Handbook of Industrial Diamonds and Diamond Films. New York: Marcel Dekker, 1998, pp19-47

64. S. Zuo, PhD Dissertation, MSU 2009

65. P. L. Kapitza, Soviet Physics, JETP, 30 (1970) 973.

66. S. Whitehair, and J. Asmussen, J. Propulsion and Power, 3, (1987) 136.

67. J.E Brandenburg, J.Kline, D. Sulliven, IEEE Trans. On Plasma Science 33, 2 Part 2, (2005) 776.

68. K.D. Diament, B. L. Ziegler, R. B. Cohen, J. of Propulsion and Power, 23 (2007) 27.

69. S. Offermans, J Appl Phys. 67, (1990) 115.

70. A. L. Vikharev, A. M. Gorbachev, A. V. Kolysko, D. B. Radishev, and A. B. Muchnikov, “Microcrystalline diamond growth in presence of argon in millimeter wave plasma assisted CVD reactor”, Diamond and Related Materials 17, 1055 (2008)

71. A Gicquel, E Anger, MF Ravet, D Fabre, G Scatena, ZZ Wang, “Diamond deposition in a bell-jar reactor: influence of the plasma and substrate parameters on the microstructure and growth rate”, Diamond Related Material 2:417-424, 1993

72. D Takeuchi, H Watanabe, S Yamanaka, H Okushi, K Kajimura, “Defects in device grade homoepitaxial diamond thin films grown with ultra-low CH_4/H_2 conditions by microwave-plasma chemical vapor deposition”, Phys Status Solidi(a) 174:101-115, 1999

73. CF Edwards, DW Hahn, Proceeding of ILASS-95 (Institute for Liquid Atomization and Spray Systems), Troy, MI 1995 p34

74. CA Wolden, Z Sitar, RF Davis, JT prater. Diamond Related Material 6:1862, 1997

75. J. Lu, Y. Gu, D. Reinhard, T. Grotjohn, J. Asmussen, “Microwave Plasma Assisted Synthesis of Single Crystal Diamond at High Pressure and High Power Densities”, 38th International Conference Plasma Science, 2011

76. Q. Liang, C. Yan, Y. Meng , J. Lai, S. Krasnicki, H. Mao, R. Hemley, J. Phys.: Condens. Matter 21 (2009) 364215

77. V. Ralchenko, Diamond and Related Materials 16 (2007) 2067-2073

78. SA Solin, K Ramdas, Phys. Rev. B,1 (1970) 1687

79. M. Muehle, “Untersuchungen der Materialqualität von mittels chemischer Gasphasenabscheidung und Hochdruck-Hochtemperatur Verfahren hergestellten Diamantkristallen”, thesis (German), 2011

80. J. Ager and M. Drory. Quantitative measurement of residual biaxial stress by Raman spectroscopy in diamond grown on a Ti alloy by chemical vapor deposition. Physical Review B, 48(4): 2601–2607, July 1993

81. A. R. Lang, M. Moore, A. P. W. Makepeace, W. Wierzchowski, and C. M. Welbourn. On the Dilatation of Synthetic Type Ib Diamond by Substitutional Nitrogen Impurity. Philosophical Transactions of the Royal Society A: Mathematical, Physical and Engineering Sciences, 337(1648): 497–520, December 1991

82. H. Windischmann, G. F. Epps, Y. Cong, and R. W. Collins. Intrinsic stress in diamond films prepared by microwave plasma CVD. Journal of Applied Physics, 69(4): 2231, 1991.

83. M. Donato. A joint macro-/micro- Raman investigation of the diamond lineshape in CVD films: the influence of texturing and stress. Diamond and

Related Materials, 10(8): 1535–1543, August 2001.

84. www.condensed-matter.uni-tuebingen.de/cms/en/facilities/sims.htm

85. www.en.wikipedia.org/wiki/Fourier_transform_infrared_spectroscopy